Structural and Functional Studies of Copper Homeostasis in Eukaryotic Cells

Submitted by

Shadi Maghool

Master of Biotechnology and Bioinformatics,
2015 La Trobe University

A thesis submitted in total fulfilment of the requirements for the degree of

Doctor of Philosophy

Department of Biochemistry and Genetics
School of Molecular Science
College of Science, Health and Engineering

La Trobe University
Victoria, Australia

June 2019

Table of Contents

Statement of authorship

This thesis includes work by the author that has been published or accepted for publication as described in the text. Except where reference is made in the text of the thesis, this thesis contains no other material published elsewhere or extracted in whole or in part from a thesis accepted for the award of any other degree or diploma. No other person's work has been used without due acknowledgment in the main text of the thesis. This thesis has not been submitted for the award of any degree or diploma in any other tertiary institution.

Shadi Maghool

28 June 2019

Acknowledgments

I would firstly like to express my deepest appreciation to my wonderful supervisor Associate Professor Megan Maher that without her endless patience, persistence support and guidance this dissertation would have not been possible. *Dear Megan: Thank you very much for all you have done for me! Thank you for providing me with opportunities to collaborate with such enthusiastic scientists at different institutes to carry out work for this thesis. Thank you for your generosity in supplying financial support that has allowed me to attend various national and international conferences during the course of my PhD.*

I would also like to acknowledge the contributions of individuals who assisted me in the experimental work presented in this thesis. The NMR experiments reported in Chapter 2 were carried out in collaboration with Dr Ann Kwan at the University of Sydney. *Dear Ann: Thank you very much for your wonderful instructions and kind hospitality you showed me on my visits to Sydney.* I'd also like to thank Dr Sharon La Fontaine (Deakin University) and Dr Blaine Roberts (Florey Institute, Melbourne University) for providing the plasmid constructs and assisting me with the SEC-ICP-MS experiments, respectively.

The studies presented in Chapter 3 and Chapter 4 were carried out in collaboration with Professor Mike Ryan laboratory at Monash University. *Dear Mike: Thank you very much for giving me the outstanding opportunity of working in your lab where I learned something new and tried something different with such entertaining and kind individuals.* The cell biology experiments in Chapter 3 were carried out in collaboration with Dr David Stroud (Bio21 Institute, Melbourne University). The cell biology experiments reported in Chapter 4 were performed by Dr Luke

Formosa (Ryan Lab, Monash University). Dinesha Cooray (La Trobe University) performed protein production and crystallisation of ^{WT}Coa6 protein in Chapter 3. Dr Pierre Faou (La Trobe Institute for Molecular Science) performed the mass spectrometry experiment in Chapter 3 and Dr Yee-Foong Mok (Bio21 Institute, Melbourne University) performed the AUC experiments presented in Chapter 4.

I would also like to acknowledge the financial support that I have received throughout my PhD candidature. This work was supported by an Australian Government Research Training Program Scholarship in addition to scholarships from the La Trobe University, International Union of Crystallography (IUCR) and the Society of Crystallographers in Australia and New Zealand (SCANZ) that have allowed me to attend various conferences.

Thank you to the past and present members of the Maher, Lee and Ryan lab. I was very lucky to experience these memorable years in a friendly environment. All the respect, support and assistance that I received made this challenging journey easier and more gratifying. *Dear Mihwa: Thank you for all your support and valuable advice. Patricia, Daniel, Moe, Jie, Saumya, Dylan, Shadiya, Dinesha, Ghruta and Nilakhi: Thank you all for being best lab mates ever!*

Finally, with everlasting gratitude and love, I would like to dedicate this humble achievement to my beloved parents, *Ja'afar* and *Mahnaz* and also treasured siblings whose presence through all struggles and trials has been a constant source of hope and happiness. *Mom, Dad, Jamshid, Mahshid and Farshid: I am so lucky to have you as my family. I love you!*

Abstract

Copper is an essential trace element for all living organisms, where it acts as an active cofactor for a wide range of biological processes, including mitochondrial respiration. However, excess intracellular copper must be strictly limited due to its toxic side effects. Human intracellular copper trafficking, including that to *trans*-Glogi network and the mitochondria are crucially important processes, with copper dysregulation being associated with disorders such as Menkes, Wilson's and mitochondrial diseases. Cytochrome *c* oxidase (COX), a terminal electron acceptor in the mitochondrial respiratory chain, requires copper ions for the construction of dinuclear Cu_A and mononuclear Cu_B sites, both of which are critical for assembly and activity of the complex. Mutations in assembly factors required for copper delivery to COX result in diminished COX activity and severe pathologic conditions in affected individuals.

Chapter 2 of this thesis investigated the regulatory role of the enzyme human glutaredoxin (hGrx1), a cytosolic thiol disulfide oxidoreductase, in intracellular copper trafficking pathways. The aims of this study were: to establish whether hGrx1 plays a role in copper delivery to the copper metallochaperone Atox1 and the metal binding domains 5 and 6 of the ATP7B (WLN5-6) and to determine the thermodynamic factors that reinforce copper trafficking. Using SEC-ICP-MS the hGrx1 protein was demonstrated to transfer copper to the metallochaperone Atox1 and to the WLN5-6 domains in an irreversible manner. Crucially, this study revealed that hGrx1 preferentially delivers copper to the WLN5-6 domains, despite the presence of Atox1. Moreover, protein-protein interactions between hGrx1, Atox1 and WLN5-6 were detected by NMR spectroscopy both in the presence and absence of copper. Interestingly, both

the Atox1 protein and WLN5-6 domains bind to a common surface on the hGrx1 protein. This study established that both the thermodynamics of the interactions between the protein pairs and that of the proteins with copper play key roles in the determination of the directionality of intracellular copper trafficking. Furthermore, Section 2.3 (Paper I) as part of Chapter 2 outline the structural features of the reduced Grx1 from yeast *Saccharomyces cerevisiae* (yGrx1). The structure of reduced yGrx1 revealed differences in the conformations of residues neighbouring the active site (Cys27-Cys30) in comparison with those of the oxidised and glutathionylated proteins owing to alterations in the redox status.

In addition, this thesis focuses on two mitochondrial COX assembly factors, the Coa6 and Coa7 proteins, which are located in the intermembrane space of mitochondria and contain intramolecular disulfide bonds. Chapter 3 investigates the detailed structural and functional characterisation of the human Coa6 protein. Coa6 binds copper with femtomolar affinity and Coa6 has been proposed to play a role in the biogenesis of the Cu_A site of COX. The W59C pathogenic mutation in Coa6 does not affect copper binding but affects the maturation and stability of the protein. In this study, the X-ray crystal structure of ^{WT}Coa6 to 1.6 Å resolution was determined and showed the protein structure is composed of a three helical bundle, where the N-terminal helical pair is tethered at each end by intramolecular disulfide bonds. This work demonstrates that the protein includes a single Cu(I) binding site, positioned between residues Cys58 and Cys90. The structure of the ^{W59C}Coa6 mutant protein, determined to 2.2 Å resolution, shows that the mutation leads to disulfide mediated protein oligomerisation, revealing the molecular basis of its pathogenesis.

Finally, Chapter 4 of this thesis focuses on the structural and functional characterisation of the human Coa7 protein. Coa7 is a metazoan-specific COX assembly factor with 13 cysteine residues in its sequence. The precise role of Coa7 in the biogenesis of COX is not completely understood. However, patients with Coa7 pathogenic mutations suffer from mitochondrial diseases owing to COX deficiency. Interestingly, recombinant Coa7 shows that the protein binds heme with micromolar affinity. Moreover, the crystal structure of the ^{WT}Coa7 protein was determined to 2.4 Å resolution, which is composed of 11 α-helices, arranged as five disulfide bridged helix-turn-helix (α/α) repeats. The structural determination of ^{WT}Coa7 allows the molecular origins of the pathogeneses observed for the patient mutations to be proposed.

List of Figures

List of Tables

List of abbreviations

Å	Angstrom
asu	Asymmetric unit
Atox1	Antioxidant protein 1
ATP	Adenosine triphosphate
ATP7A	Menkes' protein (copper transporting P-type ATPase)
ATP7B	Wilson's protein (copper transporting P-type ATPase)
ATPase	Adenosine triphosphatase
AUC	Analytical Ultracentrifugation
Bcs	Bathocuproinedisulfonic acid
BN-PAGE	Blue Native polyacrylamide gel electrophoresis
CCS	Copper chaperone for superoxide dismutase
CD	Circular dichroism
Coa6	Cytochrome *c* assembly factor 6
Coa7	Cytochrome *c* assembly factor 7
Co-IP	Co-immunoprecipitation
COX	Cytochrome *c* oxidase
COX1	Cytochrome *c* oxidase subunit 1
COX2	Cytochrome *c* oxidase subunit 2
COX3	Cytochrome *c* oxidase subunit 3
CRISPR	Clustered Regularly Interspaced Short Palindromic Repeats
cryo-EM	Cryo-electron microscopy
Ctr1	Copper transporter 1
Cys	Cysteine
Cu	Copper
CuL	Copper ligand

Da	Dalton
Dig	Digitonin
DSS	4,4-dimethyl-4-silapentane-1-sulfonic acid
E. coli	*Escherichia coli*
EDTA	Ethylenediaminetetraacetic acid
FALS	Familial amyotrophic lateral sclerosis
g	Gravitational force
Grx1	Glutaredoxin-1
GSH	Glutathione
GSSG	Glutathione disulfide
GST	Glutathione S-transferase
HEK293T	Human embryonic kidney 293 cells, large T antigen
hGrx1	Human glutaredoxin-1
His	Histidine
HSQC	Heteronuclear single quantum coherence
IM	Inner membrane
IMS	Intermembrane space
IPTG	Isopropyl β-D-1-thiogalactopyranoside
ITC	Isothermal titration calorimetry
KO	Knockout
LB	Lysogeny broth
MBD	Metal binding domain
MD	Menkes disease
MNK	Menkes' protein (copper transporting P-type ATPase)
MS/MS	Tandem mass spectrometry
Mt-DNA	Mitochondrial DNA

MW	Molecular weight
MWCO	Molecular weight cut-off
NMR	Nuclear magnetic resonance
OD_{600}	Optical Density (measures at 600 nm)
OM	Outer membrane
ORF	Open reading frame
OXPHOS	Oxidative phosphorylation
P_{1B}-ATPase	P-type ATPase of the heavy metal transporting P1B subfamily
PBS	Phosphate buffered saline
PEG	Polyethylene glycol
PCR	Polymerase chain reaction
r.m.s.d.	Root mean square deviation
ROS	Reactive oxygen species
S. cerevisiae	*Saccharomyces cerevisiae*
SD	Standard deviation
SDS-PAGE	Sodium dodecyl polyacrylamide gel electrophoresis
SEC	Size exclusion chromatography
SEC-ICP-MS	Size exclusion chromatography inductively coupled plasma mass spectrometry
SLR	Sel1-like repeat
Sod1	Cu/Zn superoxide dismutase 1
SV	Sedimentation Velocity
TCEP	tris (2-carboxyethyl) phosphine hydrochloride
TEV	Tobacco Etch Virus
TGN	*trans*-Golgi network
T_m	Melting temperature

TMD	Trans-membrane domain
TPR	Tetratricopeptide repeat
TX-100	Triton X-100
UV-vis	Ultraviolet-visible
WLN	Wilson's disease
WLN5-6	Metal binding domains 5 and 6 of ATP7B
WT	Wild-type

List of publications

Published manuscript

Maghool S*, La Fontaine S, & Maher MJ* (2019) **High-resolution crystal structure of the reduced Grx1 from *Saccharomyces cerevisiae***. *Acta crystallographica. Section F, Structural biology communications 75(Pt 5):392-396.*

*Corresponding authors.

Maghool S, Cooray NDG, Stroud DA, Aragão D, Ryan MT, & Maher MJ (2019) **Structural and functional characterization of the mitochondrial complex IV assembly factor Coa6.** *Life Science Alliance 2(5): e201900458.*

Submitted manuscripts

Maghool S, La Fontaine S, Roberts BR, Kwan AH, & Maher MJ. (2019) **Human glutaredoxin-1 can transfer copper to the isolated metal binding domains of the P_{1B}-type ATPase, ATP7B.** *Scientific reports.*

Chapter 1

An Introduction to Human Intracellular Copper Trafficking Pathways and Cytochrome *c* oxidase Assembly

1.1 Introduction

Copper is one of the vital trace elements required by the majority of living organisms. Humans acquire copper through the diet and the daily requirement for adults is recommended to be ~1 mg. The total copper content of the human body is approximately 70 mg which is significantly lower than other cations including calcium (10^6 mg) (1, 2). However, maintaining the balance of this essential metal is extensively crucial to sustain human health.

In biological systems, copper is found in two oxidation states, reduced Cu(I) (cuprous copper) with 10 valence electrons and the more bioavailable, oxidised Cu(II) (cupric copper) with 9 valence electrons. These reversible states, which allow copper to serve as both oxidant and reductant, coupled with a redox potential range of 0-800 mV render it an exceptional cofactor for redox enzymes known as oxidoreductases. Due to this redox activity, copper plays a crucial role in a wide range of ubiquitous biological processes such as mitochondrial respiration, protection against reactive oxygen species (ROS), iron homeostasis and hormone and neurotransmitter biogenesis (2-6). However, excess intracellular concentrations of copper (beyond 10 μM) (7) are toxic due to its intrinsic redox activity which, in turn, can lead to cellular oxidative damage (8, 9). For instance, upon the reaction between hydrogen peroxide and Cu(I) ions and subsequent superoxide reduction of Cu(II) ions, hydroxyl radicals are formed which deteriorate proteins, nucleic acids and lipids *via* Fenton-based chemistry (10, 11).

1.2 Cellular copper homeostasis

Within cells, handling of copper requires sophisticated mechanisms to orchestrate its acquisition, intracellular distribution and mobilisation. Since the cytosol is a reducing environment owing to presence of glutathione (GSH), intracellular copper generally exists within cells in its reduced state (Cu(I)) (12, 13). Intracellular Cu(I) tightly binds to thiol possessing molecules such as GSH and copper binding proteins (known as 'metallochaperones') (8). Both Cu(I)-metallochaperones and GSH are essential components to preserve the fine balance of required intracellular copper and therefore protect the cell against copper toxicity (12, 14). In this way, labile Cu(I) is rarely found in the cytosol and its concentration is estimated to be less than 10^{-18} M (9, 15).

Copper can bind to amino acid side-chain ligands including cysteine, histidine glutamic acid and methionine (16-18). However, according to the HSAB theory (Hard and Soft Acids and Bases) Cu(I) as a "soft" acid has a preference for sulfur atoms of cysteine or methionine residues as a ligand ("soft" bases) whereas "hard" acid Cu(II) is more selective toward nitrogen atoms of histidine residues ("hard" bases). Accordingly, high-affinity Cu(I)-binding metallochaperones possess Cys-x_n-Cys motifs where Cu(I) binds *via* coordination with the thiol groups (SH) of the Cys residues (19, 20).

Cellular copper homeostasis is primarily achieved through a complex network of numerous proteins such as copper metallochaperones, metalloregulatory proteins and membrane transporters. These proteins are responsible for both the supply of copper to the corresponding proteins and for detoxification and efflux of excess copper from cells (11, 19). Function-impairing mutations in these proteins lead to

disruptions in the regulation of copper metabolism, which in turn is commonly manifested in neurodegenerative diseases such as prion diseases, Alzheimer's disease, Parkinson's disease, fatal motor neuron diseases such as familial amyotrophic lateral sclerosis (FALS) and Menkes disease (21-23). In addition, another genetic condition named Wilson's disease leads to the accumulation of copper in the liver resulting in copper toxicity (21, 24-26).

In humans, the copper transporter 1 (Ctr1) facilitates cellular copper uptake. Once Cu(I) enters the cytosol, it is trafficked to at least three distinct cellular destinations *via* the action of metallochaperone proteins that escort Cu(I) to its specific targets (5, 27, 28) (Figure 1-1). The Cu(I)-metallochaperone CCS (copper chaperone for superoxide dismutase) delivers Cu(I) to Sod1 (Cu/Zn superoxide dismutase 1), the only copper-dependent enzyme that resides in the cytosol. Sod1 is responsible for the detoxification of superoxide radicals (O_2^-) (4, 29, 30). The Cu(I)-metallochaperone Atox1 (31-33) transfers Cu(I) to ATP7A (Menkes disease protein, MNK) (34, 35) and ATP7B (Wilson disease protein, WLN) (33, 36, 37), two Cu(I)-specific P_{1B}-type ATPases in the *trans*-Golgi network (TGN). ATP7A/7B act to deliver Cu(I) into copper dependent enzymes in the secretory pathway. Copper is also trafficked to the mitochondria. Although the precise mechanism by which Cu(I) enters the mitochondria from the cytosol is not clear, it is suggested that an anionic fluorescent molecule (also known as copper ligand (CuL)) (38) and GSH (39) might be potential candidates which carry Cu(I) into the mitochondria. Within this organelle copper is incorporated into the cytochrome *c* oxidase (COX) with the aid of additional mitochondrial copper chaperones (ie, Cox17, Cox11, Sco1, Sco2, and Coa6) (40-43).

The human glutaredoxin-1 protein (hGrx1), a cytosolic thiol disulfide oxidoreductase (44, 45) that regulates the redox status of protein thiols, actively interacts with the copper chaperone, Atox1 (32). Also, studies have proposed that interactions of a similar nature between hGrx1 and ATP7A and ATP7B might exist in the process of copper trafficking (32, 46-48).

With this emerging picture, in addition to reviewing the existing intricacies involved in intracellular copper trafficking to the secretory pathway and mitochondria, this chapter also focuses on cytochrome *c* oxidase (COX) biogenesis.

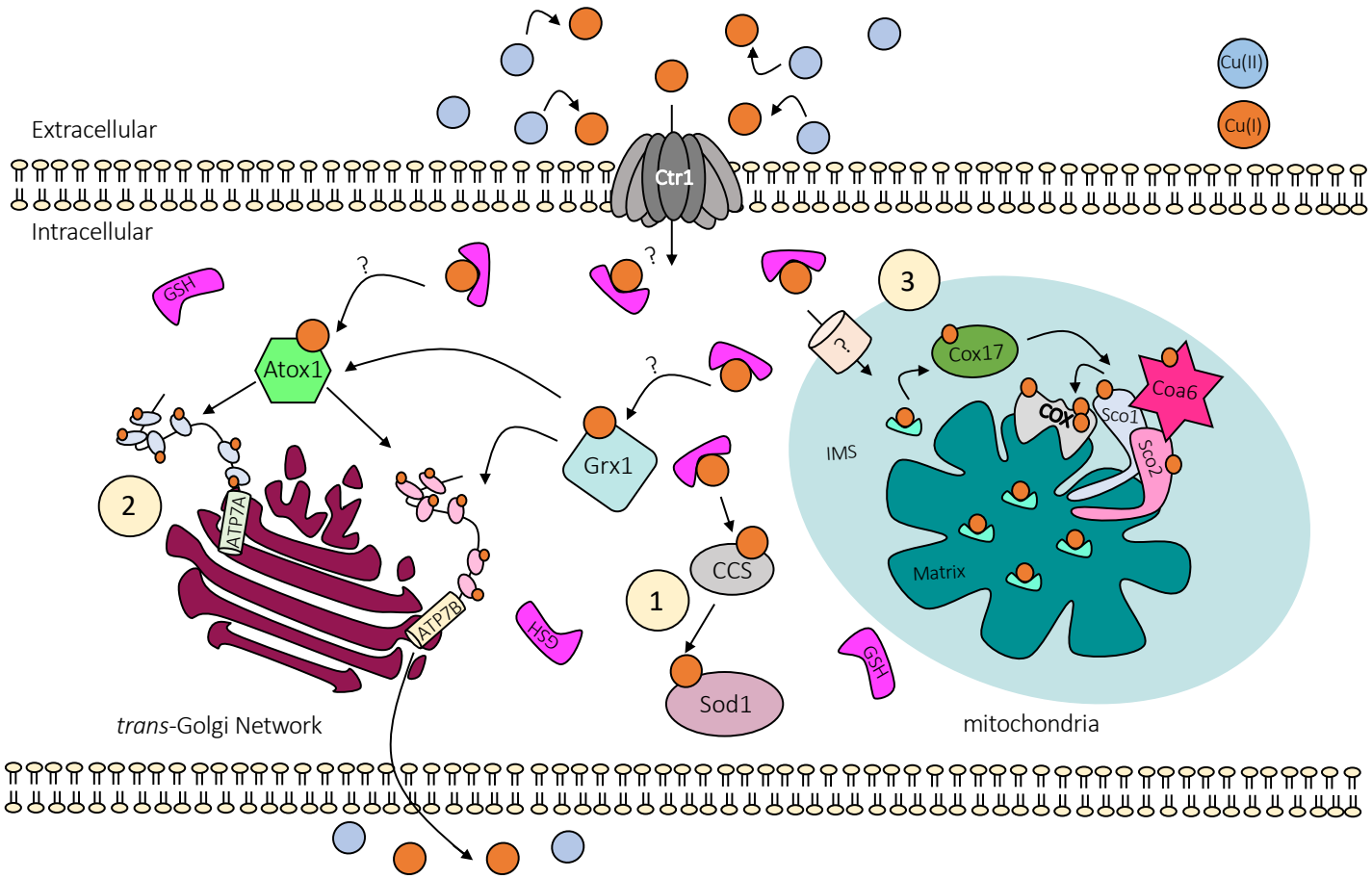

Figure 1-1 Copper trafficking pathways in human cells.

There are three major pathways of intracellular copper trafficking (1) to Sod1 (2) to the trans-Golgi network and (3) to mitochondria. These trafficking events are mediated by specific Cu(I)-metallochaperones, CCS, Atox1 and Cox17, respectively. Cu(I) and Cu(II) ions are shown as orange and blue circles, respectively.

1.3 Cu(I) entry through the Ctr1 transporter

Ctr1, the copper transporter located in the plasma membrane and endosomal vesicles plays an essential role in eukaryotic copper trafficking. This high-affinity copper importer translocates extracellular copper across the plasma membrane into the cytosol for intracellular distribution (5, 49). Ctr1 is highly selective for Cu(I). For example, treating yeast and mammalian cells with the reducing agent ascorbate, increases the copper uptake by both organisms (50-52). Moreover, it has been reported that isoelectric Ag(I), a Cu(I) surrogate, effectively competes for Ctr1 facilitated Cu(I) acquisition (52).

In humans, Ctr1 is a homotrimer where each monomer is composed of 190 amino acids (23 kDa) and possesses three trans-membrane α-helices, a 67 amino acid extracellular N-terminal domain and a 15 amino acid C-terminal intracellular tail (27, 53, 54) (Figure 1-2*A*). Until recently, low-resolution structures of the human Ctr1 *via* cryo-electron microscopy (cryo-EM) (~7 Å) (55) and two-dimensional electron crystallography (56) were the only available three-dimensional structures of Ctr1 (28). These data corroborated prior biochemical and genetic studies of the membrane topology and oligomeric assembly of the transporter where a trimeric structure with a central pore was shown to form a channel-like architecture (57-59).

Recently, the crystal structure of an engineered *Salmo salar* Ctr1 protein (sCtr1) with 78% sequence identity with the human Ctr1 has been reported in the presence and absence of Cu(I) (PDB 6M98 and PDB 6M97, respectively) (54) (Figure 1-2*B*). The crystal structure of sCtr1 revealed a similar trimeric structure as previously reported through genetic and cryo-EM studies (55, 57-59). Earlier studies indicated that Cu(I) transport across membranes *via* Ctr1 is energy-

independent and therefore this high-affinity Cu(I) importer functions as an ion channel (52).

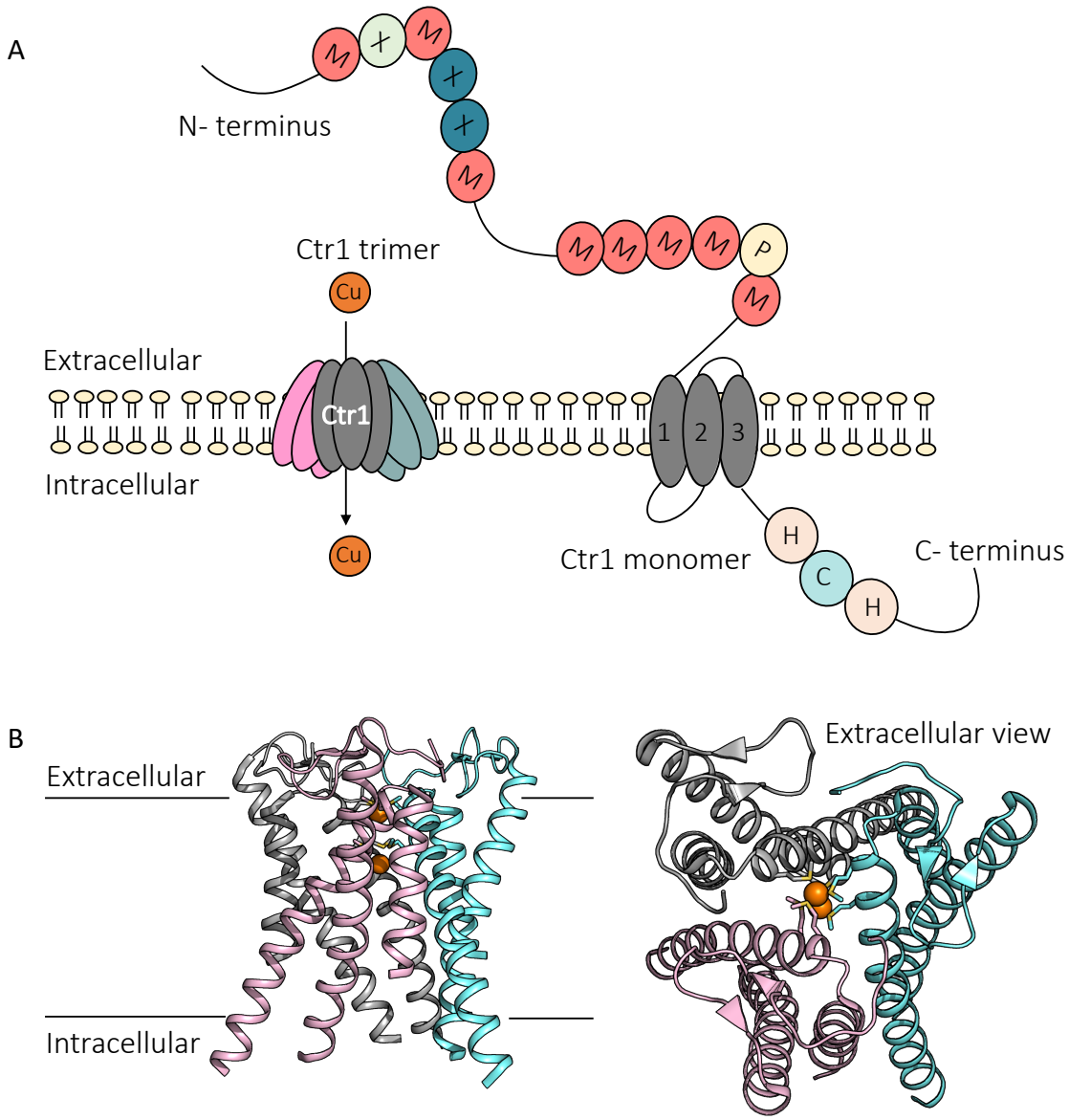

Figure 1-2 The overall architecture of sCtr1.

(A) Schematic illustrates the overall structure of monomeric and trimeric human Ctr1. (B) Crystal structure of sCtr1. Cartoon representation of the overall structure of sCtr1. Secondary structures are represented as cartoons with monomers coloured in cyan, grey and pink (PDB 6M98) (54). Cu(I) ions are shown as orange spheres. Left: Extracellular view as in right.

The Cu(I)-bound structure of sCtr1 is strikingly similar to the Cu(I) free structure (54). Cu(I)-bound sCtr1 structure shows two Cu(I) binding sites where Cu(I) ions are bound to thioether groups of the Met146 and Met150 residues from each monomer *via* three-coordinate binding sites with an ~8 Å distance between the two Cu(I) sites (54). The three thioether groups of methionine for Cu(I) coordination form the trigonal planar geometry of Cu(I) which differs from the Cu(II) four-coordinate square planner geometry. These two methionine residues in each monomer create a selectivity filter for Cu(I) in Ctr1.

A calculation of the surface electrostatics of the sCtr1 structure revealed that the central pore is composed of polar amino acid side chains, implying that the pore mediates charge movement across the hydrophobic membranes. For instance, the negatively charged region of the pore, which is located above the selectivity filter at the extracellular entrance would attract positively charged Cu(I) ions. The C-terminus might act as a gate for Cu(I) entrance to the cytosol due to presence of a His-Cys-His motif which possibly possesses a higher Cu(I)-binding affinity to that of the selectivity filter. However, further studies are required to elucidate the precise role of the C-terminus region (54).

1.4 GSH; a potential primary Cu(I) receiver in the cytosol

The detailed mechanism by which Cu(I) transfers from Ctr1 to the Cu(I)-metallochaperones in the cytosol is undefined. GSH has been proposed to buffer metals including copper in the cytosol (16, 60). GSH binds copper with picomolar affinity ($K_D = 9 \times 10^{-12}$ M) and the formation of a complex between GSH and copper inhibits unwanted copper reactions and subsequent copper toxicity (4). Given that GSH Cu(I)-binding affinity is several orders of magnitude lower than that of Cu(I)-metallochaperones (with K_D values in the range 10^{-15}-10^{-17} M) (32, 61), it acts

as a Cu(I) buffer by which Cu(I) can be effectively exchanged between GSH and Cu(I)-metallochaperones (4).

1.5 Copper trafficking to the secretory pathway

1.5.1 Atox1; an essential Cu(I)-metallochaperone for Cu(I) delivery to the secretory pathway

Various organisms are known to possess members of the Atx1-like copper transporting protein family. In humans, Atox1 (also known as Hah1), a 68 amino acid cytoplasmic protein, binds Cu(I) with K_D values in the range of 10^{-17}-10^{-19} M depending on the pH (32). It is well established that Atox1 delivers Cu(I) to the N-terminal metal binding domains (MBDs) of the ATP7A and ATP7B transporters (62-64). The structure of Cu(I)-bound Atox1 (PDB 1FEE) (65) (Figure 1-3) was the first crystal structure reported of a metallochaperone with Cu(I) present in the metal binding site. The structure showed Atox1 has a βαββαβ fold with an exposed Cys-xx-Cys motif (C12-xx-C15). In this structure, two Atox1 monomers were linked by a Cu(I) ion.

The activity of the Atox1 protein can be modulated by the intracellular redox status *via* alterations in the ratio of glutathione and oxidised glutathione (GSH: GSSG) (2, 14). For instance, in differentiating neuronal cells, due to the increased ratio of GSH: GSSG, the Atox1 Cys-xx-Cys motif undergoes complete reduction. This in turn, enhances the Cu(I) binding capability of the Atox1 and therefore more Cu(I) is trafficked to Cu(I)-ATPases. Consequently, more Cu(I) would be available for the copper dependent enzymes in the secretory pathways. On the other hand, upon a decrease of the ratio of GSH: GSSG ratio in proliferating cells, the Cys-xx-Cys motif of Atox1 is partially oxidised, which protects the protein from metalation (66).

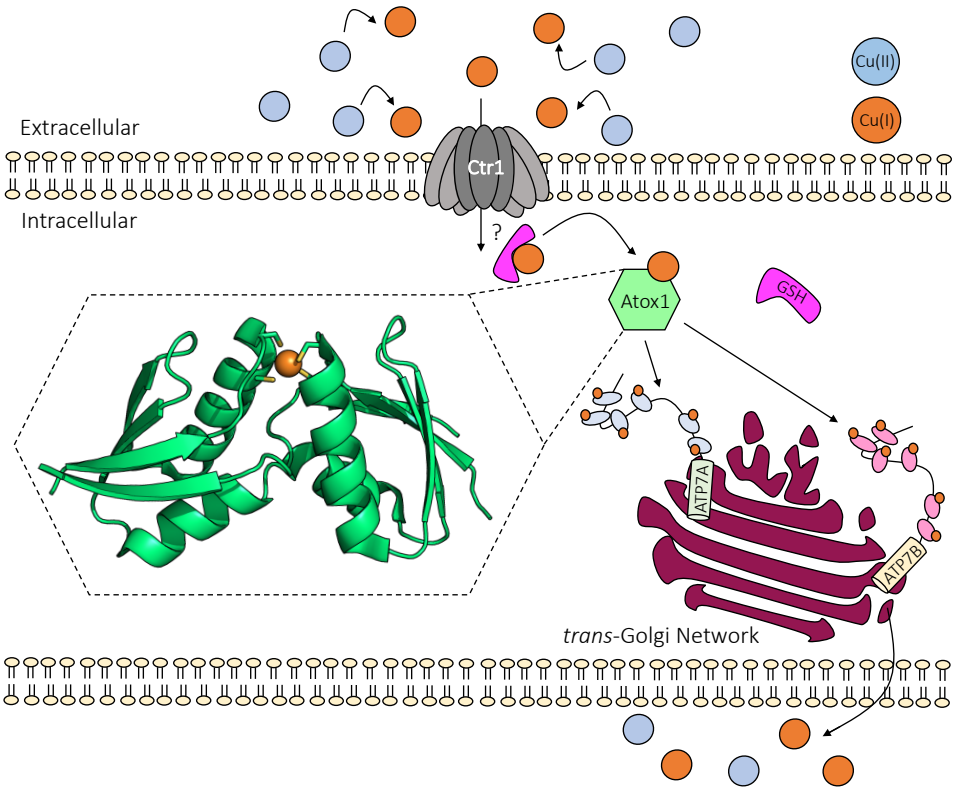

Figure 1-3 The crystal structure of Cu(I)-bound Atox1.

Crystal structure of Atox1 (PDB 1FEE) (65) is represented as a cartoon, with helices and β sheets depicted in green. Cu(I) atoms are shown as orange circles and spheres. The Cu(I)-metallochaperone Atox1 transfers Cu(I) to the metal binding domains of the Cu(I)-ATPases (ATP7A/7B). Sulfur atoms are shown as yellow sticks.

1.5.2 ATP7A and ATP7B; two Cu(I)-specific P_{1B}-type ATPases involved in Cu(I) trafficking through the secretory pathway

In humans, ATP7A and ATP7B are two Cu(I)-specific P_{1B}-ATPases in the TGN that are actively involved in the process of Cu(I) delivery to the secretory pathway (67, 68). At basal levels of intracellular Cu(I), upon receiving copper from Atox1, these Cu(I)-ATPases translocate Cu(I) across the Golgi membranes against a concentration gradient to activate copper-dependent enzymes including tyrosinase, lysyl oxidase and ceruloplasmin in the secretory pathway (33, 69). However, at elevated intracellular Cu(I) concentrations, these enzymes leave the

TGN and translocate to the cytosolic membrane and efflux excess Cu(I) from the cell *via* vesicle-mediated exocytosis (70, 71).

Although ATP7A and ATP7B share high levels of sequence similarity (67% similarity), their regulation, functions and tissue distribution are entirely different (67, 72). ATP7A is expressed in almost all tissues particularly non-hepatic tissues, including the intestine and the brain (72-74). The major role of ATP7A is in mediating copper uptake from intestinal enterocytes to the blood and copper delivery from the choroid plexus into the brain. Patients carrying pathogenic mutations in *ATP7A* suffer from Menkes disease (MD) with connective tissue abnormalities and neurological disorders due to an intracellular copper deficiency and impaired copper transfer to the brain. In MD patients, copper levels in the blood are decreased due to the accumulation of copper in the intestines and therefore diminished copper delivery to other tissues (72-74). ATP7B, on the other hand, is primarily expressed in the liver and its crucial role is to maintain the basal level of copper in this hepatic tissue by excreting unwanted copper into the bile. Pathogenic mutations in *ATP7B* lead to Wilson's disease, which is characterised by a chronic copper toxicosis and consequent liver failure (26, 75, 76).

Structurally, ATP7A and ATP7B share similar architectures with other structurally characterised P-type ATPases such as the *Legionella pneumophila* CopA (LpCopA) (77), Na^+, K^+-ATPase (78) and sarcoplasmic reticulum Ca^{2+}-ATPase (SER-CA1a) (79). The cytosolic regions of these ATPases are composed of a phosphorylation domain (P-domain), a nucleotide-binding domain (N-domain) and an actuator domain (A-domain), while the trans membrane domains (TMD) possess eight transmembrane helices for the copper translocation (36, 65) (Figure 1-4). A distinguishing feature of the Cu(I)-ATPases is the presence of a large

(630 residues), cytosolic amino terminal extension that is composed of six metal binding domains (MBDs). Each MBD (~70 residues) includes a conserved Cys-xx-Cys motif which binds Cu(I) with high affinity *via* coordination between the two cysteine residues (36, 37). Interestingly, MBDs adopt similar folds to that of Atox1 (ferredoxin-like βαββαβ fold) and are connected to each other by linkers. The linkers are flexible and facilitate copper exchange between MBDs *via* protein-protein interactions (36, 37, 65).

Although the mechanisms by which Cu(I) exchange occurs between Atox1 and the MBDs of Cu(I)-ATPases have been studied extensively using full length and truncated constructs of MBDs, the detailed steps of Cu(I) delivery from the MBDs to the TMD of the Cu(I)-ATPases for copper translocation remains ambiguous. Wilson's disease is associated with mutations in the MBDs of ATP7B protein particularly MBD5 and MBD6, which have been shown to adversely impact the interaction with Atox1 indicating the significant role of MBDs in Cu(I)-ATPase function (33, 36, 80). Earlier studies proposed that the Cu(I)-metallochaperone Atox1 transfers Cu(I) to the MBDs1-4 of ATP7B that exist close to the vesicular segment but not to the MBDs5-6 in close proximity to the membrane spanning segment (36, 70). An NMR titration experiment studying Cu(I) exchange between Cu(I)-Atox1 and ATP7B MBD constructs of MBD4 and MBDs5-6 (36) revealed that Cu(I)-Atox1 specifically transfers Cu(I) to MBD4 through formation of a stable complex and not to MBDs5-6 implying that MBDs1-4 are the key components in receiving Cu(I) from Atox1. However, MBDs5-6 are involved in trafficking Cu(I) to the TMD of the Cu(I)-ATPases for copper efflux. This differs from recent reports that have demonstrated Cu(I)-Atox1 can transfer Cu(I) to all six MBDs of ATP7B. These studies have suggested that not all MBDs are equivalent in terms of receiving Cu(I) from Atox1. Specifically, MBD2 has been proposed to act as a preferential Cu(I) receiver from Cu(I)-Atox1 while MBD4 does not interact with

the other MBDs (63, 81, 82). In this model, the MBDs1-3 play a regulatory role while MBDs5-6 are primarily involved in Cu(I) delivery to the TMD of the transporter and MBD4 act as a structural linker between MBDs1-3 and MBDs5-6 (63, 81, 83). Moreover, isothermal titration calorimetry (ITC) experiments revealed that protein constructs consisting of various numbers of MBDs bind Cu(I) with different binding affinities. For instance, individual domains exhibit similar Cu(I) binding affinities whereas two domain constructs such as MBD5-6 bind Cu(I) tighter than a construct containing only MBD5 or MBD6 (84-86).

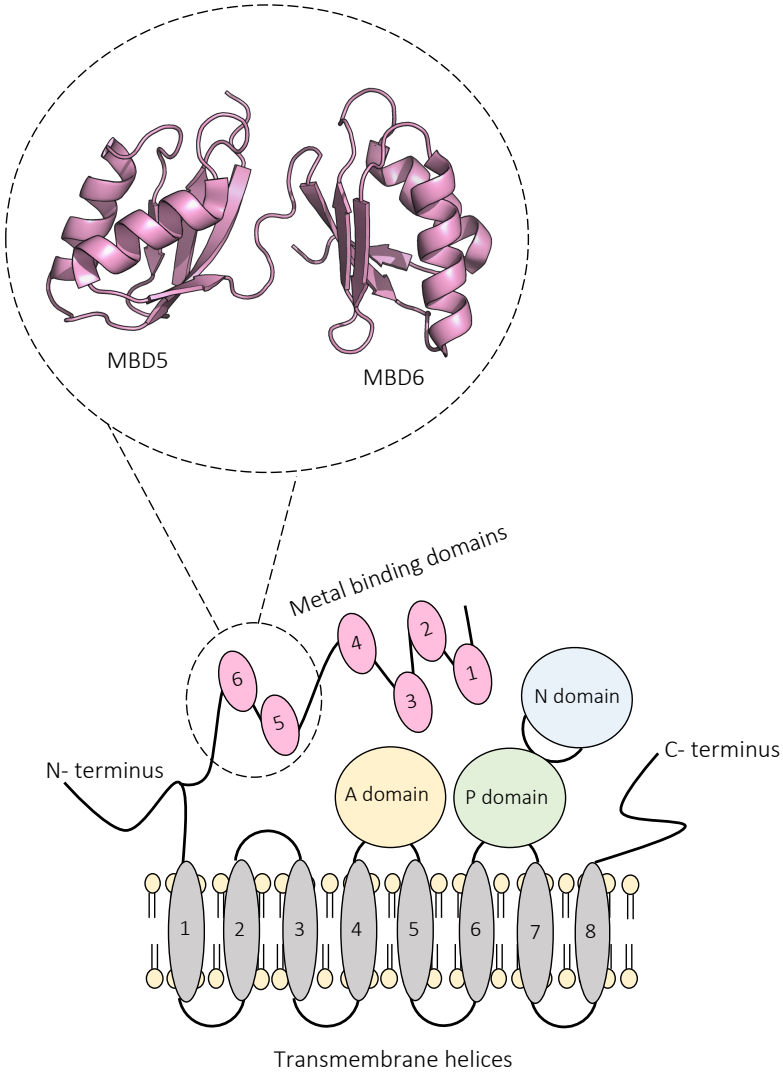

Figure 1-4 The overall architecture of ATP7B.

ATP7B is composed of a nucleotide binding domain (N domain), a phosphorylation domain (P domain), an actuator domain (A domain) and six metal binding domains (MBDs). A cartoon representation of the NMR structures of the metal binding domains 5 and 6 are shown in pink (PDB 2EW9) (36).

1.6 Grx1; a new component involved in Cu(I) delivery to the secretory pathway

Human glutaredoxin-1 (hGrx1) is a cytosolic GSH-dependent thiol-disulfide oxidoreductase, which plays a significant role in the maintenance of cellular redox homeostasis *via* the catalysis of reversible thiol-disulfide exchange reactions between protein thiols and GSSG/GSH substrates (87, 88). The crystal structure of hGrx1 (PDB 4RQR) (89) has been reported and is shown to adopt a thioredoxin fold similar to that of other Grx protein family members with an exposed Cys-xx-Cys motif (C23-xx-C26) (90, 91) (Figure 1-5*A*). Mutagenesis studies showed that this Cys-xx-Cys motif acts as the active site of the enzyme in addition to the high-affinity Cu(I)-binding site which binds Cu(I) with femtomolar affinity ($K_{D(Cu(I))} \sim 10^{-15}$ M) (32, 61). Remarkably, Cu(I)-binding inhibits the activity of hGrx1, perhaps owing to the redox changes of Cys residues (32).

Yeast two-hybrid and mammalian co-immunoprecipitation studies have revealed that Grx1 interacts with the metallochaperone Atox1 and the MBDs of ATP7A and ATP7B, with these interactions described as being copper dependent (47, 48). It has been shown that hGrx1 changes the redox status of Atox1 *via* reduction of intermolecular disulfide bond at the expense of GSH and Cu(I) availability. On the other hand, hGrx1 mediates oxidation of Atox1 through the formation of disulfide bond with oxidised glutathione in the absence of copper (14, 46) (Figure 1-5*B*).

Furthermore, hGrx1 has been shown to participate in intracellular Cu(I) delivery to the secretory pathway by activating ATP7A and ATP7B proteins *via* control of the redox states of the cysteine residues within the Cys-xx-Cys motifs in the MBDs (46). Within the cell, the MBDs of Cu(I)-ATPases exist in partially glutathionylated states, however in the pressure of excess copper, hGrx1 activates the Cu(I)-ATPases *via* reduction, which enables Cu(I) binding and transport (47). These data

together with studies of neuronal differentiation revealed that hGrx1 is actively involved in intracellular Cu(I) homeostasis and protects neuronal cells from copper toxicity (46).

Overall, hGrx1 plays a crucial role in the copper trafficking to the secretory pathway through interactions with Atox1 and the MBDs of the Cu(I)-ATPases. Further structural features of hGrx1 and its interactions with Atox1 and MBDs of ATP7B are discussed in detail in Sections 2.2 (submitted manuscript) and 2.3 (Paper I) of this thesis.

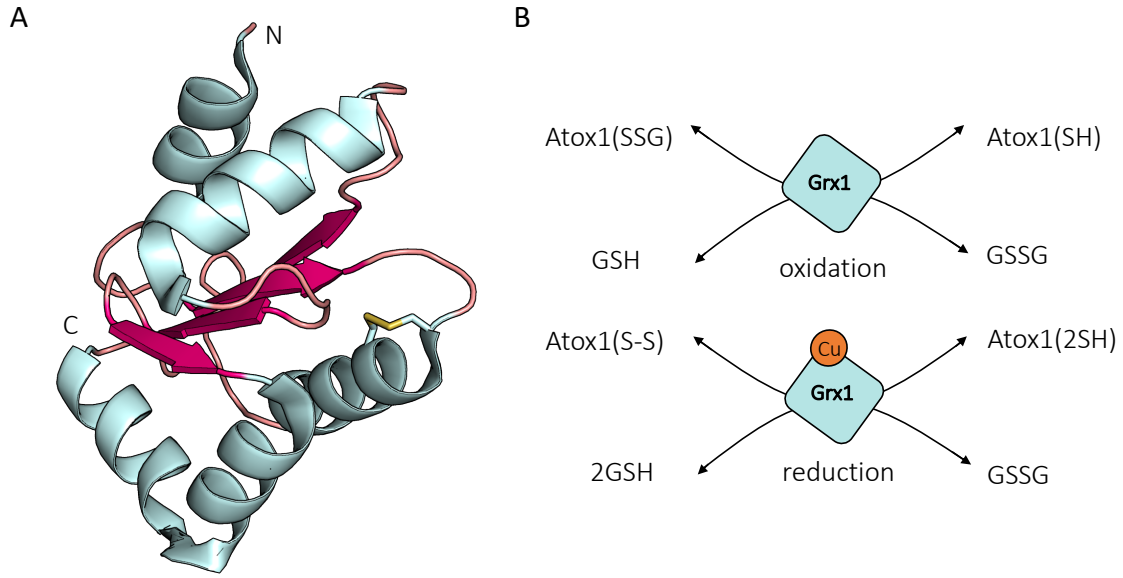

Figure 1-5 Cartoon representation of the structure of human Grx1.

(A) Secondary structures are represented as cartoons with α-helices and β-strands coloured in cyan and pink, respectively (PDB 4RQR) (89). Sulfur atoms are shown as yellow sticks. (B) The thiol-disulfide exchange reaction catalysed by Grx1 between GSSG/GSH and Atox1 thiols. Adapted from (45).

1.7 Copper trafficking to the mitochondria

1.7.1 Mitochondria

Mitochondria are crucial double membrane-bound organelles required for life in most eukaryotes, including humans. Mitochondria possess a unique architecture composed of compartments, including the outer membrane (OM), intermembrane space (IMS), inner membrane (IM), the cristae and the matrix (92-94). Mitochondria act as the power house of the cell *via* ATP production. The mitochondrial oxidative phosphorylation (OXPHOS) system is composed of five multi-subunit protein complexes in the mitochondrial IM including NADH: ubiquinone oxidoreductase (Complex I), Succinate: ubiquinone oxidoreductase (Complex II), Ubiquinol: cytochrome *c* oxidoreductase (Complex III), cytochrome *c* oxidase (Complex IV; COX) and the F_oF_1 ATP Synthase (Complex V) which together generate a membrane potential that powers ATP synthesis (95-98). This process has long been acknowledged as the key role of this organelle, however, an essential role of mitochondria in metal ion homeostasis has recently been established (99, 100). Intracellular copper trafficking, including that to and within the mitochondria, is a significantly important process for human cells. Here, our current understanding of the copper trafficking pathways within the mitochondria is discussed.

1.7.2 COX; a copper heme *a* dependent terminal oxidase of the mitochondrial respiratory chain

COX, a multi-subunit oxidoreductase of dual genetic origin, embedded in the mitochondrial IM acts as the terminal electron acceptor in the OXPHOS system. COX catalyses the reduction of molecular oxygen to water and therefore contributes to the generation of the proton motive force that is utilised by Complex V for ATP synthesis (97, 101). COX is composed of 14 subunits where

the catalytic core, conserved from α-proteobacteria to humans, contains 3 subunits (COX1, COX2, and COX3) encoded by mitochondrial DNA and the remaining 11 subunits are encoded by nuclear DNA (97, 98, 102).

The elucidation of the crystal structure of COX from bovine heart mitochondria (PDB 1OCC) (96) was a major breakthrough in the field of mitochondrial research. For the first time, the detailed architecture of the oxidase, the exact positions of the subunit components and the interface contacts between them were clearly observed in the structure (Figure 1-6). The COX1, COX2 and COX3 subunits are all integral membrane proteins. COX1 and COX3 are predominantly hydrophobic, whereas COX2 encompasses a β barrel extra-membrane domain, which extends into the IMS to interact with cytochrome *c*. This domain is connected to two transmembrane α-helices which act as a structural link between COX2 and COX1 subunits. The COX1 and COX2 subunits include the catalytic metal centres of the COX. COX1 contains a low spin heme *a*, a mononuclear Cu_B site and a high spin heme a_3 cofactor, while COX2 contains the dinuclear Cu_A site (101, 103). Molecular oxygen is reduced to water as a consequence of electron flow from the dinuclear Cu_A site of COX2 to heme *a* in COX1, which in turn transfers the electrons to the heme a_3 and mononuclear Cu_B site of COX1. This is the site where O_2 is reduced to water (97, 101).

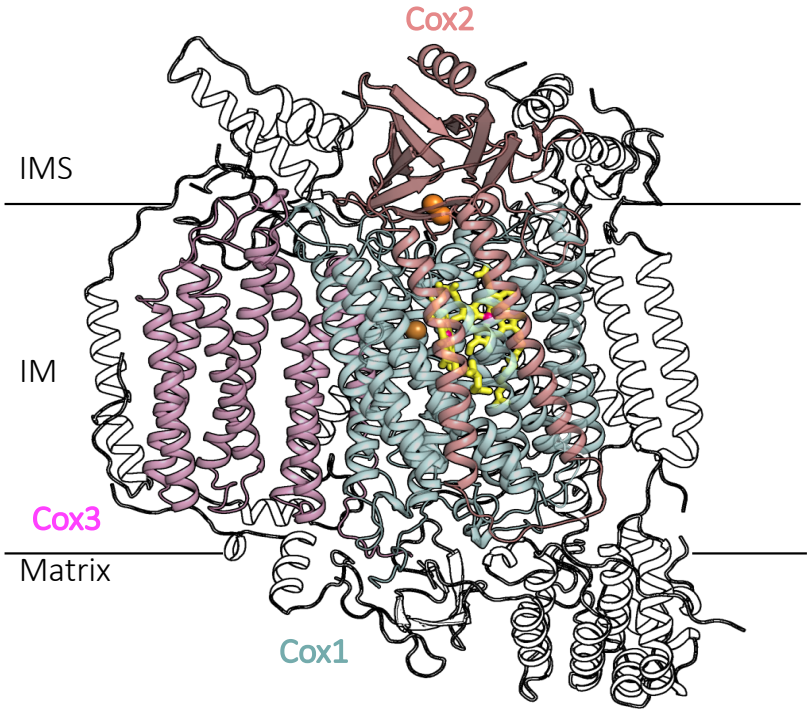

Figure 1-6 The overall structure of the monomeric bovine COX.

Cartoon representation of the overall structure of COX (PDB 1OCC) (96). All secondary structures are shown as cartoons. COX1, COX2, and COX3 subunits are coloured in cyan, salmon and pink, respectively. Copper ions are shown as orange spheres and heme a and heme a_3 are shown as yellow sticks. Other remaining subunits are not coloured for clarity.

Earlier studies proposed that COX assembly occurs *via* a linear process where the various subunits and cofactors are added in a sequential manner. However, the most recent analyses have proposed that COX assembly occurs as a combination of modular and linear processes in which the biogenesis of the catalytic core subunits are relatively independent processes with contributions of specific chaperones for the assembly of each subunit. Subsequently, modules containing different subunits are added in an ordered manner (98, 104-106). In this way, human COX assembly initiates with the independent formation of core modules that include: (1) COX1-containing module with assembly factors Cox14, Coa3, Coa1 and Surf1 (2) COX2-containing module with subunits Cox5B, Cox6C, Cox7B,

Cox7C and Cox8 and (3) COX3-containing module with subunits Cox6A, Cox6B, Cox7A and NDUFA4. Finally, the formation of the fully assembled COX occurs by engagement of COX1 with the Cox4 and Cox5a subunits prior to assembly with the COX2 and COX3 modules and remaining subunits (98, 105, 106).

1.7.3 Assembly of the metal centres of COX1

1.7.3.1 Insertion of the heme a co-factor into COX1

Hemylation of the COX1 core subunit is crucial for oxidase activity with COX the only mitochondrial enzyme that requires heme *a* as a cofactor. However, the precise mechanism of heme *a* insertion into COX1 remains unclear. The Cox10 (heme *o* synthase) and Cox15 (heme *a* synthase) enzymes, integral mitochondrial IM proteins, are the key factors in heme *a* biosynthesis (107, 108). Newly synthesised human COX1 has been shown to associate with Cox14, Coa3, and Cmc1 and not with the Cox10 or Cox15 proteins, indicating that COX1 in this complex is not hemylated and therefore that insertion of heme *a* occurs at a post-translational stage, after insertion of COX1 into the membrane (101, 109, 110). The Surf1 protein also participates in the process of COX1 hemylation (110, 111). Patients with Surf1 pathogenic mutations suffer from Leigh syndrome with associated COX deficiency (111). Studies in bacteria have revealed that Surf1 from *Rhodobacter sphaeroides* increases the assembly of heme a_3 and *Parococcus denitrificans* Surf1 binds heme *a* with micromolar affinity (112, 113). However, in both humans and yeast, the absence of Surf1 is accompanied by the accumulation of some assembled COX, implying the participation of yet undefined additional proteins that are involved in heme *a* biogenesis in COX1 (101, 114).

1.7.3.2 Assembly of the mononuclear Cu_B site

The mononuclear Cu_B site, which is located within 4.7 Å from the heme a_3 co-factor, binds a single copper ion *via* coordination with three histidine ligands (41) (Figure 1-7). The metallochaperone Cox11 is the major Cu(I)-chaperone for Cu(I) delivery to the Cu_B site. Cox11 is composed of a single transmembrane α-helix connected by a flexible linker (15 residues) to a soluble IMS located C-terminal domain, which includes a Cys-xx-Cys motif for Cu(I) binding (41). Once Cox11 binds Cu(I), it forms a dimer bridged by two Cu(I) atoms which are coordinated by the thiolate groups of two cysteine residues per monomer. An additional cysteine residue located in the flexible linker (Cys121 in humans) plays an essential role in Cu(I) delivery to COX1. The redox status of this residue is protected by Cox19 which also contains a Cx_9C motif (115). It has been hypothesised that during copper transfer the Cox11 dimer is positioned above the membrane surface with its Cu(I) cluster facing the membrane. The flexible linkers of Cox11 have been proposed to associate with the transmembrane helices of COX1. Interaction of Cu(I) cluster with the reduced Cys121 residue in the linker brings Cu(I) closer to the Cu_B site. The loop between TM7 and TM8 of COX1 move to bring histidine residues of Cu_B closer to the outer surface of COX1. This facilitates the transfer of Cu(I) to the COX1 *via* coordination of Cys121 in Cox11 and histidine ligands of Cu_B site (116, 117).

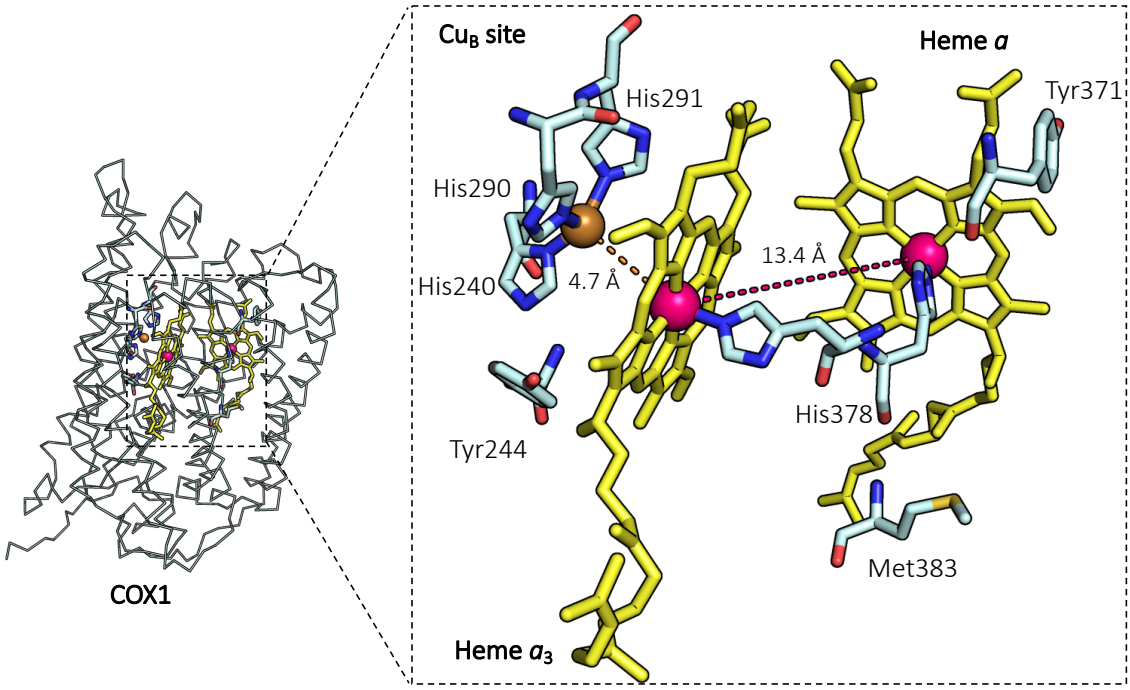

Figure 1-7 COX1 contains two metal centres.

The structure of COX1 subunit is shown as a ribbon in cyan (Right). The mononuclear Cu_B site, which is located in close proximity to the heme a_3 (4.7 Å, orange dashed line), binds one copper ion via coordination with residues His240, His290, and His291 (bovine numbering (PDB 1OCC) (96)). Residues located at the Cu_B site are shown as sticks and hydrogen bonds between residues and heme a and heme a_3 (labelled) are shown as dashed lines. The copper (Cu) and iron (Fe) atoms are shown as orange and pink sphere, respectively. Heme a and heme a_3 are shown as yellow sticks, where the distance between their Fe atoms are 13.4 Å which is shown as a pink dashed line. Carbon, oxygen, nitrogen and sulfur atoms are coloured cyan, red, blue and yellow, respectively.

1.7.4 COX2; contains the dinuclear Cu_A site

The Cu_A site of COX2, which binds two copper ions is situated in the IMS located β-barrel globular domain of COX2 which is close to the surface of COX1. A cluster of two copper ions, bridged by two cysteine residues (Cys200 and Cys204) constitutes the Cu_A site. One copper atom is coordinated by the imidazole group of residue His161 and a thioether group of Met207, while the other copper atom is coordinated by residue His204 and the carbonyl group of Glu198 (101, 118) (Figure 1-8).

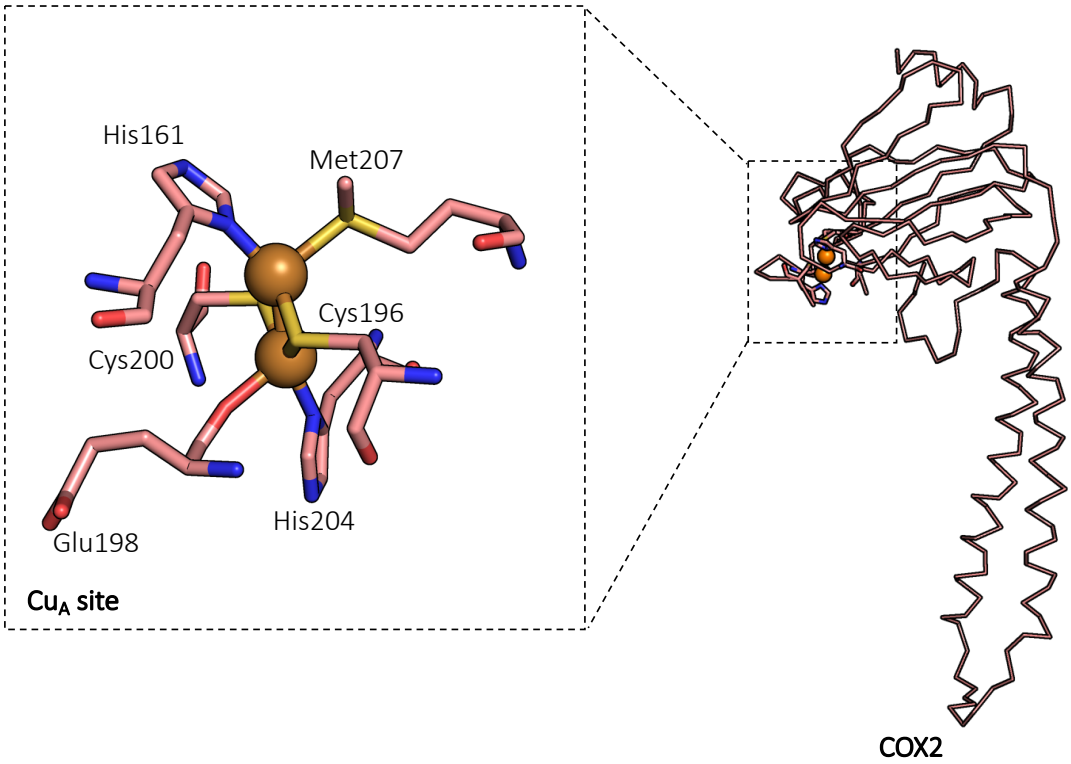

Figure 1-8 COX2 contains a dinuclear Cu_A site.

The structure of the COX2 subunit is shown as a ribbon in salmon (Left). Residues located at the Cu_A site (labelled) are shown as sticks. Copper ions are shown as orange spheres. A cluster of two copper atoms, bridged by Cys196 and Cys200 residues creates the centre of the Cu_A site. One copper ion is stabilised by coordination with an imidazole group of His161 and a thioether group of Met207 while the other copper ion is in coordination with a His204 and the carbonyl group of Glu198 residues (bovine numbering (PDB 1OCC) (96)). Carbon, oxygen, nitrogen and sulfur atoms are coloured cyan, red, blue and yellow, respectively.

A total of 36 COX assembly factors (101) are required for subunit maturation, co-factor attachment and stabilisation of intermediate assemblies of COX. Several assembly factors including Cox17, Sco1, Sco2 and Coa6 are required for the biogenesis of human COX2 (40-43). Moreover, Cox20 and Cox18 chaperones are required for membrane insertion and translocation of the C-terminus of COX2 across the mitochondrial IM, which was established by the loss of COX2 in both $Cox20^{KO}$ and $Cox18^{KO}$ HEK293T cells (118, 119).

Impaired biogenesis of COX is an important cause of human mitochondrial disease (120) where mutations in a number of assembly factors have been

identified in patients with mitochondrial disease including in Coa6 and Coa7. Given that the metalation of COX2 occurs in the mitochondrial IMS, a disulfide reductase is required for the reduction of cysteine ligands of Cu_A site for copper binding in addition to copper chaperones for transferring two copper ions. Assembly factors Cox17, Sco1, Sco2, Coa6, and newly identified Cox16 proteins are crucial factors for Cu(I) biogenesis of the Cu_A site of COX2. Patients with mutations in Sco1, Sco2 and Coa6 proteins suffer from hypertrophic cardiomyopathy owing to a defect in COX2 biogenesis which results in COX deficiency (40-43, 121).

1.7.5 Mitochondrial copper chaperones for copper biogenesis of the Cu_A site of COX2

1.7.5.1 Cox17; a major Cu(I) distributer in the mitochondrial IMS

The Cu(I)-metallochaperone Cox17 is a soluble IMS protein (62 residues) with a twin CX_9C motif sequence motif (122) and has been shown to play a significant role in the mitochondrial copper trafficking pathway (40). The NMR structure of Cox17 has been determined (PDB 2RNB) (122) and was shown to adopt a coiled-coil–helix–coiled-coil–helix (CHCH) fold (Figure 1-9). Cox17 possess six cysteine residues wherein the fully oxidised state shows three disulfide bonds between three cysteine pairs ($Cox17_{3S\text{-}S}$). The fully reduced Cox17 can bind multiple copper ions, however, partially oxidised Cox17 ($Cox17_{2S\text{-}S}$) binds a single Cu(I) ion (40, 122).

Cox17 receives copper from the mitochondrial matrix copper pool (123) where copper is bound by an anionic fluorescent molecule (also known as copper ligand (CuL)) (38). It has also been reported that CuL is found in the cytoplasm and may transfer copper to the mitochondria (123). In yeast *Saccharomyces cerevisiae*, there are two copper transporters, the mitochondrial phosphate carrier protein Pic2

(124) and the mitochondrial inner membrane iron transporter Mrs3 (125), which act in copper translocation across the mitochondrial IM to the matrix. In humans, SLC25A3, a member of mitochondrial phosphate carrier proteins (Pic) (126, 127) has been proposed to play a role in CuL translocation from the mitochondrial IM to the matrix for CuL storage. Despite recent progress in elucidating a detailed mechanism for copper delivery to COX, details on how Cox17 receives copper within the IMS remains to be fully understood. Once Cox17 is loaded with copper in the IMS, it delivers it to the Cu_A site in COX2 and the Cu_B site in COX1 *via* copper metallochaperones Sco1 and Sco2 and Cox11, respectively (40, 128, 129).

1.7.5.2 Sco1 and Sco2; two high-affinity copper binding chaperones

Both the Sco1 and Sco2 proteins play crucial roles in copper delivery to the COX2-Cu_A site and mutations in either protein lead to mitochondrial disease. The Sco proteins are able to interact with each other to facilitate copper exchange, however, in humans, these proteins show different functions (40). Structurally, both Sco proteins are composed of a single transmembrane α-helix in addition to a soluble IMS located globular domain. NMR structures of the soluble domains of Sco1 (PDB 2GQM) (130) and Sco2 (PDB 2RLI) (131) (Figure 1-9) have been determined in the presence of Cu(I). In both proteins a CXXXC motif and a conserved histidine bind either Cu(I) or Cu(II). The cysteine residues within the CXXXC motifs of Sco1 and Sco2 proteins form reversible disulfide bonds with redox potentials of -277 mV (132) and less than -300 mV (131). The highly negative redox potential values of the Sco proteins correlates with the ability of these proteins to reduce Cys residues within the Cu_A site of COX2 to facilitate copper binding. However, a recent NMR study (133) has revealed that Cu(I)-bound Sco2 acts as a thiol reductase, which reduces the cysteine ligands of Cu_A by the help of

copper ion and not by the thiols, whereas the metallochaperone Sco1 specifically transfers copper to Cu_A site (133).

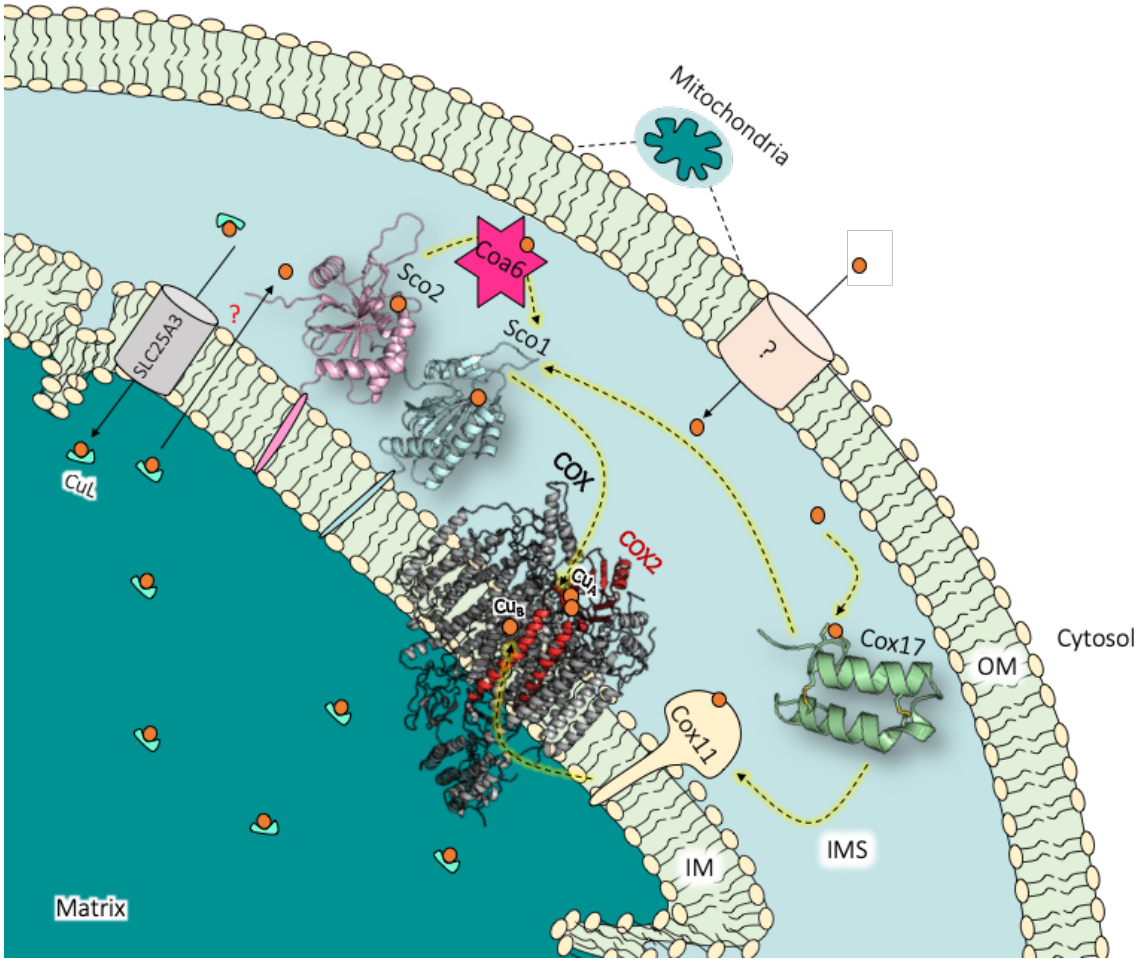

Figure 1-9 Copper trafficking within the mitochondria.

The mechanism by which cytosolic Cu(I) enters the mitochondria and details on copper efflux from the matrix to the IMS are currently unknown. Once Cox17 reaches copper in the IMS, copper is delivered to the Cu_A site in COX2 (shown as a red cartoon) and the Cu_B site in COX1 via copper metallochaperones, the Sco1 and Sco2 proteins and Cox11, respectively. The crystal structure of COX (PDB 1OCC) and NMR structures of Cox17 (PDB 2RNB), Sco1 (PDB 2GQM) and Sco2 (PDB 2RLI) are shown in grey, green, cyan and pink, respectively. Copper ions are shown as orange circles. Adopted from (128).

1.7.5.3 Coa6; a new factor involved in Cu(I) trafficking within mitochondria

Coa6 is another key assembly factor involved in COX2-Cu_A biogenesis. Coa6 is a soluble IMS protein with CX_9C–$CX_{10}C$ motif and binds Cu(I) with K_D ~10^{-17} M (43) which is an affinity similar to that of the Sco proteins. In both yeast and humans cells the deletion of Coa6 results in diminished COX assembly and activity, however, COX activity has been shown to be rescued by exogenous copper supplementation (134). Previous studies have shown that Coa6 interacts with Sco1 (43), however, another study has reported that Coa6 interacts with the metallochaperone Sco2 (135).

Pathogenic mutations of the Coa6 protein, W59C, and E87* were identified in a patient suffering from hypertrophic obstructive cardiomyopathy with a COX defect in the heart tissue and no defect in the fibroblasts (136). Another study reported a patient with a W66R mutation in Coa6 with symptoms of neonatal hypertrophic cardiomyopathy, muscular hypotonia, lactic acidosis and a clear COX defect in the fibroblasts (137).

Although it is reported that Coa6 interacts with both Sco1 and Sco2 in the cell, the precise mechanisms by which this protein mediates copper delivery to COX2-Cu_A remains unclear. Whether these interactions involve Cu(I) transfer and/or a change in the redox status of intramolecular disulfide bonds is still unknown. Further structural and functional characterisation of the wild-type Coa6 and ^{W59C}Coa6 proteins and the potential role of this protein in COX biogenesis are discussed in detail in Chapter 3 of this thesis.

1.7.6 Coa7; a metazoan specific COX assembly factor

Although the majority of assembly factors are conserved in humans and yeasts, cytochrome *c* oxidase assembly factor 7 (Coa7, also known as RESA1) is a metazoan specific COX assembly factor with no homologues identified in yeasts, fungi, and plants (138, 139). Coa7 is a cysteine-rich protein that possesses 13 cysteine residues and contains five Sel1-like repeat domains based on sequence analysis. Recently, it has been shown that Coa7 exists as an oxidised protein in the IMS where import into the IMS is mediated *via* an interaction with Mia40 through disulfide bonds (140).

Patients carrying Coa7 mutations exhibit neurological features of peripheral neuropathy with cerebellar ataxia due to COX deficiency (139, 141). It has been reported that skin fibroblasts of patients with Coa7 mutations showed different respiratory chain enzyme activities where a combination of Complex I deficiency, COX deficiency and decreased levels of fully assembled Complex I and COX were observed in different patients (141). In addition, it was previously reported that depletion of Coa7 reduces the activity of both Complex I and COX (138, 140). Further structural features of Coa7 and its potential role in COX biogenesis are discussed in detail in Chapter 4 of this thesis.

1.8 Aims of the study

The main aim of this thesis is to study copper trafficking pathways towards two distinct destinations; the *trans*-Golgi network *via* **hGrx1** and within the mitochondrial IMS by the active participation of **Coa6** together with the characterisation of COX assembly factor **Coa7** (Figure 1-10).

Specific aims of this study are:

Aim 1: To examine the protein-protein interactions that facilitate inter-protein copper exchange between **hGrx1** and the Cu(I)-metallochaperone Atox1 and the metal binding domains 5 and 6 of the ATP7B (WLN5-6) and to determine the thermodynamic factors that underpin these activities.

Aim 2: To structurally and functionally characterise the **Coa6** protein and its potential role in the biogenesis of human COX, the terminal oxidase of the mitochondrial respiratory chain

Aim 3: To structurally and functionally characterise the **Coa7** protein and its co-factor properties in order to determine its potential role in the COX biogenesis.

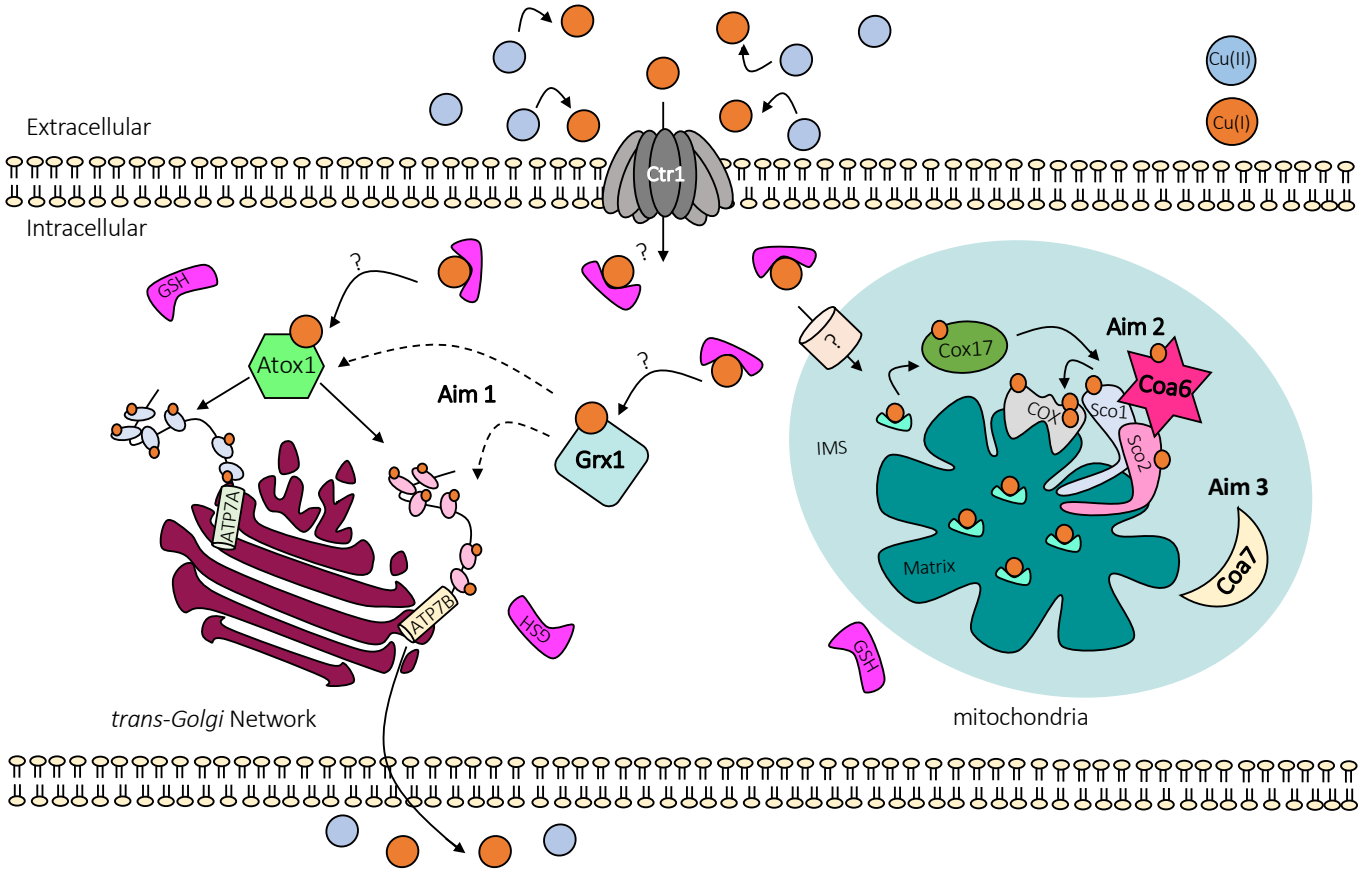

Figure 1-10 Overview of this study.

This study focuses on the Grx1 (Aim 1), Coa6 (Aim 2) and Coa7 (Aim 3) proteins.

Chapter 2

Glutaredoxin-1

2.1 Introduction

Yeast two-hybrid and mammalian co-immunoprecipitation studies have revealed that human Grx1 (hGrx1) interacts with the metallochaperone Atox1 and the MBDs of the P_{1B}-type ATPase, ATP7B with these interactions being described as copper-dependent (47, 48). The aim of the study outlined in this chapter was to investigate the *in vitro* Cu(I) delivery from the hGrx1 to the Cu(I)-metallochaperone Atox1 and the metal binding domains 5 and 6 of ATP7B (WLN5-6) and to determine the thermodynamic factors that support these interactions. The initial studies in Chapter 2 were based on the cloning, expression, purification and copper loading of hGrx1, Atox1 and WLN5-6 proteins. Here, hGrx1, ^{15}N-labeled hGrx1 and ^{15}N-^{13}C-labeled hGrx1 proteins were overexpressed with an N-terminal GST tag and purified *via* GSH affinity chromatography. The Atox1 and WLN5-6 domains were isolated by cation exchange chromatography and anion exchange chromatography, respectively. By using SEC-ICP-MS and NMR studies, we characterised the protein-protein interactions that facilitate inter-protein copper exchange for the proteins hGrx1, Atox1, and WLN5-6.

During the course of this study, one of the aims was to determine the crystal structure of the Cu(I)-bound Grx1 protein. The Grx1 proteins from human (hGrx1) and yeast *Saccharomyces cerevisiae* (yGrx1) were selected for this purpose. Despite attempts, crystals were only observed for the *apo*-yGrx1 protein. Section 2.3 (Paper I) provides details on the crystal structures of reduced yGrx1. The crystal structure of the yGrx1 were determined to 1.2 Å resolution. To study structure-function relationships of yGrx1, the crystal structure of the reduced yGrx1 was compared with the existing structures of the oxidised and glutathionylated forms. These comparisons revealed structural differences in the conformations of residues

neighboring the Cys27-Cys30 active site, which accompany alterations in the redox status of the protein.

Chapter 2 is largely presented in the form of two manuscripts. The first manuscript that is currently under review with *Antioxidants & Redox Signaling*, describes the protein-protein interactions between hGrx1 and its partner proteins *via* SEC-ICP-MS and NMR studies (Section 2.2). The second manuscript, published in *Acta Crystallographica Section F*, describes the crystal structure of the reduced yGrx1 (Section 2.3). The author contributions for each manuscript are presented in tables that preceding the manuscripts (Sections 2.2 and 2.3).

2.2 Submitted manuscript and contributions

Maghool S, La Fontaine S, Roberts BR, Kwan AH, & Maher MJ. (2019) **Human glutaredoxin-1 can transfer copper to the isolated metal binding domains of the P_{1B}-type ATPase, ATP7B.** *Scientific reports.*

Author contributions

The following table is a fair and accurate description of the individual contributions made by each author to this manuscript:

Shadi Maghool	Cloning, protein expression and purification Copper loading and copper binding experiments SEC-ICP-MS experiments and data analysis NMR experiments and data analysis with AHK Prepared all figures for the manuscript Wrote the manuscript with MJM and AHK
Sharon La Fontaine	Overall scientific direction of the project Editing and critical reading of the manuscript
Blaine R. Roberts	SEC-ICP-MS expertise Critical reading of the manuscript
Ann H. Kwan	Directed NMR experiments, carried out NMR experiments and data analysis with SM Prepared NMR figures with SM Wrote the manuscript with MJM and SM
Megan J. Maher	Overall scientific direction of the project Wrote manuscript with SM and AHK

Shadi Maghool — *Candidate*

Associate Professor Megan J. Maher — *Supervisor and co-author of the paper*

Human glutaredoxin-1 can transfer copper to the isolated metal binding domains of the P_{1B}-type ATPase, ATP7B

Shadi Maghool[1], Sharon La Fontaine[2,3], Blaine R. Roberts[3], Ann H. Kwan[4,*] and Megan J. Maher[1,5*]

[1]*Department of Biochemistry and Genetics, La Trobe Institute for Molecular Science, La Trobe University, Melbourne, VIC Australia.*
[2]*School of Life and Environmental Sciences, Deakin University, Geelong, VIC Australia.*
[3]*The Florey Institute of Neuroscience, The University of Melbourne, Parkville, VIC, Australia.*
[4]*School of Life and Environmental Sciences, The University of Sydney, Sydney, NSW Australia.*
[5]*School of Chemistry and The Bio21 Molecular Science and Biotechnology Institute, The University of Melbourne, Parkville, Australia.*

[*]Corresponding authors:
School of Chemistry and The Bio21 Moelcular Science and Biotechnology Institute,
The University of Melbourne,
Melbourne, Victoria, 3010 Australia.
Phone: +61 3 9035 7451
E-mail: megan.maher@unimelb.edu.au

Dr Ann Kwan,
School of Life and Environmental Sciences and Sydney Nano Institute,
University of Sydney,
Maze Crescent,
Sydney, NSW 2006, Australia
Phone: +61 2 9351 3911
E-mail: ann.kwan@sydney.edu.au

Keywords: copper, Wilson's disease, ATP7B, hGrx1, Atox1, NMR, protein-protein interactions

Abstract

Intracellular copper (Cu) in eukaryotic organisms is regulated by homeostatic systems, which rely on the activities of soluble metallochaperones that participate in Cu exchange through highly tuned protein-protein interactions. Recently, the human enzyme glutaredoxin-1 (hGrx1) has been shown to possess Cu metallochaperone activity. The aim of this study was to ascertain whether hGrx1 can act in Cu delivery to the metal binding domains (MBDs) of the P_{1B}-type ATPase ATP7B and to determine the thermodynamic factors that underpin this activity. hGrx1 can transfer Cu to the metallochaperone Atox1 and to the MBDs 5-6 of ATP7B (WLN5-6). This exchange is irreversible. In a mixture of the three proteins, Cu is delivered to the WLN5-6 preferentially, despite the presence of Atox1. This preferential Cu exchange appears to be driven by both the thermodynamics of the interactions between the proteins pairs and of the proteins with Cu(I). Crucially, protein-protein interactions between hGrx1, Atox1 and WLN5-6 were detected by NMR spectroscopy both in the presence and absence of Cu at a common interface. This study augments the possible activities of hGrx1 in intracellular Cu homeostasis and suggests a potential redundancy in this system, where hGrx1 has the potential to act under cellular conditions where the activity of Atox1 in Cu regulation is attenuated.

Introduction

Copper (Cu) is a redox active metal and an essential element for human health (4, 6). In biological systems, Cu is found in two oxidation states, reduced Cu(I) (cuprous copper) and oxidized Cu(II) (cupric copper). These reversible states, which allow Cu to serve as both an oxidant and reductant, render it an exceptional cofactor for redox enzymes known as oxidoreductases (4, 6), however Excess intracellular concentrations of Cu are toxic and lead to cellular oxidative damage (8, 9). In particular, the reaction of hydrogen peroxide with Cu(I) ions and the reduction of Cu(II) ions by superoxide, produce hydroxyl radicals that damage proteins, nucleic acids and lipids (10, 11).

In humans, the dysregulation of Cu metabolism is associated with diseases such as Menkes syndrome, Wilson's disease, prion diseases, Alzheimer's disease and fatal motor neuron diseases such as familial amyotrophic lateral sclerosis (21-23, 32, 142, 143). To maintain the fine balance between cellular Cu requirements and toxicity, organisms have evolved sophisticated metalloregulatory systems for the coordination of metals such as Cu to proteins within the cell, and the controlled transfer of these metals between protein partners. Soluble proteins that are responsible for copper binding and transfer are termed 'metallochaperones' (8), which transport copper in its reduced state (Cu(I)), often *via* coordination with cysteine residues (19, 144). In eukaryotes, including humans, copper concentrations are regulated through control of the levels of the copper import protein, copper transporter 1 (Ctr1) (28, 53) at the plasma membrane and the trafficking and/or activity of the copper export proteins, ATP7A or ATP7B.

In humans, ATP7A (Menkes disease protein, MNK) and ATP7B (Wilson disease protein, WLN) are two Cu(I)-specific P_{1B}-type ATPases that are essential for Cu

transport and homeostasis. These ion pumps, which are localized in the *trans*-Golgi network (TGN), utilize ATP hydrolysis to transport the metal across the TGN membrane to activate copper dependent enzymes within the secretory pathway (eg. ceruloplasmin) (64, 145, 146). In addition, in response to elevated levels of intracellular Cu, these enzymes traffic from the TGN towards the cell periphery to export the excess Cu from the cell (147, 148). Crucially, to date, only the metallochaperone Atox1 (also known as HAH1), has been implicated in facilitating Cu delivery to the ATP7A and ATP7B proteins.

The ATP7A and ATP7B proteins share high levels of sequence similarity with other P_{1B}-type ATPases, possessing an A-domain and an ATP-binding domain, which mediate their catalytic activities. The latter comprises the P-domain that includes the site of catalytic phosphorylation and the signature motifs for the P-type ATPases (DKTG, TGDN, GDGxND, where X is any amino acid), and the N (nucleotide binding)-domain (36, 84, 145, 149). However, a distinguishing feature of the ATP7A and ATP7B proteins is the presence of a large amino-terminal extension that is composed of six Cu-binding domains (~600 residues in total). These metal binding domains (MBDs) have ferredoxin-like βαββαβ folds and bind Cu(I) at C-XX-C motifs, which redox cycle between oxidized (disulfide) and reduced (thiol) states (21, 37, 76, 82, 150-155). The MBDs participate in Cu exchange *via* protein-protein interactions, which are facilitated by flexible polypeptide linkers that bridge the domains (83, 156).

The mechanism by which the MBDs act to facilitate Cu delivery to the transmembrane domain (TMD) remains under investigation, with consensus within the literature still to be achieved. The ATP7B MBDs 1-4 were shown to be actively involved in receiving Cu from Atox1 (46, 151) and an NMR titration experiment (36) comparing Cu transfer from Atox1 to the protein constructs

ATP7B MBD 4 and MBDs 5-6 indicated that Atox1 cannot transfer Cu to the MBD 5-6 protein, whereas Atox1 can participate in Cu exchange with the MBD 4 protein. This study proposed a model for Cu binding and transport by ATP7B, where the MBD 4 receives Cu from Atox1 and passes the metal to MBD 6, which transfers Cu to MBD 5 for delivery to the TMD for translocation across the membrane (36). In this way, the ATP7B MBDs 1-4 were suggested to play crucial roles in receipt of Cu by the transporter and in regulation of Cu transport, whereas the MBDs 5-6 function in passing Cu to the TMD of the transporter for efflux. However, more recent studies have established that the ATP7B MBD 4 does not interact with the other ATP7B MBDs, which has led to the proposal that this domain serves only as a structural link between the MBDs 1-3 (regulatory) and MBDs 5-6 (Cu-delivery) (36, 63, 81, 83).

Glutaredoxin-1 (Grx1) is a cytosolic member of a class of glutaredoxin enzymes, which are GSH-dependent thiol-disulfide oxidoreductases. Grx1 plays a significant role in the maintenance of cellular redox homeostasis *via* the catalysis of reversible thiol-disulfide exchange reactions between protein thiols and the substrates reduced and oxidized glutathione (GSH and GSSG, respectively) (44-46). The crystal structure of human glutaredoxin1 (hGrx1) has been determined (PDB 4RQR) (89) and was shown to adopt a thioredoxin fold (157), with an exposed C-XX-C motif (C23-XX-C26; residues numbered according to UniProtKB P35754) (158). This motif was shown by site-directed mutagenesis and related analyses to be the active site of the enzyme and also the high affinity Cu(I) binding site (32, 61, 159). Studies using yeast two hybrid and mammalian co-immunoprecipitation experiments demonstrated that hGrx1 interacts with the MBDs of the ATP7A and ATP7B proteins in a copper-dependent manner (47, 48). Furthermore, additional reports that described the overexpressing and knocking

down of hGrx1 in neuronal, non-neuronal cells and $Grx1^{KO}$ mouse embryonic fibroblast (MEF) cells, showed impact specifically on Cu homeostasis (46, 47, 160).

hGrx1 has been shown to catalyze the reduction of a protein disulfide bond in the human Cu,Zn superoxide dismutase at the expense of GSH (161) and mediate the oxidation and reduction of Atox1 with the direction of catalysis dependent on the cytoplasmic GSSG/GSH ratio and Cu availability (32). Specifically, the latter study showed that in the presence of Cu, hGrx1 could facilitate the reduction of oxidized Atox1 using GSH as a substrate, while the reverse reaction (oxidation of Atox1), catalyzed by hGrx1 (with GSSG as a substrate) was Cu independent (32). Analyses of the recombinant hGrx1 protein also demonstrated that hGrx1 binds Cu(I) with femtomolar affinity ($K_{DCu(I)} \sim 10^{-15}$ M) *via* its active site Cys residues, but that Cu(I) binding inhibits hGrx1 enzyme activity (32), potentially alluding to a mechanism for the regulation of the enzyme activity that is dependent on the intracellular reduction potential and availability of Cu(I). These data are consistent with reports that demonstrate a role for hGrx1 in Cu metabolism and in protecting neuronal cells from Cu toxicity (46, 160).

Research seeking to establish the driving factors for Cu delivery to its cellular destinations have to date focused almost exclusively on the determination of the relative Cu binding affinities of each individual protein partner (4, 61). Consistently, the binding affinities of these proteins for Cu(I) have been characterized as exceptionally tight with $K_{D(Cu(I))}$ values in the range 10^{-15}-10^{-17} M (32, 61). With such high affinity binding, the question of how Cu transfer from one protein to another is achieved has led to the hypothesis that affinity gradients between proteins determine the direction of Cu exchange (4). Few structures of a protein complex in the act of Cu transfer have so far been determined. The structures of a complex of the Atx1 and Ccc2a proteins from *Saccharomyces*

cerevisae (162) and that between Atox1 and the ATP7A MBD1 have been described by NMR (163), both of which show a Cu(I)-bridged assembly, with the Cu(I) atom coordinated by a pair of Cys residues from each protein. Despite these structural characterizations, the thermodynamics of the interactions between the two protein partners were not reported. However, these interactions were described as being Cu-dependent (162).

In the current study, we have investigated the protein-protein interactions between hGrx1, and the proteins Atox1 and ATP7B MBDs 5-6 (hereafter referred to as WLN5-6), both in Cu-bound and *apo* (Cu-free) states, in conjunction with their intermolecular Cu-transfer activities. These data show that the protein-protein interactions are not Cu-dependent and that the affinities of the protein-protein interactions differ between pairs of protein partners. We therefore propose that the affinities of protein-protein interactions in partnership with the Cu(I)-binding affinities of the individual proteins determine Cu trafficking within the cell. Critically, we establish a potential Atox1-independent mechanism for Cu delivery to ATP7B, through the action of hGrx1, and therefore an alternative pathway for the maintenance of intracellular Cu homeostasis.

Results and Discussion

Recombinant hGrx1, Atox1 and WLN5-6 proteins bind Cu(I) with sub-femtomolar affinities.

Recombinant hGrx1, Atox1 and WLN5-6 proteins were overexpressed and purified (Fig. S1). All purified proteins, including Atox1 and WLN5-6, in addition to unlabeled and/or ^{15}N- and ^{13}C/^{15}N-labelled hGrx1 were confirmed to be isolated as *apo*-proteins as determined by inductively coupled plasma mass spectrometry (ICP-MS) and a colorimetric assay with Bcs. Purified *apo*-proteins were loaded with Cu(I) as previously described (32) and after size exclusion

chromatography (SEC) to remove excess Cu(I), were analyzed for Cu(I) content. As expected, the Atox1 and hGrx1 proteins were found to bind Cu(I) with a Cu(I):protein stoichiometry of 1:1 while WLN5-6, which has two MBDs, bound Cu(I) with a stoichiometry of 2:1 (Table S1). The *apo*- and Cu(I)-bound proteins prepared in this way were used for both the Cu-exchange and nuclear magnetic resonance (NMR) experiments.

To determine the binding affinities of the individual proteins for Cu(I), purified *apo*-proteins at various concentrations were added individually to a reaction mixture containing the probe complex $[Cu^{I}Bcs_2]^{3-}$. These experiments yielded dissociation constants ($K_{D(Cu(I))}$) for the hGrx1, Atox1, and WLN5-6 proteins of $10^{-15.8}$, $10^{-17.5}$ and $10^{-17.8}$ M at pH 7.0, respectively (Table S2). These determinations agree closely with those previously reported (32, 61) (Table S2).

The hGrx1, Atox1 and WLN5-6 proteins participate in Cu(I)-transfer with apo-protein partners.

To establish whether the hGrx1 and WLN5-6 proteins could interact to facilitate Cu exchange, we performed protein co-incubation assays followed by SEC-ICP-MS. The individual *apo*- and Cu(I)- proteins were incubated together before separation by SEC. The column eluent was simultaneously monitored for the presence of protein (A_{280}) and for Cu (ICP-MS) (Fig 1A, B, C). Co-incubation of the Cu(I)-hGrx1 and *apo*-WLN5-6 proteins yielded a SEC profile with two major protein peaks where the first peak (WLN5-6), co-eluted with Cu while the second peak (hGrx1) was essentially Cu-free (Fig. 1D), indicating Cu transfer from Cu(I)-hGrx1 to *apo*-WLN5-6 to yield *apo*-hGrx1 and Cu(I)-WLN5-6. The reverse experiment (*apo*-hGrx1 with Cu(I)-WLN5-6) did not result in Cu exchange, indicating the former transfer was irreversible (Fig. 1E). In addition, through separation of the proteins by anion exchange and colorimetric analyses

of the Cu(I) content of the eluents, we were able to reproduce the results of previous studies that showed irreversible Cu exchange between Cu(I)-hGrx1 and *apo*-Atox1 and no exchange between Cu(I)-Atox1 and *apo*-WLN5-6 or Cu(I)-WLN5-6 and *apo*-Atox1 (Fig. S2, S3)(32, 36).

This demonstrates that Cu(I)-hGrx1 is able to transfer Cu to both *apo*-protein partners Atox1 and WLN5-6. However, Cu was not observed to transfer from Cu(I)-Atox1 and Cu(I)-WLN5-6 to *apo*-hGrx1. This observation correlates with the significantly weaker Cu binding affinity of hGrx1 compared with the Atox1 and WLN5-6 proteins (Table S2) (4). Crucially, the ability of Cu(I)-hGrx1 to transfer Cu to WLN5-6 has not been reported previously and augments the possible roles for hGrx1 in intracellular Cu homeostasis beyond Cu exchange with Atox1 (32).

The failure of the Atox1 and WLN5-6 proteins to participate in Cu-exchange in both directions is consistent with previously published studies and has been attributed to the inability of the proteins to interact productively for Cu transfer (36). However, the observation of Cu transfer from Cu(I)-Atox1 to individual MDBs of ATP7B appears to vary depending on the experimental conditions (36, 82, 85, 156). Specifically, the WLN5 and WLN6 domains have been shown to receive Cu from Cu(I)-Atox1, both when present as individual domains in solution (85) and as part of a multidomain (WLN1-6) protein fragment (156).

Transfer of Cu from Cu(I)-hGrx1 to WLN5-6 occurs despite the presence of Atox1. Our observations of pairwise Cu(I)-transfer between the hGrx1 and the *apo*-proteins Atox1 and WLN5-6 led us to extend the study to a mixture of all three of these proteins. Cu(I)-hGrx1 was incubated with a mixture of the *apo*-proteins Atox1 and WLN5-6 (at a molar ratio of 1:1:1), followed by re-separation by SEC-ICP-MS. Remarkably, we observed *via* SEC-ICP-MS that the majority of the

Cu co-eluted with the WLN5-6 protein, rather than the hGrx1 and Atox1 proteins which despite optimization of the conditions of the experiment, co-eluted together as a single peak (Fig. 1F). The Cu(I) distribution was estimated (through the Cu(I) contents of the corresponding eluents) at 4:1 WLN5-6:hGrx1/Atox1. This was confirmed through separation of the proteins by anion exchange and colorimetric analyses of the Cu(I) content of the eluents (Fig S2). These analyses indicat that on incubation, Cu transferred from Cu(I)-hGrx1 to the WLN5-6 protein preferentially (yielding Cu(I)-WLN5-6), despite the presence of equimolar Atox1 in the mixture. This result agrees with our observation that both the Atox1 and WLN5-6 *apo*-proteins can receive Cu from Cu(I)-hGrx1 (Fig. 1D, S2, S3).

Importantly, since Cu was not observed to transfer from Cu(I)-Atox1 to *apo*-hGrx1 or between Atox1 and WLN5-6, (the predominance of Cu(I)-WLN5-6 as a product of this experiment, indicates direct, preferential Cu-transfer from Cu(I)-hGrx1 to *apo*-WLN5-6, rather than equilibration of Cu between the proteins in the mixture. That is, the distribution of Cu between the WLN5-6 and Atox1/Grx1 peaks cannot be accounted for by consideration of the Cu(I)-binding affinities of the Atox1 and WLN5-6 proteins alone, which indicate approximate two-fold tighter binding of Cu(I) to WLN5-6 *versus* Atox1 (Table S2). We therefore hypothesized that the Cu(I)-binding affinities of the individual proteins are not the only factors that determine Cu delivery from Cu(I)-hGrx1 when multiple protein partners are present and that the affinities of the protein-protein interactions between these proteins contribute to Cu transfer. We therefore sought to examine more closely the protein-protein interactions between the Cu(I)-hGrx1 and the Atox1 and WLN5-6 proteins.

Confirmation that hGrx1 binds Cu(I) via two surface-exposed Cys residues.

To confirm the location of the Cu(I) binding site in hGrx1 (between residues C23 and C26) (32), we produced ^{15}N and $^{13}C/^{15}N$-labeled *apo*-hGrx1 and Cu(I)-hGrx1 for NMR studies. *Apo*-hGrx1 gave a high quality ^{15}N-^{1}H heteronuclear single quantum coherence (HSQC) spectrum with sharp and well dispersed peaks consistent with a well-folded and monomeric protein. Out of 115 peaks expected in the ^{15}N-^{1}H-HSQC spectrum from the 106-residue construct of *apo*-hGrx1 (excluding non-native residues from cleavage at the N-terminus), ~108 peaks were observed. Using standard triple resonance experiments, near complete HN-N, Cα and Cβ assignments of the *apo*-hGrx1 spectrum were made (96%, 95% and 95%, respectively), however peaks could not be assigned to residues T22, A50, T51, N52 and H53, suggesting this region undergoes conformational exchange (Fig. S4). In addition, Y25 and C26 presented as relatively weak peaks in most spectra. Conformational exchange for residues located at or near the C23-XX-C26 active site, was also reported in the NMR structural analysis of reduced hGrx1 (159). One peak in the *apo*-hGrx1 ^{15}N-^{1}H-HSQC spectrum (124.8/7.132 ppm) was not assigned as no corresponding signals could be observed in any of the triple resonance experiments. The assigned chemical shifts have been deposited into Biological Magnetic Resonance Bank (BMRB; accession number 27650).

A ^{15}N-^{1}H-HSQC spectrum of Cu(I)-hGrx1 was recorded and a comparison of the *apo*-hGrx1 and Cu(I)-hGrx1 spectra revealed that a subset of peaks (F18, I19, K20, C23, Y25, C26, I48, A67, T69, S84 and D85) showed significant chemical shift positional or signal intensity changes (Fig. S5A, B, C). These residues cluster in regions that encircle residues C23 and C26 (Fig. S5A, B, C), confirming these two cysteine residues are directly involved in the coordination of Cu(I). For example, the peak assigned to residue C23 showed one of the most significant positional

changes, while the weak but observable peaks assigned to residues Y25 and C26 in the *apo*-hGrx1 spectrum disappeared completely in the Cu(I)-hGrx1 spectrum (Fig. S5A, B, C). In addition, the peak assigned to residue T69, located ~8 Å from C23, shifted significantly and changed in its intensity. This residue has been demonstrated to be sensitive to the redox status and the structure of the active site including being displaced in structures minimized with the C23 thiolate group instead of a thiol (159, 164). Overall, this spectral comparison locates the Cu(I) binding site between residues C23 and C26, which agrees with previous mutagenesis and Cu binding studies of hGrx1 (32).

NMR experiments reveal a role for protein-protein interactions in Cu transfer from Cu(I)-hGrx1 and WLN5-6.

In our pairwise experiments, Cu(I)-hGrx1 was shown to transfer Cu to the *apo*-proteins Atox1 and WLN5-6 but the reverse transfers were not observed (Fig. S2, S3). To investigate the protein-protein interactions that occur during these unidirectional Cu(I)-exchange events, ^{15}N-^{1}H-HSQC titration studies were carried out by titrating unlabeled *apo*-proteins WLN5-6 or Atox1 into ^{15}N-Cu(I)-hGrx1 to final molar ratios of 3.8:1 and 7.1:1 (partner:Cu(I)-hGrx1), respectively (Fig. 2, S6A-B, S7A, B, C). The changes in the ^{15}N-^{1}H-HSQC spectra indicated that Cu was displaced from Cu(I)-hGrx1 as increasing concentrations of partner proteins were added, with the ^{15}N-^{1}H-HSQC spectra largely resembling that of *apo*-hGrx1 at higher partner:Cu(I)-hGrx1 ratios with higher partner concentrations (Fig. 2, Fig. S6A, B, S7A, B, C). These observations confirm the Cu transfer from Cu(I)-hGrx1 to the *apo* partner proteins Atox1 and WLN5-6 as was observed by SEC-ICP-MS.

At higher concentrations of partner proteins, the observed spectral changes continued to progress, such that spectra recorded at partner:Cu(I)-hGrx1 ratios of 3.8:1 and 7.1:1 (partner:Cu(I)-hGrx1; for Atox1 and WLN5-6, respectively) showed

additional spectral changes in comparison to the spectrum of *apo*-hGrx1. These observations may be ascribed to interactions between newly formed *apo*-hGrx1 and the partner proteins. That is, the formation of weak and transient *apo*-hGrx1-Cu(I)-Atox1 and *apo*-hGrx1-Cu(I)-WLN5-6 and/or *apo*-hGrx1-*apo*-Atox1 and *apo*-hGrx1-*apo*-WLN5-6 complexes. This indicates that *apo*-hGrx1-protein partner complexes persisted following Cu transfer. The spectral changes for these titrations, in terms of elucidating the molecular details and thermodynamics of these transient protein-protein complexes were challenging to decipher as they resulted from multiple hGrx1 species (*apo*-hGrx1, Cu(I)-hGrx1 and Cu(I)-hGrx1-partner, *apo*-hGrx1-Cu(I)-partner and *apo*-hGrx1-*apo*-partner protein complexes) that were present at varying concentrations throughout the titrations. Therefore, we conducted NMR titration studies with *apo*-^{15}N-hGrx1 and the *apo*-proteins Atox1 and WLN5-6 in order to simplify the analyses and to directly measure the affinities of the protein-protein interactions.

The same interaction surface facilitates Cu transfer from hGrx1 to Atox1 and WLN5-6.

Apo-^{15}N-hGrx1 was titrated with *apo*-proteins Atox1 or WLN5-6 to final molar ratios of 2.0:1 (partner:hGrx1) (Fig. S8A, B, C, S9A, B, C). In these titrations, variations were observed from the same set of peaks that showed changes at the highest partner:hGrx1 ratios in the Cu(I)-hGrx1 titrations. These included peaks assigned to residues at and surrounding the C23-XX-C26 Cu binding site, which map to a common region on the surface of hGrx1. This mapped region is consistent for both the Atox1 and WLN5-6 titrations and indicates that hGrx1 interacts with both protein partners using the same interaction surface (Fig. 3A, B). Calculation of the electrostatic surface potential of the hGrx1 structure shows that this interaction surface is predominantly positively charged (Fig. 3C). This aligns with previous studies of metallochaperone P_{1B}-ATPase MBD interactions, which have

reported that the complexes are mediated by complementary surface electrostatics (19, 162, 165). The observed peak changes were fitted to a 1:1 binding model , which yielded K_Ds of 14 ± 6 μM and 7 ± 4 μM for the hGrx1-Atox1 and hGrx1-WLN5-6 interactions, respectively (Fig S10A, B). Crucially, these observations indicate that protein-protein interactions between hGrx1 and the Atox1 and WLN5-6 proteins occur in the absence of Cu and that the affinities of these interactions are different between distinct pairs of protein partners.

Conclusion

In this study, we established that hGrx1 binds Cu in a 1:1 stoichiometry at a C23-XX-C26 site and that hGrx1 can deliver Cu to the *apo*-proteins Atox1 and WLN5-6 in solution. Importantly, Cu transfer from hGrx1 to WLN5-6 occurs preferentially in the presence of Atox1 and the interactions of hGrx1 with the Atox1 and WLN5-6 are not Cu dependent.

The Cu dependence of protein interactions that mediate intracellular Cu shuttling has been a controversial area of research. A number of studies have repeatedly stated that the interactions between proteins involved in Cu exchange are metal dependent. For example, examinations *via* NMR of Cu(I) delivery from Cu(I)-Atox1 to the multidomain protein ATP7B MBDs 1-6 (156) and the determination of the structures of the Atx1-Ccc2a (162) and complexes between Atox1 and the MBD1 of ATP7A from yeast and human, respectively (163), all described the observed intermolecular adducts as metal-mediated. This is despite the fact that extensive intermolecular interfaces between the proteins in the complexes have been defined (162, 163), that the surface electrostatics of the proteins have been shown to be crucial for complex formation (163, 165) and that only minimal structural differences have been observed between *apo*- and Cu(I)-forms of these proteins and domains (63, 166). However, NMR experiments have also

demonstrated interactions between the MBDs 4-6 of ATP7B and Atox1 in the absence of Cu (151). The results reported here give further support to the proposal that these interactions occur independently of the presence of Cu.

In a mixture of the Cu(I)-hGrx1, *apo*-Atox1, and *apo*-WLN5-6 proteins, Cu was preferentially delivered to the WLN5-6 protein, despite the fact that the *apo*-Atox1 and *apo*-WLN5-6 proteins show only a two-fold difference in their respective values for $K_{D(Cu(I))}$. This result can be reconciled by both the thermodynamics of the interactions between the proteins pairs and of the proteins with Cu(I). That is, the hGrx1 protein interacts with a higher affinity with the WLN5-6 protein than with the Atox1 and the binding affinity of WLN5-6 for Cu(I) is also higher. Interestingly, both proteins (Atox1 and WLN5-6) interact at the same interface with hGrx1, which is proximate to the Cu(I)-binding site. The predicted consequence of the different affinities of these proteins for hGrx1 is competition for binding at this common site and therefore competition for Cu exchange.

Crucially, we show here that hGrx1 is able to transfer Cu to the WLN5-6 protein, even in the presence of Atox1. To date, Atox1 has been the sole metallochaperone protein proposed to act in Cu delivery to the ATP7A and ATP7B proteins. The fact that hGrx1 can act in this way is significant for intracellular Cu homeostasis. This finding suggests a potential redundancy in this system and a role for hGrx1 under cellular conditions where the activity of Atox1 in Cu regulation is attenuated. For example, a number of lines of evidence suggest that both the cellular ratios of *apo*-Atox1/Cu(I)-Atox1 and reduced/oxidized Atox1 influence metabolic Cu flux and specifically the activity and trafficking of the Cu ATPases (63, 66, 81). There is also evidence to suggest that Atox1 is not absolutely required for Cu delivery to the Cu(I)-ATPases (167), and that other Cu carriers may supplement Atox1 function. For example, *ATOX1* knockout does not completely abrogate ATP7A function,

suggesting that ATP7A may obtain Cu from alternative metal donor(s) (167). The data presented in this study suggests that hGrx1 could assume such a role.

Methods

Protein overexpression and purification

The DNA sequence encoding hGrx1 was amplified *via* PCR and subcloned into a pGEX-6P-1 glutathione S-transferase fusion vector with an intervening PreScission Protease site for cleavage of the GST tag. The DNA sequences encoding Atox1 and the WLN5-6 protein fragment (encoding residues 486–633 of ATP7B) were amplified *via* PCR and subcloned into the pTEM-11 and pET-24d vectors, respectively. The pGEX-6p-1-hGrx1, pTEM-11-Atox1 and pET-24d-WLN5-6 plasmids were individually transformed into *Escherichia coli* strain BL21 Codon Plus (DE3). Cultures were grown in Lysogeny Broth (LB) at 37°C to an optical density OD_{600} of approximately 0.8, induced with isopropyl β-D-1-thiogalactopyranoside (IPTG, 0.5 mM) and harvested after 16 h with shaking at 25°C. The hGrx1 isotope labeled samples (^{15}N and/or ^{13}C) were grown in LB at 37°C to an OD_{600} of 0.6-0.8, harvested and washed twice in M9 salts before transfer to labeled M9 media and induction with IPTG (1.0 mM). Cells were harvested by centrifugation after 16 h with shaking at 25°C (168).

The hGrx1 and ^{15}N-^{13}C-labeled hGrx1 proteins were purified by glutathione S-transferase (GST) affinity chromatography. Frozen cell pellets were thawed at room temperature and resuspended in cell lysis buffer (phosphate-buffered saline (PBS), 1 mM Tris (2-carboxyethyl) phosphine hydrochloride (TCEP)). Cells were disrupted by passage through a TS series bench top cell disruptor (Constant Systems Ltd) at 35 kpsi. Cell debris was removed by centrifugation (Beckman JLA-25.50, 30000 g, 20 min, 4°C) and the soluble fraction was incubated with glutathione sepharose™ 4B resin (GE Healthcare) equilibrated with lysis buffer.

The GST tag was cleaved with PreScission Protease (GE Healthcare) followed by size-exclusion chromatography (SEC; HiLoad 16/600 Superdex 75 pg, GE Healthcare; 20 mM Tris-MES pH 8.0, 150 mM NaCl, 1 mM TCEP). Purified proteins were concentrated to 20 mg/mL before storage at -80°C.

The purifications of the Atox1 and WLN5-6 proteins were conducted according to previously reported protocols with minor modifications (36, 61). The Atox1 was purified by cation exchange chromatography (HiTrap™ SP FF, GE Healthcare), eluted with a linear NaCl gradient (0.0–1.0 M, 20 mM sodium acetate pH 5.0, 1 mM TCEP), followed by SEC (HiLoad 16/600 Superdex 75 pg, GE Healthcare; 20 mM potassium phosphate pH 7.0, 150 mM NaCl, 1 mM TCEP). The WLN5-6 protein was isolated by anion exchange chromatography (HiTrap™ Q FF, GE Healthcare), and was eluted with a linear NaCl gradient (0.0–1.0 M in 20 mM sodium MES pH 6.0, 0.1 mM EDTA, 1 mM TCEP), followed by SEC (HiLoad 16/600 Superdex 75 pg, GE Healthcare; 20 mM MES/Na pH 5.5, 150 mM NaCl, 1 mM TCEP). Purified proteins were concentrated to 20 mg/mL prior to storage at -80°C.

Cu loading

The purified proteins were exchanged into buffer (20 mM Tris-MES pH 8.0) by centrifugal ultrafiltration (Millipore) and incubated for 30 mins with $CuSO_4$ and reduced GSH (molar ratio 1: 5: 10; protein: $CuSO_4$: GSH). In order to remove the excess Cu from the mixture, the incubated protein sample was applied to a SEC column (HiLoad 16/600 Superdex 75 pg, GE Healthcare). The presence of Cu(I) in the peak fractions was analyzed colorimetrically using the ligand bathocuproinedisulfonic acid (Bcs) and those protein fractions containing Cu were pooled and concentrated by centrifugal ultrafiltration. The Cu(I):protein

stoichiometries of the protein samples prepared in this manner were confirmed by a colorimetric assay using Bcs (32).

Measurement of Cu-binding

The Cu(I) probe ligand Bcs, which reacts quantitatively with Cu(I) to yield a 1:2 complex $[Cu^{I}Bcs_2]^{3-}$ with a characteristic solution spectrum (ϵ = 13000 $M^{-1}cm^{-1}$ at λ_{max} 483 nm) and a defined formation constant ($\log\beta_2$ = 19.8) (32) was employed for the quantification of Cu(I) binding to all proteins (32). Briefly, purified proteins (20 mM Tris-MES, pH 7.0) were titrated at various concentrations (1–30 $M) into solutions containing buffer (20 mM Tris-MES, pH 7.0), $CuSO_4$ (20 $M), Bcs (200 $M) and reduced GSH (400 $M). The exchange of Cu(I) from the $[Cu^{I}Bcs_2]^{3-}$ complex to the proteins was monitored by measuring the absorbance of the resulting solutions at 483 nm. The data were analyzed as previously described (32, 43).

Cu-exchange

Protein samples (2 $g) of Cu(I)-loaded, *apo*-proteins and protein mixtures at 1:1 molar ratios were applied to a Bio-SEC 3 column (3 mm particle size; 150 Å pore structure; 4.6 mm i.d., Agilent Technologies) in 200 mM ammonium nitrate (pH 7.6–7.8, adjusted with ammonium hydroxide) with 10 μg/L cesium (Cs) and antimony (Sb) as internal standards. Chromatographic separations of the proteins were monitored by measuring the UV absorbance of the eluent at 280 nm (indicating the presence of protein) and inductively coupled plasma mass spectrometry (ICP-MS) (Agilent Technologies 7700 x ICP-MS) (169) was used to monitor the presence of copper.

For the analyses of protein mixtures that contained the hGrx1 and Atox1 proteins (which could not be resolved by SEC), separation of the proteins by anion exchange was carried out. Protein samples were applied to a mono Q 5/50 GL column (GE Healthcare) pre-equilibrated with binding buffer (20 mM Tris-MES, pH 8.0) and bound proteins were eluted by the application of a linear NaCl gradient (0.0-1.0 M NaCl, 20mM Tris-MES, pH 8.0). The Cu contents of the eluted fractions were determined colorimetrically with Bcs (32).

NMR Spectroscopy

^{15}N-^{1}H heteronuclear single quantum coherence (HSQC) spectra were recorded at 4°C using a Bruker Avance III 600 MHz NMR spectrometer equipped with a triple-resonance TCI cryogenic probehead. All stock protein solutions were dialyzed against MES/Na buffer (10 mM MES/Na, 50 mM NaCl, 1 mM TCEP, pH 6.0) overnight prior to titration studies. ^{15}N-^{1}H-HSQC spectra of ^{15}N-*apo* and ^{15}N-Cu(I)-hGrx1 (350–400 µl at 320–350 µM) were recorded after sequential additions of unlabeled *apo* forms of the proteins Atox1 or WLN5-6. For the titrations into ^{15}N-*apo*-hGrx1, the *apo*-proteins Atox1 or WLN5-6 (0.46 and 0.5 mM, respectively) were titrated to final molar ratios of 2.0:1 (partner:*apo*-hGrx1). For titrations into ^{15}N-Cu(I)-hGrx1, final molar ratios of 3.8:1 and 7.1:1 (partner:hGrx1) were obtained upon sequential additions of the *apo*-proteins Atox1 or WLN5-6 (0.5 and 1.5 mM, respectively). D_2O was added to each sample to a final concentration of 5% (v/v). Spectra were processed with Topspin 3.5 (Bruker Biospin) and analyzed using SPARKY (T. D. Goddard and D. G. Kneller, University of California, San Francisco). Spectral changes (either in intensity or peak position) were plotted against varying concentrations of the titrants. For peak positional changes, combined chemical shift perturbations, Δ chemical shift (ppm) were calculated based on the equation $\Delta\delta_{ppm}=[(\Delta\delta_{HN})^2+(0.154\times\Delta\delta_N)^2]^{1/2}$

where $\Delta\delta_{HN}$ and $\Delta\delta_{N}$ represent the chemical shift variations in the proton and nitrogen dimensions, respectively. Comparing *apo* and Cu(I)-hGrx1 spectra, peaks that were not overlapped and with positions changing by more than one standard deviation (SD) over the mean or those with intensity decreasing by >75% or increasing by >100% were deemed to be significantly affected. For titration with partner proteins, peaks with positions changed by more than one standard deviation (SD) over the mean or those with intensity changes > 50% at molar ratios beyond 1:1 were deemed to be significantly affected. Binding affinities were determined from non-linear-least-square curve fitting to a 1:1 binding model based on intensity changes using Origin2016.

NMR assignment of apo-hGrx1

hGrx1 assignments were unavailable from the previously determined *apo*-hGrx1 structure (PDB code (1JHB) (159)), so triple resonance experiments were recorded on a purified $^{13}C/^{15}N$-labeled hGrx1 sample (0.5 mM) to allow the assignment of the ^{15}N-^{1}H-HSQC spectrum. Spectra were analyzed with Sparky (T. D. Goddard and D. G. Kneller, University of California, San Francisco). Backbone ^{15}N, HN, and ^{13}C resonances were obtained from HNCACB, CBCA(CO)NH, HCC(CO)NH and CC(CO)NH experiments using standard methods. ^{15}N and ^{13}C chemical shifts were referenced indirectly using 4,4-dimethyl-4-silapentane-1-sulfonic acid (DSS) according to their magnetogyric ratios.

Acknowledgements

This study was funded by the Australian Research Council (DP140102746 to MJM). SM was supported by an Australian Government Research Training Program Scholarship. BRR was supported by a NHMRC Dementia Leadership Fellowship (BR, APP1138673). The support of the Florey Neuroproteomics facility

and Adam Gunn for assistance in SEC-ICP-MS data collection and analysis are also acknowledged.

Author contributions

MJM, BRR, AHK and MJM designed the experiments. SM produced the recombinant proteins. SM, and AHK carried out the NMR experiments, analyzed the data and prepared the data for publication. SM performed the copper transfer experiments with support from BRR. SM, BRR, SL, AHK and MJM wrote the manuscript.

Additional information

The authors declare they have no competing financial or non-financial interests.

Figure legends

Fig. 1 Result of Cu exchange reactions between Cu(I)-hGrx1 and partner proteins. (A) Cu(I)-hGrx1, (B) Cu(I)-WLN5-6 and (C) Cu(I)-Atox1 were applied to SEC column and fractions analyzed for the presence of protein (A_{280}, dashed lines: black) and Cu (circles: hGrx1, purple; WLN5-6, red; Atox1, green) by ICP-MS. (D) Results of Cu exchange reaction between Cu(I)-hGrx1 and *apo*-WLN5-6. Cu(I)-hGrx1 and *apo*-WLN5-6 were incubated together at 1:1 molar and re-separated using SEC (A_{280}, black dash lines). On separation, the Cu(I) elutes with the WLN5-6 protein, indicating Cu(I)-exchange (pink circles). (E) Results of Cu exchange reaction between Cu(I)-WLN5-6 and *apo*-hGrx1. The two proteins (*apo*-hGrx1 and Cu(I)-WLN5-6) were incubated together at 1:1 molar and re-separated the same technique (A_{280}, black dash lines). On separation, the Cu(I) elutes with the WLN5-6 protein, indicating no Cu-exchange (teal circles). (F) Cu exchange between Cu(I)-hGrx1, and a mixture of the *apo*-Atox1 and *apo*-WLN5-6 proteins. Cu(I)-hGrx1, *apo*-Atox1 and *apo*-WLN5-6 were incubated together at 1:1:1 molar and separated using SEC (A_{280}, black dash lines) and fractions analysed for the presence of Cu by ICP-MS (gray circles).

Fig. 2 ^{15}N-^{1}H-HSQC spectra of ^{15}N-Cu(I)-hGrx1 titrated with WLN5-6. Overlay of ^{15}N-^{1}H-HSQC spectra of Cu(I)-hGrx1 before (blue) and after additions of WLN5-6 at Cu(I)-hGrx1:WLN5-6 molar ratios of 2:1 (green) and 7:1 (pink). Residues that display significant chemical shift changes (including positional and intensity) are labeled.

Fig. 3 hGrx1 possess a common interaction site for the Atox1 and WLN5-6 proteins. (A) The hGrx1 interaction interface residues (labeled) with Atox1 are highlighted in pink on the hGrx1 surface representation (cyan). (B) The hGrx1 interaction interface residues (labeled) with WLN5-6 are highlighted in gray on the hGrx1 surface representation (cyan). (C) The hGrx1 structure as represented in (A) and (B). The hGrx1 surface is colored according to the electrostatic potentials (red, negatively charged; blue, positively charged; white, uncharged). The active site Cys pair is marked in yellow.

.

Figure 1.

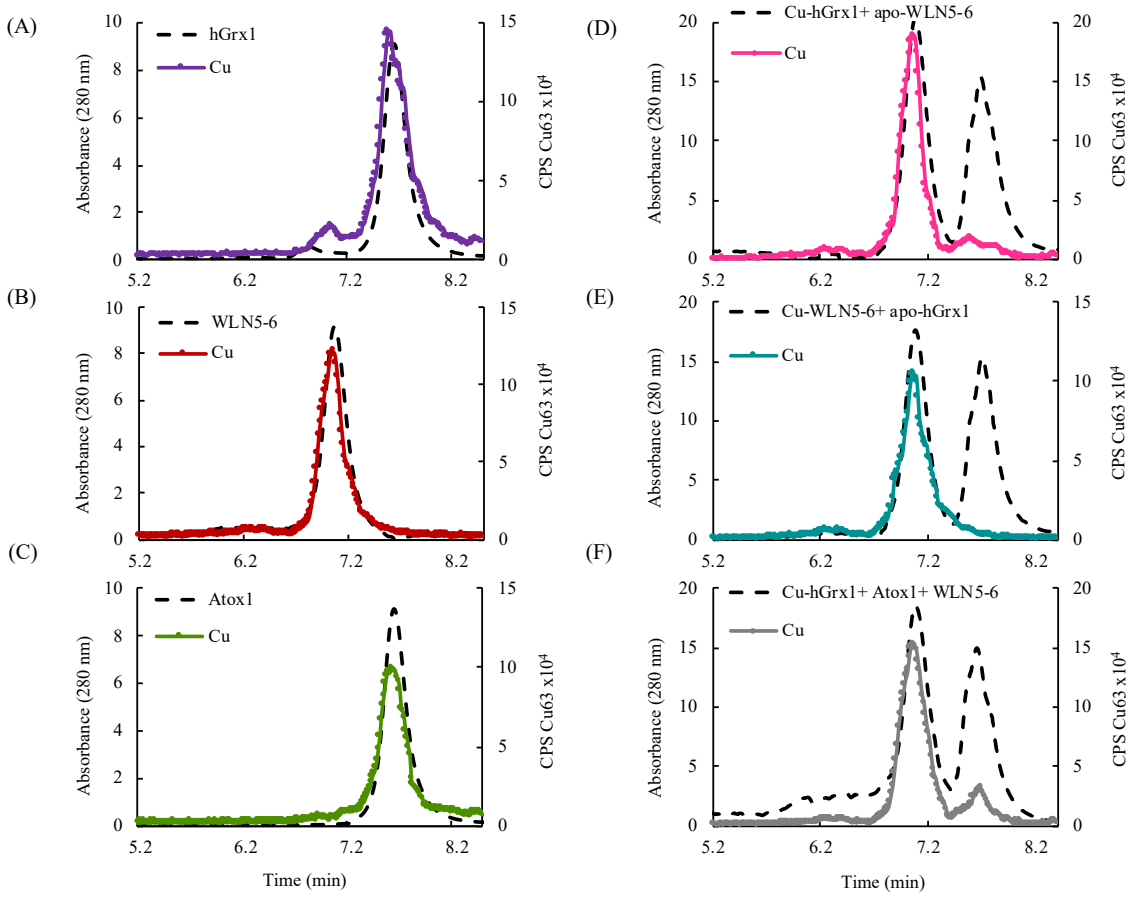
(A)
hGrx1
Cu
(B)
WLN5-6
Cu
(C)
Atox1
Cu
(D)
Cu-hGrx1+ apo-WLN5-6
Cu
(E)
Cu-WLN5-6+ apo-hGrx1
Cu
(F)
Cu-hGrx1+ Atox1+ WLN5-6
Cu
Absorbance (280 nm)
CPS Cu63 x10⁴
Time (min)

Figure 2.

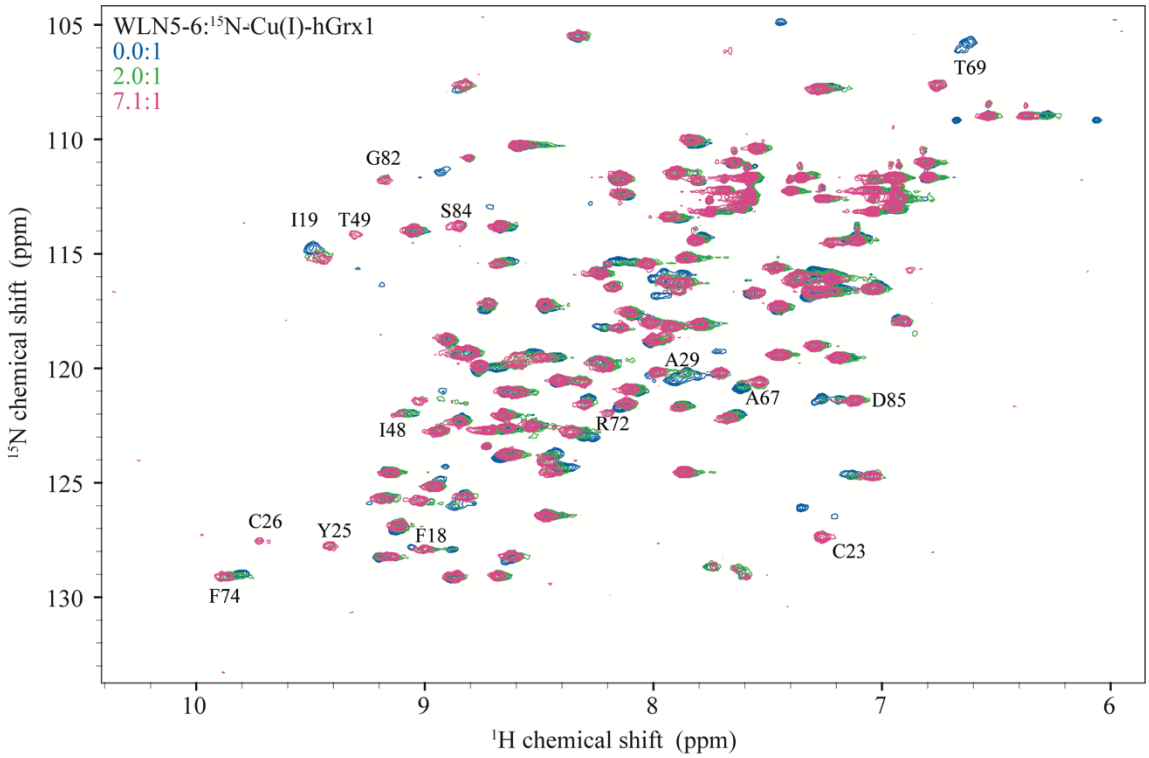
WLN5-6:15N-Cu(I)-hGrx1
0.0:1
2.0:1
7.1:1
T69
G82
I19
T49
S84
A29
A67
D85
I48
R72
C26
Y25
F18
C23
F74
105
110
115
120
125
130
15N chemical shift (ppm)
10
9
8
7
6
1H chemical shift (ppm)

Figure 3.

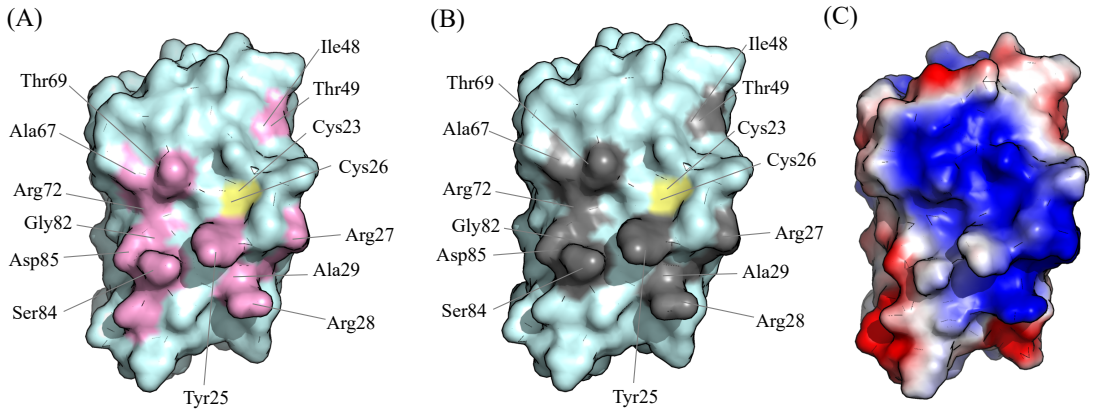
(A)
Ile48
Thr69
Thr49
Ala67
Cys23
Cys26
Arg72
Gly82
Arg27
Asp85
Ala29
Ser84
Arg28
Tyr25
(B)
Ile48
Thr69
Thr49
Ala67
Cys23
Cys26
Arg72
Gly82
Arg27
Asp85
Ala29
Ser84
Arg28
Tyr25
(C)

2.2.1 Supplementary Information

Human glutaredoxin-1 can transfer copper to the isolated metal binding domains of the P_{1B}-type ATPase, ATP7B

Shadi Maghool[1], Sharon La Fontaine[2,3], Blaine R. Roberts[3], Ann H. Kwan[4,*] and Megan J. Maher[1,5*]

[1]*Department of Biochemistry and Genetics, La Trobe Institute for Molecular Science, La Trobe University, Melbourne, VIC Australia.*
[2]*School of Life and Environmental Sciences, Deakin University, Geelong, VIC Australia.*
[3]*The Florey Institute of Neuroscience, The University of Melbourne, Parkville, VIC, Australia.*
[4]*School of Life and Environmental Sciences, The University of Sydney, Sydney, NSW Australia.*
[5]*School of Chemistry and The Bio21 Molecular Science and Biotechnology Institute, The University of Melbourne, Parkville, Australia.*

[*]Corresponding authors:
A/Prof. Megan Maher,
School of Chemistry and The Bio21 Molecular Science and Biotechnology Institute,
The University of Melbourne,
Melbourne, Victoria, 3010 Australia.
Phone: +61 3 9035 7451
E-mail: megan.maher@unimelb.edu.au

Dr Ann Kwan,
School of Life and Environmental Sciences and Sydney Nano Institute,
University of Sydney,
Maze Crescent,
Sydney, NSW 2006, Australia
Phone: +61 2 9351 3911
E-mail: ann.kwan@sydney.edu.au

Table S1 Cu:protein stoichiometries for purified proteins

Protein	[Cu]/[Protein]
hGrx1	0.97 ± 0.02
Atox1	1.01 ± 0.05
WLN5-6	1.94 ± 0.03

Table S2 Apparent Cu(I) dissociation constants K_D for the Cu(I)-binding sites for the hGrx1, Atox1 and WLN5-6 proteins, determined *via* competition with BCS.

Protein	Log K_D pH 7.0	
	This work	Ref
hGrx1	-15.8	-15.5 (32)
Atox1	-17.5	-17.4 (32, 61)
WLN5-6	-17.8	-17.6 (61)

Supplementary figure captions

Figure S1 Confirmation of purified ^{15}N-hGrx1, Atox1, hGrx1 and WLN5-6 proteins by Coomassie Brilliant Blue (CBB)-stained SDS/PAGE.

Figure S2 Results of Cu exchange reactions between Cu(I)-hGrx1 and partner proteins. (A) Cu(I)-hGrx1, (B) Cu(I)-Atox1 and (C) Cu(I)-WLN5-6 were applied to an anion exchange column and fractions analyzed for the presence of protein (A_{280}, solid lines) and for Cu(I) with Bcs (the $[Cu^{I}Bcs_2]^{3-}$ complex is detected colorimetrically at A_{483}, dashed orange lines). (D) Results of Cu exchange reaction between Cu(I)-hGrx1 and *apo*-Atox1. Cu(I)-hGrx1 and *apo*-Atox1 were incubated together at 1:1 molar and re-separated using anion exchange. (E) Cu exchange between Cu(I)-Atox1 and *apo*-hGrx1. (F) Cu exchange between Cu(I)-WLN5-6 and *apo*-Atox1 (G) Cu exchange between Cu(I)-Atox1 and *apo*-WLN5-6. (H) Cu exchange between Cu(I)-hGrx1, and a mixture of the *apo*-Atox1 and *apo*-WLN5-6 proteins. Cu(I)-hGrx1, *apo*-Atox1 and *apo*-WLN5-6 were incubated together at molar ratio of 1:1:1 and re-separated using anion exchange (A_{280}, pink solid line) and fractions colorimetrically analyzed for the presence of Cu (orange dashed line).

Figure S3 Schematic representations of related Cu exchange experiments conducted in this work. The ✓ symbol indicates that Cu transferred between proteins and the ✗ symbol indicates that it is not.

Figure S4 Assigned ^{15}N-^{1}H-HSQC spectrum of ^{15}N-^{13}C *apo*-hGrx1. Lines indicate sidechain resonances from Asn and Gln residues.

Figure S5A Comparison of ^{15}N-^{1}H-HSQC spectra of *apo*-hGrx1 and Cu(I)-hGrx1. (A) Overlay of ^{15}N-^{1}H-HSQC spectra of *apo*-hGrx1(red) and Cu(I)-hGrx1(blue). Residues that display significant chemical shift changes (including positional and intensity) are labeled. Arrows show groups of peaks that belong to the same amino acid in the two states.

Figure S5B Histogram showing combined H and N chemical shift changes comparing ^{15}N-Cu(I)-hGrx1 and ^{15}N-*apo*-hGrx1.

Figure S5C Histogram showing changes in peak heights comparing ^{15}N-Cu(I)-hGrx1 and ^{15}N-*apo*-hGrx1.

Figure S6A Histogram showing combined H and N chemical shift changes during WLN5-6 titrations to ^{15}N-Cu(I)-hGrx1. Results were shown for titrations of WLN5-6 to ^{15}N-Cu(I)-hGrx1 at molar ratios of 1:1 (blue), 2:1 (green) and 7:1 (pink).
Figure S6B Histogram showing changes in peak heights during WLN5-6 titrations during WLN5-6 titrations to ^{15}N-Cu(I)-hGrx1. Results were shown for titrations of WLN5-6 to ^{15}N-Cu(I)-hGrx1 at molar ratios of 1:1 (blue), 2:1 (green) and 7:1 (pink).

Figure S7A ^{15}N-^{1}H-HSQC spectra of ^{15}N-Cu(I)-hGrx1 titrated with Atox1. Overlay of ^{15}N-^{1}H-HSQC spectra of Cu(I)-hGrx1 before (blue) and after additions of Atox1 at Cu(I)-hGrx1:Atox1 molar ratios of 2.2:1 (green) and 3.8:1 (pink). Residues that display significant chemical shift changes (including positional and intensity) are labelled.
Figure S7B Histogram showing combined H and N chemical shift changes during Atox1 titrations to ^{15}N-Cu(I)-hGrx1. Results were shown for titrations of Atox1 to ^{15}N-Cu(I)-hGrx1 at molar ratios of 2.2:1 (blue) and 3.8:1 (pink).
Figure S7C Histogram showing changes in peak heights during Atox1 titrations during Atox1 titrations to ^{15}N-Cu(I)-hGrx1. Results were shown for titrations of Atox1 to ^{15}N-Cu(I)-hGrx1 at molar ratios of 2.2:1 (blue) and 3.8:1 (pink).

Figure S8A ^{15}N-^{1}H-HSQC spectra of ^{15}N-*apo*-hGrx1 titrated with Atox1. Overlay of ^{15}N-^{1}H-HSQC spectra of *apo*-hGrx1 before (red) and after additions of Atox1 at *apo*-hGrx1:Atox1 molar ratios of 0.1:1 (black) and 1.1:1 (cyan). Residues that display significant chemical shift changes (including positional and intensity) are labeled.
Figure S8B Histogram showing combined H and N chemical shift changes during Atox1 titrations to ^{15}N-*apo*-hGrx1. Results were shown for titrations of Atox1 to ^{15}N-*apo*-hGrx1 at molar ratios of 0.1:1 (black) and 1.1:1 (cyan).
Figure S8C Histogram showing changes in peak heights during Atox1 titrations during Atox1 titrations to ^{15}N-*apo*-hGrx1. Results were shown for titrations of Atox1 to ^{15}N-*apo*-hGrx1 at molar ratios of 0.1:1 (black) and 1.1:1 (cyan).

Figure S9A ^{15}N-^{1}H-HSQC spectra of ^{15}N-*apo*-hGrx1 titrated with WLN5-6. Overlay of ^{15}N-^{1}H-HSQC spectra of *apo*-hGrx1 before (red) and after additions of WLN5-6 at *apo*-hGrx1:WLN5-6 molar ratios of 0.2:1 (black) and 1:1 (cyan). Residues that display significant chemical shift changes (including positional and intensity) are labeled.

Figure S9B Histogram showing combined H and N chemical shift changes during WLN5-6 titrations to ^{15}N-*apo*-hGrx1. Results were shown for titrations of WLN5-6 to ^{15}N-*apo*-hGrx1 at molar ratios of 0.2:1 (black) and 1:1 (cyan).

Figure S9C Histogram showing changes in peak heights during WLN5-6 titrations during WLN5-6 titrations to ^{15}N-*apo*-hGrx1. Results were shown for titrations of WLN5-6 to ^{15}N-*apo*-hGrx1 at molar ratios of 0.2:1 (black) and 1:1 (cyan).

Figure S10A ^{15}N-^{1}H-HSQC titrations of Atox1 into ^{15}N-*apo*-hGrx1 in absence of Cu(I). Peak heights (arbitrary units, black squares) and fitted values (lines) for a 1:1 binding model are shown for residues C23 and T69. Residuals of the fits are shown as red squares in the bottom plots.

Figure S10B ^{15}N-^{1}H-HSQC titrations of WLN5-6 into ^{15}N-*apo*-hGrx1 in absence of Cu(I). Peak heights (arbitrary units, black squares) and fitted values (lines) for a 1:1 binding model are shown for residues C23 and T69. Residuals of the fits are shown as red squares in the bottom plots.

Figure S1

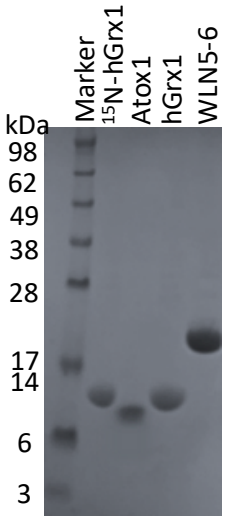

Figure S2

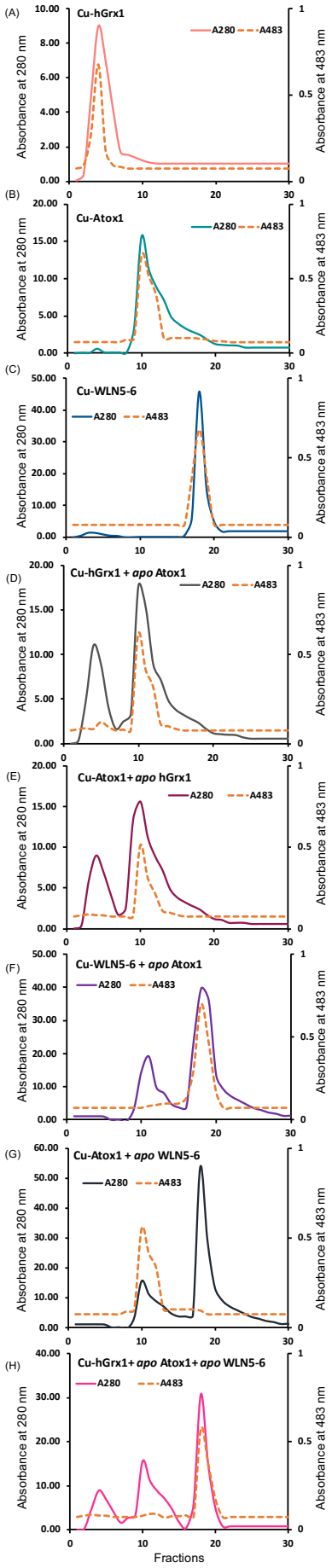
(A)
Cu-hGrx1
A280
A483
Absorbance at 280 nm
Absorbance at 483 nm
(B)
Cu-Atox1
(C)
Cu-WLN5-6
(D)
Cu-hGrx1 + apo Atox1
(E)
Cu-Atox1+ apo hGrx1
(F)
Cu-WLN5-6 + apo Atox1
(G)
Cu-Atox1 + apo WLN5-6
(H)
Cu-hGrx1+ apo Atox1+ apo WLN5-6
Fractions

Figure S3

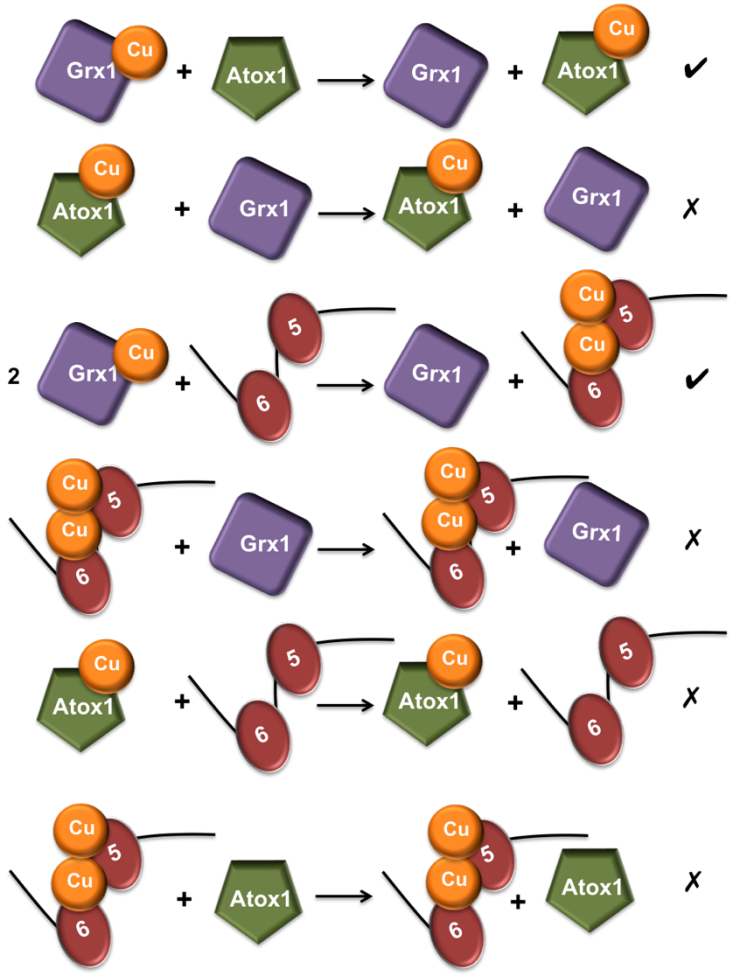
Grx1
Cu
Atox1
Grx1
Atox1
Cu
✔
Atox1
Cu
Grx1
Atox1
Cu
Grx1
✗
2
Grx1
Cu
5
6
Grx1
Cu
5
Cu
6
✔
Cu
5
Cu
6
Grx1
Cu
5
Cu
6
Grx1
✗
Atox1
Cu
5
6
Atox1
Cu
5
6
✗
Cu
5
Cu
6
Atox1
Cu
5
Cu
6
Atox1
✗

Figure S4

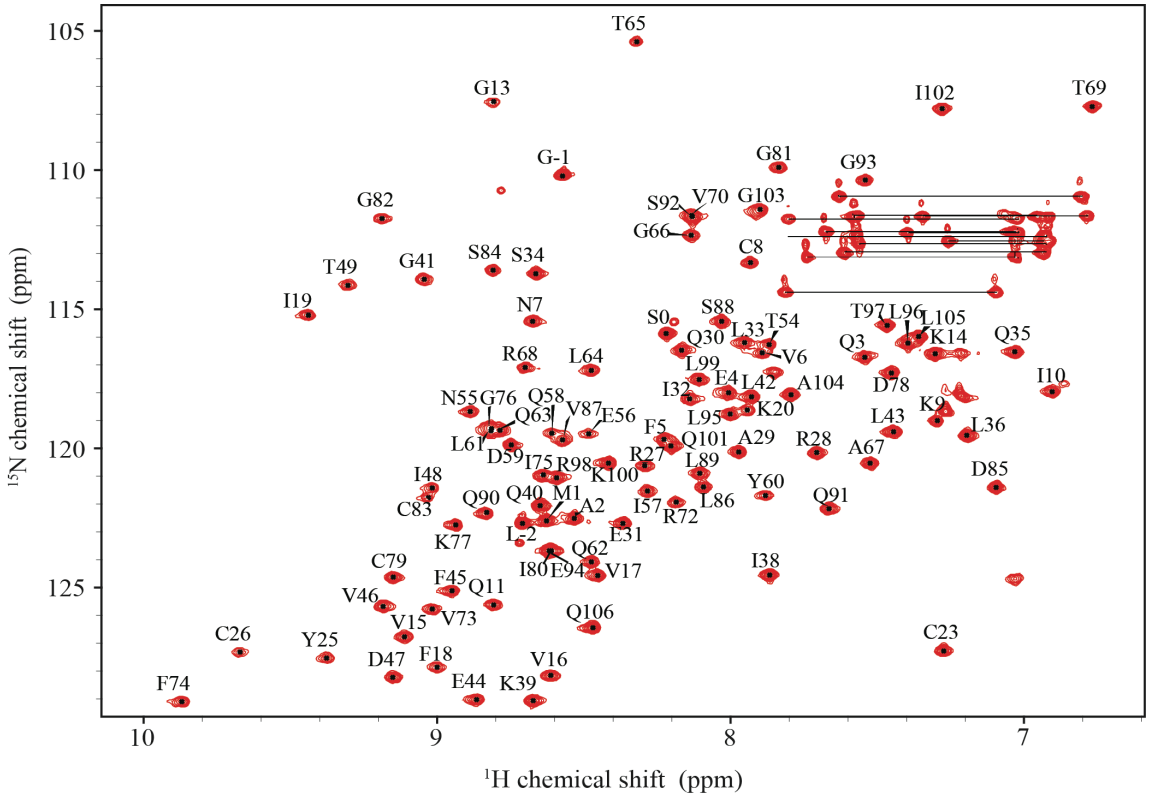
105
110
115
120
125
10
9
8
7
^{15}N chemical shift (ppm)
^{1}H chemical shift (ppm)
T65
G13
I102
T69
G-1
G81
G93
G82
S92
V70
G103
G66
C8
T49
G41
S84
S34
I19
N7
S0
S88
T54
T97
L96
L105
Q30
L33
K14
Q35
Q3
V6
R68
L64
L99
E4
L42
A104
D78
I10
I32
N55
G76
Q58
Q63
V87
E56
L95
K20
K9
L43
L36
F5
Q101
A29
R28
A67
L61
D59
I75
R98
R27
L89
K100
D85
I48
Y60
C83
Q90
Q40
M1
A2
I57
L86
Q91
R72
K77
L2
E31
Q62
C79
I80
E94
V17
I38
F45
Q11
V46
V15
V73
Q106
C26
Y25
C23
D47
F18
V16
F74
E44
K39

Figure S5A

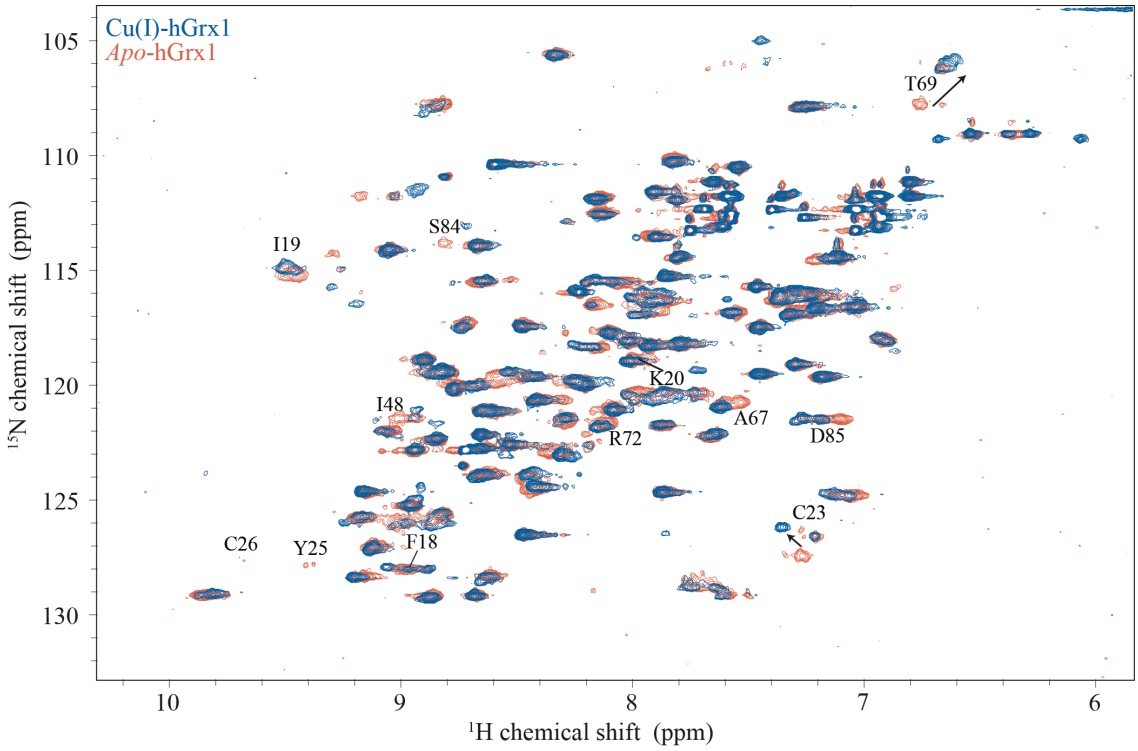
Cu(I)-hGrx1
Apo-hGrx1
T69
S84
I19
K20
I48
A67
R72
D85
C23
C26
Y25
F18
105
110
115
120
125
130
^{15}N chemical shift (ppm)
10
9
8
7
6
^{1}H chemical shift (ppm)

Figure S5B

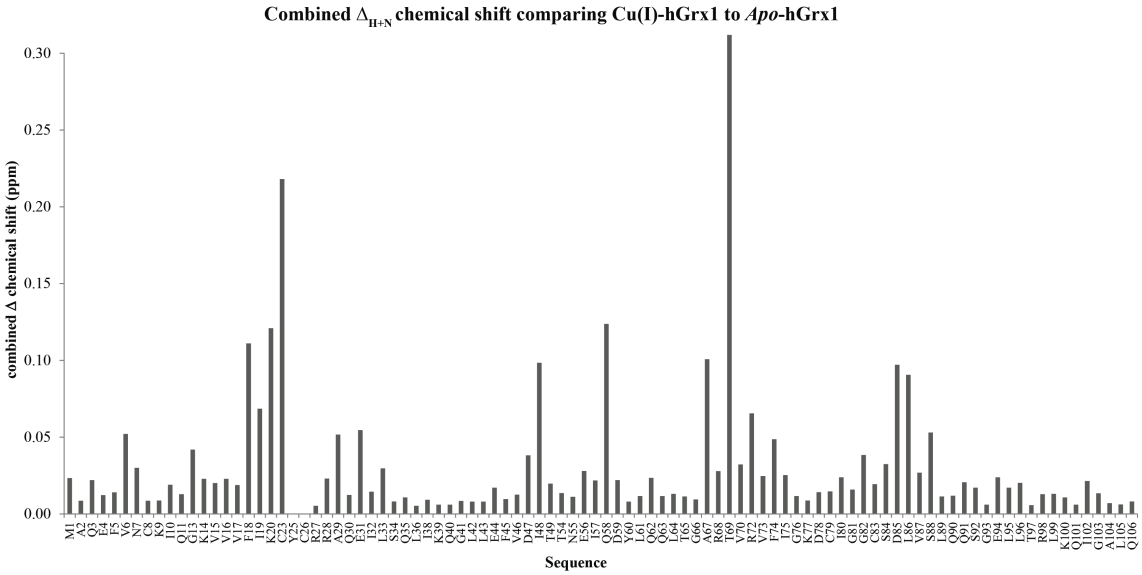

Figure S5C

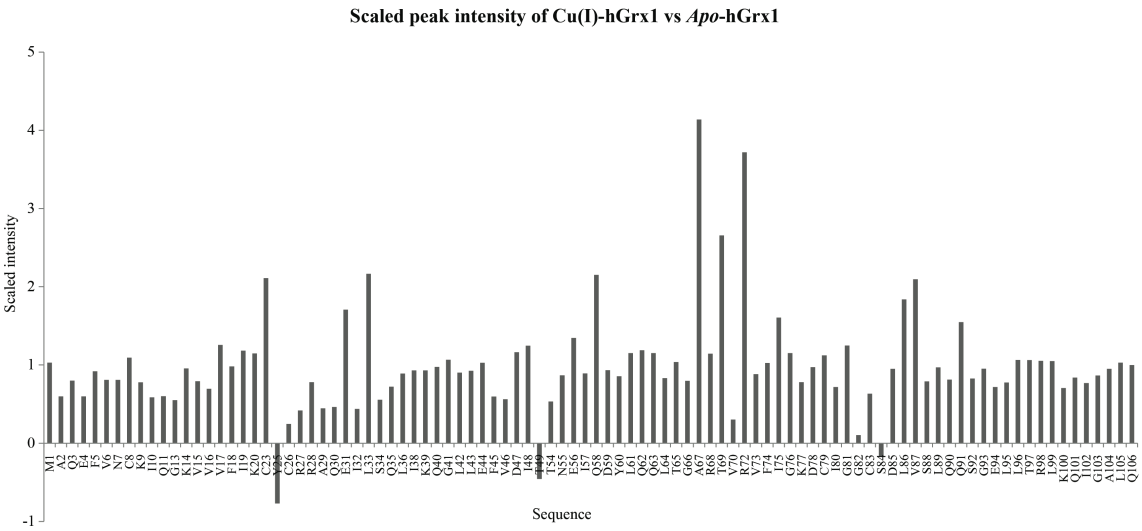

Figure S6A

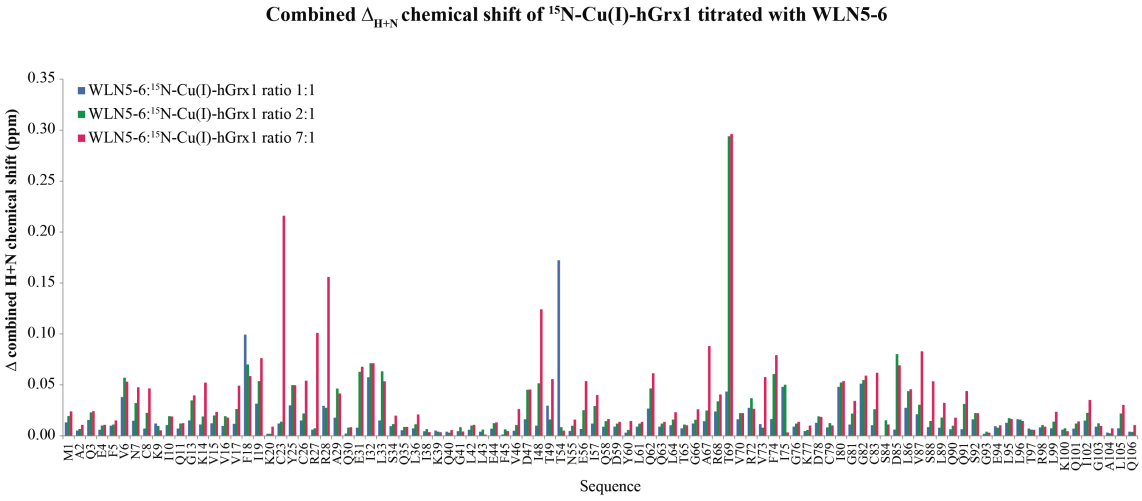

Figure S6B

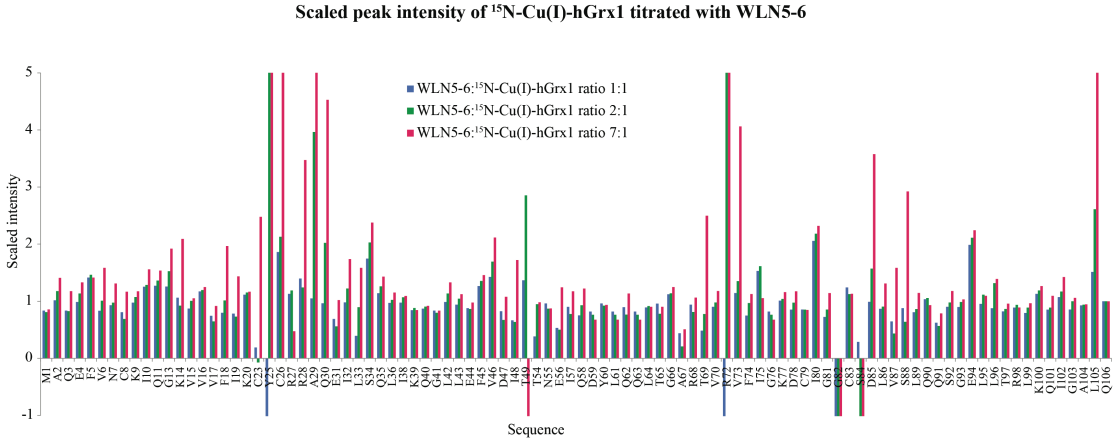

Figure S7A

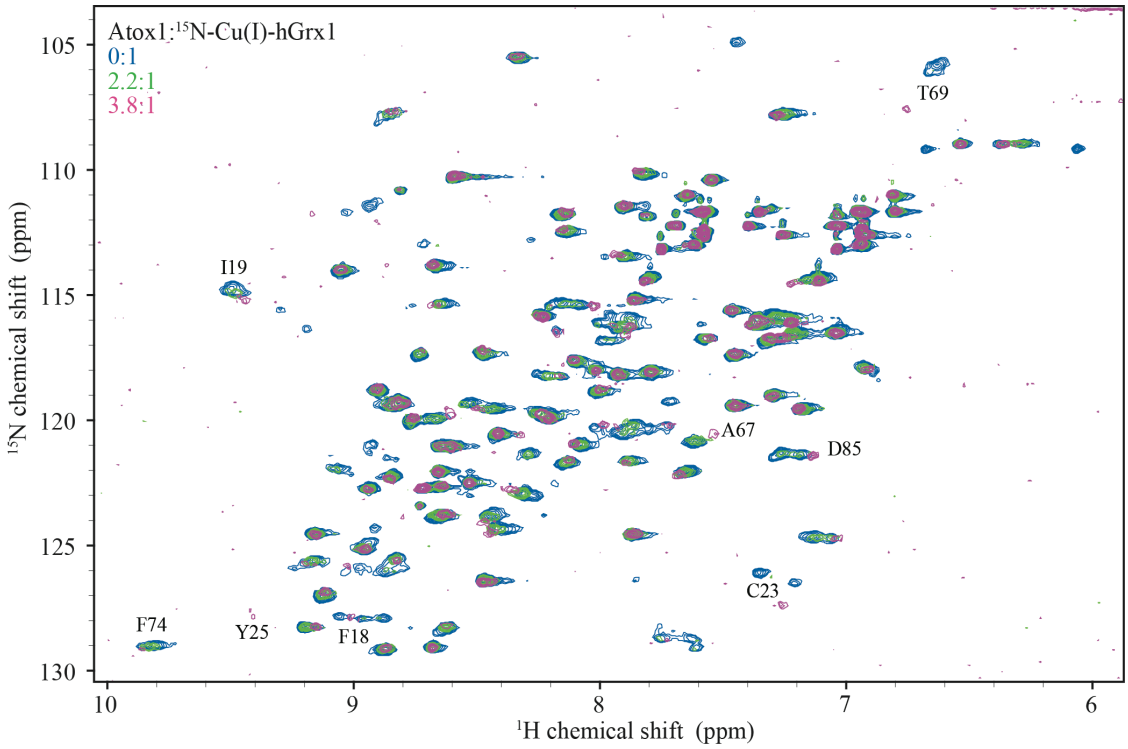
Atox1:15N-Cu(I)-hGrx1
0:1
2.2:1
3.8:1
T69
I19
A67
D85
C23
F74
Y25
F18
105
110
115
120
125
130
15N chemical shift (ppm)
10
9
8
7
6
1H chemical shift (ppm)

Figure S7B

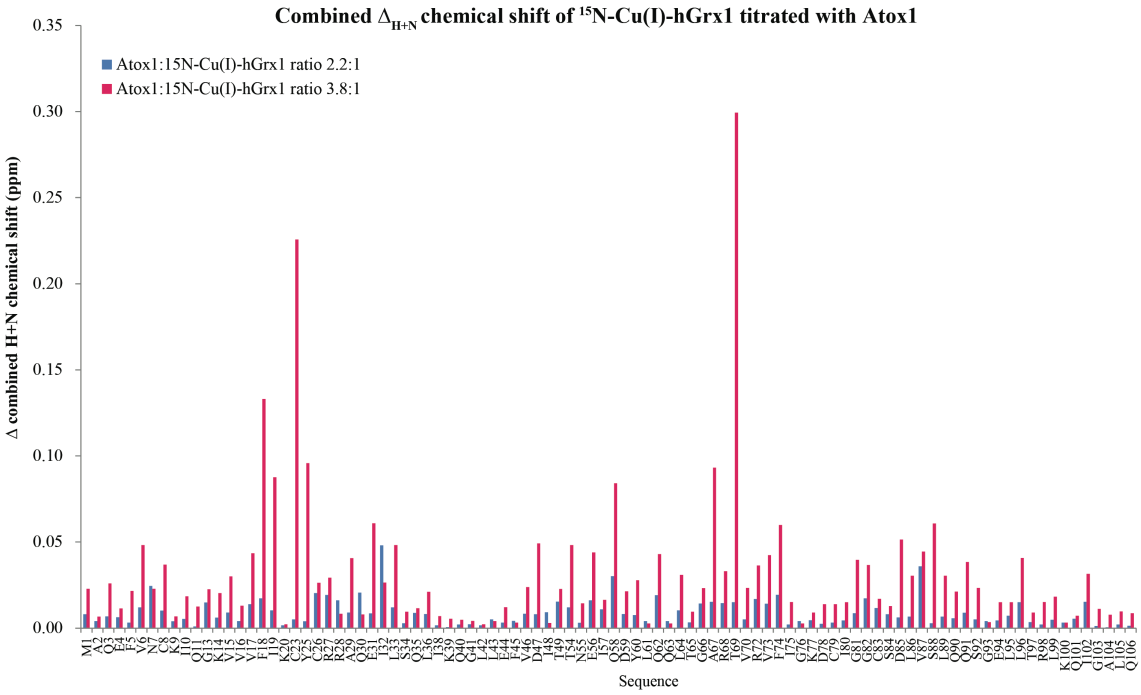

Figure S7C

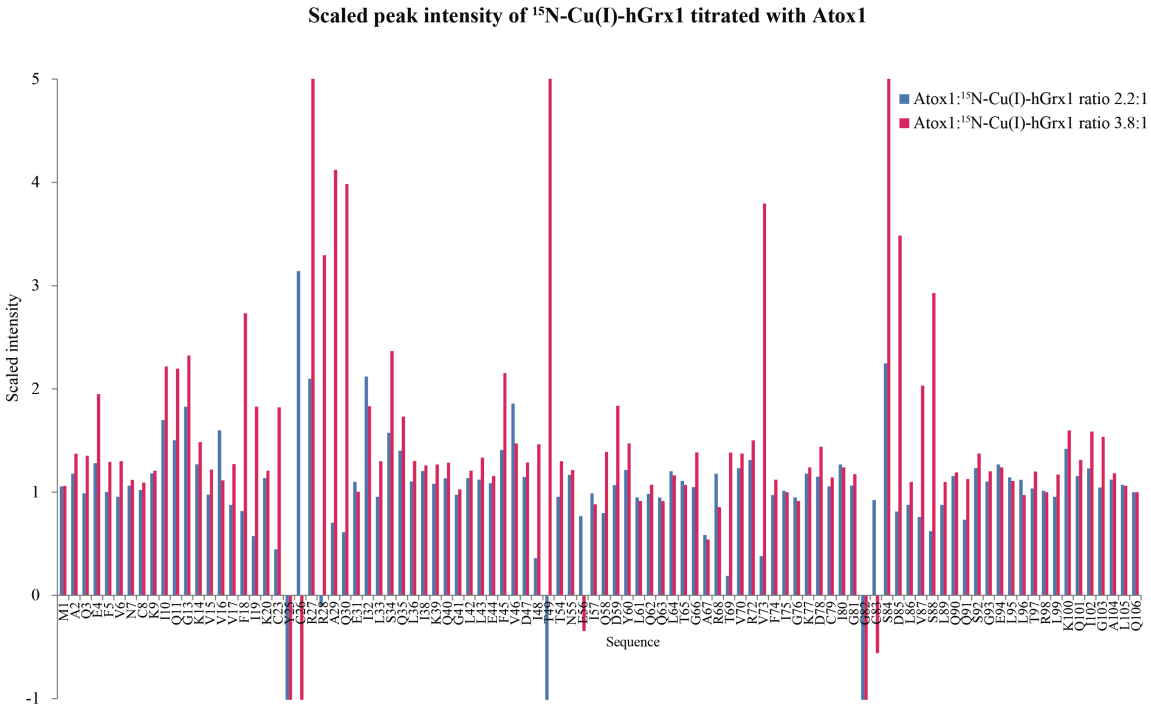

Figure S8A

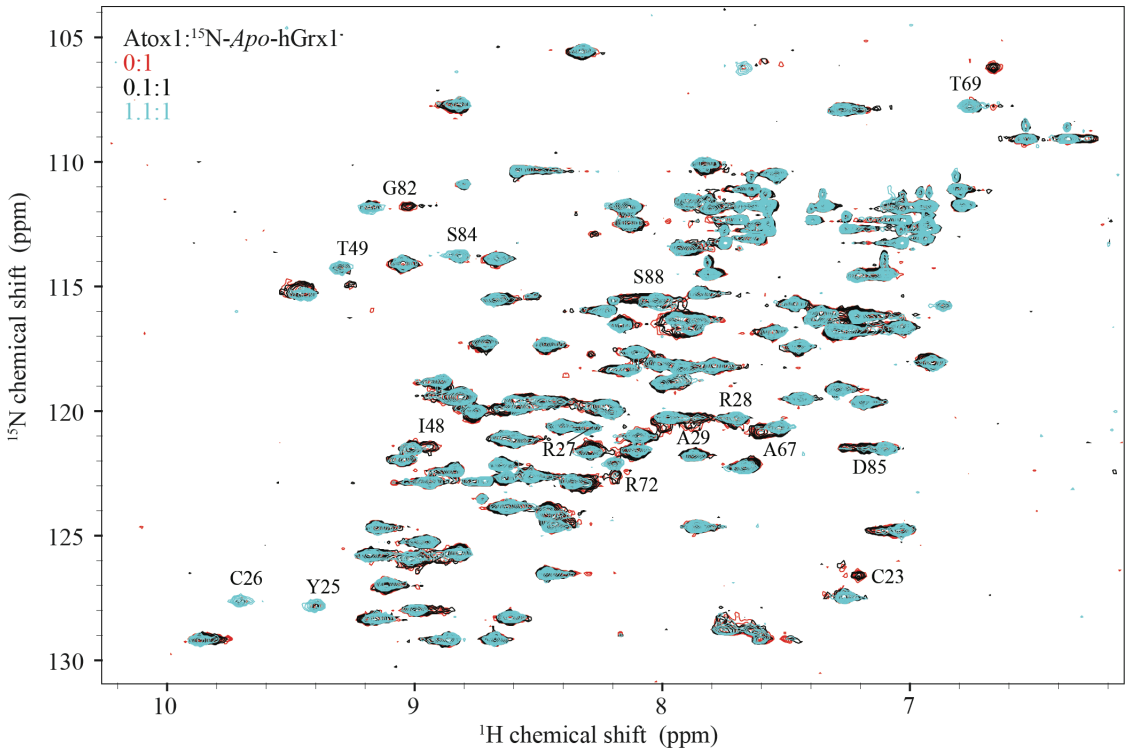

Figure S8B

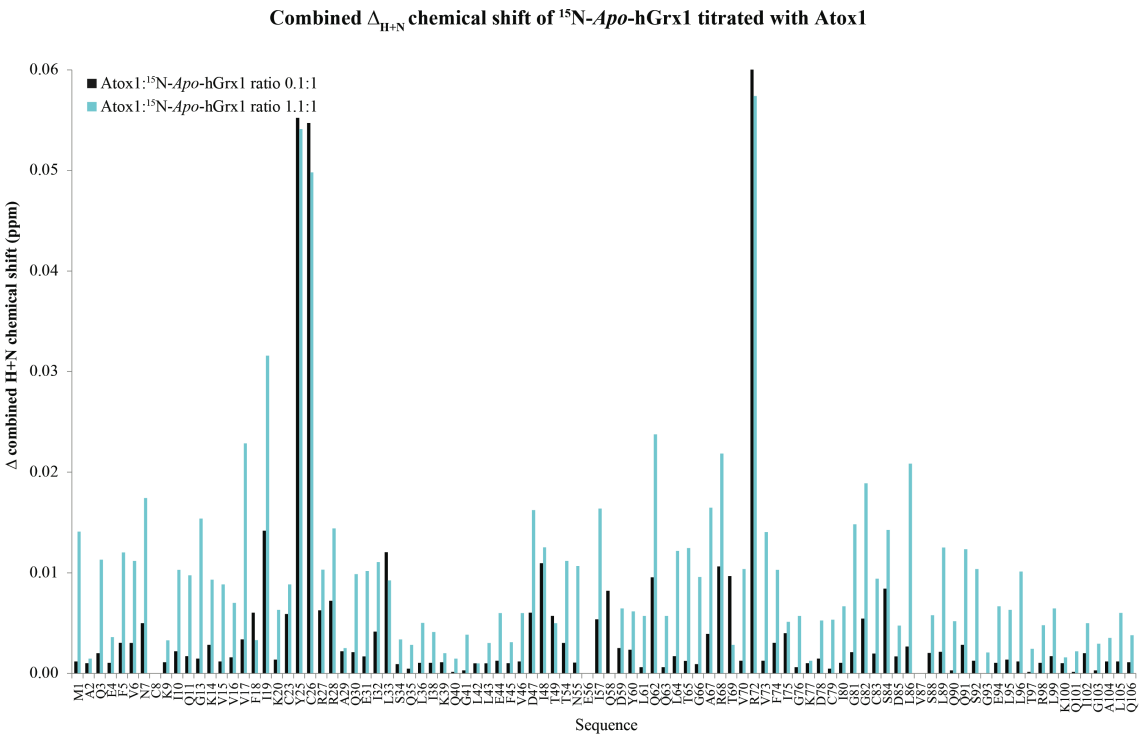

Figure S8C

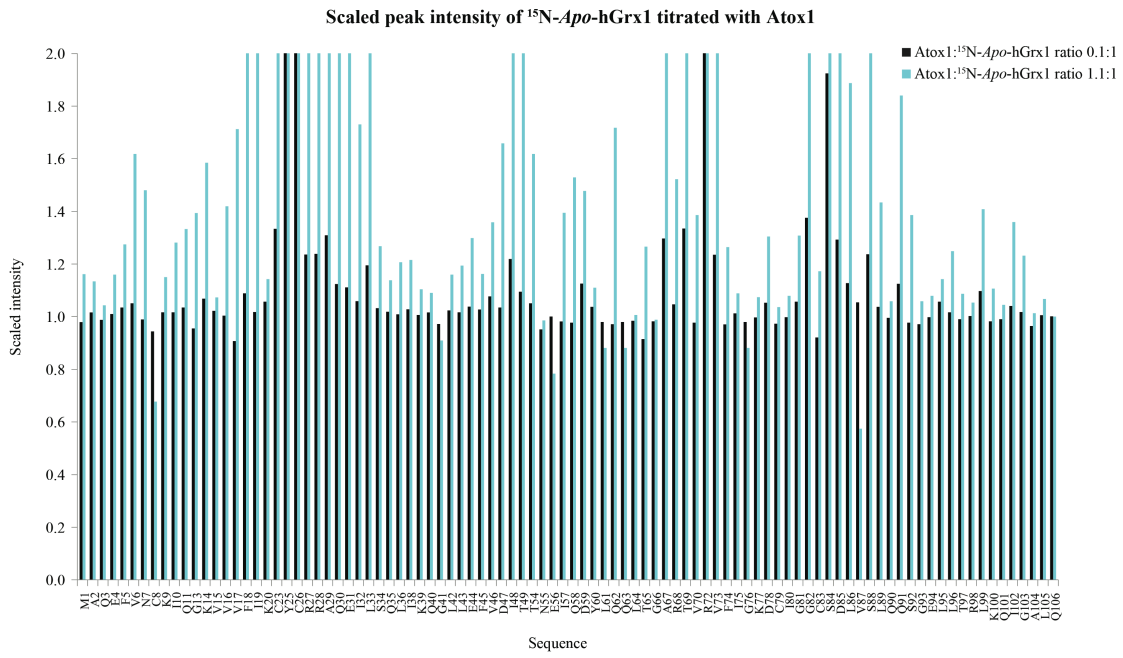

Figure S9A

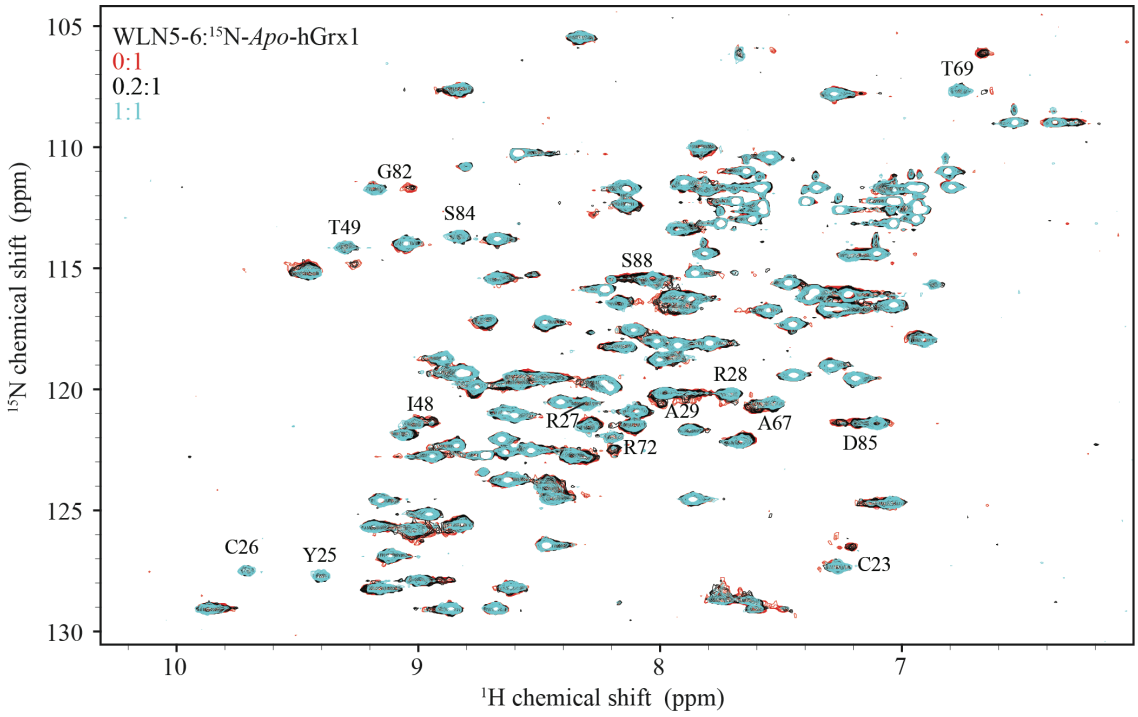

Figure S9B

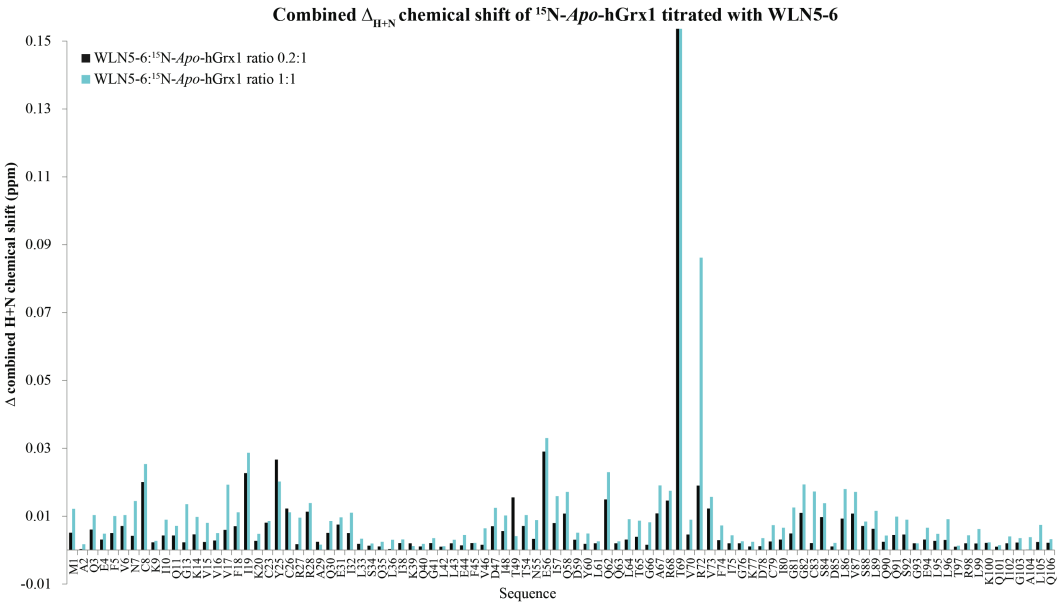

Figure S9C

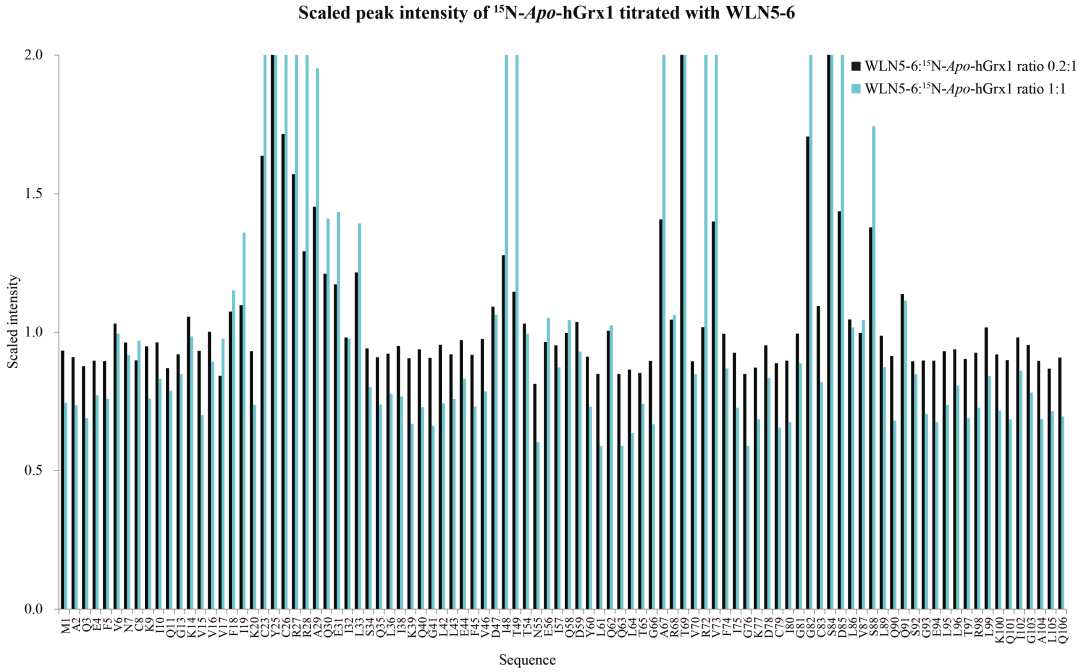

Figure S10A

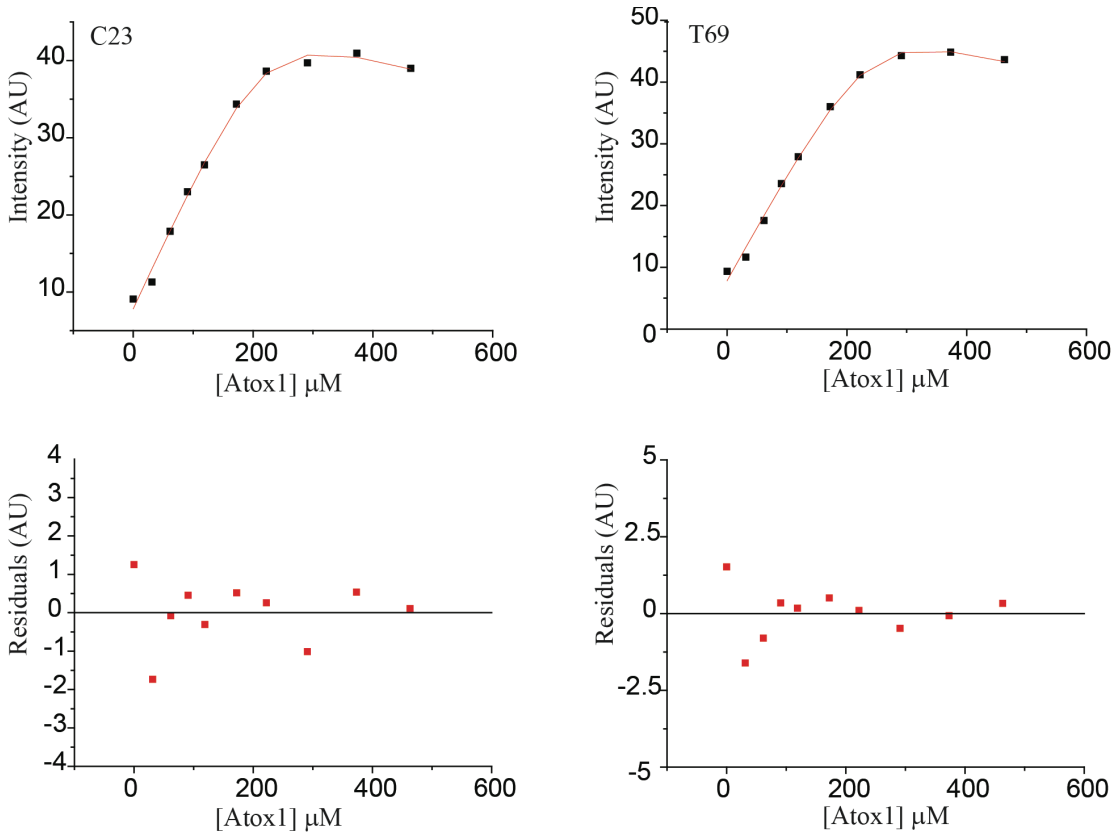

Figure S10B

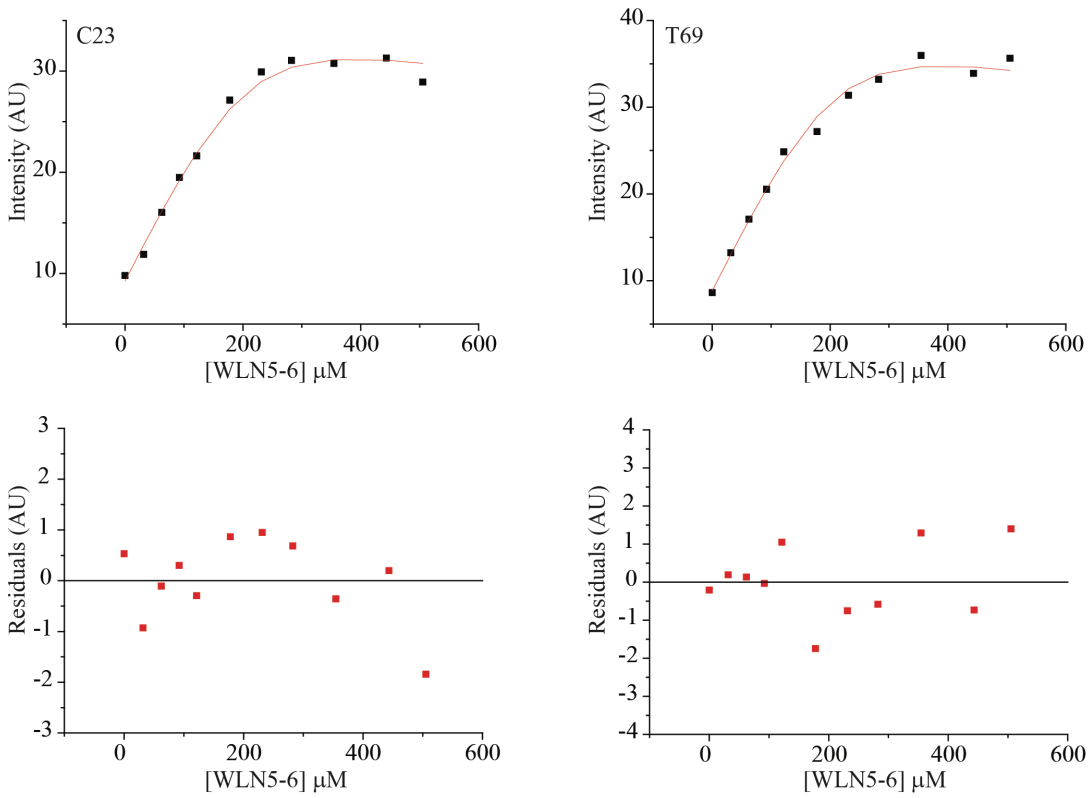

2.3 Paper I

Maghool S*, La Fontaine S, & Maher MJ* (2019) **High-resolution crystal structure of the reduced Grx1 from *Saccharomyces cerevisiae***. *Acta crystallographica. Section F, Structural biology communications 75(Pt 5):392-396.*

*Corresponding authors.

Author contributions

The following table is a fair and accurate description of the individual contributions made by each author to this publication:

Shadi Maghool	Expression, purification and crystallisation Data collection and structure solution Structure refinement and deposition of coordinates to the PDB Prepared all figures for the manuscript Wrote the manuscript with MJM
Sharon La Fontaine	Overall scientific direction of the project Critical reading of the manuscript
Megan J. Maher	Overall scientific direction of the project Wrote the manuscript with SM

Shadi Maghool
Candidate

Associate Professor Megan J. Maher
Supervisor and co-author of the paper

Acta Cryst F
STRUCTURAL BIOLOGY COMMUNICATIONS
ISSN 2053-230X

High-resolution crystal structure of the reduced Grx1 from *Saccharomyces cerevisiae*

Shadi Maghool,[a]* Sharon La Fontaine[b] and Megan J. Maher[a]*

[a]Department of Biochemistry and Genetics, La Trobe Institute for Molecular Science, La Trobe University, Melbourne, Victoria, Australia, and [b]School of Life and Environmental Sciences, Deakin University, Melbourne, Victoria, Australia. *Correspondence e-mail: s.maghool@latrobe.edu.au, m.maher@latrobe.edu.au

Received 18 November 2018
Accepted 7 March 2019

Edited by M. J. Romao, Universidade Nova de Lisboa, Portugal

Keywords: glutaredoxin; *Saccharomyces cerevisiae*; Grx1; reduced form.

PDB reference: reduced Grx1, 6mws

Supporting information: this article has supporting information at journals.iucr.org/f

Grx1, a cytosolic thiol–disulfide oxidoreductase, actively maintains cellular redox homeostasis using glutathione substrates (reduced, GSH, and oxidized, GSSG). Here, the crystallization of reduced Grx1 from the yeast *Saccharomyces cerevisiae* (yGrx1) in space group $P2_12_12_1$ and its structure solution and refinement to 1.22 Å resolution are reported. To study the structure–function relationship of yeast Grx1, the crystal structure of reduced yGrx1 was compared with the existing structures of the oxidized and glutathionylated forms. These comparisons revealed structural differences in the conformations of residues neighbouring the Cys27–Cys30 active site which accompany alterations in the redox status of the protein.

1. Introduction

Glutaredoxins (Grxs) are intracellular GSH-dependent oxidoreductase enzymes (EC 1.8.1.7). They catalyze reversible thiol–disulfide exchange reactions between protein thiols and GSSG/GSH and hence play a critical role in the maintenance of cellular redox homeostasis (Holmgren, 1989; Prinz *et al.*, 1997). Glutaredoxin enzymes act to protect cells from damage caused by reactive oxygen species (ROS) by catalyzing the reduction of protein disulfides (P-SS) and the deglutathionylation of mixed disulfides (P-SSG), and the overall direction of the reactions depend on the reduction potential of the GSSG/2GSH couple, the nature of the protein thiols involved and other solution conditions such as the presence of metal ions. In the reduction of glutathionylated disulfides (deglutathionylation reaction mechanism), the N-terminal active-site cysteine of Grx exists as a thiolate anion and attacks the glutathionyl sulfur of the P-SSG mixed disulfide, forming a Grx enzyme intermediate [Grx(SH)(SSG)] and releasing the reduced protein (P-SH). The Grx mixed disulfide is reduced by GSH, forming oxidized GSSG, which is then reduced to GSH by glutathione reductase and NADPH (Begas *et al.*, 2017; Ukuwela *et al.*, 2017, 2018). Structurally, Grxs share a common structural fold with the thioredoxin (TRX) superfamily, which is represented by a central core of four β-strands surrounded by five α-helices and an active-site C*XX*C sequence motif (Martin, 1995; Cave *et al.*, 2001).

Five Grxs have been characterized from the yeast *S. cerevisiae* to date. These include Grx1 (yGrx1) and Grx2, which contain an active-site CPYC (Luikenhuis *et al.*, 1998) motif which participates in redox processes through the formation of a disulfide bond between the two cysteine residues or *via* glutathionylation of the first cysteine residue (Holmgren, 1989; Prinz *et al.*, 1997; Ritz & Beckwith, 2001). However,

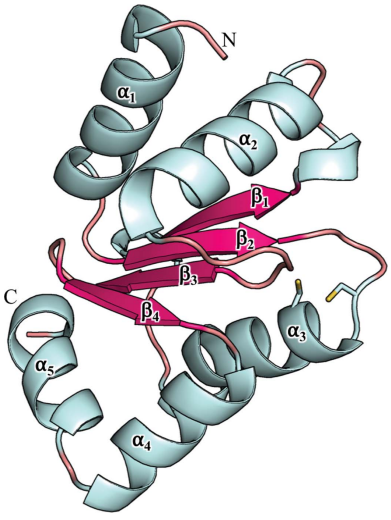

Table 1
Macromolecule-production information.

Source organism	*S. cerevisiae*
DNA source	*S. cerevisiae*
Expression vector	pGEX-6p-1
Expression host	*E. coli* strain BL21 CodonPlus (DE3)
Complete amino-acid sequence of the construct	GPLGSMVSQETIKHVKDLIAENEIFVASKTYCPYCHAALNTLFEKLKVPRSKVLVLQLNDMKEGADIQAALYEINGQRTVPNIYINGKHIGGNDDLQELRETGELEELLEPILAN

Table 2
Crystallization.

Method	Hanging-drop vapour diffusion
Plate type	VDXm plates
Temperature (K)	293
Protein concentration (mg ml^{-1})	16
Buffer composition of protein solution	20 m*M* Tris–MES pH 8.0, 150 m*M* NaCl, 1 m*M* TCEP
Composition of reservoir solution	0.23 *M* lithium sulfate monohydrate, 0.1 *M* bis-Tris pH 5.8, 26%(*w*/*v*) PEG 3350
Volume and ratio of drop	2 µl, 1:1
Volume of reservoir (µl)	500

other Grxs (Grx3, Grx4 and Grx5) from this organism contain only a single cysteine residue in an active-site CGFS motif, which catalyses the (de)glutathionylation of protein thiol groups using glutathione substrates (reduced, GSH, and oxidized, GSSG; Rodríguez-Manzaneque *et al.*, 1999). Crystal structures of the yGrx1 enzyme in the oxidized, glutathionylated (Yu *et al.*, 2008) and glutathionylated C30S mutant (Håkansson & Winther, 2007) forms have been reported previously (PDB entries 3c1r, 3c1s and 2jac, respectively). Here, we augment these structures with the first structure of yGrx1 in the reduced form in the absence of glutathionylation. A comparison of the structure of reduced yGrx1 (^{red}yGrx1; PDB entry 6mws, this work) with the structures of the oxidized (^{ox}yGrx1; PDB entry 3c1r) and glutathionylated (^{glu}yGrx1; PDB entry 3c1s) forms reveals conformational changes which accompany alterations in the redox status of this protein.

2. Materials and methods

2.1. Macromolecule production

The pGEX-6p-1-yGrx1 (GenScript) plasmid was transformed into *Escherichia coli* strain BL21 CodonPlus (DE3). Cultures were grown at 310 K in Luria Broth (LB) supplemented with ampicillin (100 µg ml^{-1}) and chloramphenicol (35 µg ml^{-1}) to an OD_{600} of 0.8, induced with isopropyl β-D-1-thiogalactopyranoside (IPTG; 0.5 m*M*) and harvested after 16 h (with shaking) at 298 K.

GST-yGrx1 was purified by GSH affinity chromatography. Frozen cell pellets were thawed at room temperature and resuspended in cell-lysis buffer [phosphate-buffered saline (PBS) pH 7.4, 1 m*M* tris(2-carboxyethyl)phosphine hydrochloride (TCEP)]. The cells were disrupted by passage through a TS series bench-top cell disruptor (Constant Systems) at 241 MPa. Cell debris was removed by centrifugation (Beckman JLA-25.50, 30 000*g*, 20 min, 277 K) and the soluble fraction was incubated for 2 h at 277 K with glutathione Sepharose 4B resin (GE Healthcare) equilibrated with lysis buffer (PBS containing 1 m*M* TCEP). The GST tag was cleaved overnight in lysis buffer with PreScission Protease followed by size-exclusion chromatography (SEC; HiLoad 16/600 Superdex 75 pg, GE Healthcare; 20 m*M* Tris–MES pH 8.0, 150 m*M* NaCl, 1 m*M* TCEP). Cleavage of the N-terminal GST tag introduced five additional residues (GPLGS) to the N-terminus of yGrx1 (Table 1). The purified protein was concentrated to 20 mg ml^{-1} before storage at 193 K.

2.2. Crystallization

Crystallization trials were conducted using commercially available screens (SaltRx HT and Index HT from Hampton Research) by sitting-drop vapour diffusion in 96-well plates (Molecular Dimensions) using pure yGrx1 samples at two different protein concentrations (10 and 20 mg ml^{-1}). Crystallization drops consisting of equal volumes (0.2 µl) of reservoir and protein solutions were dispensed using a Crystal Gryphon liquid-handling system (Art Robbins Instruments) and were equilibrated against a reservoir of screen solution (50 µl). Plates were incubated at 293 K. Multiple tiny crystals were observed within ten days in conditions F7 and G2 of the Index HT screen [0.2 *M* ammonium sulfate, 0.1 *M* bis-Tris pH 6.5, 25%(*w*/*v*) PEG 3350 and 0.2 *M* lithium sulfate monohydrate, 0.1 *M* bis-Tris pH 5.5, 25%(*w*/*v*) PEG 3350, respectively]. Optimization of these conditions was carried out by hanging-drop vapour diffusion in 24-well VDX plates (Hampton Research). Diffraction-quality crystals of yGrx1 grew after 20 days in drops consisting of equal volumes (1 µl) of yGrx1 (16 mg ml^{-1} in 20 m*M* Tris–MES pH 8.0, 150 m*M* NaCl, 1 m*M* TCEP) and reservoir [0.23 *M* lithium sulfate monohydrate, 0.1 *M* bis-Tris pH 5.8, 26%(*w*/*v*) PEG 3350] solutions equilibrated against 500 µl reservoir solution. Crystals were cryoprotected in reservoir solution containing 25%(*w*/*v*) glycerol before flash-cooling them in liquid nitrogen. Crystallization information is summarized in Table 2.

2.3. Data collection and processing

Diffraction data were recorded on beamline MX2 at the Australian Synchrotron at a wavelength of 0.954 Å at 100 K using an EIGER X 16M detector and were processed with *XDS* (Kabsch, 2010) and merged and scaled with *AIMLESS* (Evans & Murshudov, 2013). Data-collection statistics are detailed in Table 3.

2.4. Structure solution and refinement

The crystal structure of yGrx1 was solved by molecular replacement using *Phaser* (McCoy *et al.*, 2007) from the *CCP*4 suite (Winn *et al.*, 2011). The crystal structure of oxidized yGrx1 (Yu *et al.*, 2008) was used as a search model after the removal of all water molecules. The model was refined using *REFMAC*5 (Murshudov *et al.*, 2011) and manual model building was carried out in *Coot* (Emsley *et al.*, 2010). Automated water picking was carried out using *ARP*/*wARP* (Langer *et al.*, 2008) and was then checked manually in *Coot*

Table 3
Data collection and processing.

Values in parentheses are for the outer shell.

Diffraction source	MX2, Australian Synchrotron
Wavelength (Å)	0.953654
Temperature (K)	100
Detector	EIGER X 16M
Crystal-to-detector distance (mm)	150
Total rotation range (°)	180
Space group	$P2_12_12_1$
a, b, c (Å)	41.4, 51.8, 57.2
α, β, γ (°)	90.0, 90.0, 90.0
Mosaicity (°)	0.04
Resolution range (Å)	41.36–1.22 (1.25–1.22)
Total No. of reflections	474455 (17110)
No. of unique reflections	37323 (1777)
Completeness (%)	99.9 (98.3)
Multiplicity	12.7 (9.6)
$\langle I/\sigma(I)\rangle$	19.4 (4.0)
$CC_{1/2}$	0.999 (0.969)
R_{merge}	0.053 (0.319)
Overall B factor from Wilson plot (Å^2)	14.2

Table 4
Structure solution and refinement.

Values in parentheses are for the outer shell.

Resolution range (Å)	38.38–1.22 (1.25–1.22)
Completeness (%)	99.9 (98.3)
σ Cutoff	None
No. of reflections, working set	35443
No. of reflections, test set	1820
Final R_{cryst}	0.148 (0.149)
Final R_{free}	0.171 (0.159)
No. of non-H atoms	
Protein	854
Sulfate	5
Water	122
Total	981
R.m.s. deviations	
Bonds (Å)	0.010
Angles (°)	1.430
Average B factors (Å^2)	
Protein	13.731
Sulfate	14.822
Water	23.273
Ramachandran plot	
Most favoured (%)	99.1
Allowed (%)	100
MolProbity score	0.82
PDB code	6mws

(Emsley *et al.*, 2010). The quality of the structure was determined by *MolProbity* (Chen *et al.*, 2010). Refinement statistics are summarized in Table 4.

3. Results and discussion

The ^{red}yGrx1 crystallized in space group $P2_12_12_1$, with unit-cell parameters a = 41.4, b = 51.8, c = 57.2 Å. The structure was determined by molecular replacement and refined to 1.22 Å resolution. The refinement converged with residuals R_{cryst} = 14.8% and R_{free} = 17.1%. The solvent content of the crystal was 60% and the structure shows a single molecule of ^{red}yGrx1 (residues Val2–Ala109) in the asymmetric unit. Owing to an absence of interpretable electron density for the five additional N-terminal residues (GPLGS) and the N-terminal and C-terminal residues of yGrx1 (Met1 and

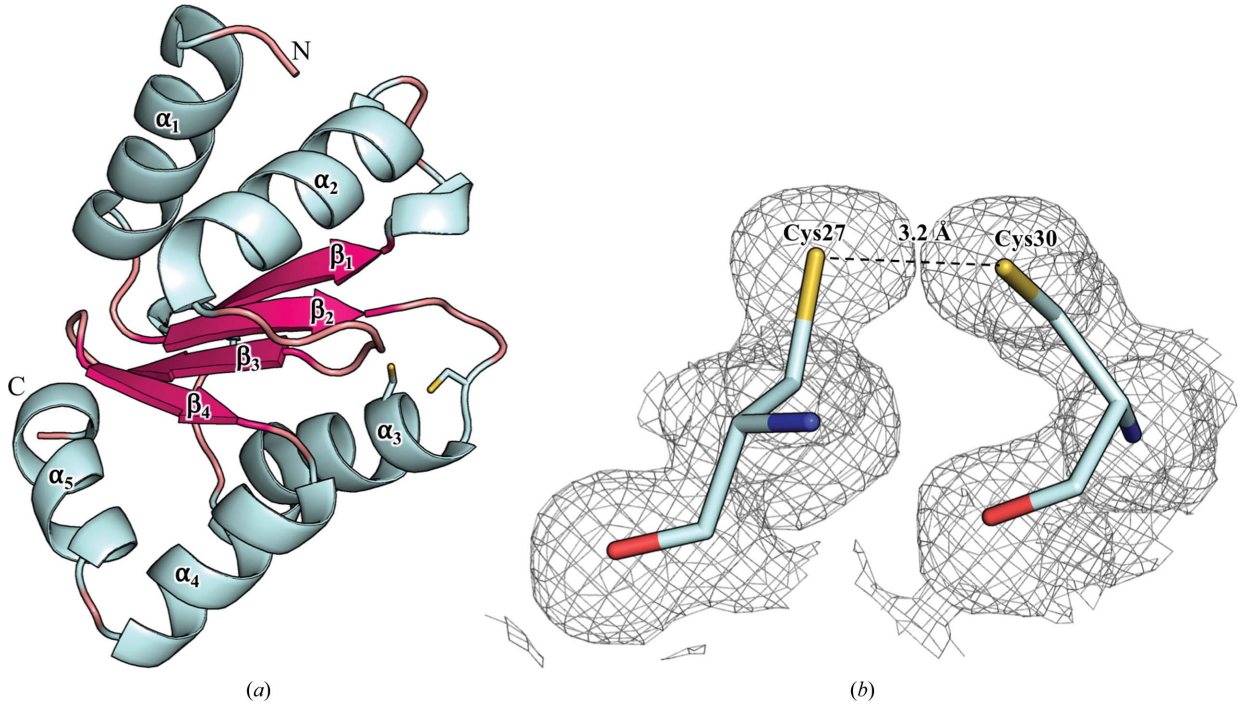

Figure 1
Cartoon representation of the overall structure of ^{red}yGrx1. (*a*) Secondary structures are represented as cartoons, with α-helices and β-strands coloured cyan and pink, respectively. The Cys27 and Cys30 residues are shown as yellow sticks. (*b*) $F_o - F_c$ difference Fourier electron-density map calculated after omission of the Cys27 and Cys30 residues from the model coordinates. C, O, N and S atoms are coloured cyan, red, blue and yellow, respectively. The $F_o - F_c$ map is contoured at 4σ.

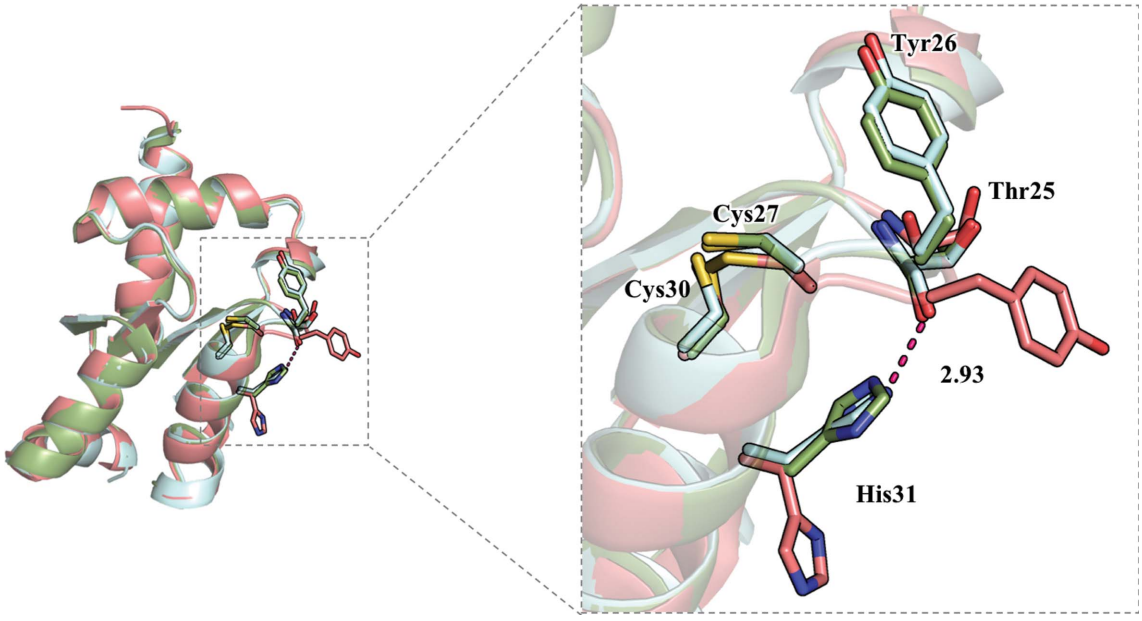

Figure 2
Details of the yGrx1 active site (CPYC) upon reduction (cyan), oxidization (salmon) and glutathionylation (green). Comparison of the ^{red}yGrx1 (cyan), ^{ox}yGrx1 (PDB entry 3c1r; salmon) and ^{glu}yGrx1 (PDB entry 3c1s; green) structures shows that upon the separation of the Cys27 and Cys30 residues owing to reduction or glutathionylation, the Thr25, Tyr26 and His31 residues (shown in stick representation) undergo conformational changes that accompany the change in redox state of the enzyme.

Asn110, respectively), these were omitted from the final model. The overall fold of ^{red}yGrx1 (Fig. 1*a*) is similar to those of the previously reported yGrx1 structures (PDB entries 3c1r, 3c1s and 2jac; Yu *et al.*, 2008; Håkansson & Winther, 2007), with four mixed β-strands in a central core structure surrounded by five α-helices.

The positions of the side chains (and in particular the thiol groups) of cysteine residues Cys27 and Cys30 were confirmed by the calculation of difference Fourier electron-density maps (using a model with the side chains of these residues removed; Fig. 1*b*). These residues were modelled with a distance between the S atoms of Cys27 and Cys30 of 3.2 Å, which is significantly greater than that observed (2.05 Å) for the ^{ox}yGrx1 structure (PDB entry 3c1r; Yu *et al.*, 2008). This indicates that the yGrx1 structure reported here is indeed that of ^{red}yGrx1 (PDB entry 6mws).

Superposition of the ^{red}yGrx1 structure with that of ^{ox}yGrx1 (PDB entry 3c1r; Yu *et al.*, 2008) gave a root-mean-square deviation (r.m.s.d.) of 0.48 Å for 108 common C^{α} positions, demonstrating that minimal conformational changes occur to the overall yGrx1 structure on oxidation and/or reduction. However, the reduction of the Cys27–Cys30 disulfide bond and separation of the thiol groups of these residues accompanies conformational rearrangements in the neighbouring protein structure, specifically residues Thr25, Tyr26 and His31 (Fig. 2). In the ^{ox}yGrx1 structure the side chain of Tyr26 faces 'away' from the Cys27–Cys30 site. In ^{red}yGrx1 Tyr26 shows a conformation rotated by approximately 180° from that observed for ^{ox}yGrx1, with the side chain orientated 'towards' the Cys27–Cys30 site. This is accompanied by a flip in the orientation of the carbonyl group of residue Thr25, so that in the ^{red}yGrx1 structure this group participates in a hydrogen-bonding interaction with the side chain of His31, which is also reorientated (Fig. 2). Interestingly, similar conformations for residues Thr25, Tyr26 and His31 were observed in the structure of ^{glu}yGrx1 (PDB entry 3c1s; Yu *et al.*, 2008), which also lacks a disulfide bond between residues Cys27 and Cys30 owing to the glutathionylation of Cys27. In addition, conformational changes of neighbouring amino acids have been reported for *E. coli* Grx1 (PDB entries 1ego and 1grx; Xia *et al.*, 1992) by NMR, in which reduction of the active-site Cys11–Cys14 disulfide bond was reported to result in an enhanced rate of exchange for the neighbouring residues Phe6, Gly7 and Ala17, indicating conformational changes in these residues.

In summary, although ^{red}yGrx1 crystallized in a different condition and space group to the reported ^{ox}yGrx1 and ^{glu}yGrx1 structures, the conformational changes of residues neighbouring the active site (CPYC), particularly Thr25, Tyr26 and His31, is consistent among the three structures. This indicates these changes are not owing to crystal packing and instead reflect the redox state of yGrx1. The precise role that these residues play in the activity of yGrx1 remains to be explored.

Acknowledgements

Aspects of this research were undertaken on the Macromolecular Crystallography beamline MX2 at the Australian Synchrotron, Victoria, Australia and we thank the beamline staff for their enthusiastic and professional support.

Funding information

This study was supported by ARC grant DP140102746 to MJM and an Australian Government Research Training Program Scholarship to SM.

References

Begas, P., Liedgens, L., Moseler, A., Meyer, A. J. & Deponte, M. (2017). *Nature Commun.* **8**, 14835.

Cave, J. W., Cho, H. S., Batchelder, A. M., Yokota, H., Kim, R. & Wemmer, D. E. (2001). *Protein Sci.* **10**, 384–396.

Chen, V. B., Arendall, W. B., Headd, J. J., Keedy, D. A., Immormino, R. M., Kapral, G. J., Murray, L. W., Richardson, J. S. & Richardson, D. C. (2010). *Acta Cryst.* D**66**, 12–21.

Emsley, P., Lohkamp, B., Scott, W. G. & Cowtan, K. (2010). *Acta Cryst.* D**66**, 486–501.

Evans, P. R. & Murshudov, G. N. (2013). *Acta Cryst.* D**69**, 1204–1214.

Håkansson, K. O. & Winther, J. R. (2007). *Acta Cryst.* D**63**, 288–294.

Holmgren, A. (1989). *J. Biol. Chem.* **264**, 13963–13966.

Kabsch, W. (2010). *Acta Cryst.* D**66**, 125–132.

Langer, G., Cohen, S. X., Lamzin, V. S. & Perrakis, A. (2008). *Nature Protoc.* **3**, 1171–1179.

Luikenhuis, S., Perrone, G., Dawes, I. W. & Grant, C. M. (1998). *Mol. Biol. Cell*, **9**, 1081–1091.

Martin, J. L. (1995). *Structure*, **3**, 245–250.

McCoy, A. J., Grosse-Kunstleve, R. W., Adams, P. D., Winn, M. D., Storoni, L. C. & Read, R. J. (2007). *J. Appl. Cryst.* **40**, 658–674.

Murshudov, G. N., Skubák, P., Lebedev, A. A., Pannu, N. S., Steiner, R. A., Nicholls, R. A., Winn, M. D., Long, F. & Vagin, A. A. (2011). *Acta Cryst.* D**67**, 355–367.

Prinz, W. A., Åslund, F., Holmgren, A. & Beckwith, J. (1997). *J. Biol. Chem.* **272**, 15661–15667.

Ritz, D. & Beckwith, J. (2001). *Annu. Rev. Microbiol.* **55**, 21–48.

Rodríguez-Manzaneque, M. T., Ros, J., Cabiscol, E., Sorribas, A. & Herrero, E. (1999). *Mol. Cell. Biol.* **19**, 8180–8190.

Ukuwela, A. A., Bush, A. I., Wedd, A. G. & Xiao, Z. (2017). *Biochem. J.* **474**, 3799–3815.

Ukuwela, A. A., Bush, A. I., Wedd, A. G. & Xiao, Z. (2018). *Chem. Sci.* **9**, 1173–1183.

Winn, M. D., Ballard, C. C., Cowtan, K. D., Dodson, E. J., Emsley, P., Evans, P. R., Keegan, R. M., Krissinel, E. B., Leslie, A. G. W., McCoy, A., McNicholas, S. J., Murshudov, G. N., Pannu, N. S., Potterton, E. A., Powell, H. R., Read, R. J., Vagin, A. & Wilson, K. S. (2011). *Acta Cryst.* D**67**, 235–242.

Xia, T.-H., Bushweller, J. H., Sodano, P., Billeter, M., Björnberg, O., Holmgren, A. & Wüthrich, K. (1992). *Protein Sci.* **1**, 310–321.

Yu, J., Zhang, N.-N., Yin, P.-D., Cui, P.-X. & Zhou, C.-Z. (2008). *Proteins*, **72**, 1077–1083.

Chapter 3

Cytochrome *c* oxidase Assembly Factor 6

3.1 Introduction

Complex IV (cytochrome *c* oxidase; COX) is the terminal complex of the mitochondrial electron transport chain. Copper is essential for COX assembly, activity and stability, and is incorporated into the dinuclear Cu_A and mononuclear Cu_B sites. COX assembly factors are required for the biogenesis of COX. The assembly factor Coa6 has been proposed to play a role in the biogenesis of the Cu_A site. A W59C Coa6 mutation has been identified in a patient suffering from hypertrophic obstructive cardiomyopathy, resulting in a COX assembly defect and attenuation in the activity of the complex.

Chapter 3 details the crystal structures of the human ^{WT}Coa6 and the pathogenic ^{W59C}Coa6 mutant proteins. The initial studies in Chapter 3 were based on the expression, purification, mutagenesis, characterisation and crystallisation of ^{WT}Coa6 and ^{W59C}Coa6 proteins. Here, recombinant proteins were overexpressed with an N-terminal GST tag and purified *via* GSH affinity chromatography. The crystal structure of the ^{WT}Coa6 and ^{W59C}Coa6 were determined to 1.6 Å and 2.2 Å resolution, respectively. These structures show that ^{WT}Coa6 has a three-helical bundle structure, with the first two helices tethered by disulfide bonds, one of which provides the copper binding site. Disulfide mediated oligomerisation of the ^{W59C}Coa6 protein provides a structural explanation for this loss-of-function mutation. Crucially, the location of the copper binding site within Coa6 was identified by mutagenesis. This chapter is presented in the form of a manuscript that is currently under review with the journal *Life Science Alliance*. The author contributions for this manuscript are presented in the table below.

3.2 Paper II

Maghool S, Cooray NDG, Stroud DA, Aragão D, Ryan MT, & Maher MJ (2019) **Structural and functional characterization of the mitochondrial complex IV assembly factor Coa6.** *Life Science Alliance 2(5): e201900458.*

Author contributions

The following table is a fair and accurate description of the individual contributions made by each author to this manuscript:

Shadi Maghool	Mutagenesis, expression, purification, characterisation and crystallisation Data collection and structure solution, structure refinement and deposition of coordinates to the PDB Copper binding experiments Prepared all figures for the manuscript Wrote the manuscript with MJM
N. Dinesha G. Cooray	Expression, purification and crystallisation of ^{WT}Coa6
David A. Stroud	Supervised SM for cell biology experiments Prepared Figure S7 Critical reading and editing of the manuscript
David Aragão	Data collection and structure solution of ^{WT}Coa6 with SM and MJM
Michael T. Ryan	Overall scientific direction of the project Critical reading and editing of the manuscript
Megan J. Maher	Overall scientific direction of the project Data collection and structure solution of ^{WT}Coa6 with SM and DA Wrote the manuscript with SM

Shadi Maghool

Candidate

Associate Professor Megan J. Maher

Supervisor and co-author of the paper

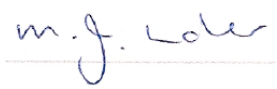

Research Article

TRANSPARENT PROCESS OPEN ACCESS

Life Science Alliance

Structural and functional characterization of the mitochondrial complex IV assembly factor Coa6

Shadi Maghool[1], N Dinesha G Cooray[1], David A Stroud[2], David Aragão[3], Michael T Ryan[4], Megan J Maher[1,5]

Assembly factors play key roles in the biogenesis of many multi-subunit protein complexes regulating their stability, activity, and the incorporation of essential cofactors. The human assembly factor Coa6 participates in the biogenesis of the Cu_A site in complex IV (cytochrome *c* oxidase, COX). Patients with mutations in Coa6 suffer from mitochondrial disease due to complex IV deficiency. Here, we present the crystal structures of human Coa6 and the pathogenic ^{W59C}Coa6-mutant protein. These structures show that Coa6 has a 3-helical bundle structure, with the first 2 helices tethered by disulfide bonds, one of which likely provides the copper-binding site. Disulfide-mediated oligomerization of the ^{W59C}Coa6 protein provides a structural explanation for the loss-of-function mutation.

DOI 10.26508/lsa.201900458 | Received 17 June 2019 | Revised 26 August 2019 | Accepted 2 September 2019 | Published online 12 September 2019

Introduction

The mitochondrial oxidative phosphorylation (OXPHOS) system generates the bulk of cellular ATP, fuelling the energy demands of most eukaryotes. Five multi-subunit protein complexes in the mitochondrial inner membrane, termed complexes I–V, comprise the OXPHOS system. Complex IV (cytochrome *c* oxidase; COX) is the last complex of the electron transport chain, transferring electrons from cytochrome *c* to molecular oxygen, and in the process, pumping four protons across the inner membrane (1). In mammals, complex IV is additionally found with complexes I and III in large multicomplex assemblies termed the respiratory chain super-complexes (2, 3). In humans, complex IV is composed of 14 subunits with the three mitochondrial DNA-encoded subunits (COX1-3) forming the catalytic core of the enzyme that is conserved from yeast to man (4). Cytochrome *c* docks onto the intermembrane space (IMS) domain of COX2, which contains a binuclear copper center, termed Cu_A that accepts the electrons. The electrons are then passed to a heme *a* group in COX1 and then to a heme a_3-Cu_B site and finally to oxygen, which is reduced to water (5). Thus, reduction of the Cu_A site in COX2 represents the critical first stage in complex IV activity.

In humans, the assembly of the Cu_A site requires the assembly factors Cox16 (6), Cox17 (7), Sco1 (8), Sco2 (9), and Coa6 (10, 11), with mutations in these proteins resulting in COX assembly defects and an attenuation in the activity of the complex (12, 13). The metallochaperone Cox17 (7) is a mitochondrial IMS located protein, which receives copper from the mitochondrial matrix copper pool where copper is bound by an anionic fluorescent molecule (also known as copper ligand, CuL) (8, 14, 15). CuL has also been reported to be located in the cytoplasm and may be a vehicle for copper transport into mitochondria (14). Cox17 is crucial for copper delivery to COX2 through a proposed sequential pathway, with Sco2 acting upstream of Sco1 (16, 17, 18, 19). Recently, Cox16 has been shown to play a role in this process, being required for the association between Sco1 and COX2 and between COX1 and COX2 for COX assembly (6).

Coa6 is a soluble IMS protein with a CX_9C–$CX_{10}C$ sequence motif, which binds Cu(I) with a $K_{D(CuI)}$ of ~10^{-17} M (11). Coa6 deletion in both yeast and human cells results in diminished COX assembly and activity; however, this defect can be partially rescued by exogenous copper supplementation (10) and in yeast by treatment with elesclomol (via a proposed elesclomol–copper complex (20)). Recent studies (11, 21) have shown that Coa6 interacts with newly synthesized COX2 (11, 21) and with both Sco1 and Sco2, leading to suggestions that Coa6 acts to facilitate Cu_A site assembly and, therefore, COX biogenesis as part of a Sco1/Sco2 (21)-containing complex and/or through the redox cycling of Sco2 (22).

Pathogenic mutations in the Coa6 protein (W59C and E87*) were identified in a patient suffering from hypertrophic obstructive cardiomyopathy, resulting in a COX defect in the heart tissue, but no defect in fibroblasts (17). An additional patient with a W66R mutation in Coa6 suffered from neonatal hypertrophic cardiomyopathy, muscular hypotonia, and lactic acidosis with a COX defect in the fibroblasts (16). One report examining the ^{W59C}Coa6 variant showed the protein was mistargeted to the mitochondrial matrix; however, our previous results (11) showed that the ^{W59C}Coa6 was

[1]Department of Biochemistry and Genetics, La Trobe Institute for Molecular Science, La Trobe University, Melbourne, Australia [2]Department of Biochemistry and Molecular Biology and The Bio21 Molecular Science and Biotechnology Institute, The University of Melbourne, Parkville, Australia [3]Australian Synchrotron, Australian Nuclear Science and Technology Organisation, Clayton, Australia [4]Department of Biochemistry and Molecular Biology, Biomedicine Discovery Institute, Monash University, Clayton, Australia [5]School of Chemistry and The Bio21 Molecular Science and Biotechnology Institute, The University of Melbourne, Parkville, Australia

Correspondence: megan.maher@unimelb.edu.au
David Aragão's present address is Diamond Light Source, Harwell Science and Innovation Campus, Didcot, UK

able to partially rescue human embryonic kidney (HEK293T) Coa6 knockout cells, suggesting that the mutant protein retains some functionality.

It is clear that Coa6 is essential for COX assembly, that it plays a role in the biogenesis of the Cu_A site, interacts with crucial factors in the IMS Cu delivery pathway, and that mutations to Coa6 are pathogenic and lead to mitochondrial disease (16, 17). However, the precise role that Coa6 plays in COX biogenesis, and therefore, the mechanism underlying ^{W59C}Coa6 pathogenesis remains to be elucidated. In this study, we have determined the crystal structures of the human wild-type Coa6 (^{WT}Coa6) and ^{W59C}Coa6 proteins by X-ray crystallography to 1.65 and 2.2 Å resolution, respectively. By mutagenesis, we propose the location of the copper-binding site within Coa6. Examination of the structures allows us to suggest the mechanism of action for this protein in COX assembly and the molecular origin of pathogenesis for the W59C mutation.

Results and Discussion

The structure of ^{WT}Coa6

Recombinant ^{WT}Coa6 protein was overexpressed in *Escherichia coli* strain SHuffle T7, which promotes the production of correctly disulfide bonded active proteins within the cytoplasm (23, 24). The fully oxidized ^{WT}Coa6 protein (including two disulfide bonds) was purified by affinity and size-exclusion chromatography (SEC). The redox state of the purified ^{WT}Coa6 protein was confirmed by Ellman's assay (25). To elucidate the atomic structure of the ^{WT}Coa6 protein, we crystallized and determined its structure to 1.65 Å resolution by X-ray crystallography (Table 1). The structure shows two monomers of ^{WT}Coa6 per asymmetric unit, arranged as an antiparallel dimer (Fig 1A). The final ^{WT}Coa6 model includes residues 52–111 from molecule A (Fig 1A, cyan) and residues 50–119 from

Table 1. Data collection and refinement statistics.[a]

Data collection			
Crystal	Native ^{WT}Coa6	Anomalous ^{WT}Coa6	^{W59C}Coa6
Wavelength (Å)	0.9918	1.722	0.954
Temperature (K)	100		
Diffraction source	Australian synchrotron (MX2)		
Detector	ADSC quantum 315r		
Space group	$P2_12_12_1$	$P2_12_12_1$	$P1$
a, b, c (Å)	32.0, 52.4, 78.3	32.2, 52.7, 78.6	41.4, 47.8, 48.1
α, β, γ (°)	90, 90, 90	90, 90, 90	116.9, 98.8, 104.1
Resolution range (Å)	50.0–1.65 (1.71–1.65)	44.0–2.28 (2.35–2.28)	50.0–2.20 (2.28–2.20)
Total no. of reflections	80,326	416,239	49,280
No. of unique reflections	16,393	6,519	15,400
Completeness (%)	99.8 (100.0)	99.5 (95.1)	98.4 (97.3)
Redundancy	4.9 (5.0)	63.9 (33.7)	3.2 (3.1)
$\langle I/\sigma(I)\rangle$	29.9 (2.3)	70.3 (5.6)	14.4 (2.1)
Rmerge (%)	4.7 (67.3)	5.8 (73.1)	5.9 (59.6)
Rpim (%)	2.3 (32.8)	0.7 (12.4)	4.1 (40.8)
Refinement statistics			
Resolution range (Å)	43.6–1.65 (1.69–1.65)		38.3–2.2 (2.129–2.185)
No. of reflections, working set	14,716		14,685
No. of reflections, test set	1,632		713
R_{work} (%)	18.8 (27.5)		20.0 (27.3)
R_{free} (%)	22.9 (33.4)		24.4 (37.2)
R.m.s.d. bond lengths (Å)	0.012		0.003
R.m.s.d. bond angles (°)	1.75		1.21
Ramachandran[b]			
Favored, %	100		98.3
Allowed, %	100		100
PDB ID code	6PCE		6PCF

[a]Values in parenthesis are for highest resolution shell.
[b]Calculated using MolProbity (67).

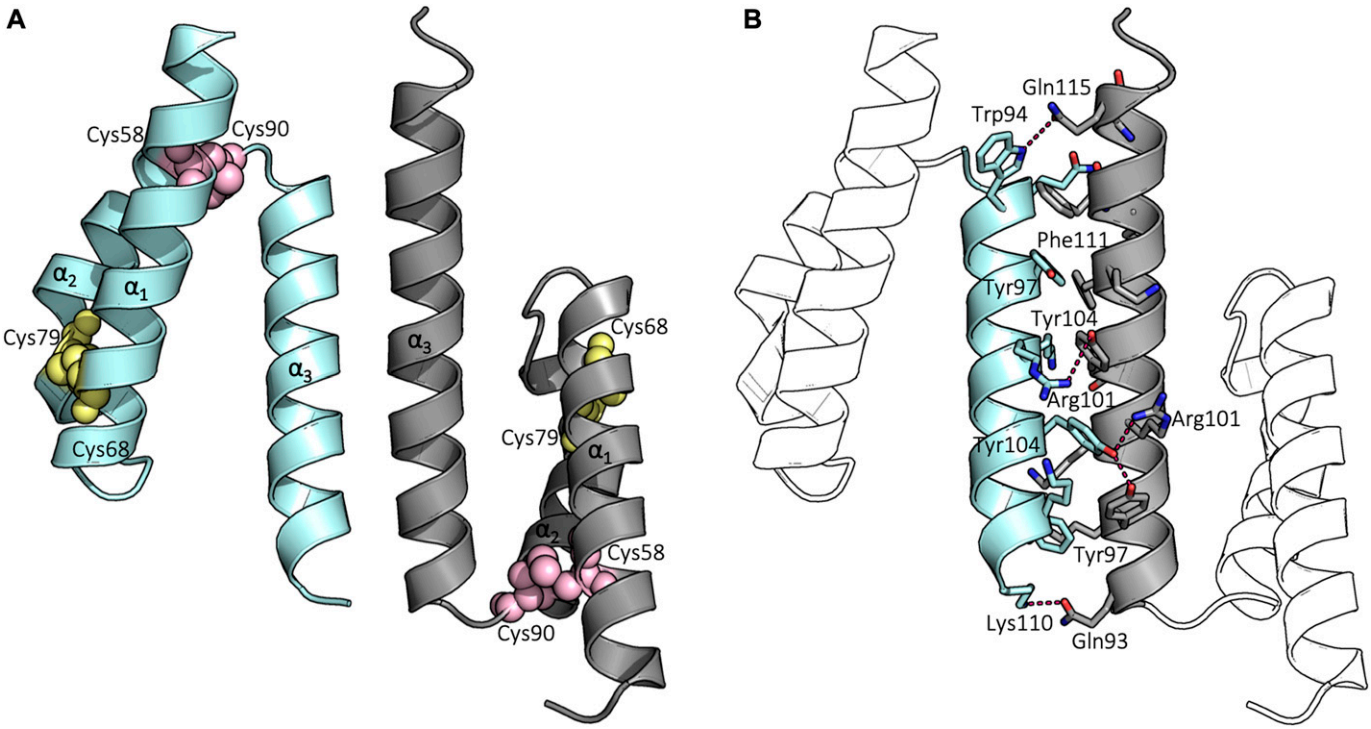

Figure 1. Structure of the ^{WT}Coa6.
(A) Cartoon representation of the overall structure of ^{WT}Coa6. Secondary structures are represented as cartoons with monomers colored in cyan and gray. Residues Cys58 and Cys90 are shown as pink spheres, whereas Cys68 and Cys79 residues are shown as yellow spheres. **(B)** Residues located at the dimer interface are shown as sticks and hydrogen bonds between residues (labeled) shown as dashed lines.

molecule B (Fig 1A, gray). Interpretable electron density was not observed for residues A47–51, A112–125, B47–49, and B120–125, and these were omitted from the final model. The superposition of molecule A with molecule B gives a root mean square deviation (r.m.s.d.) for 53 common Cα positions of 0.43 Å, indicating the structures of the two monomers are very similar.

Each monomer is composed of a 3-helical bundle, with a coiled–coil–helix–coiled–coil–helix (CHCH) fold (26) (Fig 2C). The sequence of ^{WT}Coa6 includes four Cys residues (at positions 58, 68, 79, and 90) in a CX_9C–$CX_{10}C$ sequence motif, which in the crystal structure form two intramolecular disulfide bonds per monomer, between Cys58–Cys90 and Cys68–Cys79, in accordance with the fully oxidized state of the protein (Fig 1A). These disulfides tether helices α_1 and α_2 together at each end of the helical pair.

Proteins which include twin CX_9C motifs and adopt CHCH folds include the mitochondrial copper chaperone Cox17 (7) (Fig 2A, Protein Data Bank [PDB] 2RNB), Mia40 (PDB 2K3J) (27), CMC4 (p8MTCP1; PDB 1HP8) (28), CHCHD5 (PDB 2LQL), and CHCHD7 (PDB 2LQT) (29), whose structures have been elucidated by Nuclear Magnetic Resonance. In addition, a search of the ^{WT}Coa6 coordinates against the PDB revealed (30) that ^{WT}Coa6 shares significant structural similarity with the Cox6B subunit of COX (Fig 2B, PDB 2ZXW (31), Chains H and U, r.m.s.d. 1.8 Å for 51 common Cα positions). The structure of Cox6B also shows a CHCH fold and includes four Cys residues, which are found in a CX_9C–$CX_{10}C$ sequence motif. These Cys residues also form two pairs of intramolecular disulfide bonds (between Cys29–Cys64 and Cys39–Cys53), with positions that superpose exactly with the ^{WT}Coa6 structure (Figs 2B and S1). Because of its CHCH structure, Cox6B has been included in the twin Cx9C protein family (despite showing a sequence variation: CX_9C–$CX_{10}C$). Coa6 can now also be included in that family. All structurally characterized twin CX_9C proteins listed here include an N-terminal (α_1/α_2) helical pair, which is tethered at each end by disulfide bonds (Fig 2) and most have been shown to undergo import into the mitochondrial IMS through an Mia40-mediated oxidative folding pathway (26, 32, 33). However, only the Cox17 protein has been shown to bind Cu(I) (7) and to play a role in COX assembly.

The Coa6 dimer has buried surface areas of 701 and 656 Å^2 (for molecules A and B, respectively), which are 15 and 13%, of the total surface areas of each corresponding monomer, indicating that ^{WT}Coa6 forms a stable dimer in solution (34). This agrees with our previous SEC data, which demonstrated that ^{WT}Coa6 eluted from an analytical column at a volume corresponding to the molecular weight of a dimer (11). The Coa6 dimer is entirely mediated by intermolecular contacts between Helix α_3 from each monomer. These contacts include electrostatic interactions, including hydrogen bonds and salt bridges (Fig 1B). In addition, Tyr97 of monomer A (Helix α_3, cyan, Fig 1B) forms a π-stacking interaction with Phe111 of monomer B (Helix α_3, gray, Fig 1B) at the dimer interface.

To investigate the roles of individual interface residues in the stabilization of the dimer, we generated variant proteins where interface residues were mutated to alanine (Y97A, Y104A, R101A, and Y97A/Y104A mutant proteins) and analyzed the quaternary structures

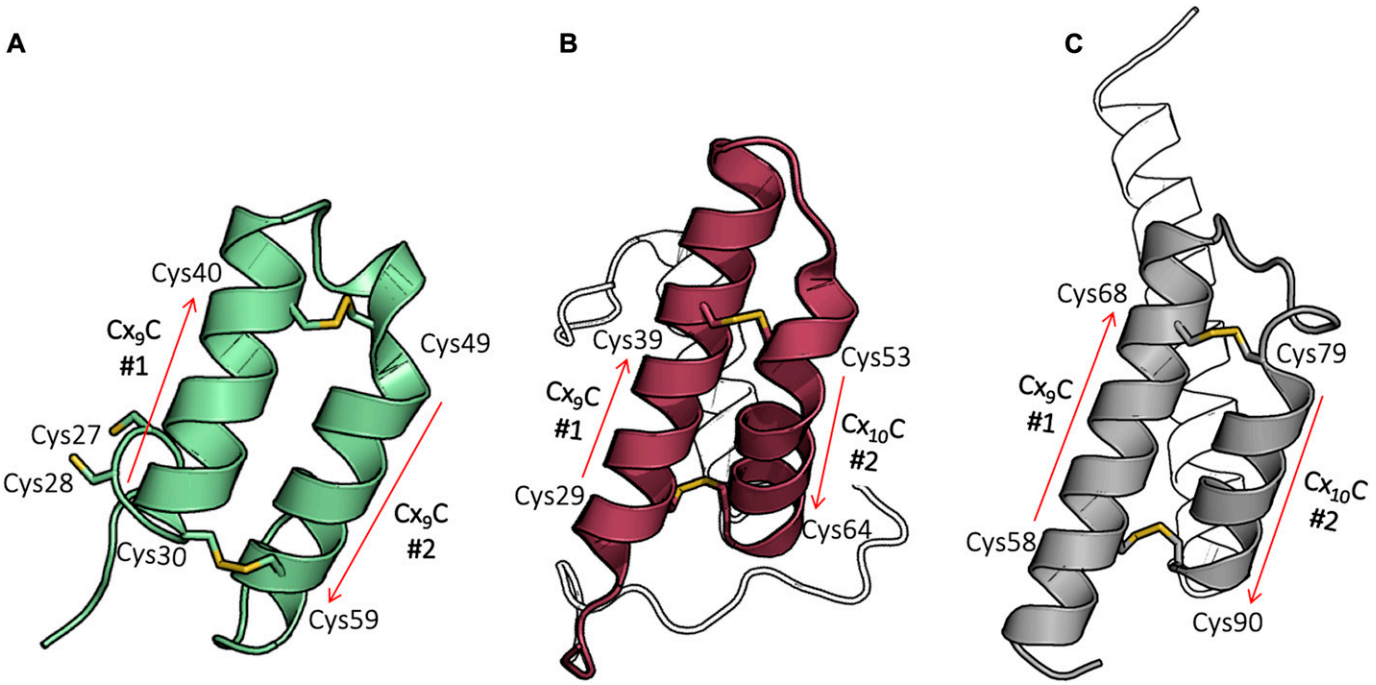

Figure 2. ^{WT}Coa6 has a twin CX_9C protein fold.
(A) Cox17 (PDB 2RNB): helices are shown in green, and cysteines in the CX_9C motifs that form disulfide bonds are shown as yellow sticks. **(B)** Cox6B (PDB 2EIJ): helices are shown in raspberry, and cysteines in the CX_9C (or $CX_{10}C$) motifs that form disulfide bonds are shown as yellow sticks. **(C)** ^{WT}Coa6 (this work): helices are shown in gray, and cysteines in the CX_9C (or $CX_{10}C$) motifs that form disulfide bonds are shown as yellow sticks. In all panels, the positions of the corresponding motifs are shown as red arrows. In panel (B), part of the N terminus and helix α_3 in panels (B) and (C) are not colored for clarity.

of these variant proteins by analytical SEC. All mutant proteins eluted from SEC at volumes similar to that for dimeric ^{WT}Coa6 (Fig S2), indicating conservation of their dimeric quaternary structures and therefore, the extensive nature of the dimer interface. Interestingly, no other twin CX_9C proteins have been characterized as dimeric and all reported structures to date have shown monomeric proteins (7, 27, 28, 29).

Mutation of residues Cys58 and Cys90 eliminates Cu(I) binding to Coa6

We have previously reported that both the ^{WT}Coa6 and ^{W59C}Coa6 proteins bind Cu(I) with $K_{DCu(I)}$ ~ 10^{-17} M (11). To determine the stoichiometry of Cu(I) binding, purified *apo*-^{WT}Coa6 was loaded with Cu(I) in the presence of the reducing agent as previously described (11, 35). Following SEC to remove excess Cu, ^{WT}Coa6 was found to bind Cu(I) with a Cu:protein stoichiometry of 1:1 (Fig S3), indicating the presence of a single Cu(I) binding site per molecule of ^{WT}Coa6.

CX_nC motifs are commonly present in soluble, high-affinity Cu(I)-binding proteins (copper metallochaperones) such as Atox1 (36), where redox cycling of the pair of Cys residues from oxidized (disulfide, S–S) to reduced (2SH) allows Cu(I) coordination between the thiolate groups of the Cys side chains. CHCH fold proteins have been characterized with redox active disulfide bonds; however, this activity is mediated not by the Cys residues that are part of the CX_9C motifs but by additional pairs of Cys residues at the N termini of the proteins (37). For example, in Cox17, an N-terminal C–C motif shows oxidoreductase activity and also binds Cu(I) with femtomolar affinity, for transfer to receiving copper proteins of the IMS, such as Cox11, Sco1, and Sco2 (8, 38, 39). Mia40 has a conserved N-terminal CPC motif that catalyzes the formation of intermolecular disulfides in CX_9C proteins within the IMS (40). The redox potentials of the N-terminal Cys pairs for Cox17 and Mia40 are −198 (41) and −200 mV (27). In addition, the human Sco1 and Sco2 proteins have been shown to possess redox-active disulfide bonds that bind Cu(I) when in the reduced state, with measured redox potentials for the respective S–S/2SH couples of −277 and less than −300 mV (9, 22, 38).

Our previous study showed that ^{WT}Coa6 exists in mitochondria in a partially reduced state, that is, with one of the two intramolecular disulfide bonds reduced (11). Reduction of one disulfide bond would facilitate Cu(I) binding and yield Cu:protein stoichiometry of 1:1. We therefore sought to determine whether a Cu(I) binding site might exist between the Cys58–Cys90 or Cys68–Cys79 disulfides in ^{WT}Coa6. To that end, we determined the redox potential of the S–S/2SH couple for the Coa6 protein (using a DTT_{Red}/DTT_{Ox} redox couple) as −349 ± 1 mV (pH 7.0, Fig S4). To determine whether this represented one or both of the S–S/2SH redox couples in ^{WT}Coa6 (i.e., the Cys58–Cys90 and/or the Cys68–Cys79 disulfides), the purified protein was incubated with DTT_{Red}/DTT_{Ox} (40:1), followed by labeling with iodoacetamide (IAA) before analyses by both Matrix Assisted Laser Desorption/Ionization-Time of Flight (MALDI-TOF) mass spectrometry (MS) (Fig S5 and Table S1) and tryptic digest and peptide analysis by tandem MS/MS (Table 2). The MALDI-TOF data revealed that the dominant species in the reduced ^{WT}Coa6 sample

Table 2. ^{WT}Coa6 mass determined via MS/MS following reduction and IAA labeling.

Peptide sequence	Predicted mass of peptide sequence (D)	Peptide position	Residue	Predicted mass upon alkylation (D)	Determined mass upon alkylation (D)
FEAGQFEPSETTAK	1541.7118	111–124	—	—	ND
SSFESS**C_{90}**PQQWIK	1526.6944	84–96	Cys90	1584.6999	1584.8
C_{68}LDENLEDASQC_{79}K	1467.6090	68–80	Cys68, Cys79	1583.6199	ND
GPLGSMAAPSMK	1146.5645	42–53	—	—	ND
QV**C_{58}**WGAR	819.3930	56–62	Cys58	877.3985	877.4
DEYWK	740.3250	63–67	—	—	ND
YFDK	572.2715	97–100	—	—	ND
DYLK	538.2871	103–106	—	—	ND

The determined masses of peptides, including Cys58 and Cys90, were detected at the predicted molecular masses of the peptide–IAA adducts, which were calculated by PEPTIDEMASS (57), indicating the reduction of the Cys58–Cys90 disulfide bond under these conditions. The alkylated residues Cys58 and Cys90 are highlighted in bold. ND, not detected.

included two free thiol groups (2SH [not 4SH], Fig S5 and Table S1). The MS/MS data showed that peptides that included residues Cys58 and Cys90 yielded molecular weights corresponding to adducts with IAA, indicating reduction of the Cys58–Cys90 disulfide bond under these conditions (Table 2).

In addition, we generated $^{C58S/C90S}$Coa6 and $^{C68S/C79S}$Coa6 variants, which were analyzed for Cu(I) binding as previously described (11). Cu(I)-binding to the $^{C58S/C90S}$Coa6-mutant protein was not detected using this assay (Fig 3). In contrast, Cu(I) binding to the $^{C68S/C79S}$Coa6 variant gave a measured $K_{D(Cu(I))}$ ~10^{-16} M, which is ~10-fold weaker than that determined for the ^{WT}Coa6 protein (11). Circular dichroism (CD) spectroscopic analyses of the mutant proteins showed that both proteins gave spectra similar to that of the ^{WT}Coa6 protein, indicating that the observed changes in Cu(I)-binding properties were not due to alterations in the secondary structures of the proteins in the presence of the mutations (Fig S6). However, the possibility exists that the mutagenesis affected the flexibility of the protein and/or its tertiary structure as observed for a similar analysis of the human Cox17 protein (42).

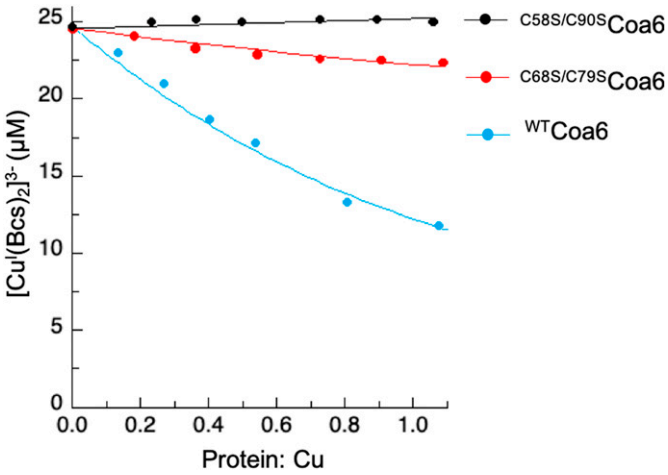

Figure 3. Determination of K_D for Cu(I) binding for the ^{WT}Coa6, $^{C58S/C90S}$Coa6, and $^{C68S/C79S}$Coa6 proteins.
The data were analyzed via a plot of the concentration of the $[Cu^{I}(BCS)_2]^{3-}$ complex (calculated from the absorption values at 483 nm versus the protein:Cu ratio) and the data fit using the equation previously described (11, 35).

Interestingly, an analysis of the geometries and potential energies of the Cys58–Cys90 and Cys68–Cys79 disulfides (43) revealed that the Cys58–Cys90 bond has a +/−RHHook geometry, which is commonly observed for disulfide bonds within thioredoxin-like proteins,beeing classified as a "catalytic" conformation. These types of disulfide bonds are observed to redox cycle, which is the foundation of their activities. This is in comparison with the geometry of the Cys68–Cys79 disulfide which shows a −LHSpiral geometry, which is the geometry commonly observed for structurally stable disulfide bonds (43, 44, 45). In addition, the structure of ^{WT}Coa6 shows that the Cys58–Cys90 site is proximate to positively charged residues (Lys53 and Arg55) and bordered by aromatic side chains (Trp59 and Trp94), which partially shield the site from the solvent (Fig S7). Positively charged residues in the vicinity of Cu(I)-binding sites within structurally characterized metallochaperone proteins such as Atox1 have been proposed to stabilize Cu(I) binding and mediate its transfer to other protein partners (46, 47). In addition, cation-π interactions (between Cu(I) and aromatic amino acid side chains), such as those observed in the crystal structure of the Cu(I)-CusF protein from *E. coli* (48), are known to stabilize copper binding.

To further investigate the position of the Cu(I)-binding site, we expressed the FLAG-tagged ^{WT}Coa6 and FLAG-tagged $^{C58S/C90S}$Coa6 double mutant in COA6^{KO} cells and compared the levels of assembled COX with control HEK293T and COA6^{KO} cells by blue native-PAGE (BN-PAGE) and Western blotting. As previously reported (11), the complementation with ^{WT}Coa6-FLAG in COA6^{KO} cells restored COX assembly. However, complementation with $^{C58S/C90S}$Coa6-FLAG was not able to rescue COX assembly and activity in COA6^{KO} cells. Examination of the cellular localization of the overexpressed $^{C58S/C90S}$Coa6-FLAG protein by immunofluorescence showed that unlike ^{WT}Coa6-FLAG, the $^{C58S/C90S}$Coa6 protein was cytosolic (Fig S8). CX_9C–$CX_{10}C$ and CX_9C proteins require the presence of the Cys residues within these motifs for

import into the IMS, and oxidative folding via Mia40 to trap the proteins in the IMS (49, 50). The absence of IMS localization of the $^{C58S/C90S}$Coa6-FLAG protein correlates with these observations and impeded our efforts to probe the role of these residues in Coa6 function and specifically COX assembly in human cells. Interestingly, however, an examination of the ^{C25A}yCoa6 and ^{C68A}yCoa6 (equivalent to human ^{C90A}Coa6) variants from yeast, showed that unlike ^{WT}yCoa6, these mutants were not able to rescue the respiratory growth defect of COA6^{KO} cells (10). In addition, these mutations were shown to disrupt the interactions (probed by co-immunoprecipitation) between yCoa6 and yCox2 and ySco1 (51).

Taken together, the redox potential of the ^{WT}Coa6 Cys58–Cys90 disulfide, the results of mutagenesis, Cu(I)-binding experiments, and analyses of the geometries of the intramolecular disulfide bonds of ^{WT}Coa6 indicate that the ^{WT}Coa6 Cys58–Cys90 disulfide may redox cycle and in the reduced state (2SH), bind Cu(I). The redox potential of the ^{WT}Coa6 Cys58–Cys90 S–S/2SH redox couple at −349 ± 1 mV indicates ^{WT}Coa6 could reduce the disulfide bonds in COX2 (−288 ± 3 mV) (22), and Sco1 (−277 ± 3 mV) (38) and could either reduce or be reduced by Sco2 (less than −300 mV) (9). In fact, a recent examination of this pathway suggested ^{WT}Coa6 may play such a role (22). Unfortunately, despite extensive attempts, we were unable to crystallize the Cu(I)-bound ^{WT}Coa6. Confirmation of Cu(I) binding and the atomic details of the Cu(I) site structure, therefore, await future investigation.

The structure of ^{W59C}Coa6 reveals a disulfide-mediated oligomerization

Finally, we determined and refined the crystal structure of the pathogenic mutant protein ^{W59C}Coa6 to 2.2 Å resolution by X-ray crystallography (Table 1). The structure of ^{W59C}Coa6 shows four molecules (A, B, C, and D) per asymmetric unit. The noncovalent dimer observed in the ^{WT}Coa6 structure (Fig 4A) is maintained for ^{W59C}Coa6 (between molecules A [cyan] and B [gray]) through

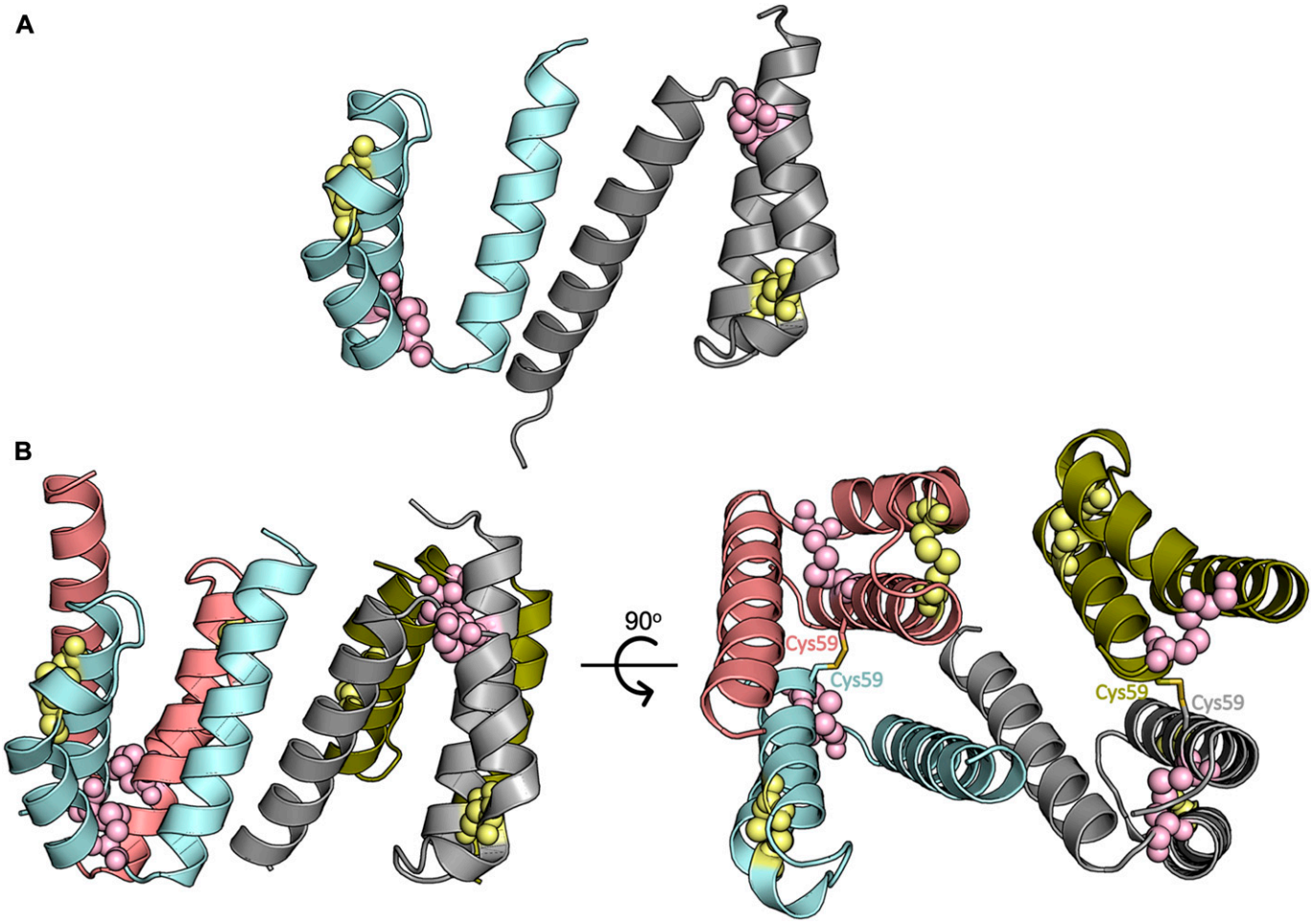

Figure 4. Structure of the ^{W59C}Coa6-mutant protein.
(A) Cartoon representation of the overall structure of ^{WT}Coa6. Secondary structures are represented as cartoons with monomers colored in cyan and gray. **(B)** Cartoon representation of the overall structure of ^{W59C}Coa6. Secondary structures are represented as cartoons with monomers colored in cyan, gray, salmon and gold. Residues Cys58 and Cys90 are shown as pink spheres and residues Cys68 and Cys79 as yellow spheres. Each monomer (cyan and gray) is linked to another monomer (salmon and gold, respectively) by an intermolecular disulfide bond (shown as yellow sticks) through the introduced Cys59 residue.

contacts along Helix α_3 from each monomer (Fig 4B). In addition, each of these molecules form a covalent dimer with another molecule of ^{W59C}Coa6 through a disulfide bond between the introduced residue Cys59 on each chain (covalent dimers between molecules A/D, [cyan and salmon] and B/C [gray and gold], Fig 4B). In this way, the asymmetric unit is composed of a dimer of dimers (a noncovalent dimer of disulfide bridged dimers). Importantly, this pattern of interactions is propagated throughout the crystal so that every molecule of ^{W59C}Coa6 interacts with two others—one through noncovalent contacts along Helix α_3 (as observed for ^{WT}Coa6, cyan and gray, Fig 4B) and the other through a disulfide bond between residue Cys59 on each molecule as a result of the mutation (cyan/salmon and gray/gold, Fig 4B).

The superposition of the ^{WT}Coa6 structure with the noncovalent A/B dimer of ^{W59C}Coa6 yields a r.m.s.d. value of 1.2 Å for 113 common Cα atoms. These minor structural differences originate from a slightly different association between the monomers in the dimers, rather than specific structural rearrangements. Importantly, in the ^{WT}Coa6 and ^{W59C}Coa6 structures, the positions of the proposed Cys58–Cys90 Cu(I)-binding sites are identical. Because the Cu(I)-binding activity of the ^{W59C}Coa6 protein is preserved in the presence of the mutation (11), these residues, being positioned at the "end" of the (α_1/α_2) helical pair presumably remain accessible to Cu(I) binding, despite the oligomerization of the ^{W59C}Coa6.

Our previous analysis of the quaternary structure of the ^{W59C}Coa6-mutant protein by SEC (11) showed a broad elution profile, indicating protein oligomerization. Under reducing conditions, the elution profile for the ^{W59C}Coa6 protein was identical to that of ^{WT}Coa6, corresponding to a dimeric protein (11). These observations agree with the crystal structure described here, which shows that ^{W59C}Coa6 oligomerization is mediated by the presence of intermolecular disulfide bonds that bridge noncovalent ^{W59C}Coa6 dimers.

Characterizations of the ^{W59C}Coa6-mutant protein in yeast (^{W26C}yCoa6) and human cells by other groups have suggested differing localizations of the mature protein: to the IMS (51) and mislocalization to the matrix (in U2OS cells (21)). Our previous study showed that complementation of ^{W59C}Coa6 in COA6^{KO} HEK293T cells only partially restored COX assembly and that in yeast, accumulation of yCoa6 in the mitochondrial IMS was impaired in the presence of the mutation W26C (equivalent to human ^{W59C}Coa6) (11). Additional studies have also shown a decrease in steady state levels of Coa6 in yeast for the ^{W26C}yCoa6-mutant protein (10) and an impaired interaction of the mutant protein with COX2 (51).

The structure of ^{W59C}Coa6 is consistent with the bulk of these data. Oligomerization of the protein, through the creation of intermolecular disulfide bonds may inhibit or eliminate targeted protein–protein interactions between Coa6 and proteins such as Sco1, Sco2, and COX2, which are critical for its function. Certainly, the structures and charge distributions on the surfaces of the ^{WT}Coa6 dimer and ^{W59C}Coa6 tetramer are different (Fig S9A and B). In particular, condensed areas of positive charge on the surface of the ^{WT}Coa6 dimer (Fig S9A) are not present in the ^{W59C}Coa6 tetramer (Fig S9B). These regions may mediate interactions with the Sco1, Sco2, and COX2 proteins through concentrated areas of negative charge on the surface structures of those proteins (Fig S9C–E).

Conclusion

Despite intense investigation, the identities of all proteins involved, their respective roles, and the sequence of their participation in complex IV biogenesis are currently not known (4, 22, 52, 53). The COX assembly factor Coa6 was identified through a proteomic survey of the mitochondrial IMS from *Saccharomyces cerevisiae* (49) and the significant number of investigations that followed, proposed its role in the biogenesis of the Cu_A site, presumably through the interaction of Coa6 with other critical proteins in the COX biogenesis pathway such as Sco1 and Sco2 (10, 11, 21, 51). However, the molecular details of how Coa6 functions in this pathway, particularly the molecular foundations of its ability to bind copper have until now been undefined. Crucially, the molecular basis of the pathogenic effect of the ^{W59C}Coa6 mutation has remained elusive.

Here, through the determination of the high-resolution crystal structures of the ^{WT}Coa6 and ^{W59C}Coa6 proteins, we have contributed to the interpretation of the role of Coa6 in COX biogenesis. The ^{WT}Coa6 structure shows a 3-helical bundle fold, where the N-terminal helical pair is tethered at each end by intramolecular disulfide bonds. We propose that in the mitochondrial IMS, the Cys58–Cys90 disulfide redox cycles between oxidized and reduced states and that when reduced, may constitute a Cu(I)-binding site. This proposal is supported by our data showing that the Coa6 protein in human mitochondria is partially reduced, that residues Cys58 and Cys90 can be labeled by IAA under reducing conditions, and that in the structure of ^{WT}Coa6, the Cys58–Cys90 disulfide shows a geometry and surrounding protein structure that are amenable to redox cycling and copper binding, respectively. Finally, site-directed mutagenesis of residues Cys58 and Cys90 to Ser eliminates Cu(I) binding. However, the question remains as to the precise role of Coa6 in COX biogenesis. The question of whether Coa6 directly facilitates copper delivery to the COX Cu_A site or mediates the activities and redox states of other proteins in the pathway remains.

What is known is that the biogenesis pathway for the COX Cu_A site relies on the execution of finely tuned protein–protein interactions. The disulfide-mediated oligomerization, which occurs for the ^{W59C}Coa6-mutant protein inhibits these interactions and, therefore, leads to the pathogenic outcome of complex IV deficiency.

During the revision of this article, Soma et al (54) reported the characterization of the solution structure of ^{WT}Coa6 and determination of its redox properties. Consistent with our studies, they found that ^{WT}Coa6 has a CHCH fold, determined a comparable redox potential for the protein (−330 mV, pH 7.0), and suggested that the pathogenic effects of the ^{W59C}Coa6 variant may stem from changes in the interactions between Coa6 and other

members of the COX assembly pathway (such as Sco1 and COX2). There are some differences between the findings of the Soma et al report and the current work, however, which must await further investigation.

Materials and Methods

Throughout this study, ^{WT}Coa6 refers to Coa6 isoform 3 (11), which is composed of residues 47–125 of the full-length Coa6, isoform 1 (UniProtKB: Q5JTJ3). Residue numbering for all protein constructs described here (^{WT}Coa6, ^{W59C}Coa6, $^{C58S/C90S}$Coa6, $^{C68S/C79S}$Coa6, ^{Y97A}Coa6, ^{Y104A}Coa6, ^{R101A}Coa6, and $^{Y97A/Y104A}$Coa6), including the structural descriptions and the submitted PDB coordinates follows the PDB convention, numbered according to the full-length Coa6, including the signal sequence. Therefore, the N-terminal residue of ^{WT}Coa6 is numbered Met47.

Protein overexpression, purification, and characterization

The ^{WT}Coa6 and ^{W59C}Coa6 cDNAs encoding Coa6 isoform 1 residues 47–125 were amplified via PCR and subcloned into a pGEX-6P-1 GST fusion vector with an intervening PreScission Protease site for cleavage of the GST tag. Double cysteine mutations ($^{C58S/C90S}$Coa6 and $^{C68S/C79S}$Coa6) and mutations located at dimer interface (^{Y97A}Coa6, ^{Y104A}Coa6, ^{R101A}Coa6, and $^{Y97A/Y104A}$Coa6) were introduced into the ORF encoding the ^{WT}Coa6 protein using a Q5 Site-Directed Mutagenesis kit (New England Biolabs), according to the manufacturer's instructions. We also introduced a C58S/C90S double mutation into the ORF encoding the ^{WT}Coa6 protein in the pBABE-puro plasmid (Addgene) for cell culture and complementation studies using the same method.

Forward and reverse primers for all mutant proteins were designed using NEBaseChanger online tool (http://nebasechanger.neb.com/). The DNA sequence encoding all variants were individually amplified via PCR followed by ligation and template DNA removal using KLD enzyme mix (containing a kinase, a ligase, and DpnI, New England BioLabs).

The pGEX-6P-1 plasmids containing DNA sequences encoding ^{WT}Coa6, ^{W59C}Coa6, $^{C58S/C90S}$Coa6, $^{C68S/C79S}$Coa6, ^{Y97A}Coa6, ^{Y104A}Coa6, ^{R101A}Coa6, and $^{Y97A/Y104A}$Coa6 were individually transformed into *E. coli* strain SHuffle T7 (New England Biolabs). Shuffle T7 cells are engineered *E. coli* K12, which constitutively express a chromosomal copy of the disulfide bond isomerase DsbC. DsbC promotes the correction of mis-oxidized proteins into their correct form in the cytoplasm (23, 24). Cultures were grown at 30°C in Luria Broth supplemented with ampicillin (100 μg·ml^{-1}), chloramphenicol (35 μg·ml^{-1}), and streptomycin (50 μg·ml^{-1}) to an OD_{600} of 0.8, induced with IPTG (0.2 mM) and harvested after 16 h (with shaking) at 16°C.

GST tagged ^{WT}Coa6, ^{W59C}Coa6, $^{C58S/C90S}$Coa6, $^{C68S/C79S}$Coa6, ^{Y97A}Coa6, ^{Y104A}Coa6, ^{R101A}Coa6, and $^{Y97A/Y104A}$Coa6 were purified by glutathione (GSH) affinity chromatography. Frozen cell pellets were thawed at room temperature and resuspended in PBS (pH 7.4). Cells were disrupted by passage through a TS series bench top cell disruptor (Constant Systems Ltd) at 35 kpsi. Cell debris was removed by centrifugation (Beckman JLA-25.50, 30,000*g*, 20 min, 4°C) and the soluble fraction was incubated with glutathione Sepharose 4B resin (GE Healthcare) equilibrated with PBS. The GST tag was cleaved with PreScission Protease followed by SEC (HiLoad 16/600 Superdex 75 pg, GE Healthcare; 20 mM Tris-MES, pH 8.0, and 150 mM NaCl). Cleavage of the N-terminal GST tag introduced five additional residues (GPLGS) to the N terminus of all proteins. The purified proteins were concentrated to 20 mg·ml^{-1} before storage at −80°C.

Ellman's assay

Purified ^{WT}Coa6 samples (72 μM) were added to Ellman's reaction buffer (2.5 ml; 0.1 M sodium phosphate, pH 8.0, 1 mM EDTA, and 2% wt/vol SDS) containing 50 μl of Ellman's reagent (4 mg·ml^{-1}) and incubated at room temperature for 15 min. A solution of Ellman's reagent produces a measurable yellow-colored product when it reacts with sulfhydryl groups. The reaction was monitored by measuring the absorbance of the resulting solutions at 412 nm. In the absence of free sulfhydryls, the Ellman's reagent exhibits no reaction and, therefore, OD_{412} = 0.0 (25).

Protein copper loading

Purified ^{WT}Coa6 was exchanged into buffer (20 mM Tris-MES, pH 8.0) by centrifugal ultrafiltration (Millipore) and incubated for 30 min with $CuSO_4$ and reduced GSH (molar ratio 1: 5: 10; protein: $CuSO_4$: GSH). To remove the excess Cu from the mixture, the incubated protein sample was applied to a SEC column (HiLoad 16/600 Superdex 75 pg, GE Healthcare). The presence of Cu(I) in the peak fractions was analyzed colorimetrically using the ligand bathocuproinedisulfonic acid (Bcs) and those protein fractions containing Cu were pooled and concentrated by centrifugal ultrafiltration. The Cu:protein stoichiometries of the protein samples prepared in this manner were confirmed by a colorimetric assay using Bcs (35), with protein concentration determined by a BCA assay (Pierce BCA Protein Assay Kit; Thermo Fisher Scientific) according to the manufacturer's instructions.

Protein copper-binding experiments

Measurements of the copper-binding affinities of the ^{WT}Coa6 and mutant proteins (^{W59C}Coa6, $^{C58S/C90S}$Coa6, and $^{C68S/C79S}$Coa6) were performed as previously described (11). Briefly, purified proteins (in 20 mM Tris-MES, pH 8.0) were titrated at various concentrations (1–30 μM) into solutions containing buffer (20 mM Tris-MES, pH 7.0), $CuSO_4$ (20 μM), Bcs (200 μM), and NH_2OH (1 mM). The exchange of Cu(I) from the $[Cu^{I}Bcs_2]^{3-}$ complex to the proteins was monitored by measuring the absorbance of the resulting solutions at 483 nm. The data were analyzed by plotting $[Cu^{I}Bcs_2]^{3-}$ (as determined from the absorbance values at 483 nm) versus protein:Cu ratios, and the data fitted using the equation previously described (11, 35).

CD spectroscopy

The secondary structures of the ^{WT}Coa6, $^{C58S/C90S}$Coa6, and $^{C68S/C79S}$Coa6 proteins were determined by CD spectroscopy in 1.0-mm path length quartz cuvettes, using an Aviv Model 420 (CD) Spectrometer. Protein samples were prepared at 0.162 mg·ml^{-1} in CD

buffer (10 mM sodium fluoride, 50 mM potassium phosphate, pH 8.5, 0.5 mM tris(2-carboxyethyl)phosphine [TCEP]), and wavelength scans were recorded at 20°C between 190 and 250 nm. Data were converted to mean residue ellipticity and the secondary structure compositions of the protein samples estimated using the CDPro software with CONTINLL and CDSSTR algorithms (55).

Analytical SEC

^{WT}Coa6, ^{Y97A}Coa6, ^{Y104A}Coa6, ^{R101A}Coa6, and $^{Y97A/Y104A}$Coa6 proteins (100 μg) were applied to an analytical SEC column (Superdex 200 Increase 3.2/300; GE Healthcare) pre-equilibrated with 20 mM Tris-MES, pH 8.0, and 150 mM NaCl buffer and eluted at 0.05 ml·min^{-1} in the same buffer. Elution volumes for each variant were compared with that of ^{WT}Coa6, which was applied to and eluted from the column under the same conditions.

MS

A sample of ^{WT}Coa6 (200 μM) was reduced with 4 mM DTT and then alkylated with 50 mM IAA for 30 min before MALDI-TOF. In addition, IAA-labeled and unlabeled samples were subjected to trypsin digestion and tandem MS/MS sequencing using a Thermo Fisher Scientific LTQ Orbitrap Elite ETD Mass Spectrometer as previously reported (56). Upon digestion, peptides containing the free sulfhydryl groups on the cysteine residues shift by 58 Da because of the alkylation. The predicted mass of alkylated peptides were calculated using PEPTIDEMASS (57).

Determination of redox potential of ^{WT}Coa6

Redox potential of the S–S/SH redox couple of ^{WT}Coa6 was determined as previously described (58). Briefly, ^{WT}Coa6 (200 μM) was incubated at room temperature in 100 mM phosphate buffer and 1 mM EDTA (pH 7.0) containing 20 mM oxidized DTT and increasing concentrations of reduced DTT (0–800 mM). After 2-h incubation, the reactions were stopped by addition of 10% trichloroacetic acid and centrifuged (13,000*g*). The precipitated protein pellets were washed with ice-cold 100% acetone, dissolved in 4′-acetamido-4′-maleimidylstilbene-2,2′-disulfonic acid (AMS) buffer (2 mM AMS, 1% SDS, and 50 mM Tris [pH 7.0]) to label free thiols and analyzed by SDS–PAGE to separate the oxidized and AMS-bound reduced forms. The fractions of reduced protein were quantified using the ImageJ software (59) and plotted against the buffer ratio $[DTT_{Red}]/[DTT_{Ox}]$. The fraction of thiolate as a function of $[DTT_{Red}]/[DTT_{Ox}]$ was plotted to calculate the equivalent intrinsic redox potential as described previously (60).

Cell culture

HEK293T COA6^{KO} cell lines were previously described (11). The cells were grown in high glucose DMEM (Invitrogen) containing 10% (vol/vol) FBS and penicillin/streptomycin and 50 μg·ml^{-1} uridine at 37°C under an atmosphere of 5% CO_2. Isoform 3 of COA6 was used for complementation studies, and constructs were subcloned into pBABE-puro (Addgene) as previously described (11). Retroviral constructs along with packaging plasmids were transfected into HEK293T cells using Lipofectamine 2000. Viral supernatant was collected at 48 h post-transfection and used to infect COA6^{KO} cells in the presence of 8 μg·ml^{-1} polybrene. Transduced cells were expanded following selection for 48 h under 1 μg·ml^{-1} puromycin.

BN-PAGE and Western blot analysis

Mitochondria were isolated as previously described (61). Mitochondria were solubilized in 1% digitonin and separated on 4–10% acrylamide–bisacrylamide BN-PAGE gels as previously described (62) and detected by Western blot using a total OXPHOS Rodent WB Antibody Cocktail (ab110413; Abcam).

Immunofluorescence assay

Cells were fixed with 4% (wt/vol) paraformaldehyde in PBS (pH 7.4) for 10 min followed by permeabilization with 0.2% (wt/vol) Triton X-100 in PBS before incubation with primary antibodies against Tom20 (rabbit polyclonal, 1:500; Santa Cruz, SC11415) and Flag (mouse monoclonal, 1:100; Sigma-Aldrich, F1804-1MG) for 90 min in 3% BSA, 0.02% Tween-20 in PBS at room temperature. Primary antibodies were labeled with either Alexa Fluor488-conjugated antimouse-IgG or Alexa Fluor568-conjugated antirabbit-IgG secondary antibodies (A-11001 and A-11011; Thermo Fisher Scientific, respectively). Hoechst 33,258 (1 μg·ml^{-1}) was used to stain nuclei. Confocal microscopy was performed using a Leica TCS SP8 confocal microscope (405, 488, 552, and 647 nm; Leica Microsystems) equipped with HyD detectors. Z-sectioning was performed using 300-nm slices and combined. All images were processed using ImageJ (59).

Protein crystallization and data collection

Crystallization trials were conducted using commercially available screens (SaltRx HT and Index HT [Hampton Research]) by sitting drop vapor diffusion in 96-well plates (Molecular Dimensions) using pure ^{WT}Coa6 and ^{W59C}Coa6 samples at two different protein concentrations (10 and 20 mg·ml^{-1}). Crystallization drops consisting of equal volumes (0.2 μl) of reservoir and protein solutions were dispensed using a Crystal Gryphon Liquid Handling System (Art Robbins Instruments) and were equilibrated against a reservoir of screen solution (50 μl). Plates were incubated at 20°C. Several tiny crystals of ^{WT}Coa6 were observed within 2 wk in conditions D8 and D9 of the Index HT screen (0.1 M Hepes, pH 7.5, 25% [wt/vol] PEG 3350, and 0.1 M Tris, pH 8.5, 25% [wt/vol] PEG 3350, respectively) and multiple small ^{W59C}Coa6 crystals were obtained after 5 d in conditions G10, G11, G6, and G7 of the Index HT screen (0.2 M magnesium chloride hexahydrate, 0.1 M Bis-Tris, pH 5.5, 25% wt/vol polyethylene glycol 3350; 0.2 M magnesium chloride hexahydrate, 0.1 M Bis-Tris, pH 6.5, 25% wt/vol polyethylene glycol 3350; 0.2 M ammonium acetate, 0.1 M Bis-Tris, pH 5.5, 25% wt/vol polyethylene glycol 3350; and 0.2 M ammonium acetate, 0.1 M Bis-Tris, pH 6.5, 25% wt/vol polyethylene glycol 3350, respectively). Optimization of these conditions was carried out by hanging-drop vapor diffusion in 24-well VDX plates (Hampton Research). Diffraction-quality crystals of ^{WT}Coa6 grew after 7 d at 20°C by hanging-drop vapor diffusion with drops containing equal volumes (1 μl) of ^{WT}Coa6 (30 mg·ml^{-1} in

20 mM Tris-MES, pH 8.0, and 150 mM NaCl) and crystallization solution (0.1 M Hepes, pH 7.6, and 29% [wt/vol] PEG 3350) equilibrated against 500 μl reservoir solution. ^{W59C}Coa6 was crystallized at 20°C by hanging-drop vapor diffusion with drops consisting of equal volumes (1 μl) of protein (25 mg·ml^{-1} in 20 mM Tris-MES, pH 8.0, and 150 mM NaCl) and reservoir solution (0.1 M Bis-Tris, pH 5.7, 0.23 M $MgCl_2 \cdot 6H_2O$, and 29% [wt/vol] PEG 3350). Both ^{WT}Coa6 and ^{W59C}Coa6 crystals were cryoprotected in reservoir solution containing 25% (vol/vol) glycerol before flash-cooling in liquid nitrogen.

Diffraction data were recorded on an ADSC Quantum 315r detector at the Australian Synchrotron on beamline MX2 at wavelengths of 0.9918, 1.722 and 0.954 Å for the ^{WT}Coa6 native data set, ^{WT}Coa6 anomalous data set and ^{W59C}Coa6, respectively. All data were collected at 100 K and were processed and scaled with HKL2000 (63). Data collection statistics are detailed in Table 1.

Structure solution and refinement

The crystal structure of ^{WT}Coa6 was determined by sulfur single-wavelength anomalous dispersion. Eight sulfur sites were identified using SHELXD and phasing performed by SHELXE within the CCP4 suite (64). Statistical phase improvement and solvent flattening was carried out using the program PIRATE from the CCP4 suite (64). Initial model building was carried out using BUCCANEER from the CCP4 suite (64) with manual model building and the addition of water molecules were carried out in COOT (65). The model was refined using REFMAC5 (66). The quality of the structure was determined by MOLPROBITY (67) (Table 1).

The crystal structure of ^{W59C}Coa6 was solved by molecular replacement using the program PHASER (68) from the CCP4 suite (64). The crystal structure of ^{WT}Coa6 was used as a search model after removal of all water molecules. The model was refined using REFMAC5 (66) and manual model building and the addition of water molecules were carried out in COOT (65). The quality of the structure was determined by MOLPROBITY (67) (Table 1).

Structure superpositions and the calculation of r.m.s.d's were carried out with LSQKAB (as part of the CCP4 suite) (65) and analyses of oligomeric protein complexes and buried surface areas were performed with the PDBePISA server (69).

Supplementary Information

Supplementary Information is available at https://doi.org/10.26508/lsa.201900458.

Acknowledgements

This study was funded by the Australian Research Council (DP140102746 to MJ Maher), the National Health and Medical Research Council (GNT1165217 to MT Ryan and MJ Maher; GNT1140851 to DA Stroud), and an Australian Government Research Training Program Scholarship to S Maghool. Aspects of this research were undertaken on the Macromolecular Crystallography beamline MX2 at the Australian Synchrotron (Victoria, Australia) and we thank the beamline staff for their enthusiastic and professional support. We also acknowledge the La Trobe University Comprehensive Proteomics Platform for providing infrastructure for this study.

Author Contributions

S Maghool: data curation, formal analysis, investigation, and writing—original draft, review, and editing.
NDG Cooray: investigation.
DA Stroud: conceptualization, data curation, formal analysis, supervision, funding acquisition, investigation, and writing—review and editing.
D Aragão: data curation, investigation, methodology, and writing—review and editing.
MT Ryan: conceptualization, formal analysis, supervision, funding acquisition, and writing—review and editing.
MJ Maher: conceptualization, data curation, formal analysis, supervision, funding acquisition, validation, investigation, project administration, and writing—original draft, review, and editing.

Conflict of Interest Statement

The authors declare that they have no conflict of interest.

References

1. Ferguson-Miller S, Babcock GT (1996) Heme/copper terminal oxidases. *Chem Rev* 96: 2889–2908. doi:10.1021/cr950051s
2. Soto IC, Fontanesi F, Liu J, Barrientos A (2012) Biogenesis and assembly of eukaryotic cytochrome c oxidase catalytic core. *Biochim Biophys Acta* 1817: 883–897. doi:10.1016/j.bbabio.2011.09.005
3. Fernandez-Vizarra E, Tiranti V, Zeviani M (2009) Assembly of the oxidative phosphorylation system in humans: What we have learned by studying its defects. *Biochim Biophys Acta* 1793: 200–211. doi:10.1016/j.bbamcr.2008.05.028
4. Timon-Gomez A, Nyvltova E, Abriata LA, Vila AJ, Hosler J, Barrientos A (2018) Mitochondrial cytochrome c oxidase biogenesis: Recent developments. *Semin Cell Dev Biol* 76: 163–178. doi:10.1016/j.semcdb.2017.08.055
5. Tsukihara T, Aoyama H, Yamashita E, Tomizaki T, Yamaguchi H, Shinzawa-Itoh K, Nakashima R, Yaono R, Yoshikawa S (1996) The whole structure of the 13-subunit oxidized cytochrome c oxidase at 2.8 A. *Science* 272: 1136–1144. doi:10.1126/science.272.5265.1136
6. Aich A, Wang C, Chowdhury A, Ronsor C, Pacheu-Grau D, Richter-Dennerlein R, Dennerlein S, Rehling P (2018) COX16 promotes COX2 metallation and assembly during respiratory complex IV biogenesis. *eLife* 7: e32572. doi:10.7554/elife.32572
7. Banci L, Bertini I, Ciofi-Baffoni S, Janicka A, Martinelli M, Kozlowski H, Palumaa P (2008) A structural-dynamical characterization of human Cox17. *J Biol Chem* 283: 7912–7920. doi:10.1074/jbc.m708016200
8. Banci L, Bertini I, Ciofi-Baffoni S, Hadjiloi T, Martinelli M, Palumaa P (2008) Mitochondrial copper(I) transfer from Cox17 to Sco1 is coupled to electron transfer. *Proc Natl Acad Sci U S A* 105: 6803–6808. doi:10.1073/pnas.0800019105
9. Banci L, Bertini I, Ciofi-Baffoni S, Gerothanassis IP, Leontari I, Martinelli M, Wang S (2007) A structural characterization of human SCO2. *Structure* 15: 1132–1140. doi:10.1016/j.str.2007.07.011
10. Ghosh A, Trivedi PP, Timbalia SA, Griffin AT, Rahn JJ, Chan SS, Gohil VM (2014) Copper supplementation restores cytochrome c oxidase assembly defect in a mitochondrial disease model of COA6 deficiency. *Hum Mol Genet* 23: 3596–3606. doi:10.1093/hmg/ddu069
11. Stroud DA, Maher MJ, Lindau C, Vogtle FN, Frazier AE, Surgenor E, Mountford H, Singh AP, Bonas M, Oeljeklaus S, et al (2015) COA6 is a

mitochondrial complex IV assembly factor critical for biogenesis of mtDNA-encoded COX2. *Hum Mol Genet* 24: 5404–5415. doi:10.1093/hmg/ddv265

12. Baker ZN, Cobine PA, Leary SC (2017) The mitochondrion: A central architect of copper homeostasis. *Metallomics* 9: 1501–1512. doi:10.1039/c7mt00221a
13. Rak M, Benit P, Chretien D, Bouchereau J, Schiff M, El-Khoury R, Tzagoloff A, Rustin P (2016) Mitochondrial cytochrome c oxidase deficiency. *Clin Sci* 130: 393–407. doi:10.1042/CS20150707
14. Cobine PA, Pierrel F, Bestwick ML, Winge DR (2006) Mitochondrial matrix copper complex used in metallation of cytochrome oxidase and superoxide dismutase. *J Biol Chem* 281: 36552–36559. doi:10.1074/jbc.m606839200
15. Cobine PA, Ojeda LD, Rigby KM, Winge DR (2004) Yeast contain a non-proteinaceous pool of copper in the mitochondrial matrix. *J Biol Chem* 279: 14447–14455. doi:10.1074/jbc.m312693200
16. Baertling F, A M van den Brand M, Hertecant JL, Al-Shamsi A, P van den Heuvel L, Distelmaier F, Mayatepek E, Smeitink JA, Nijtmans LG, Rodenburg RJ (2015) Mutations in COA6 cause cytochrome c oxidase deficiency and neonatal hypertrophic cardiomyopathy. *Hum Mutat* 36: 34–38. doi:10.1002/humu.22715
17. Calvo SE, Compton AG, Hershman SG, Lim SC, Lieber DS, Tucker EJ, Laskowski A, Garone C, Liu S, Jaffe DB, et al (2012) Molecular diagnosis of infantile mitochondrial disease with targeted next-generation sequencing. *Sci Transl Med* 4: 118ra10. doi:10.1126/scitranslmed.3003310
18. Stiburek L, Vesela K, Hansikova H, Hulkova H, Zeman J (2009) Loss of function of Sco1 and its interaction with cytochrome c oxidase. *Am J Physiol Cell Physiol* 296: C1218–C1226. doi:10.1152/ajpcell.00564.2008
19. Leary SC (2010) Redox regulation of SCO protein function: Controlling copper at a mitochondrial crossroad. *Antioxid Redox Signal* 13: 1403–1416. doi:10.1089/ars.2010.3116
20. Soma S, Latimer AJ, Chun H, Vicary AC, Timbalia SA, Boulet A, Rahn JJ, Chan SSL, Leary SC, Kim BE, et al (2018) Elesclomol restores mitochondrial function in genetic models of copper deficiency. *Proc Natl Acad Sci U S A* 115: 8161–8166. doi:10.1073/pnas.1806296115
21. Pacheu-Grau D, Bareth B, Dudek J, Juris L, Vogtle FN, Wissel M, Leary SC, Dennerlein S, Rehling P, Deckers M (2015) Cooperation between COA6 and SCO2 in COX2 maturation during cytochrome c oxidase assembly links two mitochondrial cardiomyopathies. *Cell Metab* 21: 823–833. doi:10.1016/j.cmet.2015.04.012
22. Morgada MN, Abriata LA, Cefaro C, Gajda K, Banci L, Vila AJ (2015) Loop recognition and copper-mediated disulfide reduction underpin metal site assembly of CuA in human cytochrome oxidase. *Proc Natl Acad Sci U S A* 112: 11771–11776. doi:10.1073/pnas.1505056112
23. Bessette PH, Aslund F, Beckwith J, Georgiou G (1999) Efficient folding of proteins with multiple disulfide bonds in the Escherichia coli cytoplasm. *Proc Natl Acad Sci U S A* 96: 13703–13708. doi:10.1073/pnas.96.24.13703
24. Levy R, Weiss R, Chen G, Iverson BL, Georgiou G (2001) Production of correctly folded Fab antibody fragment in the cytoplasm of Escherichia coli trxB gor mutants via the coexpression of molecular chaperones. *Protein Expr Purif* 23: 338–347. doi:10.1006/prep.2001.1520
25. Ellman GL (1959) Tissue sulfhydryl groups. *Arch Biochem Biophys* 82: 70–77. doi:10.1016/0003-9861(59)90090-6
26. Cavallaro G (2010) Genome-wide analysis of eukaryotic twin CX9C proteins. *Mol Biosyst* 6: 2459–2470. doi:10.1039/c0mb00058b
27. Banci L, Bertini I, Cefaro C, Ciofi-Baffoni S, Gallo A, Martinelli M, Sideris DP, Katrakili N, Tokatlidis K (2009) MIA40 is an oxidoreductase that catalyzes oxidative protein folding in mitochondria. *Nat Struct Mol Biol* 16: 198–206. doi:10.1038/nsmb.1553
28. Barthe P, Yang YS, Chiche L, Hoh F, Strub MP, Guignard L, Soulier J, Stern MH, van Tilbeurgh H, Lhoste JM, et al (1997) Solution structure of human p8MTCP1, a cysteine-rich protein encoded by the MTCP1 oncogene, reveals a new alpha-helical assembly motif. *J Mol Biol* 274: 801–815. doi:10.1006/jmbi.1997.1438
29. Banci L, Bertini I, Ciofi-Baffoni S, Jaiswal D, Neri S, Peruzzini R, Winkelmann J (2012) Structural characterization of CHCHD5 and CHCHD7: Two atypical human twin CX9C proteins. *J Struct Biol* 180: 190–200. doi:10.1016/j.jsb.2012.07.007
30. Krissinel E, Henrick K (2004) Secondary-structure matching (SSM), a new tool for fast protein structure alignment in three dimensions. *Acta Crystallogr D Biol Crystallogr* 60: 2256–2268. doi:10.1107/s0907444904026460
31. Aoyama H, Muramoto K, Shinzawa-Itoh K, Hirata K, Yamashita E, Tsukihara T, Ogura T, Yoshikawa S (2009) A peroxide bridge between Fe and Cu ions in the O2 reduction site of fully oxidized cytochrome c oxidase could suppress the proton pump. *Proc Natl Acad Sci U S A* 106: 2165–2169. doi:10.1073/pnas.0806391106
32. Chacinska A, Koehler CM, Milenkovic D, Lithgow T, Pfanner N (2009) Importing mitochondrial proteins: Machineries and mechanisms. *Cell* 138: 628–644. doi:10.1016/j.cell.2009.08.005
33. Sideris DP, Tokatlidis K (2010) Oxidative protein folding in the mitochondrial intermembrane space. *Antioxid Redox Signal* 13: 1189–1204. doi:10.1089/ars.2010.3157
34. Jones S, Thornton JM (1995) Protein-protein interactions: A review of protein dimer structures. *Prog Biophys Mol Biol* 63: 31–65. doi:10.1016/0079-6107(94)00008-w
35. Brose J, La Fontaine S, Wedd AG, Xiao Z (2014) Redox sulfur chemistry of the copper chaperone Atox1 is regulated by the enzyme glutaredoxin 1, the reduction potential of the glutathione couple GSSG/2GSH and the availability of Cu(I). *Metallomics* 6: 793–808. doi:10.1039/c4mt00020j
36. Xiao Z, Brose J, Schimo S, Ackland SM, La Fontaine S, Wedd AG (2011) Unification of the copper(I) binding affinities of the metallo-chaperones Atx1, Atox1, and related proteins: Detection probes and affinity standards. *J Biol Chem* 286: 11047–11055. doi:10.1074/jbc.m110.213074
37. Banci L, Bertini I, Ciofi-Baffoni S, Tokatlidis K (2009) The coiled coil-helix-coiled coil-helix proteins may be redox proteins. *FEBS Lett* 583: 1699–1702. doi:10.1016/j.febslet.2009.03.061
38. Banci L, Bertini I, Ciofi-Baffoni S, Leontari I, Martinelli M, Palumaa P, Sillard R, Wang S (2007) Human Sco1 functional studies and pathological implications of the P174L mutant. *Proc Natl Acad Sci U S A* 104: 15–20. doi:10.1073/pnas.0606189103
39. Horng YC, Cobine PA, Maxfield AB, Carr HS, Winge DR (2004) Specific copper transfer from the Cox17 metallochaperone to both Sco1 and Cox11 in the assembly of yeast cytochrome C oxidase. *J Biol Chem* 279: 35334–35340. doi:10.1074/jbc.m404747200
40. Ostergaard H, Tachibana C, Winther JR (2004) Monitoring disulfide bond formation in the eukaryotic cytosol. *J Cell Biol* 166: 337–345. doi:10.1083/jcb.200402120
41. Voronova A, Meyer-Klaucke W, Meyer T, Rompel A, Krebs B, Kazantseva J, Sillard R, Palumaa P (2007) Oxidative switches in functioning of mammalian copper chaperone Cox17. *Biochem J* 408: 139–148. doi:10.1042/bj20070804
42. Banci L, Bertini I, Cefaro C, Ciofi-Baffoni S, Gallo A (2011) Functional role of two interhelical disulfide bonds in human Cox17 protein from a structural perspective. *J Biol Chem* 286: 34382–34390. doi:10.1074/jbc.m111.246223
43. Wong JW, Hogg PJ (2010) Analysis of disulfide bonds in protein structures. *J Thromb Haemost* 8: 2345. doi:10.1111/j.1538-7836.2010.03894.x
44. Schmidt B, Ho L, Hogg PJ (2006) Allosteric disulfide bonds. *Biochemistry* 45: 7429–7433. doi:10.1021/bi0603064
45. Marques JR, da Fonseca RR, Drury B, Melo A (2010) Conformational characterization of disulfide bonds: A tool for protein classification. *J Theor Biol* 267: 388–395. doi:10.1016/j.jtbi.2010.09.012

46. Boal AK, Rosenzweig AC (2009) Structural biology of copper trafficking. *Chem Rev* 109: 4760–4779. doi:10.1021/cr900104z

47. Wernimont AK, Huffman DL, Lamb AL, O'Halloran TV, Rosenzweig AC (2000) Structural basis for copper transfer by the metallochaperone for the Menkes/Wilson disease proteins. *Nat Struct Biol* 7: 766–771. doi:10.1038/78999

48. Xue Y, Davis AV, Balakrishnan G, Stasser JP, Staehlin BM, Focia P, Spiro TG, Penner-Hahn JE, O'Halloran TV (2008) Cu(I) recognition via cation-pi and methionine interactions in CusF. *Nat Chem Biol* 4: 107–109. doi:10.1038/nchembio.2007.57

49. Vogtle FN, Burkhart JM, Rao S, Gerbeth C, Hinrichs J, Martinou JC, Chacinska A, Sickmann A, Zahedi RP, Meisinger C (2012) Intermembrane space proteome of yeast mitochondria. *Mol Cell Proteomics* 11: 1840–1852. doi:10.1074/mcp.m112.021105

50. Banci L, Bertini I, Cefaro C, Cenacchi L, Ciofi-Baffoni S, Felli IC, Gallo A, Gonnelli L, Luchinat E, Sideris D, et al (2010) Molecular chaperone function of Mia40 triggers consecutive induced folding steps of the substrate in mitochondrial protein import. *Proc Natl Acad Sci U S A* 107: 20190–20195. doi:10.1073/pnas.1010095107

51. Ghosh A, Pratt AT, Soma S, Theriault SG, Griffin AT, Trivedi PP, Gohil VM (2016) Mitochondrial disease genes COA6, COX6B and SCO2 have overlapping roles in COX2 biogenesis. *Hum Mol Genet* 25: 660–671. doi:10.1093/hmg/ddv503

52. Leary SC, Cobine PA, Kaufman BA, Guercin GH, Mattman A, Palaty J, Lockitch G, Winge DR, Rustin P, Horvath R, et al (2007) The human cytochrome c oxidase assembly factors SCO1 and SCO2 have regulatory roles in the maintenance of cellular copper homeostasis. *Cell Metab* 5: 9–20. doi:10.1016/j.cmet.2006.12.001

53. Jett KA, Leary SC (2018) Building the CuA site of cytochrome c oxidase: A complicated, redox-dependent process driven by a surprisingly large complement of accessory proteins. *J Biol Chem* 293: 4644–4652. doi:10.1074/jbc.r117.816132

54. Soma S, Morgada MN, Naik MT, Boulet A, Roesler AA, Dziuba N, Ghosh A, Yu Q, Lindahl PA, Ames JB, et al (2019) COA6 is structurally tuned to function as a thiol-disulfide oxidoreductase in copper delivery to mitochondrial cytochrome c oxidase. *Cell Reports*

55. Sreerama N, Woody RW (2000) Estimation of protein secondary structure from circular dichroism spectra: Comparison of CONTIN, SELCON, and CDSSTR methods with an expanded reference set. *Anal Biochem* 287: 252–260. doi:10.1006/abio.2000.4880

56. Harten SK, Oey H, Bourke LM, Bharti V, Isbel L, Daxinger L, Faou P, Robertson N, Matthews JM, Whitelaw E (2015) The recently identified modifier of murine metastable epialleles, rearranged L-Myc fusion, is involved in maintaining epigenetic marks at CpG island shores and enhancers. *BMC Biol* 13: 21. doi:10.1186/s12915-015-0128-2

57. Wilkins MR, Lindskog I, Gasteiger E, Bairoch A, Sanchez JC, Hochstrasser DF, Appel RD (1997) Detailed peptide characterization using PEPTIDEMASS: A world-wide-web-accessible tool. *Electrophoresis* 18: 403–408. doi:10.1002/elps.1150180314

58. Inaba K, Ito K (2002) Paradoxical redox properties of DsbB and DsbA in the protein disulfide-introducing reaction cascade. *EMBO J* 21: 2646–2654. doi:10.1093/emboj/21.11.2646

59. Schneider CA, Rasband WS, Eliceiri KW (2012) NIH image to ImageJ: 25 years of image analysis. *Nat Methods* 9: 671–675. doi:10.1038/nmeth.2089

60. Kurz M, Iturbe-Ormaetxe I, Jarrott R, Shouldice SR, Wouters MA, Frei P, Glockshuber R, O'Neill SL, Heras B, Martin JL (2009) Structural and functional characterization of the oxidoreductase alpha-DsbA1 from Wolbachia pipientis. *Antioxid Redox Signal* 11: 1485–1500. doi:10.1089/ars.2008.2420

61. Johnston AJ, Hoogenraad J, Dougan DA, Truscott KN, Yano M, Mori M, Hoogenraad NJ, Ryan MT (2002) Insertion and assembly of human tom7 into the preprotein translocase complex of the outer mitochondrial membrane. *J Biol Chem* 277: 42197–42204. doi:10.1074/jbc.m205613200

62. McKenzie M, Lazarou M, Thorburn DR, Ryan MT (2007) Analysis of mitochondrial subunit assembly into respiratory chain complexes using Blue Native polyacrylamide gel electrophoresis. *Anal Biochem* 364: 128–137. doi:10.1016/j.ab.2007.02.022

63. Otwinowski Z, Minor W (1997) [20] Processing of x-ray diffraction data collected in oscillation mode. *Methods Enzymol* 276: 307–326. doi:10.1016/s0076-6879(97)76066-x

64. Winn MD, Ballard CC, Cowtan KD, Dodson EJ, Emsley P, Evans PR, Keegan RM, Krissinel EB, Leslie AG, McCoy A, et al (2011) Overview of the CCP4 suite and current developments. *Acta Crystallogr D Biol Crystallogr* 67: 235–242. doi:10.1107/s0907444910045749

65. Emsley P, Lohkamp B, Scott WG, Cowtan K (2010) Features and development of Coot. *Acta Crystallogr D Biol Crystallogr* 66: 486–501. doi:10.1107/s0907444910007493

66. Murshudov GN, Skubak P, Lebedev AA, Pannu NS, Steiner RA, Nicholls RA, Winn MD, Long F, Vagin AA (2011) REFMAC5 for the refinement of macromolecular crystal structures. *Acta Crystallogr D Biol Crystallogr* 67: 355–367. doi:10.1107/s0907444911001314

67. Chen VB, Arendall WB 3rd, Headd JJ, Keedy DA, Immormino RM, Kapral GJ, Murray LW, Richardson JS, Richardson DC (2010) MolProbity: All-atom structure validation for macromolecular crystallography. *Acta Crystallogr D Biol Crystallogr* 66: 12–21. doi:10.1107/s0907444909042073

68. McCoy AJ, Grosse-Kunstleve RW, Adams PD, Winn MD, Storoni LC, Read RJ (2007) Phaser crystallographic software. *J Appl Crystallogr* 40: 658–674. doi:10.1107/s0021889807021206

69. Krissinel E, Henrick K (2007) Inference of macromolecular assemblies from crystalline state. *J Mol Biol* 372: 774–797. doi:10.1016/j.jmb.2007.05.022

70. Banci L, Bertini I, Calderone V, Ciofi-Baffoni S, Mangani S, Martinelli M, Palumaa P, Wang S (2006) A hint for the function of human Sco1 from different structures. *Proc Natl Acad Sci U S A* 103: 8595–8600. doi:10.1073/pnas.0601375103

71. Zong S, Wu M, Gu J, Liu T, Guo R, Yang M (2018) Structure of the intact 14-subunit human cytochrome c oxidase. *Cell Res* 28: 1026–1034. doi:10.1038/s41422-018-0071-1

3.2.1 Supplementary Information

Supplementary figure captions:

Figure S1 Comparison of the ^{WT}Coa6 (gray) and COX6B (raspberry) structures. ^{WT}Coa6 shares significant structural similarity with the Cox6B subunit of COX (PDB 2ZXW, Chains H and U) (180).

Figure S2 Analytical size-exclusion chromatography analysis of ^{WT}Coa6 and mutant Coa6 proteins. All the mutated proteins eluted at a volume similar to the ^{WT}Coa6 dimeric form from an analytical size-exclusion column. ^{WT}Coa6, ^{R101A}Coa6, ^{Y97A}Coa6, ^{Y104A}Coa6 and $^{Y97A/Y104A}$Coa6 are shown as blue, green, black, red and gray lines, respectively.

Figure S3 Determination of copper content of copper loaded ^{WT}Coa6. A standard curve (top) was used to determine the copper content of the ^{WT}Coa6 (bottom).

Figure S4 Redox potential measurements for ^{WT}Coa6. SDS-PAGE analysis of ^{WT}Coa6 (200 $M) incubated for 2 h with increasing concentrations of reduced DTT (0 to 800 mM) followed by AMS labelling. The reduced fractions were quantified using the ImageJ software (56). The fraction of thiolate as a function of $[DTT_{Red}]/[DTT_{Ox}]$ is plotted to calculate the equivalent intrinsic redox potential (- 348.6 mV for ^{WT}Coa6 at pH 7.0).

Figure S5 ^{WT}Coa6 mass determined *via* MS/MS following reduction and iodoacetamide labeling. The determined masses of peptides including Cys58 and Cys90 were detected at the predicted molecular masses of the peptide-iodoacetamide adducts, which were calculated by PEPTIDEMASS (197), indicating the reduction of the Cys58-Cys90 disulfide bond under these conditions. The alkylated peptides containing Cys58 and Cys90 are highlighted in pink.

Figure S6 Secondary structure analyses of the ^{WT}Coa6, $^{C58S/C90S}$Coa6 and $^{C68S/C79S}$Coa6 mutant proteins. CD spectra for ^{WT}Coa6 (solid circle), $^{C58S/C90S}$Coa6 (circle) and $^{C68S/C79S}$Coa6 (diamond) at 0.16 mgml^{-1} and at 20°C. CD spectra show minima at 222 nm and 208 nm characteristic of α-helical structures.

Figure S7 Positively charged residues in the vicinity of the Cu(I) binding site in ^{WT}Coa6. *(A)* Cartoon representation of the chain B of ^{WT}Coa6. The structure of ^{WT}Coa6 shows that the Cys58-Cys90 site is proximate to positively charged residues Lys53 and Arg55, which are shown as sticks (labeled) and bordered by the aromatic side chains of residues Trp59 and Trp94 (sticks, labeled), which partially shield the site from solvent. (*B*) Surface representation of chain B of ^{WT}Coa6. The protein surfaces are colored according to their electrostatic potentials (red, negatively charged; blue, positively charged; white, uncharged). Cysteine residues are shown as spheres for clarity.

Figure S8 Loss of Coa6 results in Complex IV deficiency. (A) Cells were solubilized in digitonin and subjected to BN-PAGE and immunoblot analysis using a total OXPHOS antibody cocktail. SC, supercomplexes consisting of CI, CIII and CIV. *(B)* Unlike ^{WT}Coa6, the $^{C58S/C90S}$Coa6 mutant localizes in the cytosol. The FLAG-tagged ^{WT}Coa6 and FLAG-tagged $^{C58S/C90S}$Coa6 double mutant were expressed in COA6^{KO} cells. Immunofluorescence was performed using Flag and Tom20 antibodies. The resulting images were merged using ImageJ software. The scale bar represents 10 $ m.

Figure S9 Surface electrostatic patterns of ^{WT}Coa6, ^{W59C}Coa6, Sco1, Sco2 and soluble domain of COX2 proteins. *(A)* ^{WT}Coa6. *(B)* ^{W59C}Coa6. *(C)* Sco1 (PDB code 2GVP) (68). *(D)* Sco2 (PDB code 2RLI) (9). *(E)* Soluble domain of human COX2 (PDB code 5Z62) (69). Top panels; The molecular surface of proteins is colored according to the electrostatic potentials (red, negatively charged; blue, positively charged; white, uncharged). Bottom panels; Secondary structures are represented as cartoons as represented in top panels. ^{WT}Coa6 monomers colored in cyan and gray; ^{W59C}Coa6 monomers colored in cyan, gray, orange and green; Sco1 colored in yellow; Sco2 colored in pink and soluble domain of COX2 colored in cyan.

Figure S1

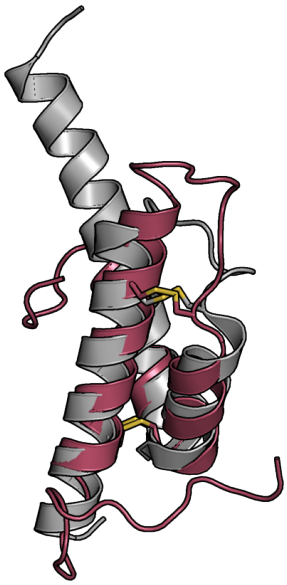

Figure S2

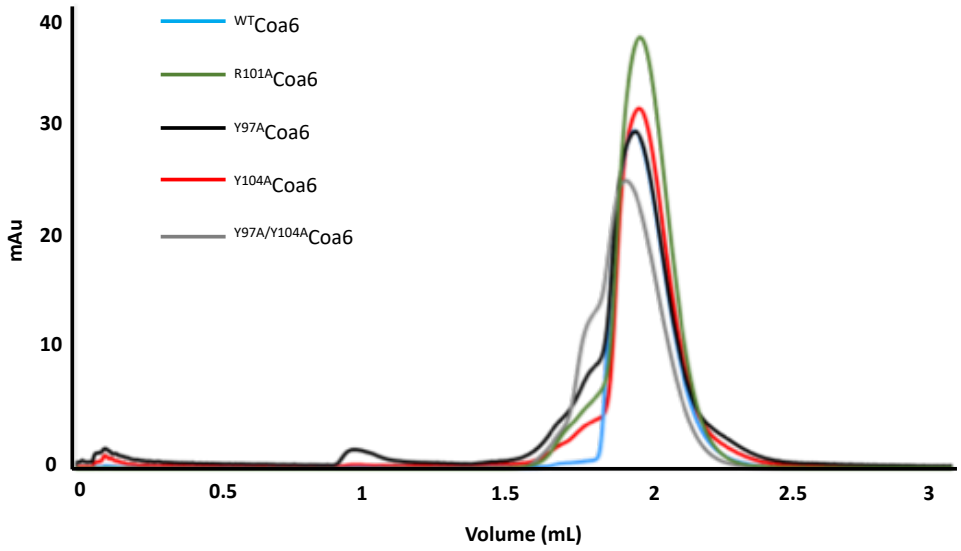
40
30
20
10
0
mAu
WTCoa6
R101ACoa6
Y97ACoa6
Y104ACoa6
Y97A/Y104ACoa6
0
0.5
1
1.5
2
2.5
3
Volume (mL)

Figure S3

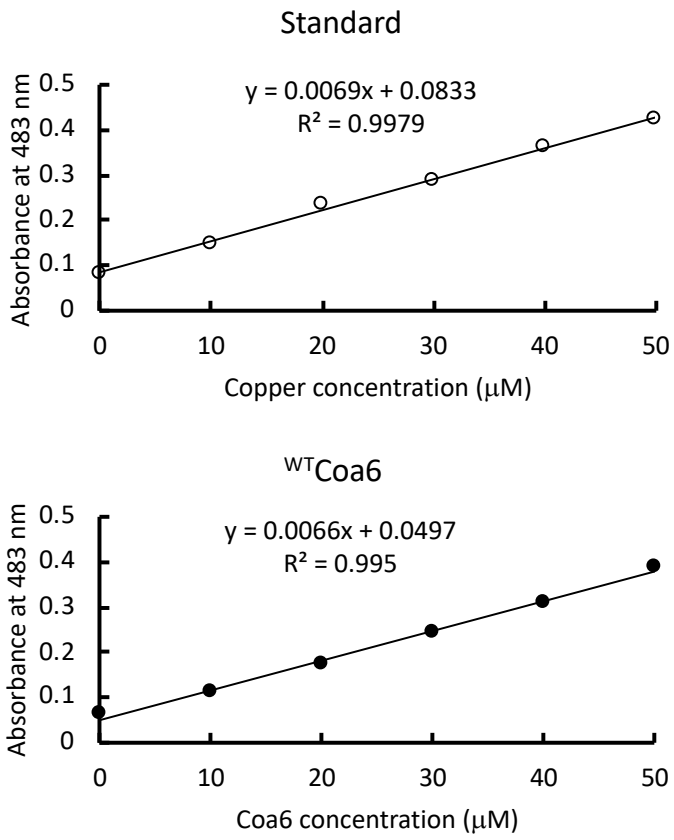
Standard
y = 0.0069x + 0.0833
R² = 0.9979
Absorbance at 483 nm
0.5
0.4
0.3
0.2
0.1
0
0
10
20
30
40
50
Copper concentration (μM)
WTCoa6
y = 0.0066x + 0.0497
R² = 0.995
Absorbance at 483 nm
0.5
0.4
0.3
0.2
0.1
0
0
10
20
30
40
50
Coa6 concentration (μM)

Figure S4

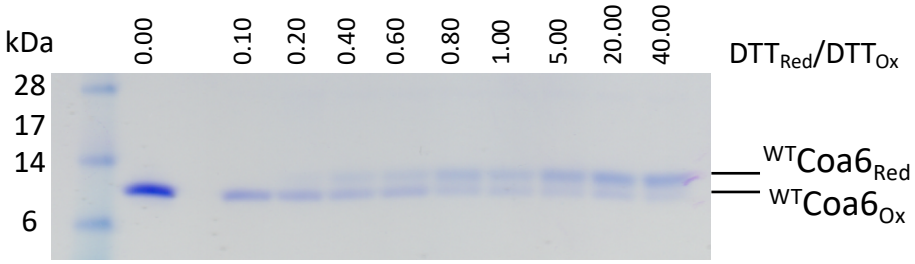
kDa
0.00
0.10
0.20
0.40
0.60
0.80
1.00
5.00
20.00
40.00
DTT$_{Red}$/DTT$_{Ox}$
28
17
14
6
^{WT}Coa6$_{Red}$
^{WT}Coa6$_{Ox}$

Figure S5

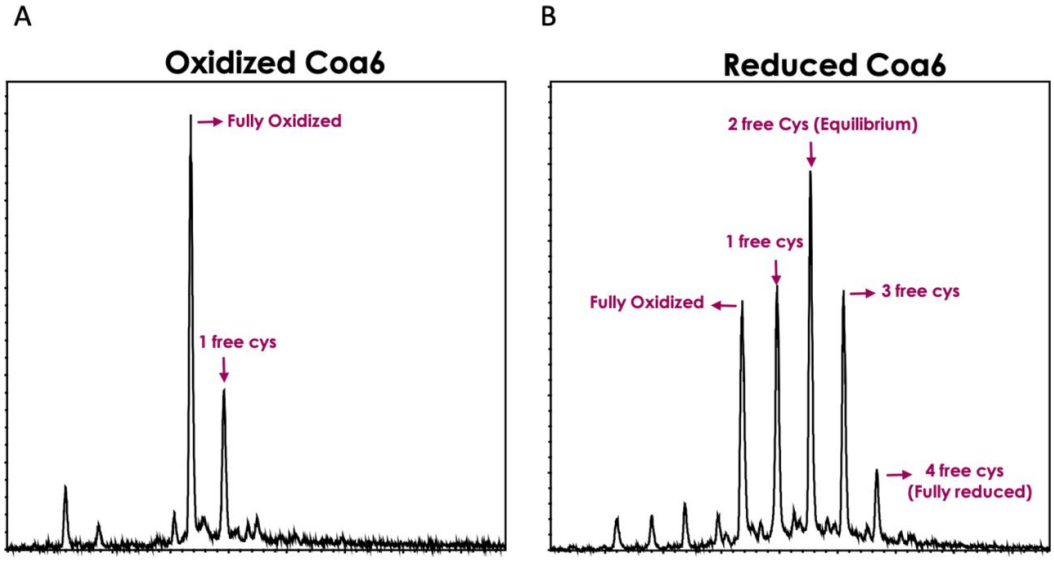
A
Oxidized Coa6
Fully Oxidized
1 free cys
B
Reduced Coa6
2 free Cys (Equilibrium)
1 free cys
Fully Oxidized
3 free cys
4 free cys
(Fully reduced)

Figure S6

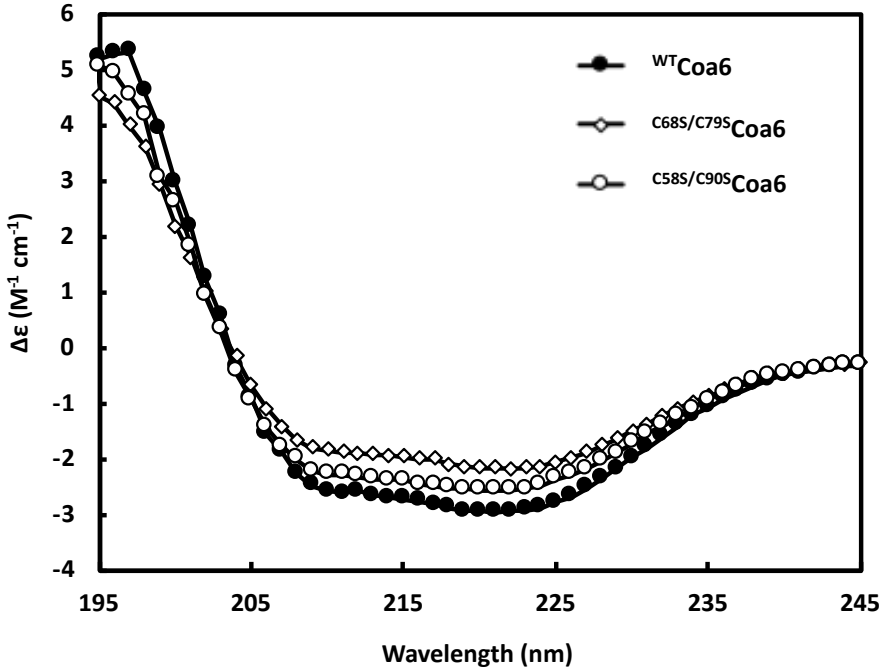
6
5
4
3
2
1
0
-1
-2
-3
-4
Δε (M-1 cm-1)
195
205
215
225
235
245
Wavelength (nm)
WTCoa6
C68S/C79SCoa6
C58S/C90SCoa6

Figure S7

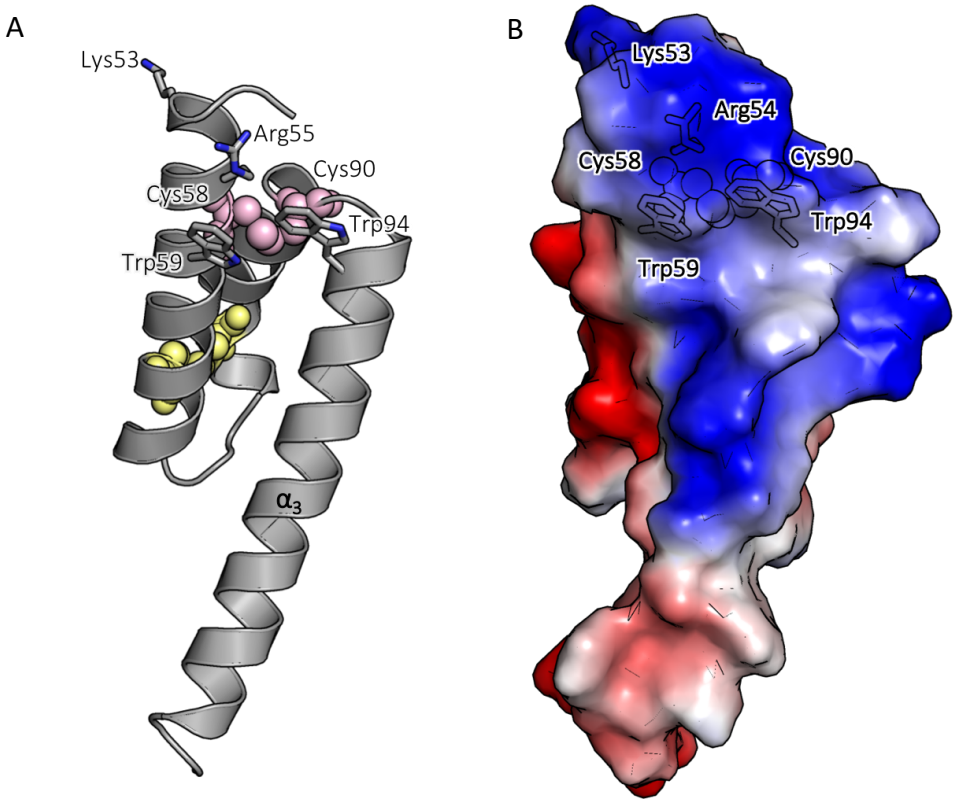
A
Lys53
Arg55
Cys90
Cys58
Trp94
Trp59
α3
B
Lys53
Arg54
Cys58
Cys90
Trp94
Trp59

Figure S8

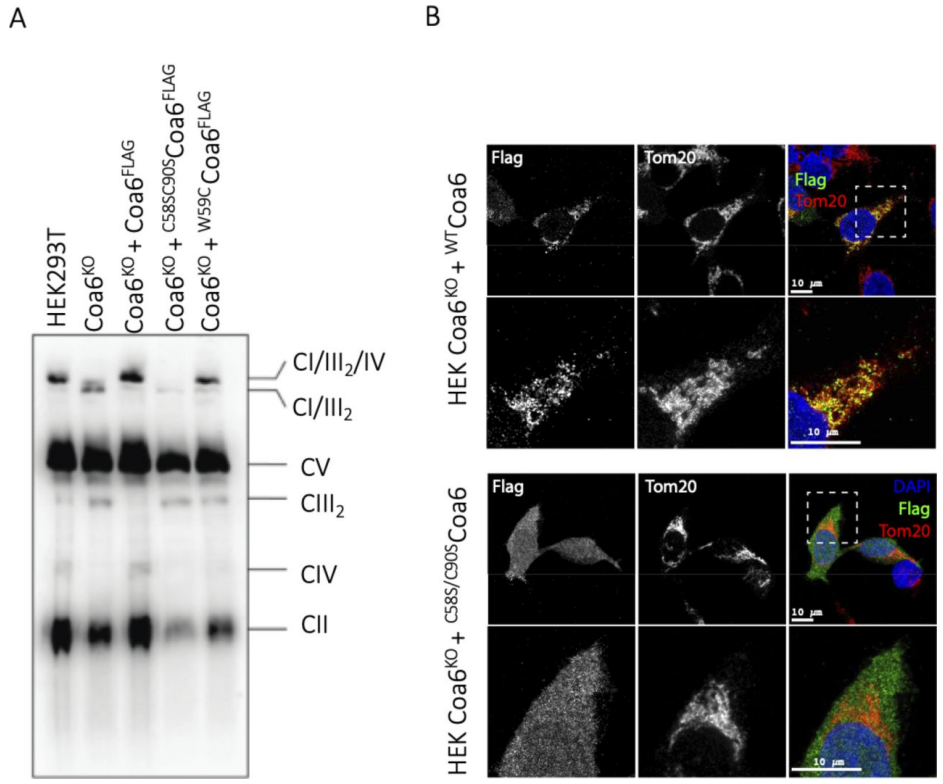
A
B
HEK293T
Coa6KO
Coa6KO + Coa6FLAG
Coa6KO + C58SC90SCoa6FLAG
Coa6KO + W59CCoa6FLAG
CI/III2/IV
CI/III2
CV
CIII2
CIV
CII
HEK Coa6KO + WTCoa6
HEK Coa6KO + C58S/C90SCoa6
Flag
Tom20
DAPI
10 µm

Figure S9

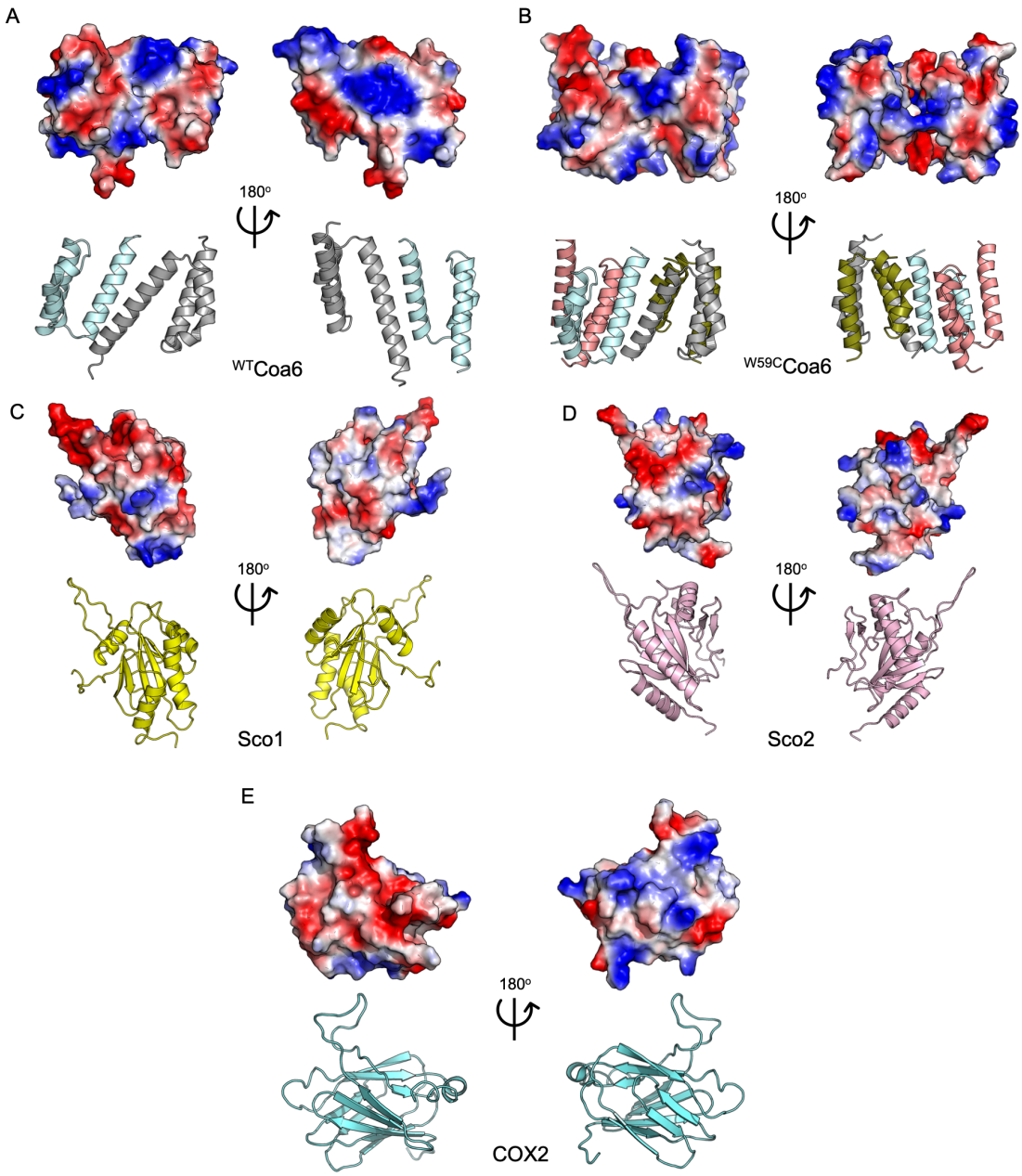

Chapter 4

Cytochrome *c* oxidase Assembly Factor 7

4.1 Introduction

As mentioned in Chapter 3, COX assembly factors are pivotal players in the biogenesis of COX and regulating its stability and activity. Chapter 4 focuses on another mitochondrial COX assembly factor, the Coa7 protein that is located in the intermembrane space of mitochondria and contains five intramolecular disulfide bonds. The precise role of Coa7 in the biogenesis of COX is not understood. However, patients with Coa7 pathogenic mutations suffer from mitochondrial diseases characterised by COX deficiency.

Since Coa7 mutations result in COX assembly defects, the aim of the study described in this chapter was to investigate whether Coa7 functions in co-factor incorporation into COX. The initial studies in Chapter 4 were based on the expression, purification, mutagenesis, characterisation and crystallisation of ^{WT}Coa7 and ^{Y137C}Coa7 proteins. Here, recombinant proteins were overexpressed with an N-terminal GST tag and purified *via* GSH affinity chromatography. The crystal structure of the ^{WT}Coa7 was determined to 2.4 Å resolution. The ^{WT}Coa7 structure is comprised of 11 α-helices, arranged as five SLR (α/α) repeats. SLR proteins are often involved in ligand- and protein-protein interactions due to their extensive solvent accessible surfaces (209-212). Intriguingly, recombinant ^{WT}Coa7 indicates that the protein binds heme with micromolar affinity implying heme as a potential co-factor for Coa7.

For consistency with the rest of the thesis this chapter is presented in the form of a manuscript (Section 4.2). We are awaiting the result of some additional cell biology experiments and expect the manuscript to be submitted soon after submission of this thesis. Section 4.3 provides additional details on the cloning, expression and purification of His_6-tagged proteins and crystallisation of the

^{WT}Coa7 and ^{Y137C}Coa7 samples that were not detailed in the manuscript. The author contributions for this manuscript are presented in the table below.

4.2 Manuscript in preparation

Formosa LE*, Maghool S*, Stroud DA, Maher MJ, & Ryan MT. **Structural and functional characterization of the mitochondrial complex IV assembly factor Coa7.**

** These authors contributed equally to this work.*

Author contributions

The following table is a fair and accurate description of the individual contributions made by each author to this manuscript:

Luke E. Formosa	Sample preparation and data analysis of CRISPR-Cas9, mutagenesis, pulse-chase labelling of mtDNA encoded subunits, co-immunoprecipitation experiments. Provided figures 1 and 2 Wrote the cell biology sections with SM
Shadi Maghool	Mutagenesis, protein expression, purification, characterisation and crystallisation. ^{WT}Coa7 data collection and structure solution with MJM Structure refinement and deposition to the PDB Heme binding experiments Prepared all figures excluding figures 1 and 2 Wrote the manuscript with MJM and LEF
David A. Stroud	Performed proteomics and data analysis
Megan J. Maher	Overall scientific direction of the project ^{WT}Coa7 data collection and structure solution with SM Wrote the manuscript with SM and LEF
Michael T. Ryan	Overall scientific direction of the project Critical reading and editing of the manuscript

Shadi Maghool — *Candidate*

Associate Professor Megan J. Maher — *Supervisor and co-author of the paper*

Structural and functional characterization of the mitochondrial complex IV assembly factor Coa7

Luke E. Formosa[a*], Shadi Maghool[b*], David A. Stroud[c], Megan J. Maher[b,d] and Michael T. Ryan[a,1]

[a]*Department of Biochemistry and Molecular Biology, Biomedicine Discovery Institute, Monash University, Clayton 3800, Australia.*

[b]*Department of Biochemistry and Genetics, La Trobe Institute for Molecular Science, La Trobe University, Melbourne 3086, Australia.*

[c]*Department of Biochemistry and Molecular Biology and Bio21 Molecular Science and Biotechnology Institute, The University of Melbourne, Parkville, Victoria 3010, Australia.*

[d]*School of Chemistry and Bio21 Molecular Science and Biotechnology Institute, The University of Melbourne, Parkville, Victoria 3010, Australia.*

** These authors contributed equally to this work.*

[1]Corresponding author: M.T. Ryan: E-mail: michael.ryan@monash.edu

Keywords: Coa7, mitochondria, Cytochrome *c* oxidase, heme, X-ray crystallography

Introduction

Wide ranges of cellular homeostatic processes, particularly energy production through ATP synthesis, are localized in the mitochondria, which are essential organelles for the function of most eukaryotic cells. ATP production occurs through the activities of five multi-subunit protein complexes in the inner mitochondrial membrane (IMM), known as Complex I to V, which constitute the oxidative phosphorylation (OXPHOS) system (95). Cytochrome *c* oxidase (COX; Complex IV) is copper-heme *a* terminal oxidase of the MRC, which catalyzes electron transfer from cytochrome *c* in the intermembrane space (IMS) to molecular oxygen in the matrix, and contributes to the generation of the proton gradient, which powers ATP synthesis. Mammalian Complex IV is composed of 14 subunits, including three core subunits (COX1, COX2 and COX3) encoded by mitochondrial DNA (mtDNA) (96-98). Complex IV requires the incorporation of three copper ions, heme *a* and heme a_3 cofactors for the biogenesis of the COX1 and COX2 subunits and assembly of the complex.

There are several mitochondrial import machineries that mediate the import of nuclear-encoded mitochondrial proteins into the mitochondria and facilitate the proper localization of these proteins into the sub-compartments, including the outer membrane (OM), IMS, IMM and matrix (92-94). In addition, 36 Complex IV assembly factors (101) have been identified, which are required for subunit maturation, co-factor incorporation and stabilization of intermediate assemblies of Complex IV in humans. Loss-of-function mutations in both mtDNA and nuclear DNA genes encoding mitochondrial proteins, including Complex IV subunits and assembly factors, lead to Complex IV deficiency and mitochondrial disease.

The cytochrome *c* oxidase assembly factor 7 (Coa7, also known as RESA1) is a metazoan-specific Complex IV assembly factor with no homologues in yeast, fungi and plants. Coa7 is a cysteine-rich protein (13 cysteine residues), which contains five Sel1-like repeat domains, based on sequence analysis. Sel1-like repeat (SLR) proteins are a sub-class of the tetratricopeptide repeat (TPR) proteins, which belong to the α/α repeat family of solenoid proteins (212, 213). SLRs are distinguished from TPRs by the number of amino acids that constitute the α/α repeats. TPR α/α repeats consist of 34 amino acids (214), whereas SLR sequences can vary in length from 36 to 44 amino acids (212). The structures of these proteins show large solvent accessible surfaces, suitable for the binding of both large and small substrates (212-214). Accordingly, solenoid proteins, including TPRs and SLRs often function in DNA-, peptide- and protein-protein interactions (212-214), which facilitate cellular processes such as signaling, the cell-cycle and inter-compartmental transport (209-212).

A number of pathogenic mutations in the gene encoding Coa7 have been identified in patients exhibiting neurological symptoms of peripheral neuropathy, ataxia and leukoencephalopathy (139, 141). The first of these studies described an isolated deficiency of Complex IV in patient skin fibroblasts and skeletal muscle in the presence of heterozygous mutations in *COA7* (p. Tyr137Cys and Coa7-exon2Δ), resulting in the expression of Coa7 mutant proteins Y137C and an in-frame deletion mutant (with residues 37-83 absent). The lentiviral-mediated expression of Coa7 in the patient fibroblasts led to the recovery of Complex IV expression and activity. A second study examined a cohort of Japanese patients with recessive mutations in *COA7*, where skin fibroblasts from these patients showed significant decreases in Complex I and Complex IV activities. These mutations included the single amino acid mutations, p.Asp6Gly (D6G),

p.Arg39Trp (R39W) and p.Ser149Ile (S149I) (141). All point mutated residues are highly conserved among Coa7 proteins from different species (Fig. S1).

Determinations of the sub-mitochondrial localization of Coa7 have produced conflicting results. Two reports (using fluorescence microscopy and examining mitochondrial protein import *via* Mia40) concluded that Coa7 is localized within the IMS (138, 140) with another reporting matrix localization (139). Coa7 has been established as a new non-canonical substrate of Mia40 and proposed to exist as an oxidized protein in the IMS (with five intramolecular disulfide bonds) (140). Despite these studies, the function of Coa7 is unknown. Evidence presented to date implicates Coa7 in Complex IV assembly, however the molecular details of its function remain undefined.

In the present study, we have investigated the role of Coa7 in Complex IV assembly. Characterization of the recombinant Coa7 shows that the protein binds heme with micromolar affinity. We report the crystal structure of the human ^{WT}Coa7 to 2.4 Å resolution, which allows us to propose the molecular origins of the pathogeneses observed for the patient mutations.

Results and Discussion

Loss of Coa7 results in Complex IV dysfunction

In order to investigate Coa7 function in the biogenesis of the respiratory chain, CRISPR-Cas9 mediated gene editing (215) was used to generate *COA7* deletion HEK293T cell lines. Following transfection, the HEK293T cells were sorted to generate individual clones. Then, to determine if any clonal populations harboured an OXPHOS defect, a glucose/galactose assay was performed by culturing cells in media containing either glucose or galactose. The OXPHOS deficient cells did not grow on galactose media, so they were grown on glucose

media only. Clones deficient in their ability to grow on galactose media, and therefore respiration deficient, were selected for further analyses. Upon sequencing, two clones (termed $COA7^{KO}$-1 and $COA7^{KO}$-2) were found to contain frameshift deletions to the *COA7* gene where the gRNA was targeted. Mitochondria were isolated from both control and $COA7^{KO}$ cells, solubilized in digitonin and subjected to blue native polyacrylamide gel electrophoresis (BN-PAGE) and immunoblotted for the Complex I subunit NDUFA9, Complex II subunit SDHA, Complex III subunit UQCRC1 and Complex IV subunit COX2 (Fig. 1*A*). Analysis of the respiratory chain complexes revealed that CRISPR-Cas9-mediated disruption of Coa7 resulted in a significant Complex IV assembly defect and modest decreases in the intensities of bands representing Complexes I and II in both $COA7^{KO}$ cell lines (Fig. 1*A*). Re-expression of ^{WT}Coa7 into $Coa7^{KO}$ cells was able to restore the defects observed indicating that loss of Coa7 was the cause of the defects observed.

Next, the translation and stability of mtDNA-encoded subunits in control and $COA7^{KO}$ cells were assessed using pulse-chase analysis using [^{35}S]-Methionine labeling. Analysis of the mtDNA-encoded proteins revealed that in $COA7^{KO}$ cells, the Complex IV subunit COX2 is rapidly degraded, suggesting destabilization of COX2 in the absence of Coa7 (Fig. 1*B*).

To expand the analysis to cover the mitoproteome, quantitative SILAC proteomics was performed to investigate the relative abundance of proteins (216). This analysis (Fig. 1C) indicated that in the absence of Coa7, a number of Complex IV proteins may be destabilized and have a lower mitochondrial abundance. These subunits affected included the mtDNA-encoded COX2 and COX3 subunits, as

well as the nuclear-encoded COX6A1, COX7A2, COX6B-1 and NDUFA4 proteins (98, 102).

Coa7 interacts with CPOX, AK2 and AIF

To investigate the interactions between Coa7 and other mitochondrial proteins, co-immunoprecipitation (Co-IP) was performed using isolated mitochondria from control and ^{WT}Coa7-FLAG expressing COA7^{KO} cells. Analysis of proteins enriched with ^{WT}Coa7-FLAG surprisingly failed to identify any structural Complex IV proteins or assembly factors. However, ^{WT}Coa7-FLAG did appear to enrich a number of IMS proteins including apoptosis-inducing factor 1 (AIFM1) required for biogenesis of the protein, adenylate kinase 2 (AK2) and coproporphyrinogen oxidase (CPOX) proteins, required for nucleotide metabolism and heme biosynthesis respectively (Fig. 1*D*).

Complementation of COA7 knockout cell line with ^{WT}Coa7 and Coa7 patient mutants

In order to investigate the effects of the patient-derived mutations on the ability of recover Complex IV assembly, and stability of COX2, we generated lentiviral plasmids encoding each of the mutations for stable expression in COA7^{KO} cells. Upon expression of ^{WT}Coa7-FLAG, the levels of COX2 could be recovered (Fig. 2, compare lanes 2 and 3). However, upon expression of ^{D6G}Coa7-FLAG, ^{R39W}Coa7-FLAG, ^{Y137C}Coa7-FLAG and ^{S149I}Coa7-FLAG proteins, the levels of COX2 were not able to be restored to the same extent, indicating that these mutations were less active relative to ^{WT}Coa7 (Fig. 2 lanes 4, 5, 6 and 8, respectively). In summary, these experiments showed that the various Coa7 pathogenic mutations differed in their abilities to restore COX2 levels and thus Complex IV biogenesis.

Expression, purification and characterization of the ^{WT}Coa7 and ^{Y137C}Coa7 proteins

Recombinant GST-^{WT}Coa7 and GST-^{Y137C}Coa7 proteins were overexpressed and purified by GSH affinity and size exclusion chromatography (SEC; following cleavage of the N-terminal GST tag with PreScission Protease yielding preparations of ^{WT}Coa7 and ^{Y137C}Coa7 of approximate 95% and 92% purity (Fig. 3*D*)). The analytical SEC elution profile of the resulting purified ^{WT}Coa7 showed a broad elution peak with an elution volume corresponding to a molecular weight of ~55 kDa, indicating the presence of dimeric species in solution (the monomeric molecular weight of Coa7 is 25.65 kDa, calculated from sequence; Fig. 3*A*). The SDS-PAGE analysis of the purified ^{WT}Coa7 protein under reducing and non-reducing conditions showed an intense band at ~25 kDa, corresponding to the molecular weight of monomeric ^{WT}Coa7 (Fig. 3*D*). The analytical SEC profile of purified ^{Y137C}Coa7 showed two major peaks at elution volumes corresponding to molecular weights of ~80 and ~40 kDa (Fig. 3*B*). The SDS-PAGE analysis of the purified ^{Y137C}Coa7 protein under reducing and non-reducing conditions showed an intense band at ~25 kDa (Fig. 3*D*). These SEC and SDS-PAGE analyses of the purified ^{WT}Coa7 and ^{Y137C}Coa7 proteins indicated the possibility of exchangeable protein oligomeric states (such as monomer-dimer) in solution.

The secondary structure compositions of the ^{WT}Coa7 and ^{Y137C}Coa7 proteins were determined by circular dichroism (CD) spectroscopy, which yielded spectra with minima at 222 nm and 208 nm, characteristic of α-helical structures for both proteins (Fig. 3*C*). Given the observed variable SEC behaviour of the proteins, the quaternary structures of the ^{WT}Coa7 and ^{Y137C}Coa7 proteins were determined by analytical ultracentrifugation (AUC), using sedimentation velocity (SV)

experiments at protein concentrations of 2 $M and 10 $M. These data were fitted to a continuous size distribution model, which yielded sedimentation coefficients of 1.9 S and 3.5 S for ^{WT}Coa7 and 2.1 S and 3.5 S for the ^{Y137C}Coa7, demonstrating these samples contained a mixture of monomeric and dimeric species (Fig. 3*E* and *F*, Table S2), with the relative proportions of these species observed to vary with protein concentration, indicating concentration-dependent oligomerization behavior. Importantly, for the ^{Y137C}Coa7 protein, minor features between ~7-12 S were observed in the analysis of the 10 $M sample that were not present at the same intensity for the ^{WT}Coa7 protein (Fig 3*F*, Table S2). These features may indicate the formation of higher order oligomeric or aggregate species at this concentration.

In order to determine whether the observed oligomerization/aggregation of the ^{Y137C}Coa7 mutant protein was due to decreased thermal stability, the melting temperatures (T_m) of the ^{WT}Coa7 and ^{Y137C}Coa7 proteins were measured by differential scanning fluorimetry (DSF) (217). This analysis yielded T_m = 56.5 ± 0.9°C and 45.5 ± 1.1°C for the ^{WT}Coa7 and ^{Y137C}Coa7, respectively, indicating reduced protein stability on the introduction of the mutation.

The structure of ^{WT}Coa7.

In order to elucidate the molecular architecture of the ^{WT}Coa7 protein, we crystallized and determined its structure by X-ray crystallography. The structure was solved and refined in space group $I4_1$ to 2.4 Å resolution, with a single molecule of ^{WT}Coa7 per asymmetric unit (asu) (Fig. 4*A*). The final ^{WT}Coa7 model includes residues Glu10-His218 and refinement of the model converged with residuals R = 20.5% and R_{free} = 25.5% (Table S1).

The ^{WT}Coa7 structure is comprised of 11 α-helices, arranged as five helix-turn-helix (α/α) repeats, (which are vary in length from 30-36 residues) and an additional C-terminal helix (Fig. 4*A*). Together, these form an elongated, right-handed super-helix, with one concave and one convex face. The ^{WT}Coa7 sequence includes 13 cysteine residues (at positions 24, 28, 37, 62, 71, 95, 100, 111, 142, 150, 172, 179 and 187), with the structure showing intramolecular disulfide bonds between residues Cys28-Cys37, Cys62-Cys71, Cys100-Cys111, Cys142-Cys150 and Cys179-Cys185 (Fig. 4*B*). These disulfide bonds bridge pairs of helices within each of the five α/α repeats. The ten Cys residues that participate in the intramolecular disulfide bonds are conserved in Coa7 sequences across all metazoans, however, the cysteine residues at positions 24, 95 and 172 (which are not observed within disulfide bonds in this structure) are found in Coa7 sequences from vertebrates only (Fig S1) (140).

A search of the ^{WT}Coa7 coordinates against the PDB (179) revealed that ^{WT}Coa7 shares significant structural similarity with the Helicobacter cysteine-rich proteins B and C (HcpB; PDB 1klx and HcpC; PDB 1ouv, respectively) (218, 219) from *Helicobacter pylori* (Fig. S2). Hcp proteins are composed of α/α repeats and belong to the SLR protein family. The presence of disulfide bonds within the repeats for both the Hcps and ^{WT}Coa7 is unusual for this protein family (212, 219). Indeed, to our knowledge, Coa7 is the first characterised human SLR protein possessing disulfide-bridged α/α repeats.

The outer convex surface of the ^{WT}Coa7 molecule is highly negatively charged due to the presence of a number of Glu and Asp residues (located within repeats 1, 2 and the linkers between repeats 3, 4 and 4, 5 and the C-terminal helix) (Fig. 5). In addition, the presence of lysine residues 49, 56, 59, 73, 82, 105 and 106 on the inner

concave surface of the ^{WT}Coa7 molecule, creates a positive charged surface in this region (Fig. 5), which is bounded by a hydrophobic pocket that results from clustering of several hydrophobic residues (Ile108, Ala109, Gly144, Gly145, Leu181 and Gly182) (Fig. 5).

Interestingly, the application of crystallographic symmetry operators reveals that in the crystal, this pocket is occupied by the N-terminal helix (residues Glu10-His30) of a neighbouring molecule of Coa7 (Fig. S2*B*), such that the crystal is composed of an infinite network of protein-protein interactions (Fig. S2*A*). This interaction is mediated by hydrogen bonds and electrostatic interactions, with a total buried surface area of 1614 Å^2, representing ~7% of the surface areas of the two molecules combined (179). The shape complementarity statistic for this interaction is 0.71, which is a typical value for antibody/antigen interfaces (220). Given the limited extent of this interaction, it is unlikely to represent a stable oligomeric structure in solution (179, 182), which correlates with the concentration-dependent oligomerization behaviour observed for the protein in solution by AUC. However, this contact may indicate a molecular mechanism for an interaction between Coa7 and protein partners or ligands in the mitochondrial IMS. Similar direct protein-protein interactions have been previously observed for other TPR proteins, including HcpC (218), the Hsp70/Hsp90 organizing protein (Hop; PDB code 1ELR) (221, 222) and the peroxisomal targeting signal-1 (PEX5; PDB code 1FCH) (223). In the case of the HcpC structure, an interaction between the C terminus of one molecule and the hydrophobic pocket of the neighbouring molecule facilitates the formation of an extended protein network in the crystal. This was proposed to represent a mechanism for protein-protein interactions in the cell (218).

The predicted structural consequences of Coa7 pathogenic mutations

The ^{WT}Coa7 structure shows that residue Tyr137 is located on the N-terminal helix of repeat 4 and forms a hydrogen bond with the side chain of residue Glu101, located on the N-terminal helix of repeat 3 (Fig. 6). We predict that the mutation of Tyr137 to Cys will disrupt this hydrogen bond and lead to an increased flexibility of the overall structure. This prediction is supported by our analysis of the quaternary structure of the ^{Y137C}Coa7 mutant protein by AUC, which showed the presence of aggregated and/or higher order oligomeric species in solution (Fig. 3*F*, Table S2). It also correlates with the observed decrease in melting temperature for the ^{Y137C}Coa7 protein, relative to ^{WT}Coa7. The decreased stability of the ^{Y137C}Coa7 protein also may explain its observed mislocalization (140).

Furthermore, we performed mutagenesis on the Glu101 residue to generate the E101A mutation, which normally forms a hydrogen bond interaction with Tyr137. Expression of ^{E101A}COA7-FLAG was still able to restore the levels of COX2 suggesting that the loss of this stabilizing H-bond may not the only reason for the pathogenicity observed (Fig. 2, lane 7) implying that Y137C variant requires further investigation.

A recent analysis of the ^{WT}Coa7 and ^{Y137C}Coa7 proteins *via* molecular modeling and simulation studies, proposed that the presence of residue Cys137, may lead to the disruption of the Cys100-Cys111 disulfide bond and the dynamic formation of alternative disulfide bonds between the introduced Cys137 and residues Cys100 and Cys111 (140). The structure reported here shows that the formation of an alternative Cys137-Cys111 disulfide bond would be possible in the presence of the Y137C mutation and accompanying cleavage of the ^{WT}Coa7 Cys100-Cys111 disulfide bond without major structural rearrangement. However, the predicted

distance between the thiolate groups of the introduced Cys137 and residue Cys100 is too long (3.9 Å) indicating that a Cys137-Cys100 bond would not form in the absence of a major structural reorganisation (Fig S4).

In the case of the Coa7 S149I pathogenic mutation, residue Ser149 is also located on the C-terminal helix of repeat 4 and forms a hydrogen bond with His112, located on the C-terminal helix of repeat 3 (Fig. 6). Like the Y137C mutation, the ^{S149I}Coa7 variant is likely to be destabilized, relative to the ^{WT}Coa7 structure. Interestingly, both the Y137C and S149I mutations are located in the 'middle' of the crescent-shaped structure. Hydrogen bonds and other intramolecular interactions in this region presumably provide rigidity within the structure, scaffolding one half of the assembly, relative to the other.

We also performed mutagenesis on the His112 residue, which is stabilized by Ser149 to generate the H112A and H112F point mutations. Analysis of ^{H112A}Coa7-FLAG and ^{H112F}Coa7-FLAG revealed that while the H112A mutation remained partially functional, the H112F mutation was not able to restore the levels of COX2, suggesting that this interaction or residue may be important for Coa7 function (Fig. 2, lanes 9 and 10).

Finally, in the case of R39W variant, residue Arg39 (located on the C-terminal helix of repeat 1) is exposed on the outer surface of the Coa7 molecule. The introduction of the R39W mutation would alter the surface charge in this region of the protein surface, the consequences of which require further investigation.

Coa7 binds heme with micromolar affinity

Since Coa7 mutations result in Complex IV assembly defects, we sought to investigate whether Coa7 functions in cofactor incorporation into Complex IV. Soluble, high affinity Cu(I)-binding proteins (copper metallochaperones) such as Atox1 (61) , Cox17 (122) and recently identified Cu(I)-binding protein, Coa6 (43) all show $CysX_nCys$ sequence motifs, bind Cu(I) and function in copper delivery to protein partners within the cell. Due to the presence of multiple Cys residues within the Coa7 sequence, we sought to determine whether Coa7 binds copper (specifically, Cu(I)) using a competition assay with the $[Cu^{I}Bcs_2]^{3-}$ complex (32, 43). Cu(I)-binding to the ^{WT}Coa7 was not detected using this assay, however, Cu(I) binding could be observed to the recombinant Atox1 protein, which was included as a positive control (Fig. S5).

The described Co-IP experiments revealed that Coa7 interacts with the CPOX enzyme, which is involved in the heme biosynthesis pathway, where it catalyzes the aerobic oxidative decarboxylation of coproporphyrinogen-III to yield protoporphyrinogen-IX (224). We, therefore, sought to test whether Coa7 might be involved in heme incorporation into Complex IV by measuring whether the purified protein was able to bind heme in solution by UV-visible (UV-Vis) spectrophotometry (225, 226). Upon titration of ^{WT}Coa7 with hemin, difference spectra revealed a soret band at 416 nm and alpha and beta bands at 520 and 630 nm, respectively (Fig. 7*A*), which increased in intensity with the addition of increasing concentrations of hemin. Fitting of these titration data yielded $K_{D(heme)} = 1.09 \pm 0.19$ μM for ^{WT}Coa7. This value is similar to those measured for other heme binding proteins. For instance, the HemQ (chlorite dismutase-like protein) from *Listeria monocytogenes*, which is involved in heme acquisition by the

bacterium binds heme with $K_{D(heme)}$ = 16.2 μM (227). Moreover, the cytoplasmic heme binding protein Phus from *Pseudomonas aeruginosa* binds heme with $K_{D(heme)}$ = 29 μM (228). The titration of the ^{Y137C}Coa7 variant with hemin yielded a similar binding affinity ($K_{D(heme)}$ = 0.92 ± 0.11 μM) to that of ^{WT}Coa7, indicating that the mutation of residue Tyr137 does not affect heme binding by Coa7 (Fig. 7*B*).

In addition, the overexpression of ^{WT}Coa7 in hemin-containing growth media followed by purification by affinity chromatography and SEC led to the co-purification of ^{WT}Coa7 with hemin. UV-Vis spectra of the heme bound ^{WT}Coa7 protein before and after SEC were compared to those of *apo*-^{WT}Coa7 and free hemin (Fig. 8). The spectrum of ^{WT}Coa7 prior to SEC purification showed two major peaks, with a peak at 385 nm corresponding to the presence of free hemin and the peak at 416 nm corresponding to protein-bound hemin (Fig. 8). In contrast, the SEC purified protein sample showed only a maximum at 416 nm (Fig. 8), indicating co-purification of Coa7 with bound heme.

At present, the precise position of the heme binding site within Coa7 is unknown. A recent analysis of the HusA protein from *Porphyromonas gingivalis* revealed a TPR structure of four α/α repeats and iron-independent heme (that is, porphyrin) binding (229). Despite the presence of the TPRs, the HusA structure bears little similarity to that of Coa7 in that it shows a relatively 'closed' structure compared with Coa7 and does not include disulfide bonds. Unbiased docking studies using the HusA solution structure identified a single heme/porphyrin binding groove bounded predominantly by hydrophobic residues. It is possible that the binding groove observed in the Coa7 structure, which in this crystal form mediates the interaction with the N-terminal helix of a symmetry-related molecule, is the site of heme binding. If this is the case, the current crystal form would be incompatible

with the crystallization of a heme-bound protein. Interestingly, residues Tyr72, His112 and Tyr146 line this binding groove. Histidine and tyrosine residues are commonly present in protein heme binding sites, where they provide axial coordination to the bound heme iron atom. Examples include the human heme oxygenase-1 and -2 (HO-1; PDB code 1N45 and HO-2; PDB code 2QPP, respectively) (230, 231) and the human serum albumin (PDB code 1N5U) (232). Moreover, the human STEAP4 (PDB code 6HD1) binds two heme ligands through coordination to histidine and tyrosine residues (233).

Conclusion

Despite the importance of Complex IV assembly in health and mitochondrial disease, we have only a basic understanding of the molecular basis of the biogenesis of this enzyme owing to a lack of knowledge about the identities, structures and roles of all crucial Complex IV assembly factors. The present study showed that deletion of Coa7 resulted in a significant Complex IV assembly defect and modest decreases in the assembly of Complexes I and II in both $COA7^{KO}$ cell lines. Crucially, the absence of Coa7 causes specific defects in the maturation of the COX2, resulting in its degradation and therefore halting/interfering with Complex IV biogenesis.

In this study, the high-resolution crystal structure of the human Coa7 protein exhibits that the protein is composed of five SLRs and an additional C-terminal helix. The overall fold of ^{WT}Coa7 (Fig. S3) is similar to bacterial Hcp proteins, which are also composed of disulfide-bridged α/α repeats.

TPRs and SLRs are often involved in protein-protein interactions due to their extensive solvent accessible surfaces (209-212). It has been reported that the

concave surface, present in the structures of TPRs and SLRs is the potential site of interaction with protein partners (212, 221, 234). The observation of contacts between Coa7 molecules in the crystal mediated through this surface, suggests that this may represent an interface by which protein-protein or protein-ligand interactions are executed.

Both the ^{WT}Coa7 and ^{Y137C}Coa7 proteins bind heme in solution. Whether this also occurs in the mitochondria requires further investigation. It is tempting to propose that Coa7 functions in Complex IV biogenesis through a role as a 'heme chaperone', however, the confirmation of this hypothesis must await further structural and biochemical examination.

Materials and Methods

The sample preparation and data analysis of CRISPR-Cas9 design and construction, mutagenesis, [^{35}S]-Met pulse-chase labeling of mtDNA encoded subunits, co-immunoprecipitation of exogenously expressed FLAG-tagged protein and proteomics experiments were kindly performed by Dr Luke Formosa (Ryan Lab, Monash University).

Protein overexpression, purification, and characterization

Tyr137Cys mutation was introduced into the ORF encoding the ^{WT}Coa7 protein in the pGEX-6P-1-Coa6 plasmid using Q5® Site-Directed Mutagenesis kit (New England, BioLabs), according to the manufacturer's instructions. Forward and reverse primers for all mutant proteins were designed using NEBaseChanger online tool ((http://nebasechanger.neb.com/)). The DNA sequence encoding the variant was amplified *via* PCR followed by ligation and template DNA removal

using KLD enzyme mix (containing a kinase, a ligase and DpnI, New England BioLabs®).

The pGEX-6P-1 plasmids containing DNA sequence encoding ^{WT}Coa7 and ^{Y137C}Coa7 were individually transformed into *Escherichia coli* strain SHuffle® T7 (New England, BioLabs). Cultures were grown at 30°C in Lysogeny Broth (LB) supplemented with ampicillin (100 μgml^{-1}), chloramphenicol (35 μgml^{-1}) and streptomycin (50 μgml^{-1}) to an OD_{600} of 0.8, induced with isopropyl β-D-1-thiogalactopyranoside (IPTG, 0.2 mM) and harvested after 16 hours (with shaking) at 16°C.

GST tagged ^{WT}Coa7, heme-loaded ^{WT}Coa7 and ^{Y137C}Coa7 were purified by GSH affinity chromatography. Frozen cell pellets were thawed at room temperature and resuspended in PBS (phosphate-buffered saline pH 7.4). Cells were disrupted by passage through a TS series bench top cell disruptor (Constant Systems Ltd) at 35 kpsi. Cell debris were removed by centrifugation (Beckman JLA-25.50, 30000 g, 20 min, 4°C) and the soluble fraction was incubated with glutathione sepharose™ 4B resin (GE Healthcare) equilibrated with PBS. The GST tag was cleaved with PreScission Protease followed by size-exclusion chromatography (SEC; HiLoad 16/600 Superdex 75 pg, GE Healthcare; 20 mM NaHepes pH 7.2, 50 mM NaCl). Cleavage of the N-terminal GST tag introduced five additional residues (GPLGS) to the N-terminus of all proteins. The purified proteins were concentrated to 20 mgml^{-1} before storage at -80°C.

Sedimentation velocity analysis

^{WT}Coa7 and ^{Y137C}Coa7 samples were analysed using an XL-I analytical ultracentrifuge (Beckman Coulter, Fullerton, CA) equipped with an AnTi-60 rotor. Protein samples were loaded in the sample compartment of double-sector epon

centrepieces, with buffer (20 mM NaHepes pH 7.5, 50 mM NaCl) in the reference compartment. Radial absorbance data was acquired at 20°C using a rotor speed of 50,000 rpm and a wavelength of 280 nm, with radial increments of 0.003 cm in continuous scanning mode. The sedimenting boundaries were fitted to a model that describes the sedimentation of a distribution of sedimentation coefficients with no assumption of heterogeneity (*c(s)*) using the program SEDFIT (235). Data were fitted using a regularization parameter of p = 0.95, floating frictional ratios, and 100 sedimentation coefficient increments in the range of 0–15 S.

Circular dichroism spectroscopy

The secondary structures of the ^{WT}Coa7 and ^{Y137C}Coa7 proteins were determined by circular dichroism (CD) spectroscopy in 1.0 mm path length quartz cuvettes, using an Aviv Model 420 (CD) Spectrometer. ^{WT}Coa7 and ^{Y137C}Coa7 samples were prepared at 0.162 mgml^{-1} in CD buffer (10 mM sodium fluoride, 50 mM potassium phosphate pH 8.5, 0.5 mM TCEP) and wavelength scans were recorded at 20°C between 190 and 250 nm. Data were converted to mean residue ellipticity and the secondary structure compositions of the protein samples estimated using the CDPro software with CONTINLL and CDSSTR algorithms (195).

Differential scanning fluorimetry

The melting temperatures (T_m) were measured by differential scanning fluorimetry (DSF) using ^{WT}Coa7 and ^{Y137C}Coa7 proteins in 20 mM NaHepes pH 7.2, 50 mM NaCl (1 mgml^{-1}). DSF experiments were performed at the CSIRO Collaborative Crystallisation Centre (http://www.csiro.au/C3), Melbourne, Australia.

Copper binding experiments

Measurements of the copper binding affinities of the ^{WT}Coa7 and Atox1 were performed as previously described (43). Briefly, purified proteins (in 20 mM Tris-MES pH 8.0) were titrated at various concentrations (1–30 $M) into solutions containing buffer (20 mM Tris-MES pH 7.0), $CuSO_4$ (20 $M), Bcs (200 $M) and NH_2OH (1 mM). The exchange of Cu(I) from the $[Cu^{I}Bcs_2]^{3-}$ complex to the proteins was monitored by measuring the absorbance of the resulting solutions at 483 nm. The data were analyzed by plotting $[Cu^{I}Bcs_2]^{3-}$ (as determined from the absorbance values at 483 nm) versus protein:Cu ratios, and the data fitted using the equation previously described (32, 43).

Spectrophotometric properties of heme-titrated ^{WT}Coa7 and ^{Y137C}Coa7 proteins

The heme binding assay on ^{WT}Coa7 and ^{Y137C}Coa7 proteins were performed by difference spectroscopy at room temperature and aerobically using a double beam UV spectrophotometry (Cary 5000 UV-Vis-NIR spectrophotometer) as previously described (225, 226). A baseline was selected by scanning samples from 280 to 750 nm, buffer (20 mM NaHepes pH 7.2, 50 mM NaCl) in the reference cuvette and 100 nM of purified protein (in 20 mM NaHepes pH 7.2, 50 mM NaCl) in the sample cuvette. After the baseline was set, increasing concentrations of hemin (0-10 μM) were added to both the sample and the reference cuvettes, therefore the readings only reflect the binding of protein with hemin and not the absorbance of the free hemin. The data were analysed by plotting absorbance at 416 nm versus hemin concentration and the data fitted using equation describing a single binding site ($Y = \frac{B\max * X}{Kd + X}$) using the GraphPad Prism software.

Protein crystallization and data collection

Initial high-throughput crystallization experiments using ^{WT}Coa7 (20 mgml^{-1}) were performed at the CSIRO Collaborative Crystallisation Centre

(http://www.csiro.au/C3), Melbourne, Australia using c3 salty screens (c3_5 and c3_6) by sitting drop vapor diffusion in 96-well plates. Diffraction-quality plate-like crystals of ^{WT}Coa7 grew overnight to a maximum size of 250 µm x 30 µm at 20°C by hanging-drop vapor diffusion with drops containing equal volumes (1 $L) of ^{WT}Coa7 (20 mgml^{-1} in 20 mM NaHepes pH 7.2, 50 mM NaCl) and crystallisation solution (0.23 M sodium MES pH 6.72, 2.35 M ammonium sulfate, 8.2% (v/v) ethanol and 4.5% (v/v) pentaerythritol ethoxylate (3/4 EO/OH) equilibrated against 500 $L reservoir solution. ^{WT}Coa7 crystals were cryoprotected in reservoir solution containing 25% (v/v) glycerol before flash-cooling in liquid nitrogen. Diffraction data were recorded on an EIGER X 16M detector at the Australian Synchrotron on beamline MX2 at a wavelength of 0.954 Å. All data were collected at 100 K and were processed and scaled with XDS (236) and AIMLESS (237). Data collection statistics are detailed in Table S1.

Structure solution and refinement

The crystal structure of ^{WT}Coa7 was solved by molecular replacement using the program PHASER (206) from the CCP4 suite (202). A model including residues 33-104 and 110-216 of the HcpC crystal structure (PDB 1ouv) (218) were used as the search model after removal of all water molecules. The structure was refined using REFMAC5 (204), with manual model building and the addition of water molecules carried out in COOT (203). The refinement of the model converged with residuals R = 0.20 and R_{free} = 0.25 (Table S1) and showed excellent geometry as determined by MOLPROBITY (205) (Table S1).

Figure captions

Figure 1. Loss of Coa7 results in a Complex IV deficiency. (*A*) Mitochondria were solubilized in digitonin and subjected to BN-PAGE and immunoblot analysis using antibodies against NDUFA9 (CI), SDHA and SDHB (CII), UQCRC1 (CIII) and COX2 (CIV). SC, supercomplexes consisting of CI, CIII and CIV. (*B*) MtDNA-encoded subunits were radiolabeled in control or $COA7^{KO}$ cells and chased for the indicated times. Isolated mitochondria were analyzed by SDS-PAGE. (*C*) Mitochondria from 'heavy' or 'light' amino acid labeled HEK293T and $COA7^{KO}$ cells were mixed and analyzed by LC-MS. (*D*) Coa7 interacts with CPOX, AK2 and AIF. Mitochondria from 'heavy' or 'light' amino acid labeled $COA7^{KO}$ cells expressing Coa7-FLAG were solubilized in 1% digitonin and bound to anti-FLAG affinity gel. Elutions were mixed and analyzed by LC-MS.

Figure 2. Complementation of Coa7 knockout cell line with ^{WT}Coa7 and Coa7 patient mutants. Mitochondria were isolated from control HEK293T, $COA7^{KO}$ cells expressing ^{WT}Coa7-FLAG, ^{D6G}Coa7-FLAG, ^{R39W}Coa7-FLAG, ^{Y137C}Coa7-FLAG, ^{E101A}Coa7-FLAG, ^{S149I}Coa7-FLAG, ^{H112A}Coa7-FLAG and ^{H112F}Coa7-FLAG, subjected to SDS-PAGE and immunoblotted with antibodies against COX2 (Complex IV) and Coa7. SE (short exposure) and LE (long exposure).

Figure 3. Purification and characterization of the ^{WT}Coa7 and ^{Y137C}Coa7 proteins. (*A*) Elution profile of purified ^{WT}Coa7 relative to indicated protein standards analyzed by size-exclusion chromatography. (*B*) Elution profile of purified ^{Y137C}Coa7 mutant relative to indicated protein standards analyzed by size-exclusion chromatography. (*C*) Overlay of the CD spectra of the ^{WT}Coa7 (teal) and ^{Y137C}Coa7 (pink) proteins. The CD spectra show minima at 222 nm and 208 nm characteristic of α-helical structures. (*D*) Purified ^{WT}Coa7 and ^{Y137C}Coa7 proteins were analyzed by SDS-PAGE in the presence and/or absence of β-mercaptoethanol (βME) as indicated. (*E*) Analytical ultracentrifugation sedimentation velocity analysis of the purified ^{WT}Coa7. Sedimentation velocity continuous size [*c(s)*] distribution best fit for ^{WT}Coa7 measured at protein concentrations of 2 μM (dashed lines, teal) and 10 μM (solid lines, teal). (*F*) Analytical ultracentrifugation sedimentation velocity analysis of the purified ^{Y137C}Coa7. Sedimentation velocity continuous size [*c(s)*] distribution best fit for

^{Y137C}Coa7 measured at protein concentrations of 2 μM (dashed lines, pink) and 10 μM (solid lines, pink).

Figure 4. Structure of the ^{WT}Coa7. (*A*) Cartoon representation of the overall structure of ^{WT}Coa7. Secondary structures are represented as cartoons with repeats colored in gray, raspberry, cyan, teal and green. (*B*) Cysteine residues (labeled) involving in intramolecular disulfide bonds formation are shown as yellow spheres, whereas free Cysteines residues are shown as salmon spheres.

Figure 5. Coa7 concave and convex surfaces. The molecular surface of Coa7 is colored according to the electrostatic potentials (red, negatively charged; blue, positively charged; white, uncharged). The Top images show the side view of Coa7 structure. The left and right bottom images show concave and convex views, respectively.

Figure 6. Coa7 pathogenic mutation. Patient mutations are shown as pink sticks and hydrogen bonds between residues (labeled) shown as dashed lines.

Figure 7. Coa7 can bind heme. (*A*) Difference spectroscopy titration of heme binding to Coa7. (*B*) Difference spectroscopy titration of heme binding to ^{Y137C}Coa7. Difference absorption spectra and titration curves of ^{WT}Coa7 (100 nM) and ^{Y137C}Coa7 (100 nM) with increasing concentrations of Fe^{3+} hemin (from 0 to 10 μM) as indicated. The curves were generated from fits to an equation describing a single binding site (Y = Bmax * X=K_D + X) with GraphPad Prism.

Figure 8. Coa7 co-eluting with heme. Free hemin has a UV-vis absorption spectrum with maxima at 365 and 385 nm (dashed lines), whereas bound hemin has a UV-vis absorption spectrum with maxima at 412 and 420 nm. The UV-visible spectrophotometry data show that before SEC sample contains two major peaks (green); first peak corresponds to free hemin (385 nm) and second peak corresponds to bound hemin with a soret maximum at 416 nm. However, after SEC sample (pink) only shows a soret band with maxima at 416 nm.

Figure 1.

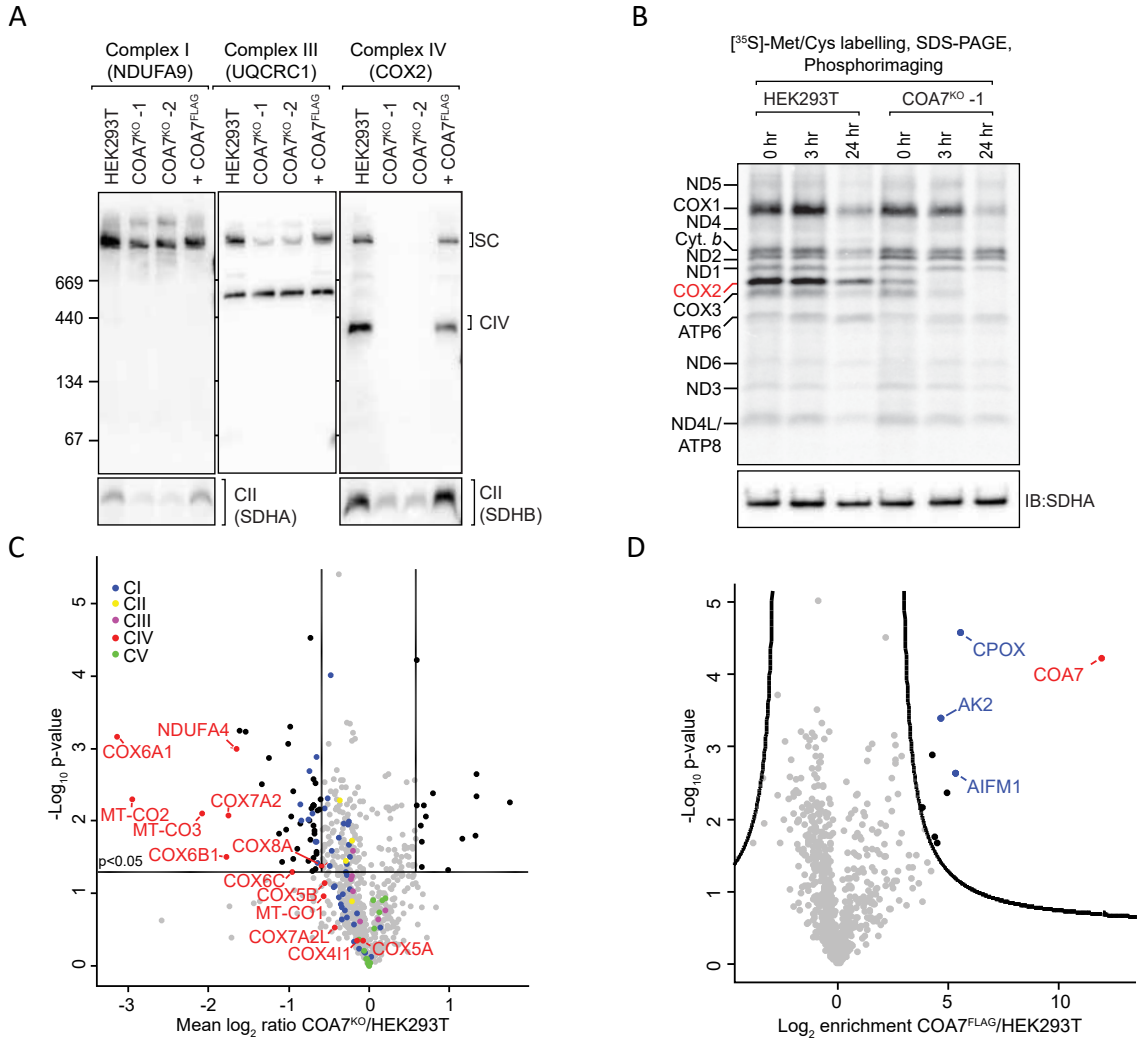
A
Complex I (NDUFA9)
Complex III (UQCRC1)
Complex IV (COX2)
HEK293T
COA7KO -1
COA7KO -2
+ COA7FLAG
669
440
134
67
]SC
] CIV
CII (SDHA)
CII (SDHB)
B
[35S]-Met/Cys labelling, SDS-PAGE, Phosphorimaging
HEK293T
COA7KO -1
0 hr
3 hr
24 hr
ND5
COX1
ND4
Cyt. b
ND2
ND1
COX2
COX3
ATP6
ND6
ND3
ND4L/ ATP8
IB:SDHA
C
CI
CII
CIII
CIV
CV
NDUFA4
COX6A1
MT-CO2
MT-CO3
COX7A2
COX8A
COX6B1
p<0.05
COX6C
COX5B
MT-CO1
COX7A2L
COX4I1
COX5A
-Log10 p-value
Mean log2 ratio COA7KO/HEK293T
D
CPOX
COA7
AK2
AIFM1
-Log10 p-value
Log2 enrichment COA7FLAG/HEK293T

Figure 2.

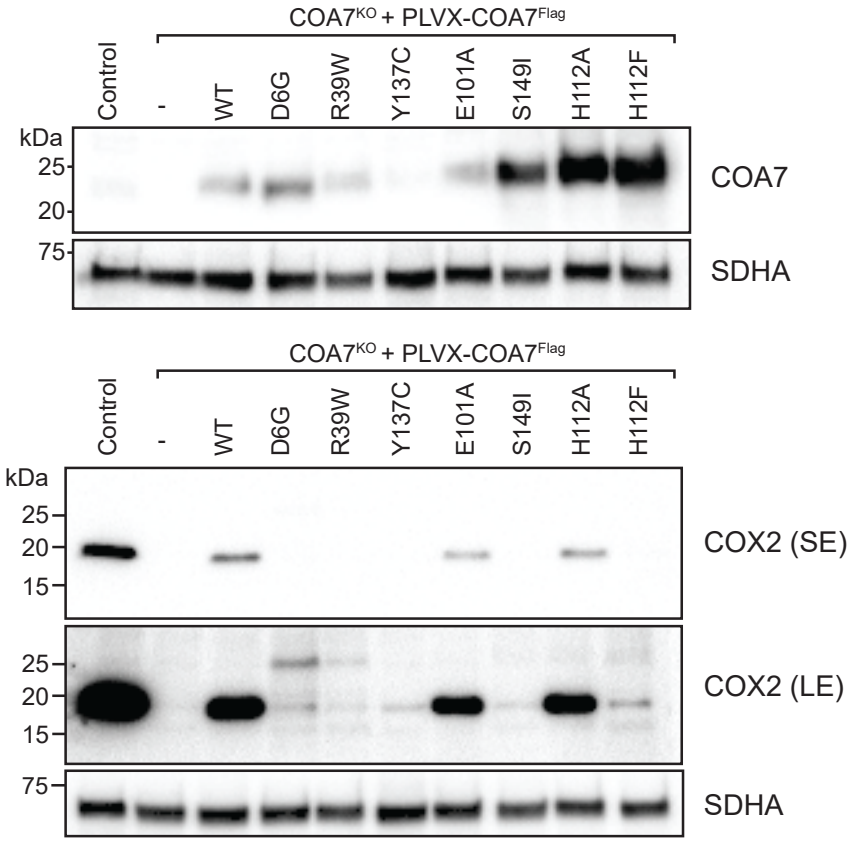
COA7KO + PLVX-COA7Flag
Control
-
WT
D6G
R39W
Y137C
E101A
S149I
H112A
H112F
kDa
25
20
75
COA7
SDHA
COA7KO + PLVX-COA7Flag
Control
-
WT
D6G
R39W
Y137C
E101A
S149I
H112A
H112F
kDa
25
20
15
COX2 (SE)
25
20
15
COX2 (LE)
75
SDHA

Figure 3.

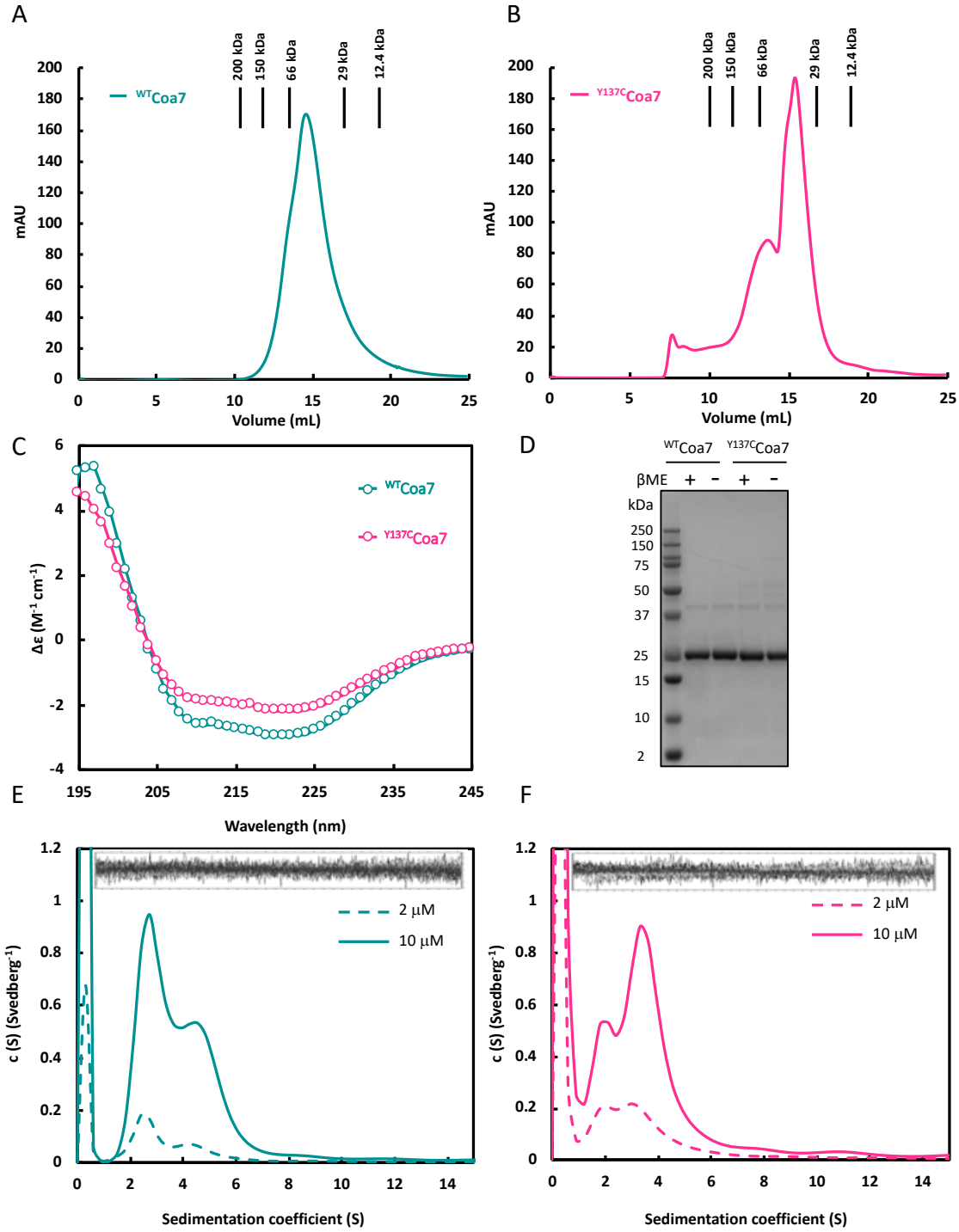
A
200 kDa
150 kDa
66 kDa
29 kDa
12.4 kDa
WTCoa7
mAU
Volume (mL)
B
Y137CCoa7
C
Δε (M-1 cm-1)
Wavelength (nm)
D
WTCoa7
Y137CCoa7
βME
kDa
250
150
75
50
37
25
15
10
2
E
2 μM
10 μM
c (S) (Svedberg-1)
Sedimentation coefficient (S)
F

Figure 4.

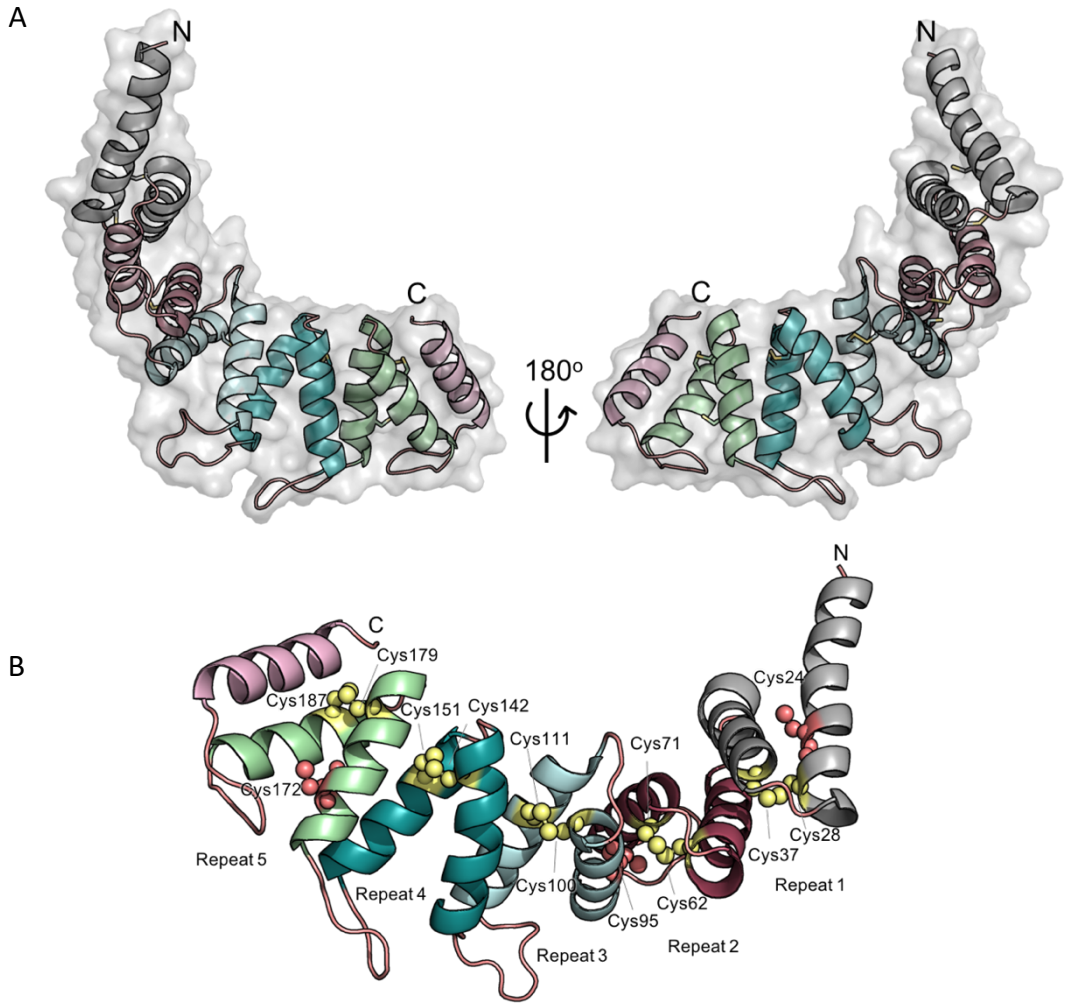
A
N
C
180°
N
C
B
N
C
Cys179
Cys187
Cys151
Cys142
Cys111
Cys71
Cys24
Cys172
Cys28
Cys37
Repeat 5
Repeat 4
Cys100
Cys62
Cys95
Repeat 1
Repeat 3
Repeat 2

Figure 5.

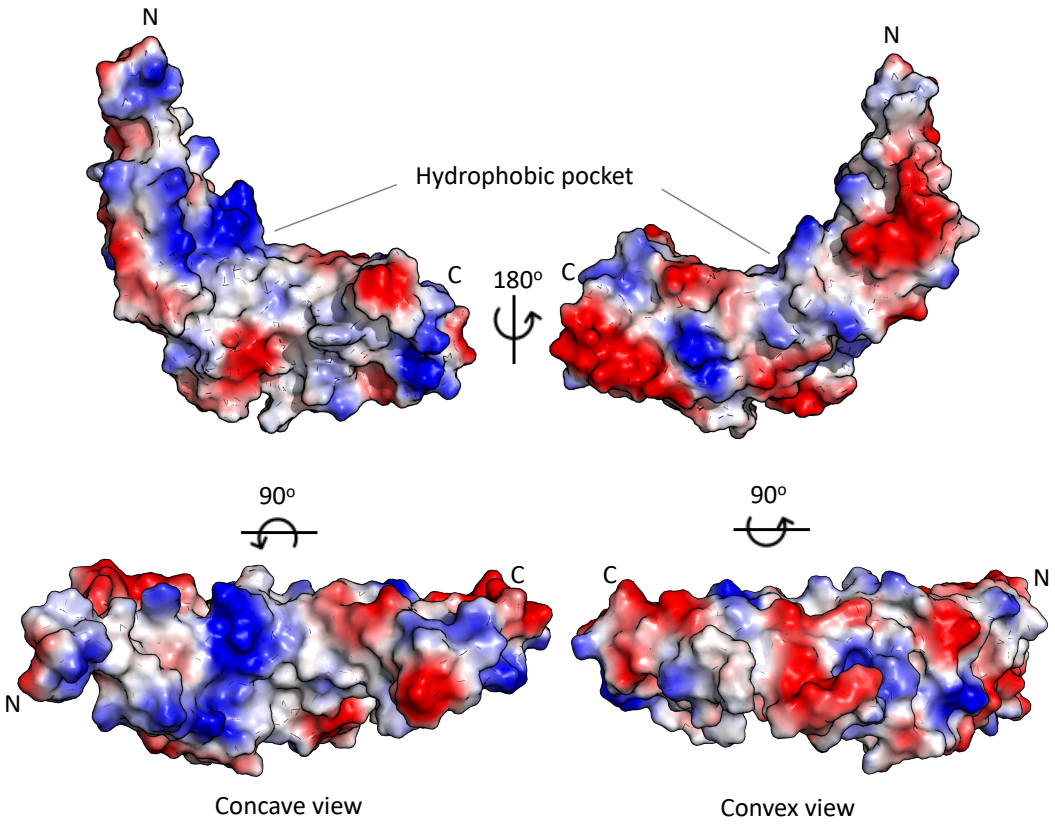
N
N
Hydrophobic pocket
C
180°
C
90°
90°
C
C
N
N
Concave view
Convex view

Figure 6.

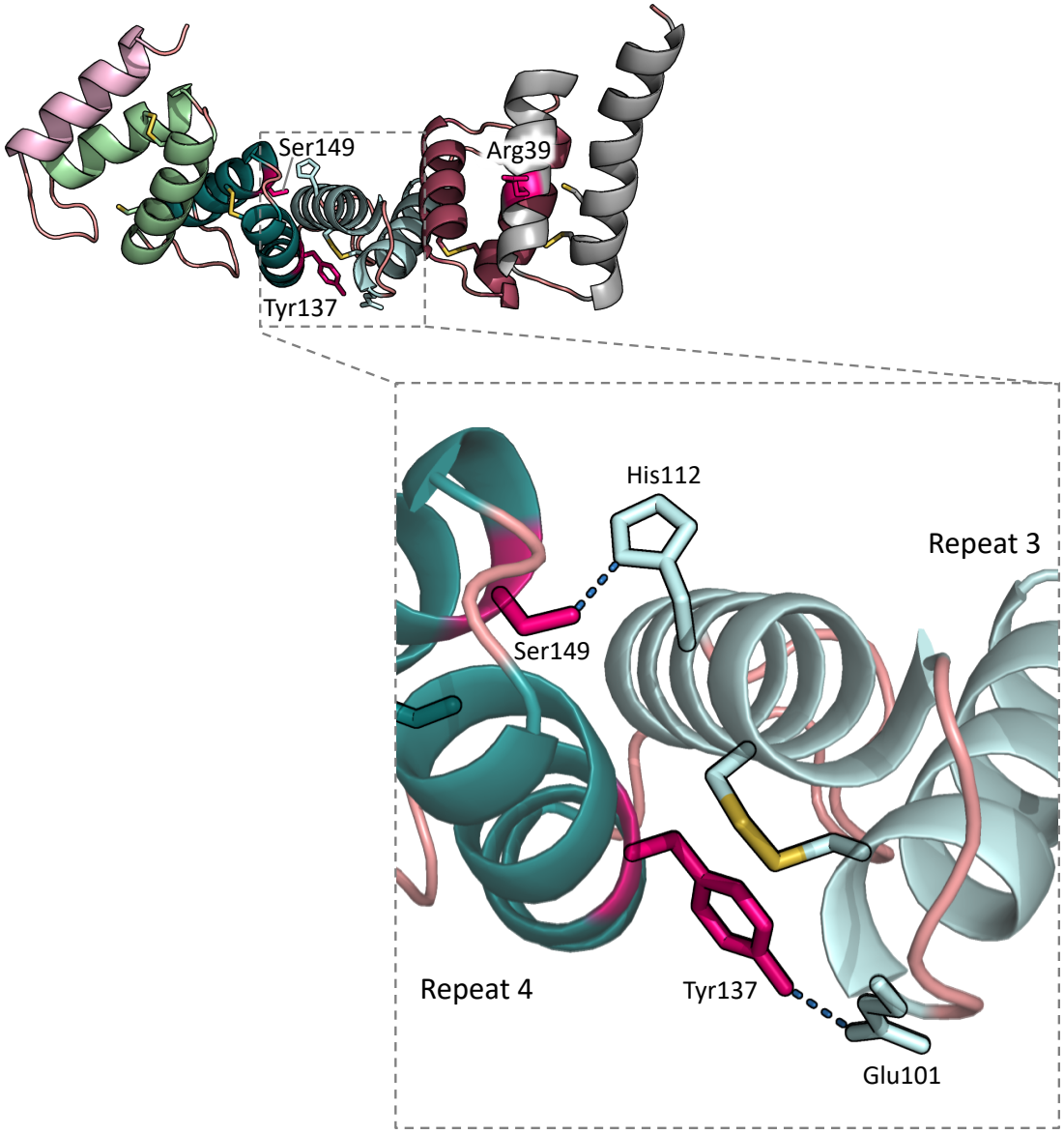
Ser149
Arg39
Tyr137
His112
Repeat 3
Ser149
Repeat 4
Tyr137
Glu101

Figure 7.

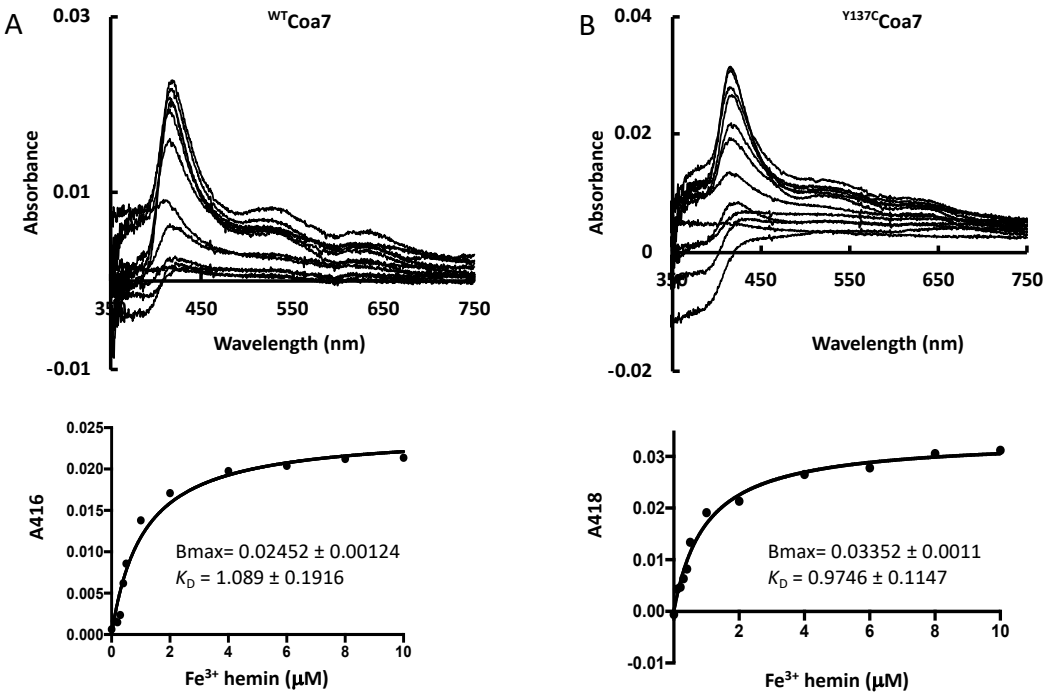
A
WTCoa7
Absorbance
0.03
0.01
-0.01
350
450
550
650
750
Wavelength (nm)
B
Y137CCoa7
Absorbance
0.04
0.02
0
-0.02
350
450
550
650
750
Wavelength (nm)
A416
Bmax= 0.02452 ± 0.00124
K_D = 1.089 ± 0.1916
Fe3+ hemin (μM)
A418
Bmax= 0.03352 ± 0.0011
K_D = 0.9746 ± 0.1147
Fe3+ hemin (μM)

Figure 8.

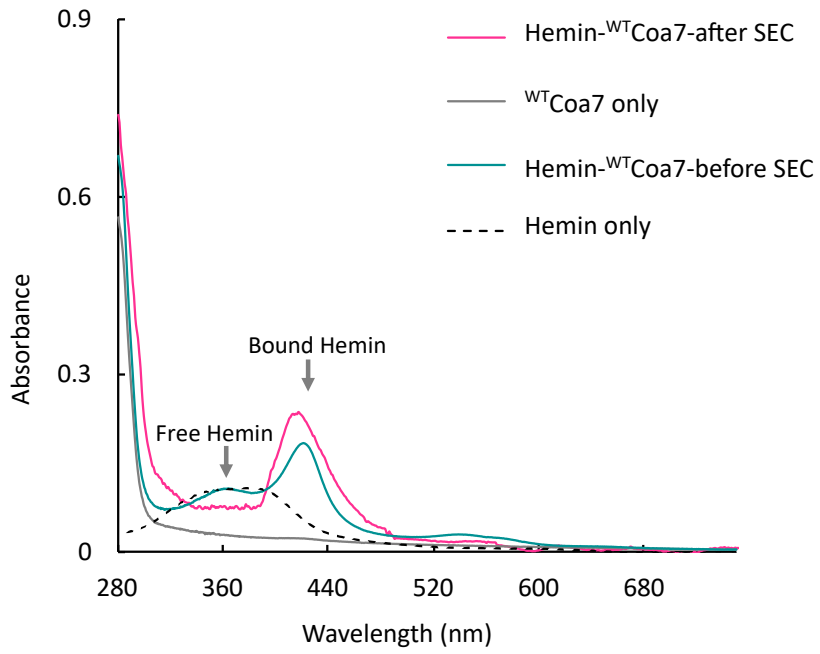
0.9
0.6
0.3
0
Absorbance
280
360
440
520
600
680
Wavelength (nm)
Hemin-WTCoa7-after SEC
WTCoa7 only
Hemin-WTCoa7-before SEC
Hemin only
Bound Hemin
Free Hemin

4.2.1 Supplementary Information

Supplementary figure captions

Figure S1 Sequence alignment between Coa7 proteins across metazoans using *Clustal omega* and rendered with *ESPript*. Numbering is relative to human Coa7. Conserved cysteine residues are highlighted in yellow. Pathogenic mutations are highlighted in pink. Gray boxes indicate cysteine residues that are not conserved across eukaryotes. All remaining conserved residues are highlighted in blue.

Figure S2 Comparison of the ^{WT}Coa7 (pink), HcpB (green) and HcpC (gray) structures. The overall fold of ^{WT}Coa7 is similar to Hcp proteins composing of disulfide-bridged α/α repeats. Cysteine residues involving in intramolecular disulfide bonds formation are shown as spheres.

Figure S3 ^{WT}Coa7 crystal packing. (*A*) the application of crystallographic symmetry operators reveals that in the crystal, this pocket is occupied by the N-terminal helix (pink) of a neighboring molecule of Coa7, such that the crystal is composed of an infinite network of protein-protein interactions (*B*) Interactions observed in Coa7 crystal contact. The molecular surface of Coa7 is colored according to the electrostatic potential (negative potential, red; positive potential, blue). The main chain of the symmetry-related Coa7 molecule is shown as a ribbon. Side-chains of N-terminal helix are recognized by hydrophobic interactions which shown as yellow sticks.

Figure S4 The Y137C pathogenic mutation may lead to the disruption of the Cys100-Cys111 disulfide bond. The ^{WT}Coa7 structure shows that the formation of an alternative Cys137-Cys111 disulfide bond would be possible in the presence of the Y137C mutation (2.7 Å). However, the predicted distance between the thiolate groups of introduced Cys137 and residue Cys100 is too long, at 3.9 Å, indicating that a Cys137-Cys100 bond would not form in the absence of a major structural reorganisation.

Figure S5 ^{WT}Coa7 exhibit no copper binding. Known concentrations (1–30 $M) of recombinant ^{WT}Coa7 and Atox1 were added to a complex of 24 $M $[Cu^{I}Bcs_2]^{3-}$, and the absorbance was measured at 483 nm. The data were analyzed using plots

of $[Cu^{I}Bcs_2]^{3-}$ versus Atox1:copper ratio, and the data fit using Equation (2) as previously described (32, 43).

Table S1. Data collection and refinement statistics

Data collection	
Crystal	^{WT}Coa7
Wavelength (Å)	0.953654
Temperature (K)	100
Diffraction source	Australian Synchrotron (MX2)
Detector	EIGER X 16M
Space group	$I4_1$
a, b, c (Å)	100.01, 100.01, 50.34
α, β, γ (°)	90.00, 90.00, 90.00
Resolution range (Å)	44.97-2.39 (2.48-2.39)
Total No. of reflections	68093
No. of unique reflections	10025
Completeness (%)	99.7 (96.9)
Redundancy	6.8 (6.7)
$\langle I/\sigma(I)\rangle$	10.5 (1.6)
*R*merge (%)	9.3 (73.0)
*R*pim (%)	3.9 (30.1)
Refinement statistics	
Resolution range (Å)	70.72-2.39 (2.448-2.39)
No. of reflections, working set	949720
No. of reflections, test set	521
R_{work} (%)	20.52 (29.1)
R_{free} (%)	25.47 (35.9)
Rmsd bond lengths (Å)	0.010
Rmsd bond angles (°)	1.301
Ramachandron†	
Favored, %	99.1
Allowed, %	100
PDB ID code	6P15

*Values in parenthesis are for highest-resolution shell.

†Calculated using MolProbity (208).

Table S2 Hydrodynamics properties of the ^{WT}Coa7 and ^{Y137C}Coa7 proteins.

Protein	**M_r (Da)[a]**	**s (S)[b]**	**M (kDa)[c]**	***f*/*f*$_0$**
^{WT}Coa7	25649	1.9	26	1.3
		3.5	54	
^{Y137C}Coa7	25620	2.1	28	1.2
		3.5	64	

[a] Molecular mass of the proteins were determined from the protein primary sequences.

[b] Modal sedimentation coefficients were taken from the ordinate maximum of the *c(s)* distribution best fit for sedimentation velocity data generated at initial protein concentrations of 10 μM for ^{WT}Coa7, ^{Y137C}Coa7 proteins (Fig. 4E and F, respectively).

[c] Molar masses were determined from the *c(M)* distribution best fit (data not shown).

Figure S1

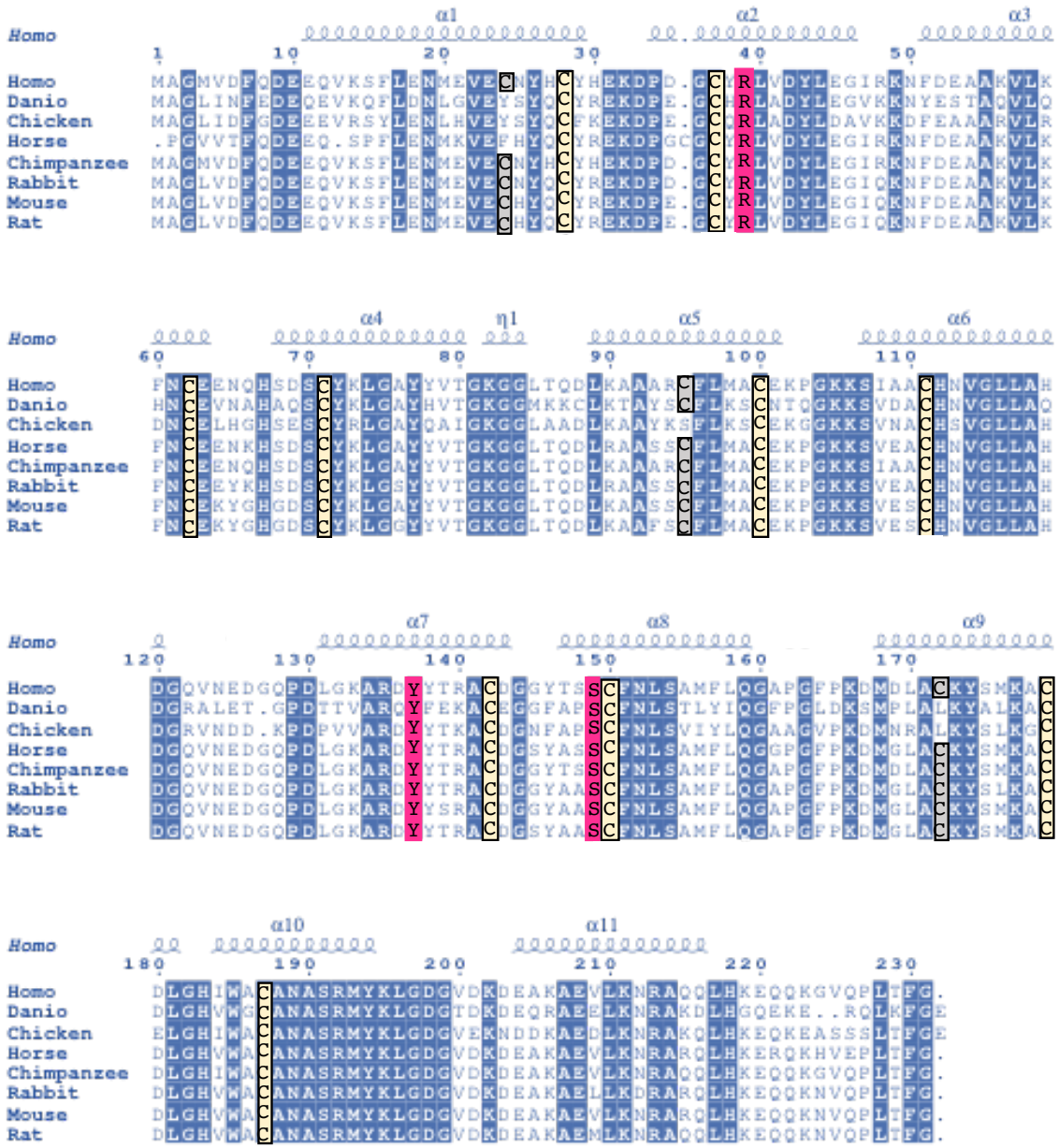

Figure S2

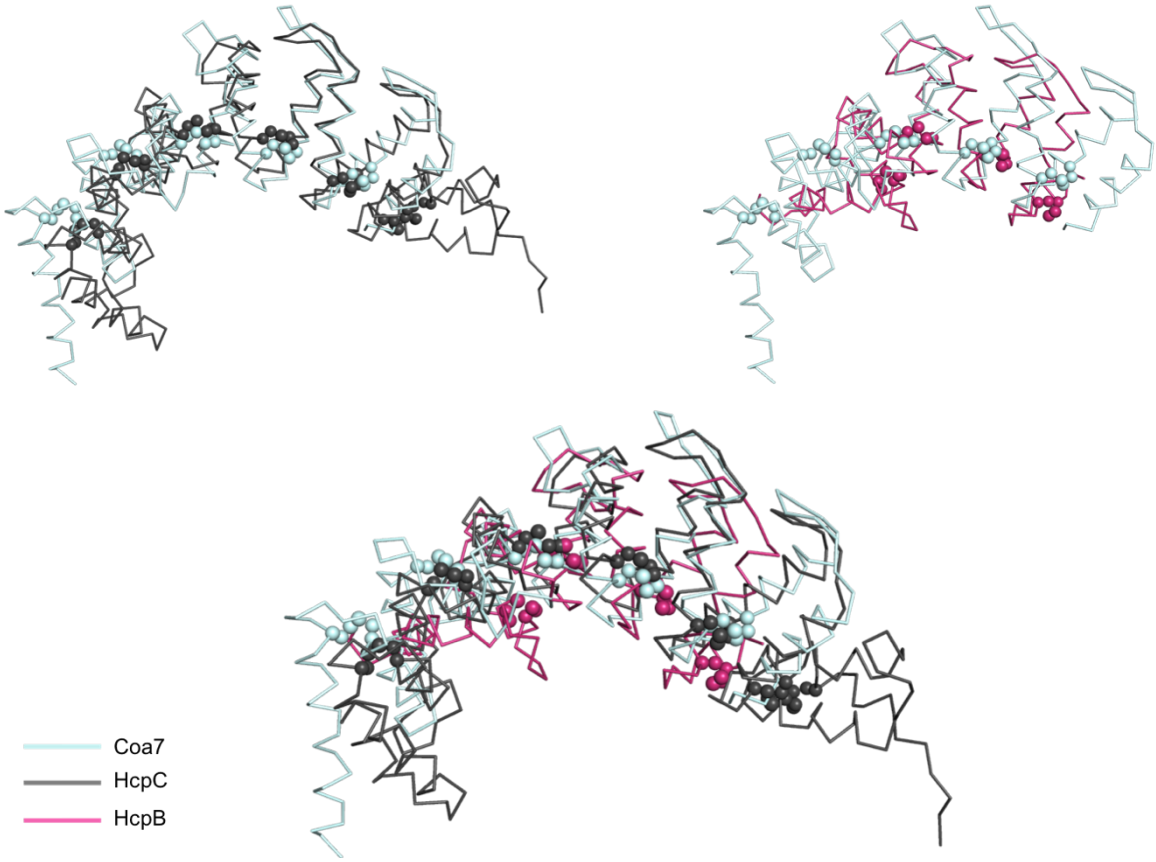

Figure S3

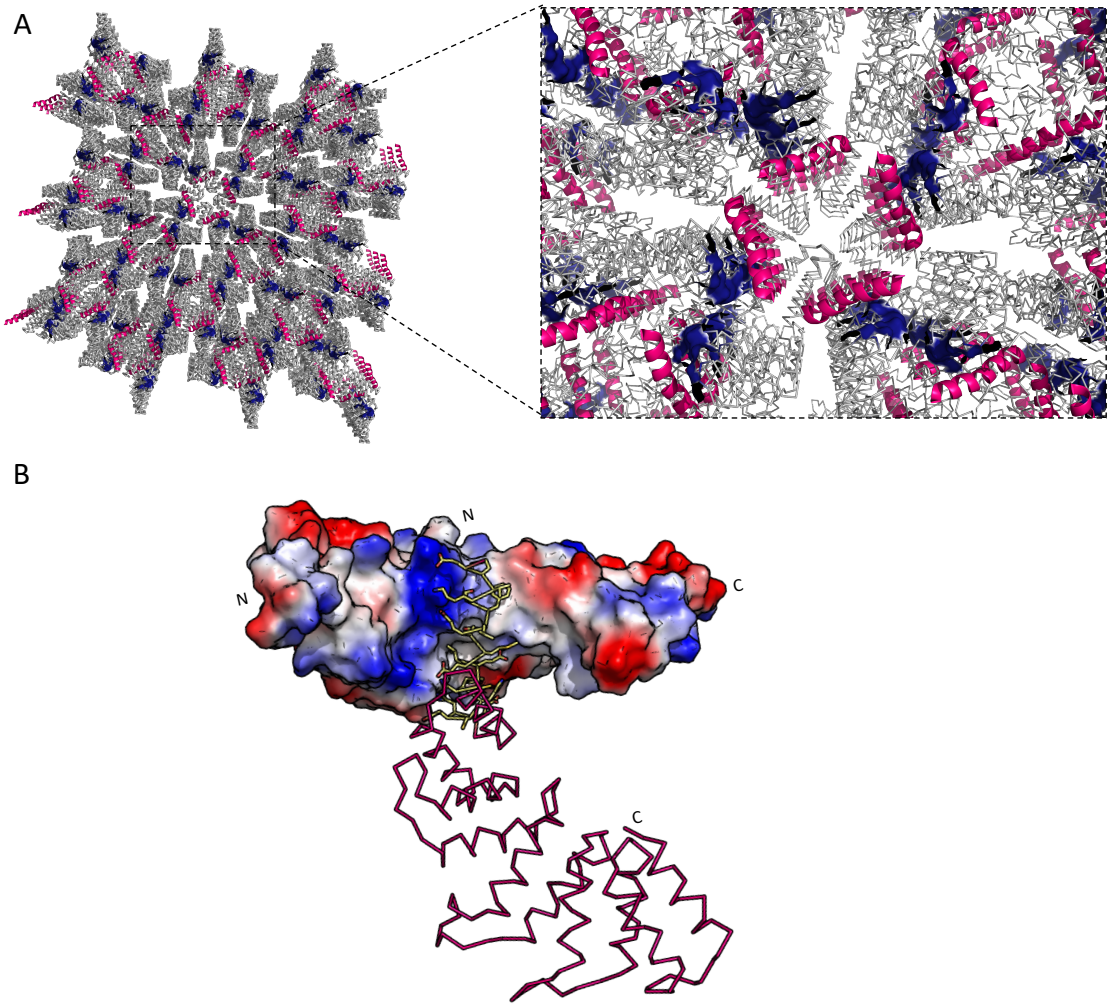

Figure S4

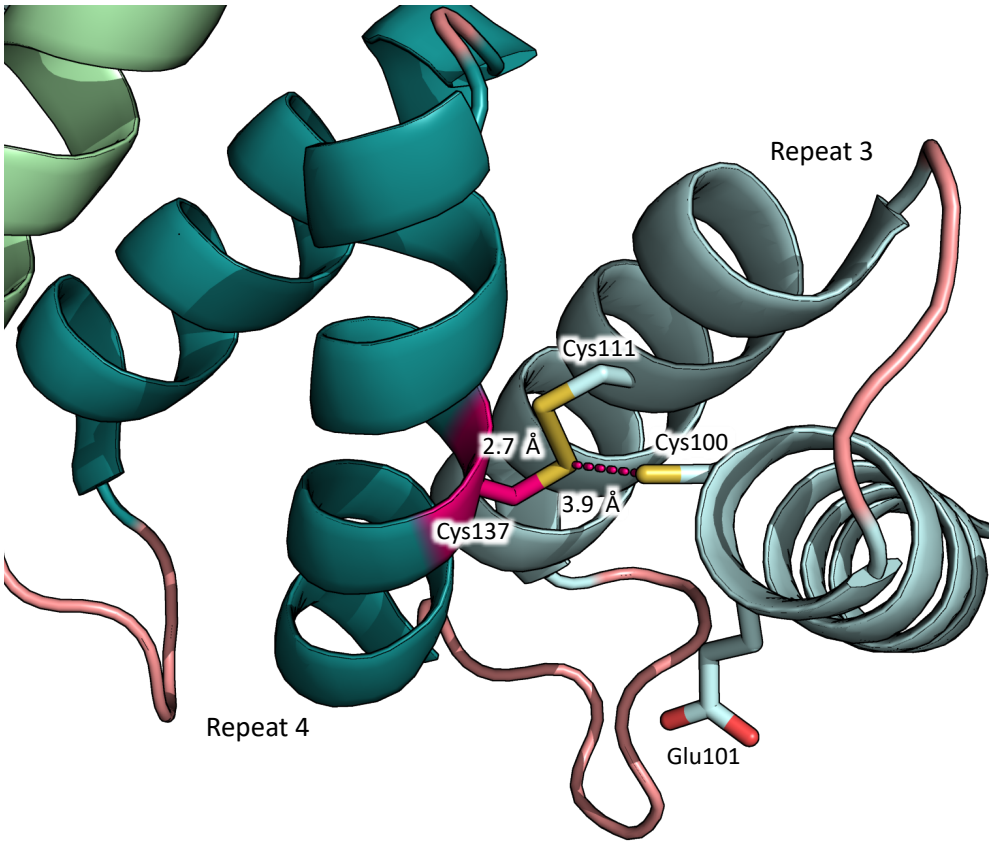

Figure S5

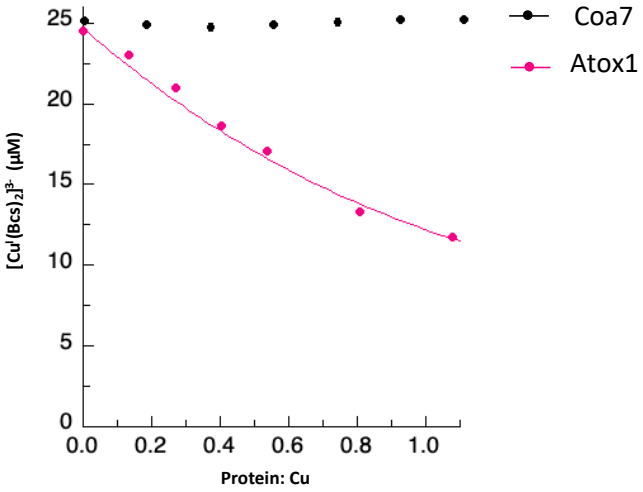
Coa7
Atox1
25
20
15
10
5
0
0.0
0.2
0.4
0.6
0.8
1.0
Protein: Cu
[Cu^I(Bcs)2]^3- (μM)

4.3 The crystallisation strategy for Coa7 structural elucidation

One of the key aims of the Chapter 4 study was to determine the crystal structure of the Coa7 protein. Extensive attempts were made in this work to crystallise ^{WT}Coa7 and ^{Y137C}Coa7 proteins. For crystallisation purposes, the ^{WT}Coa7 and ^{Y137C}Coa7 proteins were purified using two different affinity chromatography methods: 1) Glutathione affinity chromatography *via* a pGEX-6P-1 glutathione S-transferase fusion vector with an intervening PreScission Protease site for cleavage of the GST tag as described in Section 4.2. and 2) Immobilised metal affinity chromatography (IMAC) *via* a pETM-11 plasmid for the N-terminally hexahistidine-tagged proteins. Here, the details of recombinant His_6 tagged proteins production and characterisation in addition to a detailed crystallisation strategy employed for the ^{WT}Coa7 and ^{Y137C}Coa7 proteins are described.

4.3.1 Materials and Methods

4.3.1.1 Cloning, expression and purification of His_6 tagged ^{WT}Coa7 and ^{Y137C}Coa7

The DNA sequence encoding ^{WT}Coa7 and ^{Y137C}Coa7 were amplified *via* PCR using primers (GAATCTTTATTTTCAGGGCATGGCGGGTATGG and GCTCGAGTGCGGCCGTCAGCCGAAGGTCAGC; overhangs are underlined) and subcloned into pETM-11 plasmid (EMBL) with an intervening Tobacco Etch Virus (TEV) protease site for cleavage of the polyhistidine affinity tag using Gibson Assembly® Cloning Kit (New England, BioLabs).

The recombinant His_6 tagged ^{WT}Coa7 and ^{Y137C}Coa7 proteins were overexpressed in *Escherichia coli* strain SHuffle® T7 (New England, BioLabs). Cultures were grown at 30°C in Lysogeny Broth (LB) supplemented with ampicillin (100 μgml^{-1}), chloramphenicol (35 μgml^{-1}) and streptomycin (50 μgml^{-1}) to an OD_{600} of

0.8, induced with isopropyl β-D-1-thiogalactopyranoside (IPTG, 0.2 mM) and harvested after 16 hours (with shaking) at 16°C.

His_6-^{WT}Coa7 and His_6-^{Y137C}Coa7 were purified by immobilised metal affinity chromatography (IMAC) using a Ni-Sepharose™ 6 Fast Flow resin. Bacterial cell pellets were resuspended in lysis buffer (20 mM NaHepes pH 7.2, 50 mM NaCl). Cells were disrupted by passage through a TS series bench top cell disruptor (Constant Systems Ltd) at 35 kpsi. Cell debris were removed by centrifugation (Beckman JLA-25.50, 30000 g, 20 min, 4°C) and the soluble fraction was incubated with Ni-Sepharose™ 6 Fast Flow resin (GE Healthcare) equilibrated with lysis buffer. The proteins were eluted in 20 mM NaHepes pH 7.2, 50 mM NaCl, 40 mM imidazole followed by SEC (HiLoad 16/600 Superdex 75 pg, GE Healthcare; 20 mM NaHepes pH 7.2, 50 mM NaCl). The purified proteins were concentrated to 20 $mgml^{-1}$ before storage at -80°C.

4.3.2 Results

4.3.2.1 His_6-tagged protein overexpression, purification and characterisation

Recombinant His_6-^{WT}Coa7 and His_6-^{Y137C}Coa7 were overexpressed and purified by IMAC and SEC. Both the purified His_6-^{WT}Coa7 and His_6-^{Y137C}Coa7 proteins eluted from analytical SEC as split peaks with elution volumes approximating the molecular weight of a Coa7 dimer (that is, ~55 kDa; Figure 4-1*A, B*). SDS-PAGE analyses of the purified proteins under reducing and non-reducing conditions showed single bands only for the His_6-^{WT}Coa7 and His_6-^{Y137C}Coa7 proteins at ~25 kDa, approximating the calculated molecular weights of monomeric species (calculated from sequence as 27.4 kDa, including the His_6 tag) (Figure 4-1*D*). The secondary structure compositions of the His_6-^{WT}Coa7 and His_6-^{Y137C}Coa7 proteins were determined by circular dichroism (CD) spectroscopy, which yielded spectra

with minima at 222 nm and 208 nm, characteristic of α-helical structures for both proteins (Figure 4-1*C*). SV analyses of the His_6-^{WT}Coa7 and His_6-^{Y137C}Coa7 proteins yielded major peaks with sedimentation coefficients of 2.7 S for His_6-^{WT}Coa7 and 2.8 S for the His_6-^{Y137C}Coa7 protein indicating that both proteins exist predominantly as monomers in solution, at both protein concentrations tested (Figure 4-1*E, F*). For the His_6-^{Y137C}Coa7 protein, an additional species was also observed at 4.3 S for the 10 $M sample, which was not present at the same intensity for the His_6-^{WT}Coa7 protein. This may indicate the formation of higher order oligomeric or aggregate species at this concentration (Figure 4-1*F*).

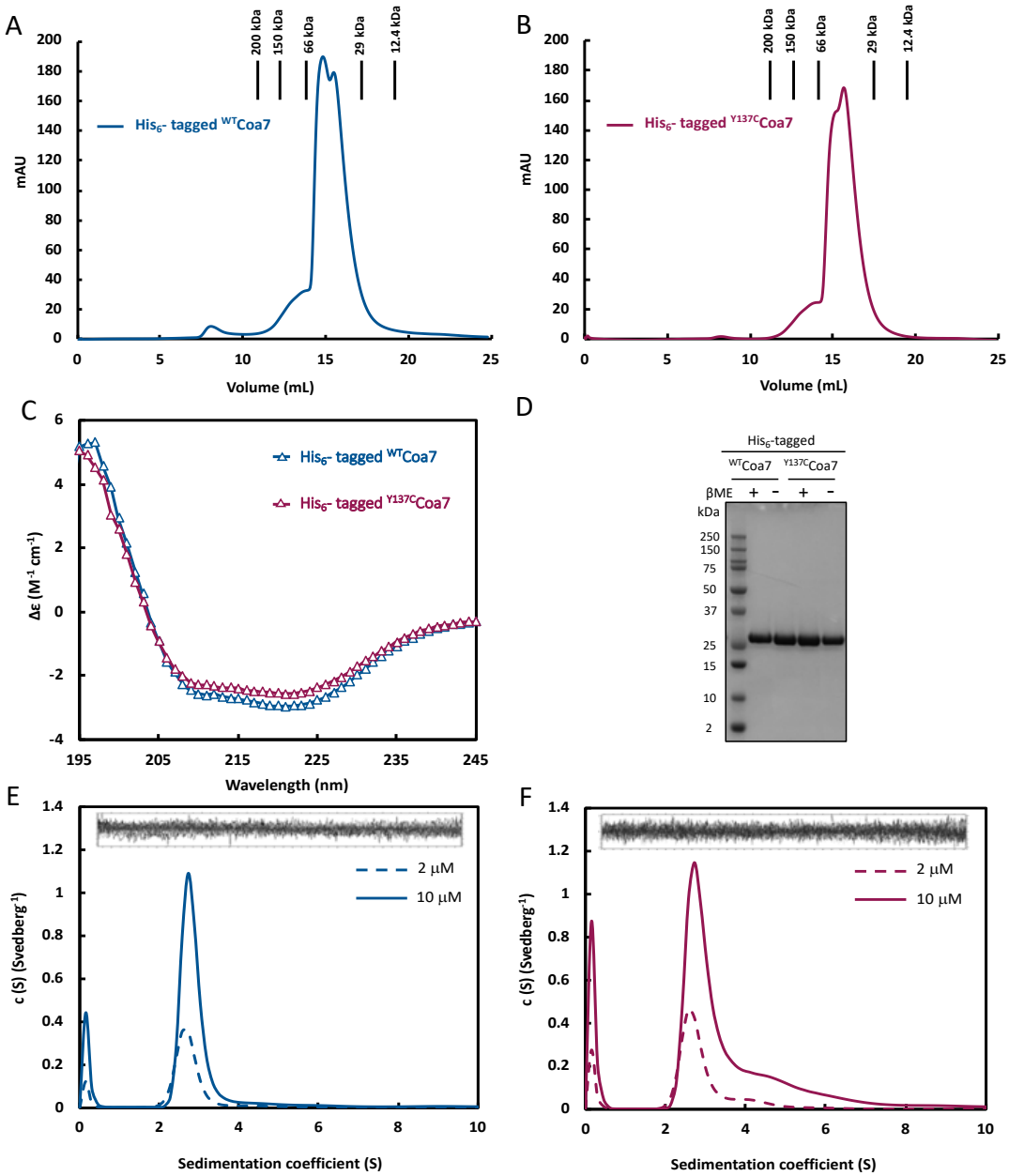

Figure 0-1 Purification and characterisation of the His$_6$-^{WT}Coa7 and His$_6$-^{Y137C}Coa7 proteins.

(A) Elution profile of purified His$_6$-^{WT}Coa7 relative to indicated protein standards analysed by SEC. (B) Elution profile of purified His$_6$-^{Y137C}Coa7 mutant relative to indicated protein standards analysed by SEC. (C) Overlay of the CD spectra of the His$_6$-^{WT}Coa7 (blue) and His$_6$-^{Y137C}Coa7 (red) proteins. The CD spectra show minima at 222 nm and 208 nm characteristic of α-helical structures. (D) Purified His$_6$-^{WT}Coa7 and His$_6$-^{Y137C}Coa7 proteins were analysed by SDS-PAGE in the presence or absence of β-mercaptoethanol (βME) as indicated. (E) Analytical ultracentrifugation sedimentation velocity analysis of the purified His$_6$-^{WT}Coa7. Sedimentation velocity continuous size [c(s)] distribution best fit for His$_6$-^{WT}Coa7 measured at protein concentrations of 2 μM (dashed lines, blue) and 10 μM (solid lines, blue). (F) Analytical ultracentrifugation sedimentation velocity analysis of the purified His$_6$-^{Y137C}Coa7. Sedimentation velocity continuous size [c(s)] distribution best fit for His$_6$-^{Y137C}Coa7 measured at protein concentrations of 2 μM (dashed lines, red) and 10 μM (solid lines, red). SEC; size-exclusion chromatography.

4.3.3 Approach to screening and optimisation of the ^{WT}Coa7 crystals

Crystallisation trials were conducted using a commercially available screen, Index™ (Hampton Research), by sitting drop vapor diffusion in 96-well plates (Molecular Dimensions). Conditions for crystallisation of the ^{WT}Coa7 protein were initially screened at two different protein concentrations (10 and 20 mgml^{-1}), with crystallisation drops consisting of equal volumes (0.2 $L) of reservoir and protein solutions. Drops were dispensed using a Crystal Gryphon Liquid Handling System (Art Robbins Instruments) and were equilibrated against a reservoir of screen solution (50 $L). Plates were incubated at 20°C. However, heavy precipitates were observed in most of the drops that contained polyethylene glycol (PEG) as the precipitant.

A pre-crystallisation test (Hampton Research) was performed using crystallisation conditions that contained either ammonium sulfate or PEG as the precipitant (Table 4.1). Interestingly, drops containing PEG (A2 and B2 conditions, 0.1 M Tris hydrochloride pH 8.5, 2.0 M magnesium chloride hexahydrate, 30% w/v PEG 4,000 and 0.1 M Tris hydrochloride pH 8.5, 0.2 M Magnesium chloride hexahydrate, 15% w/v Polyethylene glycol 4,000, respectively) heavily precipitated after 5 minutes implying that conditions containing PEG should be avoided for Coa7 crystallisation. On the other hand, light precipitates were observed in drops containing ammonium sulfate (A1 and B1 conditions, 0.1 M Tris hydrochloride pH 8.5, 2.0 M ammonium sulfate and 0.1 M Tris hydrochloride pH 8.5, 1.0 M ammonium sulfate, respectively) indicating salt as a precipitant can be a better choice for Coa7 crystallisation.

Table 0-1 Pre-crystallisation conditions for the ^{WT}Coa7 crystallisation.

Buffer	Condition
Buffer A1	0.1 M Tris hydrochloride pH 8.5, 2.0 M ammonium sulfate
Buffer B1	0.1 M Tris hydrochloride pH 8.5, 1.0 M ammonium sulfate
Buffer A2	0.1 M Tris hydrochloride pH 8.5, 2.0 M magnesium chloride hexahydrate, 30% w/v PEG 4,000
Buffer B2	0.1 M Tris hydrochloride pH 8.5, 0.2 M magnesium chloride hexahydrate, 15% w/v PEG 4,000

Initial high-throughput crystallisation experiments were therefore carried out at the CSIRO Collaborative Crystallisation Centre (http://www.csiro.au/C3), Melbourne, Australia using c3 salty screens (c3_5 and c3_6) which primarily include ammonium sulfate as a precipitant. Sitting drop vapour diffusion experiments were established in 96-well plates with the purified ^{WT}Coa7 (20 and 40 mgml^{-1}), ^{Y137C}Coa7 (8 and 16 mgml^{-1}), Heme-loaded ^{WT}Coa7 (10 and 20 mgml^{-1}) (as describes in Section 4.2), His$_6$-^{WT}Coa7 (10 and 20 mgml^{-1}) and His$_6$-^{Y137C}Coa7 (15 and 30 mgml^{-1}) proteins (Section 4.3.2). All the purified proteins were in 20 mM NaHepes pH 7.5, 50 mM NaCl buffer. Despite extensive attempts, crystals were observed for the ^{WT}Coa7 and ^{Y137C}Coa7 proteins only.

4.3.3.1 Crystallisation of the ^{WT}Coa7 protein

Several tiny star-like crystals of ^{WT}Coa7 (Figure 4-2*A, B*) were observed in crystallisation drops consisting of equal volumes (0.2 $L) of reservoir and protein solutions within 2 days in conditions D8 and E9 of the c3_5 screen (Table 4.2).

Table 0-2 Crystallisation conditions for the ^{WT}Coa7 protein identified by crystallisation trials with the c3_5 screen.

Screen number	Condition
c3_5 D8	0.1 M ADA pH 6.5, 2.0 M ammonium sulfate, 10% (v/v) ethanol
c3_5 E9	0.05 M sodium MES pH 6.5, 2.5 M ammonium sulfate, 6% (v/v) ethanol

Optimisation of these conditions was carried out by hanging drop vapour diffusion in 24-well VDX plates (Hampton Research) by varying the sodium MES concentration (from 0.05-0.30 M), the pH (from 6.0-7.0), the ammonium sulfate concentration (from 1.5-2.8 M) and the ethanol concentration (from 4-12% v/v). These thin star-like crystals were typically ~20 μm x 2 μm x 2 μm. Further optimisation yielded crystals of ~50 μm x 5 μm x 5 μm in 0.25 M sodium MES pH 6.6, 2.4 M ammonium sulfate, 10% (v/v) ethanol condition. These crystals were cryoprotected in reservoir solution containing 25% (v/v) glycerol before flash-cooling in liquid nitrogen. Diffraction data were recorded on an EIGER X 16M detector at the Australian Synchrotron on beamline MX2 at a wavelength of 0.954 Å. However, the best diffracting star-like ^{WT}Coa7 crystal showed diffraction to approximately 7 Å resolution only.

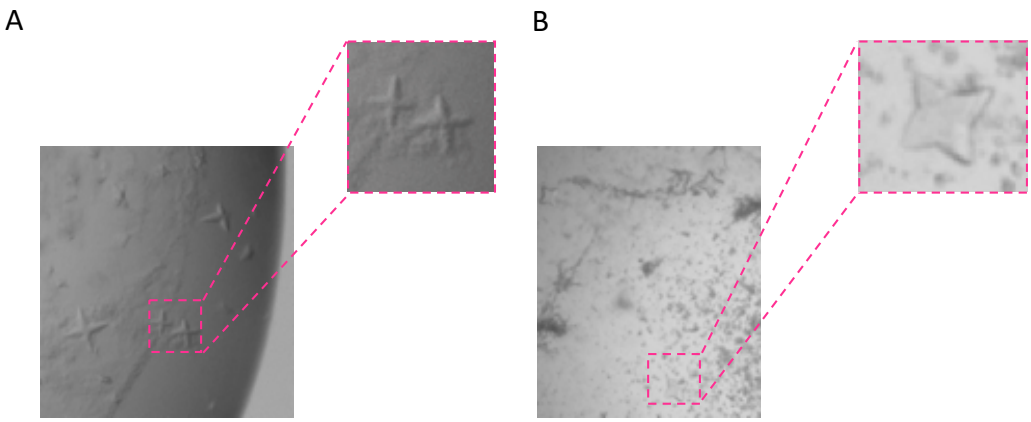

Figure 0-2 Crystals of the ^{WT}Coa7 protein from the c3-5 screen.

(A) Star-like crystals (< 20 µm) from the initial crystallisation screen in c3-5 condition D8 (0.1 M ADA pH 6.5, 2.0 M ammonium sulfate, 10% (v/v) ethanol). (B) Star-like crystals (< 20 µm) from the initial crystallisation screen in c3-5 condition E9 (0.05 M sodium MES pH 6.5, 2.5 M ammonium sulfate, 6% (v/v) ethanol).

4.3.3.2 Additive screening for optimisation of the ^{WT}Coa7 crystals

An Additive Screen™ (Hampton Research) carried out in order to improve the size and change the morphology of the ^{WT}Coa7 crystals with a view to improving the diffraction quality. An initial additive screening was performed at the CSIRO Collaborative Crystallisation Centre (http://www.csiro.au/C3), Melbourne, Australia using Additive Screen™ (Hampton Research) by sitting drop vapour diffusion in 96-well plates using ^{WT}Coa7 (20 and 40 mgml^{-1}) samples and 0.25 M sodium MES pH 6.6, 2.4 M ammonium sulfate, 10% (v/v) ethanol condition as a reservoir. Small plate-like crystals (25 µm x 5 µm x 5 µm) were observed after 5 days in a condition containing 4% (v/v) pentaerythritol ethoxylate (3/4 EO/OH) (Figure 4-3*A*). Further optimisations were carried out by hanging drop vapour diffusion in 24-well VDX plates by the addition of the pentaerythritol ethoxylate (3/4 EO/OH) (from 4-6% v/v) to the crystallisation conditions. Diffraction-quality plate-like crystals of ^{WT}Coa7 grew overnight to a maximum size of 250 µm x 50 µm x 50 µm at 20°C from drops containing equal volumes (1 µL) of

^{WT}Coa7 (20 mgml^{-1} in 20 mM NaHepes, pH 7.2, 50 mM NaCl) and crystallisation solution (0.23 M sodium MES pH 6.72, 2.35 M ammonium sulfate, 8.2% (v/v) ethanol and 4.5% (v/v) pentaerythritol ethoxylate (3/4 EO/OH)) equilibrated against 500 µL reservoir solution (Figure 4-3*B*). ^{WT}Coa7 crystals were cryoprotected in reservoir solution containing 25% (v/v) glycerol before flash-cooling in liquid nitrogen. The diffraction properties of approximately 60 crystals were tested at the Australian Synchrotron on beamline MX2, with only one ^{WT}Coa7 crystal yielding diffraction data to 2.4 Å resolution. The data collection and refinement statistics of this ^{WT}Coa7 crystal are detailed in Table S1, Section 4.2.

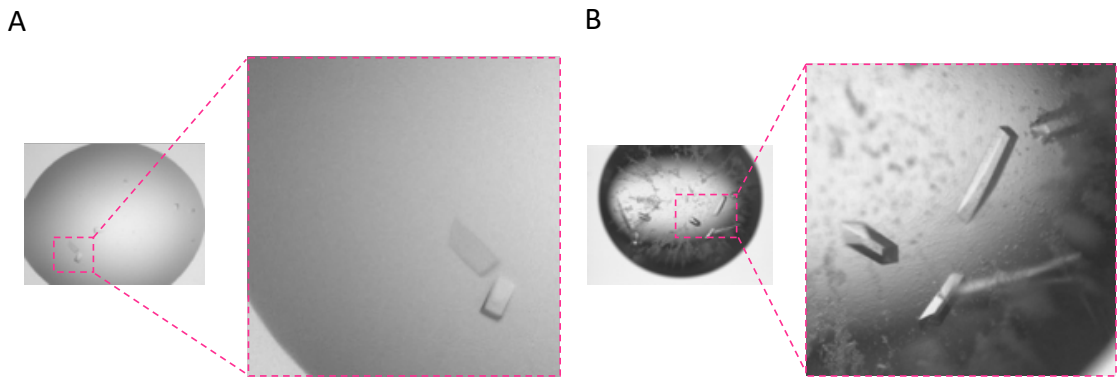

Figure 0-3 Crystals from additive screening of the ^{WT}Coa7 protein.

(A) ^{WT}Coa7 crystals from the initial additive screening in 0.25 M sodium MES pH 6.6, 2.4 M ammonium sulfate, 10% (v/v) ethanol and 4% (v/v) pentaerythritol ethoxylate (3/4 EO/OH). (B) ^{WT}Coa7 Crystals from the optimisation of additive screen in 0.23 M sodium MES pH 6.72, 2.35 M ammonium sulfate, 8.2% (v/v) ethanol and 4.5% (v/v) pentaerythritol ethoxylate (3/4 EO/OH).

4.3.4 Approach to screening and optimisation of the ^{Y137C}Coa7 crystals

Using the c3_5 screen, a few plate-like crystals (~60 µm x 20 µm x 20 µm) of ^{Y137C}Coa7 were observed in a condition containing 0.1 M sodium MES pH 6.5, 1.6 M ammonium sulfate and 10% (v/v) dioxane (Condition C4) after 5 days

(Figure 4-4*A*). Further optimisation experiments were carried out by hanging drop vapour diffusion in 24-well VDX plates by varying the sodium MES concentration (from 0.05-0.20 M), the pH (from 6.0-7.0), the ammonium sulfate concentration (from 1.0-2.5 M) and the dioxane concentration (from 5-14% v/v). ^{Y137C}Coa7 crystals grew after 10 days to a maximum size of 180 µm x 20 µm x 20 µm at 20°C from drops containing equal volumes (1 µL) of ^{Y137C}Coa7 (10 mgml^{-1} in 20 mM NaHepes pH 7.2, 50 mM NaCl) and crystallisation solution (0.17 M sodium MES pH 6.2, 1.8 M ammonium sulfate and 9.5% (v/v) dioxane) equilibrated against 500 µL reservoir solution (Figure 4-4*B*).

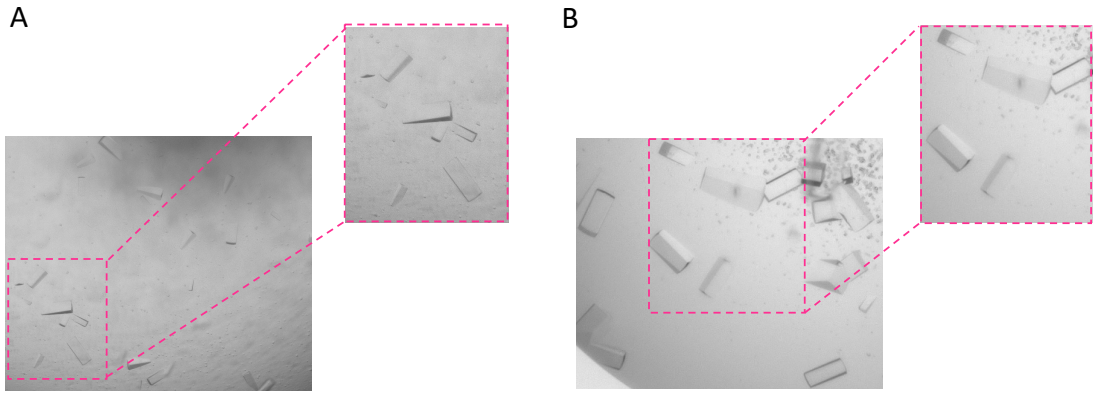

Figure 0-4 Crystals of the ^{Y137C}Coa7 protein from the c3-5 screen.

(A) Plate-like crystals (~60 µm) from the initial crystallisation screen in c3-5 condition 0.1 M sodium MES pH 6.5, 1.6 M ammonium sulfate and 10% (v/v) dioxane (C4). (B) ^{Y137C}Coa7crystals (~180 µm) from the crystallisation optimisation experiments in 0.17 M sodium MES pH 6.2, 1.8 M ammonium sulfate and 9.5% (v/v) dioxane.

The best diffracting ^{Y137C}Coa7 crystal showed diffraction to 3.7 Å resolution. The diffraction data from this crystal indexed in space group *P*4 with unit cell dimensions of a = 97.67, b= 97.67, c = 65.11 Å. Diffraction data were recorded on an EIGER X 16M detector at the Australian Synchrotron on beamline MX2 at a wavelength of 0.954 Å at 100 K and were processed with XDS (236) and merged and scaled with AIMLESS (237). Data collection statistics are detailed in Table 4.3. Despite extensive attempts, we were unable to solve the crystal structure of the

^{Y137C}Coa7 by molecular replacement using the crystal structure of ^{WT}Coa7 as a search model due to the poor quality of the data set. Additional optimisation of the condition and additive screening of the ^{Y137C}Coa7 were not undertaken due to the time constraints.

Table 0-3 Data collection and processing.

Values for the outer shell are given in parentheses.

Diffraction source	Australian Synchrotron (MX2)
Wavelength (Å)	0.953654
Temperature (K)	100
Detector	EIGER X 16M
Crystal-detector distance (mm)	150
Total rotation range (°)	180
Space group	*P*4
a, *b*, *c* (Å)	97.67, 97.67, 65.11
α, β, γ (°)	90.0, 90.0, 90.0
Mosaicity (°)	0.04
Resolution range (Å)	48.83-3.70 (4.05-3.70)
Total No. of reflections	18236 (4329)
No. of unique reflections	6430 (1562)
Completeness (%)	95.8 (96.8)
Redundancy	2.7 (2.8)
$\langle I/\sigma(I)\rangle$	4.7 (0.5)
CC(1/2)	0.996 (0.449)
*R*merge	0.094 (1.796)

Chapter 5

Concluding Remarks and Future Directions

5.1 Summary of the findings from Chapter 2 (hGrx1)

Although copper acts as an essential cofactor in a wide range of biological processes, excess intracellular copper is toxic due to its intrinsic redox activity which leads to cellular oxidative damage (8, 9). In humans, copper deficiency and copper toxicity lead to disorders such as Menkes and Wilson diseases, respectively (21-26). Once Cu(I) enters the cell *via* Ctr1, the Cu(I)-metallochaperone Atox1 delivers Cu(I) to the secretory pathway where Cu(I)-ATPases (ATP7A and ATP7B) located in TGN are the primary Cu(I) acceptors. Recent studies have shown that hGrx1, a cytosolic thiol disulfide oxidoreductase, can also play a role in intracellular Cu(I) delivery where it exchanges copper with Atox1 and the metal binding domains of the Cu(I)-ATPases and therefore protects neuronal cells from Cu(I) toxicity (46-48).

Until recently, investigations to define the driving force for directional Cu(I)-protein exchange have been proposed to be Cu(I)-binding affinity gradients. In this way metabolites like GSH ($K_D = 9 \times 10^{-12}$ M) (4) readily exchanges Cu(I) with Cu(I)-metallochaperones (with K_D values in the range 10^{-15}-10^{-17} M) (32, 61) due to its weaker Cu(I)-binding affinity. Discussions of directionality have been dominated by studies of K_D's toward Cu(I), but the affinity and productivity of critical protein-protein interactions have been virtually ignored.

Our aim in Chapter 2 was to structurally and functionally characterise the hGrx1 protein and its interactions with Atox1 and WLN5-6 (metal binding domains 5 and 6 of ATP7B) proteins in order to understand the mechanism of copper exchange between these proteins and also to determine the thermodynamic factors that underpin these copper exchanges.

In this study, hGrx1 was found to bind Cu(I) with a Cu:protein stoichiometry of 1:1, indicating the presence of a single Cu(I) binding site per molecule of hGrx1. Using NMR, we established that hGrx1 binds Cu(I) *via* coordination to two cysteine residues at a C23-x-x-C26 site. This entirely agrees with previous mutagenesis studies (32).

The SEC-ICP-MS data and NMR experiments revealed that Cu(I)-hGrx1 transfers Cu(I) to *apo* partner proteins Atox1 and WLN5-6. Importantly, *apo*-hGrx1 can also interact with these proteins in both the presence and absence of Cu(I). This indicates that protein interactions between hGrx1 and Atox1 and WLN5-6 are not Cu(I) dependent. Intriguingly, hGrx1 shares a common interaction site for the Atox1 and WLN5-6 proteins which is proximate to the C23-x-x-C26 motif.

Although *apo*-Atox1 and *apo*-WLN5-6 exhibit similar Cu(I)-binding affinities ($10^{-17.5}$ M and $10^{-17.8}$ M, respectively), our SEC-ICP-MS data revealed that in a mixture of the Cu(I)-hGrx1 and *apo* partner proteins (*apo*-Atox1 and *apo*-WLN5-6 proteins), Cu(I) was predominantly transferred to the WLN5-6 protein. This can be explained by the thermodynamics of the interactions between the protein pairs coupled with individual protein Cu(I) binding affinities. Although both Atox1 and WLN5-6 interact with hGrx1 through the same interface, hGrx1 protein interacts with a higher affinity to WLN5-6 domains than with Atox1 and the binding affinity of WLN5-6 for Cu(I) is also higher. Crucially, this specifies that hGrx1 can deliver Cu(I) to WLN5-6 protein even in the presence of Atox1, which suggests that hGrx1 might be an alternative Cu(I)-metallochaperone for Cu(I) delivery to the secretory pathway. Taken together, thermodynamics of the interactions between the protein pairs coupled with affinities for Cu(I) binding are the main factors in the Cu(I) delivery and therefore intracellular copper trafficking process.

Despite extensive attempts, we were unable to crystallise hGrx1 either as *apo*-protein or in the Cu(I)-bound state. The atomic details of the Cu(I) site structure, therefore, await future investigation. However, we successfully solved the structure of reduced Grx1 from yeast *Saccharomyces cerevisiae* (yGrx1) to 1.22 Å resolution. A comparison of the structure of reduced yGrx1 with those of the oxidised and glutathionylated proteins revealed differences in the conformations of residues neighbouring the Cys27-Cys30 active site, which accompany alterations in the redox status of the protein.

When the research described in Chapter 2 commenced, Atox1 was known as the sole Cu(I)-metallochaperone for Cu(I) delivery to the secretory pathway. However, based on our findings, we propose that hGrx1 can be an alternative Cu(I)-metallochaperone which is able to transfer Cu(I) to WLN5-6 even in the presence of Atox1. It has been shown that Cu(I) trafficking to the Cu(I)-ATPases can occur even in the absence of Atox1 suggesting that other proteins also show metallochaperone activities (167). Our data suggest that hGrx1 may be a potential candidate for replacing Atox1 function in the absence of this protein.

5.1.1 Closing remarks on the hGrx1 protein

Although this work has shown that hGrx1 is able to deliver Cu(I) to Atox1 and WLN5-6 proteins, it would be of interest to examine the role of hGrx1 in the context of other Cu(I) binding proteins. For instance, does hGrx1 interact with, transfer Cu(I) to, or receive Cu(I) from any of other metal binding domains (MBDs 1-4) of ATP7B or even the full-length ATPases? Does hGrx1 interact with Ctr1, particularly the C-terminal domain? This would reveal whether hGrx1 essentially acts as a transitional mediator of Cu(I) exchange between many other proteins or as an independent trafficking bridge only between the Atox1 and ATP7B proteins. Similarly, the studies on hGrx1 could be extended to determine whether this

protein plays a role in trafficking to other organelles including the mitochondria. To reveal whether hGrx1 plays a role in mitochondrial copper trafficking, it would be worth determining whether hGrx1 interacts and exchanges copper with the mitochondrial Cu(I)-metallochaperone Cox17? Also, to probe the effect of deletion of hGrx1 in $GRX1^{KO}$ cells to determine if it affects the COX assembly? Similar SEC-ICP-MS and NMR experiments can be used to answer some of these questions. Further attempts should be made to determine the crystal structure of Cu(I)-loaded hGrx1 and its potential complexes with other partner proteins. This approach would enhance our insight toward the molecular mechanisms of the copper trafficking pathway.

5.2 Summary of the findings from Chapter 3 (Coa6)

Copper plays an essential role in the biogenesis of COX, the terminal complex of the electron transport chain, where it is incorporated into the dinuclear Cu_A and mononuclear Cu_B sites. The mechanisms for Cu(I) entry into mitochondria remain undetermined. However, it is known that COX assembly factors such as Cox17 and Sco1/Sco2 are actively involved in the process of Cu(I) delivery to Cu_A site (40, 128, 129). Once Cox17 receives Cu(I) in the IMS it transfers the metal to the Sco proteins for copper delivery to the Cu_A site. Coa6 (cytochrome *c* oxidase assembly factor) is an IMS located protein which binds Cu(I) with K_D ~10^{-17} M (43). W59C mutation in Coa6 were identified in a patient suffering from hypertrophic obstructive cardiomyopathy, resulting in a COX defect in the heart tissue (136). It has been reported that Coa6 interacts with Sco proteins and therefore may be involved in the Cu(I) delivery to Cu_A site (43, 135). However, the precise role of Coa6 in the mitochondrial Cu(I) delivery remains uncertain.

The aim of Chapter 3 was to structurally and functionally characterise the ^{WT}Coa6 and ^{W59C}Coa6 proteins and the potential role of this protein in the biogenesis of COX in addition to the molecular origin of the pathogenesis for the W59C mutation.

In this study, we crystallised and determined the crystal structures of the human ^{WT}Coa6 and ^{W59C}Coa6 proteins by X-ray crystallography to 1.6 and 2.2 Å resolution, respectively. The ^{WT}Coa6 structure was a dimer with two monomers of ^{WT}Coa6 per asu. Each monomer adopts a CHCH fold owing to its CX_9C–$CX_{10}C$ sequence motif, which is similar to those of twin CX_9C motif proteins, including Cox17 (122). Cysteine residues (at positions 58, 68, 79 and 90) in the CX_9C–$CX_{10}C$ motif form two intramolecular disulfide bonds per monomer and tether the first two helices at each end of the helical pair. Using mutagenesis studies, together with copper binding assays, we found that the $^{C68S/C79S}$Coa6 mutant gave a measured $K_{D(Cu(I))} \sim 10^{-16}$ M, which is ~10 fold weaker than that determined for the ^{WT}Coa6 protein ($K_{D(Cu(I))} \sim 10^{-17}$ M) (43). However, the $^{C58S/C90S}$Coa6 variant exhibited no Cu(I) binding indicating that the copper binding site of ^{WT}Coa6 is located between residues Cys58 and Cys90.

The pathogenic mutant ^{W59C}Coa6 structure showed a non-covalent dimer of disulfide bridged dimers (a dimer of dimers) where in the crystal every molecule of ^{W59C}Coa6 interacts with two others – one through non-covalent contacts along helix α_3 (as observed for ^{WT}Coa6) and the other through a disulfide bond between residue Cys59 on each molecule as a result of the mutation. A previous study by our laboratory reported that the Cu(I)-binding activity of the ^{W59C}Coa6 was preserved (43). Accordingly, the ^{W59C}Coa6 structure revealed that the Cys58/Cys90 copper binding site was not altered by the W59C mutation. This

suggests that the COX defect that results from this mutation does not originate from a loss of Cu(I) binding activity.

5.2.1 Closing remarks on the Coa6 protein

Although this work has clearly contributed to the interpretation of the role of Coa6 in COX biogenesis from a structural aspect, the question remains as to the specific function of Coa6 in COX assembly. Further studies are required to investigate whether Coa6 can directly deliver Cu(I) to the Cu_A site of the COX2 subunit? Or, does it act as an oxidoreductase to facilitate Cu(I) binding between Cys residues at the Cu_A site? It is also possible that Coa6 facilitates the activities of other proteins in the mitochondrial copper trafficking pathway such as Sco1 and Sco2 proteins. It would also be interesting to find out whether copper bound Coa6 acts as a thiol reductase for Sco proteins to reduce their Cys residues for copper binding or whether it acts as a metallochaperone and delivers copper to these proteins.

5.3 Summary of the findings from Chapter 4 (Coa7)

More than 30 assembly factors play significant roles in the biogenesis of COX through the regulation of its stability, activity, and the incorporation of essential cofactors. Coa7 is a soluble cysteine-rich protein, which is located in the mitochondrial IMS (138, 140). Pathogenic mutations in Coa7 cause Complex I and COX defects leading to mitochondrial disease (138, 139).

Despite the importance of COX assembly in health and mitochondrial disease, we have only a limited understanding of the molecular basis of this oxidase owing to a lack of knowledge about identities, structures and role of all the crucial COX assembly factors. Our aim in Chapter 4 was to structurally and functionally

characterise the Coa7 protein and to investigate whether Coa7 functions in co-factor incorporation into COX.

This study revealed that deletion of Coa7 resulted in a significant COX assembly defect and modest decreases in Complexes I and II in $COA7^{KO}$ cell lines. Crucially, the absence of Coa7 caused specific defects in the maturation of the COX2, resulting in its degradation and therefore inhibition of COX assembly. In this study, we presented the crystal structure of the human ^{WT}Coa7 protein which is composed of five Sel1-like α/α repeats. The overall fold of ^{WT}Coa7 is similar to that of bacterial Hcp proteins which are composed of disulfide-bridged α/α repeats (218, 219). This feature renders Coa7 the first human SLR protein to be revealed as possessing disulfide-bridged α/α repeats.

TPRs and SLRs are often involved in protein-protein interactions due to their significant solvent accessible surfaces (209-212). It has been reported that the concave surface which is a feature of TPR and SLR structures is the potential site of ligand binding (212, 221, 234). Interestingly, in the Coa7 structure reported here, a hydrophobic pocket on the concave surface of the protein structure was observed to participate in hydrogen bonding and electrostatic interactions with the N-terminal helix of a neighbouring molecule. This suggests a potential role for this concave surface in mediating protein-protein interactions or ligand binding.

From our heme binding experiments and co-purification of Coa7 with heme, we showed that both the ^{WT}Coa7 and ^{Y137C}Coa7 proteins bind heme with micromolar affinities. This suggests that a potential ligand for Coa7 could be heme. However, the precise position of the heme observed binding site remains undefined. Histidine and tyrosine residues are commonly present in protein heme binding sites, where they provide axial coordination to the bound heme iron atom.

Examples include the human heme oxygenase-1 and -2 (HO-1; PDB code 1N45 and H2-O; PDB code 2QPP, respectively) (230, 231) and human serum albumin (PDB code 1N5U) (232). Interestingly, ^{WT}Coa7 residues Tyr72, His112, Tyr138 and Tyr146 are located in close proximity to the concave surface and therefore represent potential candidates for mediating heme binding to this protein. However, no heme binding proteins have yet been characterised that adopt folds that feature disulfide-bridged α/α repeats. The HusA protein from *Porphyromonas gingivalis* with four TPR α/α repeats and no disulfide bonds showed iron-independent heme (that is, porphyrin) binding (229). Despite the presence of the α/α repeats, the HusA structure shows little similarity to that of Coa7 structure. Unbiased docking studies using the HusA solution structure identified a single heme/porphyrin binding groove bounded predominantly by hydrophobic residues.

5.3.1 Closing remarks on the Coa7 protein

Although our *in vitro* experiments with recombinant ^{WT}Coa7 and ^{Y137C}Coa7 proteins demonstrated that these proteins bind heme, *in vivo* heme binding experiments have yet to be established for the endogenous mitochondrial proteins. The heme binding ability of Coa7 proposes that this protein might act in the mitochondrial heme synthesis and/or delivery processes, however, the precise role of Coa7 in this process remains to be explored. It will be interesting to determine, if Coa7 binds heme *in vivo*, in which step of heme synthesis and/or delivery processes it plays a role? Does it act as a heme chaperone? Does it deliver heme *a* or heme a_3 to COX1 subunit? Or, does it transfer heme to other heme binding proteins such as Surf1? Future structural characterisation of the heme bound Coa7, NMR titrations and mutagenesis approaches will assist to investigate the heme binding site of this protein. Biophysical characterisation using

isothermal titration calorimetry (ITC) and surface plasmon resonance (SPR) techniques can be carried out to measure K_D values toward heme and porphyrin. Advanced spectroscopy techniques can be used to monitor the heme binding and also heme transfer between Coa7 and other proteins.

5.4 Afterword

At the beginning of this thesis, Cu was introduced as an essential nutrient for human health yet also potentially toxic with its imbalance causing disease. Cells require sophisticated mechanisms to mitigate this challenge and tightly regulate the acquisition, trafficking and storage of Cu such that the metal ion is rarely found in its free form in the cell (4, 12). The work described in this thesis was undertaken to further our understanding of human cellular Cu handling pathways and in particular how protein systems contribute to copper trafficking toward two distinct destinations; the *trans*-Golgi network and within the mitochondria.

At the outset of this study (Chapter 2), Atox1 had been firmly established as an unique Cu(I) metallochaperone for Cu(I) delivery to the secretory pathway where this protein delivers Cu(I) to the MBDs of the ATP7A and ATP7B transporters (62-64). However, the work of this thesis led to a crucial finding with regard to this system: that the human Glutaredoxin-1 (hGrx1) delivers Cu(I) to the metallochaperone Atox1 and the MBDs of ATP7B (WLN5-6). This suggests that hGrx1 could be as a potential Cu(I)-metallochaperone that acts under cellular conditions where the activity of Atox1 in Cu regulation is attenuated.

Since Cu plays an essential role in the biogenesis of COX, the remainder of this thesis examined two mitochondrial COX assembly factors: Coa6 and Coa7. Patients with mutations in these proteins suffer from mitochondrial COX deficiency. Upon commencement of the work described in Paper II (Chapter 3), little was known about the structure or copper binding site of Coa6. Earlier studies have demonstrated that Coa6 binds Cu(I) and interacts with Sco proteins: therefore the hypothesis that Coa6 may be involved in the Cu(I) delivery to Cu_A site of COX2 (43, 135) was proposed. The crystal structures of Coa6 determined as part of this work revealed the overall structure of the wild-type protein in addition to the molecular origin of the pathogenesis for the W59C mutation. During the course of this research, despite extensive attempts, structures with Cu(I) bound were not determined. This may have been due to the redox activity of Cu ions and the thiolate groups of the cysteine residues or the possibility that the Cu(I)-bound protein does not form crystals.

When the work described in Chapter 4 commenced, we knew only that Coa7 is a soluble cysteine-rich protein, which is located in the mitochondrial IMS and that mutations to Coa7 that cause COX assembly defects leading to mitochondrial disease had been identified (138, 139). The fact that Coa7 mutations result in COX assembly defects (similar to Coa6 mutations) and also the observation of the presence of multiple Cys residues within the Coa7 sequence, led us to investigate whether Coa7 binds Cu and functions in Cu incorporation into COX. Surprisingly, Cu(I)-binding to the ^{WT}Coa7 was not detected. This revealed that not all the proteins containing CXnC motif are able to bind Cu(I).

However, the Co-immunoprecipitation experiments revealed that Coa7 interacts with the CPOX enzyme, which is involved in the heme biosynthesis pathway and intriguingly Coa7 exhibited heme binding with micromolar affinity. The structural determination of Coa7 protein described here is key step toward understanding he mechanism of action for this protein in COX assembly and the molecular origins of the pathogeneses observed for the patient mutations. Now that we understand some of the structural features of this proteins, coupling these structural insights with broader cell biology visions will uncover how Coa7 protein participate in COX biogenesis.

References

References

[1] Emsley, J. (2012) Nature's Building Blocks: Everything You Need to Know about the Elements (new edition), *Reference Reviews* ***26,*** 43-44.

[2] Hatori, Y., Inouye, S., and Akagi, R. (2017) Thiol-based copper handling by the copper chaperone Atox1, *IUBMB life* ***69***, 246-254.

[3] Ridge, P. G., Zhang, Y., and Gladyshev, V. N. (2008) Comparative genomic analyses of copper transporters and cuproproteomes reveal evolutionary dynamics of copper utilization and its link to oxygen, *PLoS One* ***3***, e1378.

[4] Banci, L., Bertini, I., Ciofi-Baffoni, S., Kozyreva, T., Zovo, K., and Palumaa, P. (2010) Affinity gradients drive copper to cellular destinations, *Nature* ***465***, 645-648.

[5] Zhou, B., and Gitschier, J. (1997) hCTR1: a human gene for copper uptake identified by complementation in yeast, *Proc Natl Acad Sci U S A* ***94***, 7481-7486.

[6] Prohaska, J. R., and Gybina, A. A. (2004) Intracellular copper transport in mammals, *The Journal of nutrition* ***134***, 1003-1006.

[7] Cerchiaro, G., Manieri, T. M., and Bertuchi, F. R. (2013) Analytical methods for copper, zinc and iron quantification in mammalian cells, *Metallomics : integrated biometal science* ***5***, 1336-1345.

[8] Pufahl, R. A., Singer, C. P., Peariso, K. L., Lin, S. J., Schmidt, P. J., Fahrni, C. J., Culotta, V. C., Penner-Hahn, J. E., and O'Halloran, T. V. (1997) Metal ion chaperone function of the soluble Cu(I) receptor Atx1, *Science* ***278***, 853-856.

[9] Rae, T. D., Schmidt, P. J., Pufahl, R. A., Culotta, V. C., and O'Halloran, T. V. (1999) Undetectable intracellular free copper: the requirement of a copper chaperone for superoxide dismutase, *Science* ***284***, 805-808.

[10] Halliwell, B., and Gutteridge, J. M. (1984) Oxygen toxicity, oxygen radicals, transition metals and disease, *Biochem J* ***219***, 1-14.

[11] Rosenzweig, A. C. (2001) Copper delivery by metallochaperone proteins, *Acc Chem Res* ***34***, 119-128.

[12] Kaplan, J. H., and Maryon, E. B. (2016) How Mammalian Cells Acquire Copper: An Essential but Potentially Toxic Metal, *Biophys J* ***110***, 7-13.

[13] Lopez-Mirabal, H. R., and Winther, J. R. (2008) Redox characteristics of the eukaryotic cytosol, *Biochim Biophys Acta* ***1783***, 629-640.

[14] Hatori, Y., Clasen, S., Hasan, N. M., Barry, A. N., and Lutsenko, S. (2012) Functional partnership of the copper export machinery and glutathione balance in human cells, *J Biol Chem* ***287***, 26678-26687.

[15] Cotruvo, J. A., Jr., Aron, A. T., Ramos-Torres, K. M., and Chang, C. J. (2015) Synthetic fluorescent probes for studying copper in biological systems, *Chemical Society reviews* ***44***, 4400-4414.

[16] Maryon, E. B., Molloy, S. A., Ivy, K., Yu, H., and Kaplan, J. H. (2013) Rate and regulation of copper transport by human copper transporter 1 (hCTR1), *J Biol Chem* ***288***, 18035-18046.

[17] Franz, K. J. (2008) Copper shares a piece of the pi, *Nat Chem Biol* ***4***, 85-86.

[18] Turski, M. L., and Thiele, D. J. (2009) New roles for copper metabolism in cell proliferation, signaling, and disease, *J Biol Chem* ***284***, 717-721.

[19] Rosenzweig, A. C., Huffman, D. L., Hou, M. Y., Wernimont, A. K., Pufahl, R. A., and O'Halloran, T. V. (1999) Crystal structure of the Atx1 metallochaperone protein at 1.02 A resolution, *Structure* ***7***, 605-617.

[20] Ralle, M., Lutsenko, S., and Blackburn, N. J. (2003) X-ray absorption spectroscopy of the copper chaperone HAH1 reveals a linear two-coordinate Cu(I) center capable of adduct formation with exogenous thiols and phosphines, *J Biol Chem* ***278***, 23163-23170.

[21] DiDonato, M., and Sarkar, B. (1997) Copper transport and its alterations in Menkes and Wilson diseases, *Biochim Biophys Acta* ***1360***, 3-16.

[22] Dusek, P., Roos, P. M., Litwin, T., Schneider, S. A., Flaten, T. P., and Aaseth, J. (2015) The neurotoxicity of iron, copper and manganese in Parkinson's and Wilson's diseases, *Journal of trace elements in medicine and biology : organ of the Society for Minerals and Trace Elements* ***31***, 193-203.

[23] Pal, A., Siotto, M., Prasad, R., and Squitti, R. (2015) Towards a unified vision of copper involvement in Alzheimer's disease: a review connecting basic, experimental, and clinical research, *Journal of Alzheimer's disease : JAD* ***44***, 343-354.

[24] Mercer, J. F. (2001) The molecular basis of copper-transport diseases, *Trends in molecular medicine* ***7***, 64-69.

[25] Madsen, E., and Gitlin, J. D. (2007) Copper and iron disorders of the brain, *Annual review of neuroscience* ***30***, 317-337.

[26] de Bie, P., Muller, P., Wijmenga, C., and Klomp, L. W. (2007) Molecular pathogenesis of Wilson and Menkes disease: correlation of mutations with molecular defects and disease phenotypes, *Journal of medical genetics* ***44***, 673-688.

[27] Gupta, A., and Lutsenko, S. (2009) Human copper transporters: mechanism, role in human diseases and therapeutic potential, *Future medicinal chemistry* ***1***, 1125-1142.

[28] Aller, S. G., and Unger, V. M. (2006) Projection structure of the human copper transporter CTR1 at 6-A resolution reveals a compact trimer with a novel channel-like architecture, *Proc Natl Acad Sci U S A* ***103***, 3627-3632.

[29] Banci, L., Bertini, I., Cantini, F., D'Amelio, N., and Gaggelli, E. (2006) Human SOD1 before harboring the catalytic metal: solution structure of copper-depleted, disulfide-reduced form, *J Biol Chem* ***281***, 2333-2337.

[30] Robinson, N. J., and Winge, D. R. (2010) Copper metallochaperones, *Annual review of biochemistry* ***79***, 537-562.

[31] Hatori, Y., and Lutsenko, S. (2016) The Role of Copper Chaperone Atox1 in Coupling Redox Homeostasis to Intracellular Copper Distribution, *Antioxidants (Basel, Switzerland)* ***5***, 25.

[32] Brose, J., La Fontaine, S., Wedd, A. G., and Xiao, Z. (2014) Redox sulfur chemistry of the copper chaperone Atox1 is regulated by the enzyme glutaredoxin 1, the reduction potential of the glutathione couple GSSG/2GSH and the availability of Cu(I), *Metallomics* ***6***, 793-808.

[33] Arioz, C., Li, Y., and Wittung-Stafshede, P. (2017) The six metal binding domains in human copper transporter, ATP7B: molecular biophysics and disease-causing mutations, *Biometals* ***30***, 823-840.

[34] Voskoboinik, I., and Camakaris, J. (2002) Menkes copper-translocating P-type ATPase (ATP7A): biochemical and cell biology properties, and role in Menkes disease, *J Bioenerg Biomembr* ***34***, 363-371.

[35] Bhattacharjee, A., Yang, H., Duffy, M., Robinson, E., Conrad-Antoville, A., Lu, Y. W., Capps, T., Braiterman, L., Wolfgang, M., Murphy, M. P., Yi, L., Kaler, S. G., Lutsenko, S., and Ralle, M. (2016) The Activity of Menkes Disease Protein ATP7A Is Essential for Redox Balance in Mitochondria, *J Biol Chem* ***291***, 16644-16658.

[36] Achila, D., Banci, L., Bertini, I., Bunce, J., Ciofi-Baffoni, S., and Huffman, D. L. (2006) Structure of human Wilson protein domains 5 and 6 and their interplay with domain 4 and the copper chaperone HAH1 in copper uptake, *Proc Natl Acad Sci U S A* ***103***, 5729-5734.

[37] Fatemi, N., and Sarkar, B. (2002) Structural and functional insights of Wilson disease copper-transporting ATPase, *J Bioenerg Biomembr* ***34***, 339-349.

[38] Cobine, P. A., Ojeda, L. D., Rigby, K. M., and Winge, D. R. (2004) Yeast contain a non-proteinaceous pool of copper in the mitochondrial matrix, *J Biol Chem* ***279***, 14447-14455.

[39] Gu, M., Owen, A. D., Toffa, S. E., Cooper, J. M., Dexter, D. T., Jenner, P., Marsden, C. D., and Schapira, A. H. (1998) Mitochondrial function, GSH and iron in neurodegeneration and Lewy body diseases, *J Neurol Sci* ***158***, 24-29.

[40] Banci, L., Bertini, I., Ciofi-Baffoni, S., Hadjiloi, T., Martinelli, M., and Palumaa, P. (2008) Mitochondrial copper(I) transfer from Cox17 to Sco1 is coupled to electron transfer, *Proc Natl Acad Sci U S A* ***105***, 6803-6808.

[41] Banci, L., Bertini, I., Cantini, F., Ciofi-Baffoni, S., Gonnelli, L., and Mangani, S. (2004) Solution structure of Cox11, a novel type of beta-immunoglobulin-like fold involved in CuB site formation of cytochrome c oxidase, *J Biol Chem* ***279***, 34833-34839.

[42] Leary, S. C., Kaufman, B. A., Pellecchia, G., Guercin, G. H., Mattman, A., Jaksch, M., and Shoubridge, E. A. (2004) Human SCO1 and SCO2 have

independent, cooperative functions in copper delivery to cytochrome c oxidase, *Human molecular genetics* ***13***, 1839-1848.

[43] Stroud, D. A., Maher, M. J., Lindau, C., Vogtle, F. N., Frazier, A. E., Surgenor, E., Mountford, H., Singh, A. P., Bonas, M., Oeljeklaus, S., Warscheid, B., Meisinger, C., Thorburn, D. R., and Ryan, M. T. (2015) COA6 is a mitochondrial complex IV assembly factor critical for biogenesis of mtDNA-encoded COX2, *Hum Mol Genet* ***24***, 5404-5415.

[44] Aon-Bertolino, M. L., Romero, J. I., Galeano, P., Holubiec, M., Badorrey, M. S., Saraceno, G. E., Hanschmann, E. M., Lillig, C. H., and Capani, F. (2011) Thioredoxin and glutaredoxin system proteins-immunolocalization in the rat central nervous system, *Biochim Biophys Acta* ***1810***, 93-110.

[45] Xiao, Z., La Fontaine, S., Bush, A. I., and Wedd, A. G. (2019) Molecular Mechanisms of Glutaredoxin Enzymes: Versatile Hubs for Thiol-Disulfide Exchange between Protein Thiols and Glutathione, *J Mol Biol* ***431***, 158-177.

[46] Cater, M. A., Materia, S., Xiao, Z., Wolyniec, K., Ackland, S. M., Yap, Y. W., Cheung, N. S., and La Fontaine, S. (2014) Glutaredoxin1 protects neuronal cells from copper-induced toxicity, *Biometals* ***27***, 661-672.

[47] Singleton, W. C., McInnes, K. T., Cater, M. A., Winnall, W. R., McKirdy, R., Yu, Y., Taylor, P. E., Ke, B. X., Richardson, D. R., Mercer, J. F., and La Fontaine, S. (2010) Role of glutaredoxin1 and glutathione in regulating the activity of the copper-transporting P-type ATPases, ATP7A and ATP7B, *J Biol Chem* ***285***, 27111-27121.

[48] Lim, C. M., Cater, M. A., Mercer, J. F., and La Fontaine, S. (2006) Copper-dependent interaction of glutaredoxin with the N termini of the copper-ATPases (ATP7A and ATP7B) defective in Menkes and Wilson diseases, *Biochem Biophys Res Commun* ***348***, 428-436.

[49] Dancis, A., Yuan, D. S., Haile, D., Askwith, C., Eide, D., Moehle, C., Kaplan, J., and Klausner, R. D. (1994) Molecular characterization of a copper transport protein in S. cerevisiae: an unexpected role for copper in iron transport, *Cell* ***76***, 393-402.

[50] Hassett, R., and Kosman, D. J. (1995) Evidence for Cu(II) reduction as a component of copper uptake by Saccharomyces cerevisiae, *J Biol Chem* ***270***, 128-134.

[51] Martins, L. J., Jensen, L. T., Simon, J. R., Keller, G. L., and Winge, D. R. (1998) Metalloregulation of FRE1 and FRE2 homologs in Saccharomyces cerevisiae, *J Biol Chem* ***273***, 23716-23721.

[52] Lee, J., Pena, M. M., Nose, Y., and Thiele, D. J. (2002) Biochemical characterization of the human copper transporter Ctr1, *J Biol Chem* ***277***, 4380-4387.

[53] Nose, Y., Rees, E. M., and Thiele, D. J. (2006) Structure of the Ctr1 copper trans'PORE'ter reveals novel architecture, *Trends Biochem Sci* ***31***, 604-607.

[54] Ren, F., Logeman, B. L., Zhang, X., Liu, Y., Thiele, D. J., and Yuan, P. (2019) X-ray structures of the high-affinity copper transporter Ctr1, *Nature communications* ***10***, 1386.

[55] De Feo, C. J., Aller, S. G., Siluvai, G. S., Blackburn, N. J., and Unger, V. M. (2009) Three-dimensional structure of the human copper transporter hCTR1, *Proc Natl Acad Sci U S A* ***106***, 4237-4242.

[56] Tsigelny, I. F., Sharikov, Y., Greenberg, J. P., Miller, M. A., Kouznetsova, V. L., Larson, C. A., and Howell, S. B. (2012) An all-atom model of the structure of human copper transporter 1, *Cell biochemistry and biophysics* ***63***, 223-234.

[57] Puig, S., Lee, J., Lau, M., and Thiele, D. J. (2002) Biochemical and genetic analyses of yeast and human high affinity copper transporters suggest a conserved mechanism for copper uptake, *J Biol Chem* ***277***, 26021-26030.

[58] Eisses, J. F., and Kaplan, J. H. (2002) Molecular characterization of hCTR1, the human copper uptake protein, *J Biol Chem* ***277***, 29162-29171.

[59] Klomp, A. E., Tops, B. B., Van Denberg, I. E., Berger, R., and Klomp, L. W. (2002) Biochemical characterization and subcellular localization of human copper transporter 1 (hCTR1), *Biochem J* ***364***, 497-505.

[60] Maryon, E. B., Molloy, S. A., and Kaplan, J. H. (2013) Cellular glutathione plays a key role in copper uptake mediated by human copper transporter 1, *American journal of physiology. Cell physiology* ***304***, C768-779.

[61] Xiao, Z., Brose, J., Schimo, S., Ackland, S. M., La Fontaine, S., and Wedd, A. G. (2011) Unification of the copper(I) binding affinities of the metallo-chaperones Atx1, Atox1, and related proteins: detection probes and affinity standards, *J Biol Chem* ***286***, 11047-11055.

[62] Hamza, I., Faisst, A., Prohaska, J., Chen, J., Gruss, P., and Gitlin, J. D. (2001) The metallochaperone Atox1 plays a critical role in perinatal copper homeostasis, *Proc Natl Acad Sci U S A* ***98***, 6848-6852.

[63] Yu, C. H., Dolgova, N. V., and Dmitriev, O. Y. (2017) Dynamics of the metal binding domains and regulation of the human copper transporters ATP7B and ATP7A, *IUBMB life* ***69***, 226-235.

[64] La Fontaine, S., and Mercer, J. F. (2007) Trafficking of the copper-ATPases, ATP7A and ATP7B: role in copper homeostasis, *Arch Biochem Biophys 463*, 149-167.

[65] Wernimont, A. K., Huffman, D. L., Lamb, A. L., O'Halloran, T. V., and Rosenzweig, A. C. (2000) Structural basis for copper transfer by the metallochaperone for the Menkes/Wilson disease proteins, *Nat Struct Biol* ***7***, 766-771.

[66] Hatori, Y., Yan, Y., Schmidt, K., Furukawa, E., Hasan, N. M., Yang, N., Liu, C. N., Sockanathan, S., and Lutsenko, S. (2016) Neuronal differentiation is associated with a redox-regulated increase of copper flow to the secretory pathway, *Nature communications* ***7***, 10640.

[67] Hamza, I., Schaefer, M., Klomp, L. W., and Gitlin, J. D. (1999) Interaction of the copper chaperone HAH1 with the Wilson disease protein is essential for copper homeostasis, *Proc Natl Acad Sci U S A* ***96***, 13363-13368.

[68] Lutsenko, S. (2016) Copper trafficking to the secretory pathway, *Metallomics : integrated biometal science* ***8***, 840-852.

[69] Yu, C. H., Dolgova, N. V., and Dmitriev, O. Y. (2017) Dynamics of the metal binding domains and regulation of the human copper transporters ATP7B and ATP7A, *IUBMB life* ***69***, 226-235.

[70] Cater, M. A., La Fontaine, S., and Mercer, J. F. (2007) Copper binding to the N-terminal metal-binding sites or the CPC motif is not essential for copper-induced trafficking of the human Wilson protein (ATP7B), *Biochem J* ***401***, 143-153.

[71] Banci, L., Bertini, I., Cantini, F., Della-Malva, N., Migliardi, M., and Rosato, A. (2007) The different intermolecular interactions of the soluble copper-binding domains of the menkes protein, ATP7A, *J Biol Chem* ***282***, 23140-23146.

[72] Lutsenko, S., Barnes, N. L., Bartee, M. Y., and Dmitriev, O. Y. (2007) Function and regulation of human copper-transporting ATPases, *Physiological reviews* ***87***, 1011-1046.

[73] Daniel, K. G., Harbach, R. H., Guida, W. C., and Dou, Q. P. (2004) Copper storage diseases: Menkes, Wilsons, and cancer, *Front Biosci* ***9***, 2652-2662.

[74] Mercer, S. W., Wang, J., and Burke, R. (2017) In vivo Modelling of the Pathogenic Effect of Copper Transporter Mutations that cause Menkes and Wilson Disease, Motor Neuropathy and Susceptibility to Alzheimer's Disease, *J Biol Chem* ***292***, 4113-4122.

[75] Bandmann, O., Weiss, K. H., and Kaler, S. G. (2015) Wilson's disease and other neurological copper disorders, *The Lancet. Neurology* ***14***, 103-113.

[76] Rodriguez-Granillo, A., Crespo, A., and Wittung-Stafshede, P. (2009) Conformational dynamics of metal-binding domains in Wilson disease protein: molecular insights into selective copper transfer, *Biochemistry* ***48***, 5849-5863.

[77] Gourdon, P., Liu, X. Y., Skjorringe, T., Morth, J. P., Moller, L. B., Pedersen, B. P., and Nissen, P. (2011) Crystal structure of a copper-transporting PIB-type ATPase, *Nature* ***475***, 59-64.

[78] Morth, J. P., Pedersen, B. P., Toustrup-Jensen, M. S., Sorensen, T. L., Petersen, J., Andersen, J. P., Vilsen, B., and Nissen, P. (2007) Crystal structure of the sodium-potassium pump, *Nature* ***450***, 1043-1049.

[79] Olesen, C., Sorensen, T. L., Nielsen, R. C., Moller, J. V., and Nissen, P. (2004) Dephosphorylation of the calcium pump coupled to counterion occlusion, *Science* ***306***, 2251-2255.

[80] Lorincz, M. T. (2018) Wilson disease and related copper disorders, *Handbook of clinical neurology* ***147***, 279-292.

[81] Yu, C. H., Yang, N., Bothe, J., Tonelli, M., Nokhrin, S., Dolgova, N. V., Braiterman, L., Lutsenko, S., and Dmitriev, O. Y. (2017) The metal chaperone Atox1 regulates the activity of the human copper transporter ATP7B by modulating domain dynamics, *J Biol Chem* ***292***, 18169-18177.

[82] Walker, J. M., Huster, D., Ralle, M., Morgan, C. T., Blackburn, N. J., and Lutsenko, S. (2004) The N-terminal metal-binding site 2 of the Wilson's Disease Protein plays a key role in the transfer of copper from Atox1, *J Biol Chem* ***279***, 15376-15384.

[83] Huang, Y., Nokhrin, S., Hassanzadeh-Ghassabeh, G., Yu, C. H., Yang, H., Barry, A. N., Tonelli, M., Markley, J. L., Muyldermans, S., Dmitriev, O. Y., and Lutsenko, S. (2014) Interactions between metal-binding domains modulate intracellular targeting of Cu(I)-ATPase ATP7B, as revealed by nanobody binding, *J Biol Chem* ***289***, 32682-32693.

[84] Wernimont, A. K., Yatsunyk, L. A., and Rosenzweig, A. C. (2004) Binding of copper(I) by the Wilson disease protein and its copper chaperone, *J Biol Chem* ***279***, 12269-12276.

[85] Yatsunyk, L. A., and Rosenzweig, A. C. (2007) Cu(I) binding and transfer by the N terminus of the Wilson disease protein, *J Biol Chem* ***282***, 8622-8631.

[86] Banci, L., Bertini, I., Cantini, F., Rosenzweig, A. C., and Yatsunyk, L. A. (2008) Metal binding domains 3 and 4 of the Wilson disease protein: solution structure and interaction with the copper(I) chaperone HAH1, *Biochemistry* ***47***, 7423-7429.

[87] Holmgren, A. (1989) Thioredoxin and glutaredoxin systems, *J Biol Chem* ***264***, 13963-13966.

[88] Prinz, W. A., Aslund, F., Holmgren, A., and Beckwith, J. (1997) The role of the thioredoxin and glutaredoxin pathways in reducing protein disulfide bonds in the Escherichia coli cytoplasm, *J Biol Chem* ***272***, 15661-15667.

[89] Parker, A. R., Petluru, P. N., Nienaber, V. L., Badger, J., Leverett, B. D., Jair, K., Sridhar, V., Logan, C., Ayala, P. Y., Kochat, H., and Hausheer, F. H. (2015) Cysteine specific targeting of the functionally distinct peroxiredoxin and glutaredoxin proteins by the investigational disulfide BNP7787, *Molecules* ***20***, 4928-4950.

[90] Martin, J. L. (1995) Thioredoxin--a fold for all reasons, *Structure* ***3***, 245-250.

[91] Cave, J. W., Cho, H. S., Batchelder, A. M., Yokota, H., Kim, R., and Wemmer, D. E. (2001) Solution nuclear magnetic resonance structure of a protein disulfide oxidoreductase from Methanococcus jannaschii, *Protein Sci* ***10***, 384-396.

[92] Chacinska, A., Koehler, C. M., Milenkovic, D., Lithgow, T., and Pfanner, N. (2009) Importing mitochondrial proteins: machineries and mechanisms, *Cell* ***138***, 628-644.

[93] Schmidt, O., Pfanner, N., and Meisinger, C. (2010) Mitochondrial protein import: from proteomics to functional mechanisms, *Nat Rev Mol Cell Biol* ***11***, 655-667.

[94] Neupert, W., and Herrmann, J. M. (2007) Translocation of proteins into mitochondria, *Annual review of biochemistry* ***76***, 723-749.

[95] Fernandez-Vizarra, E., Tiranti, V., and Zeviani, M. (2009) Assembly of the oxidative phosphorylation system in humans: what we have learned by studying its defects, *Biochim Biophys Acta* ***1793***, 200-211.

[96] Tsukihara, T., Aoyama, H., Yamashita, E., Tomizaki, T., Yamaguchi, H., Shinzawa-Itoh, K., Nakashima, R., Yaono, R., and Yoshikawa, S. (1996) The whole structure of the 13-subunit oxidized cytochrome c oxidase at 2.8 A, *Science* ***272***, 1136-1144.

[97] Mick, D. U., Fox, T. D., and Rehling, P. (2011) Inventory control: cytochrome c oxidase assembly regulates mitochondrial translation, *Nat Rev Mol Cell Biol* ***12***, 14-20.

[98] Balsa, E., Marco, R., Perales-Clemente, E., Szklarczyk, R., Calvo, E., Landazuri, M. O., and Enriquez, J. A. (2012) NDUFA4 is a subunit of complex IV of the mammalian electron transport chain, *Cell metabolism* ***16***, 378-386.

[99] Chandel, N. S. (2015) Evolution of Mitochondria as Signaling Organelles, *Cell metabolism* ***22***, 204-206.

[100] Mehta, M. M., Weinberg, S. E., and Chandel, N. S. (2017) Mitochondrial control of immunity: beyond ATP, *Nature reviews. Immunology* ***17***, 608-620.

[101] Timon-Gomez, A., Nyvltova, E., Abriata, L. A., Vila, A. J., Hosler, J., and Barrientos, A. (2018) Mitochondrial cytochrome c oxidase biogenesis: Recent developments, *Seminars in cell & developmental biology* ***76***, 163-178.

[102] Pitceathly, R. D., Rahman, S., Wedatilake, Y., Polke, J. M., Cirak, S., Foley, A. R., Sailer, A., Hurles, M. E., Stalker, J., Hargreaves, I., Woodward, C. E., Sweeney, M. G., Muntoni, F., Houlden, H., Taanman, J. W., and Hanna, M. G. (2013) NDUFA4 mutations underlie dysfunction of a cytochrome c oxidase subunit linked to human neurological disease, *Cell reports* ***3***, 1795-1805.

[103] Smith, A. D., Logeman, B. L., and Thiele, D. J. (2017) Copper Acquisition and Utilization in Fungi, *Annual Review of Microbiology* ***71***, 597-623.

[104] McStay, G. P., Su, C. H., and Tzagoloff, A. (2013) Modular assembly of yeast cytochrome oxidase, *Molecular biology of the cell* ***24***, 440-452.

[105] Glerum, D. M., and Tzagoloff, A. (1997) Submitochondrial distributions and stabilities of subunits 4, 5, and 6 of yeast cytochrome oxidase in assembly defective mutants, *FEBS Lett* ***412***, 410-414.

[106] Vidoni, S., Harbour, M. E., Guerrero-Castillo, S., Signes, A., Ding, S., Fearnley, I. M., Taylor, R. W., Tiranti, V., Arnold, S., Fernandez-Vizarra, E., and Zeviani, M. (2017) MR-1S Interacts with PET100 and PET117 in

Module-Based Assembly of Human Cytochrome c Oxidase, *Cell reports* ***18***, 1727-1738.

[107] Barros, M. H., Carlson, C. G., Glerum, D. M., and Tzagoloff, A. (2001) Involvement of mitochondrial ferredoxin and Cox15p in hydroxylation of heme O, *FEBS Lett* ***492***, 133-138.

[108] Glerum, D. M., and Tzagoloff, A. (1994) Isolation of a human cDNA for heme A:farnesyltransferase by functional complementation of a yeast cox10 mutant, *Proc Natl Acad Sci U S A* ***91***, 8452-8456.

[109] Clemente, P., Peralta, S., Cruz-Bermudez, A., Echevarria, L., Fontanesi, F., Barrientos, A., Fernandez-Moreno, M. A., and Garesse, R. (2013) hCOA3 stabilizes cytochrome c oxidase 1 (COX1) and promotes cytochrome c oxidase assembly in human mitochondria, *J Biol Chem* ***288***, 8321-8331.

[110] Soto, I. C., Fontanesi, F., Liu, J., and Barrientos, A. (2012) Biogenesis and assembly of eukaryotic cytochrome c oxidase catalytic core, *Biochim Biophys Acta* ***1817***, 883-897.

[111] Smith, D., Gray, J., Mitchell, L., Antholine, W. E., and Hosler, J. P. (2005) Assembly of cytochrome-c oxidase in the absence of assembly protein Surf1p leads to loss of the active site heme, *J Biol Chem* ***280***, 17652-17656.

[112] Bundschuh, F. A., Hannappel, A., Anderka, O., and Ludwig, B. (2009) Surf1, associated with Leigh syndrome in humans, is a heme-binding protein in bacterial oxidase biogenesis, *J Biol Chem* ***284***, 25735-25741.

[113] Bundschuh, F. A., Hoffmeier, K., and Ludwig, B. (2008) Two variants of the assembly factor Surf1 target specific terminal oxidases in Paracoccus denitrificans, *Biochim Biophys Acta* ***1777***, 1336-1343.

[114] Bestwick, M., Jeong, M. Y., Khalimonchuk, O., Kim, H., and Winge, D. R. (2010) Analysis of Leigh syndrome mutations in the yeast SURF1 homolog reveals a new member of the cytochrome oxidase assembly factor family, *Mol Cell Biol* ***30***, 4480-4491.

[115] Bode, M., Woellhaf, M. W., Bohnert, M., van der Laan, M., Sommer, F., Jung, M., Zimmermann, R., Schroda, M., and Herrmann, J. M. (2015) Redox-regulated dynamic interplay between Cox19 and the copper-binding protein Cox11 in the intermembrane space of mitochondria facilitates biogenesis of cytochrome c oxidase, *Molecular biology of the cell* ***26***, 2385-2401.

[116] van Dijk, A. D., Ciofi-Baffoni, S., Banci, L., Bertini, I., Boelens, R., and Bonvin, A. M. (2007) Modeling protein-protein complexes involved in the cytochrome C oxidase copper-delivery pathway, *J Proteome Res* ***6***, 1530-1539.

[117] Thompson, A. K., Smith, D., Gray, J., Carr, H. S., Liu, A., Winge, D. R., and Hosler, J. P. (2010) Mutagenic analysis of Cox11 of Rhodobacter sphaeroides: insights into the assembly of Cu(B) of cytochrome c oxidase, *Biochemistry* ***49***, 5651-5661.

[118] Bourens, M., Boulet, A., Leary, S. C., and Barrientos, A. (2014) Human COX20 cooperates with SCO1 and SCO2 to mature COX2 and promote the assembly of cytochrome c oxidase, *Human molecular genetics* ***23***, 2901-2913.

[119] Bourens, M., and Barrientos, A. (2017) Human mitochondrial cytochrome c oxidase assembly factor COX18 acts transiently as a membrane insertase within the subunit 2 maturation module, *J Biol Chem* ***292***, 7774-7783.

[120] Vafai, S. B., and Mootha, V. K. (2012) Mitochondrial disorders as windows into an ancient organelle, *Nature* ***491***, 374-383.

[121] Aich, A., Wang, C., Chowdhury, A., Ronsor, C., Pacheu-Grau, D., Richter-Dennerlein, R., Dennerlein, S., and Rehling, P. (2018) COX16 promotes COX2 metallation and assembly during respiratory complex IV biogenesis, *eLife* ***7***.

[122] Banci, L., Bertini, I., Ciofi-Baffoni, S., Janicka, A., Martinelli, M., Kozlowski, H., and Palumaa, P. (2008) A structural-dynamical characterization of human Cox17, *The Journal of biological chemistry* ***283***, 7912-7920.

[123] Cobine, P. A., Pierrel, F., Bestwick, M. L., and Winge, D. R. (2006) Mitochondrial matrix copper complex used in metallation of cytochrome oxidase and superoxide dismutase, *J Biol Chem* ***281***, 36552-36559.

[124] Vest, K. E., Leary, S. C., Winge, D. R., and Cobine, P. A. (2013) Copper import into the mitochondrial matrix in Saccharomyces cerevisiae is mediated by Pic2, a mitochondrial carrier family protein, *J Biol Chem* ***288***, 23884-23892.

[125] Vest, K. E., Wang, J., Gammon, M. G., Maynard, M. K., White, O. L., Cobine, J. A., Mahone, W. K., and Cobine, P. A. (2016) Overlap of copper and iron uptake systems in mitochondria in Saccharomyces cerevisiae, *Open biology* ***6***, 150223.

[126] Boulet, A., Vest, K. E., Maynard, M. K., Gammon, M. G., Russell, A. C., Mathews, A. T., Cole, S. E., Zhu, X., Phillips, C. B., Kwong, J. Q., Dodani, S. C., Leary, S. C., and Cobine, P. A. (2018) The mammalian phosphate carrier SLC25A3 is a mitochondrial copper transporter required for cytochrome c oxidase biogenesis, *J Biol Chem* ***293***, 1887-1896.

[127] Seifert, E. L., Ligeti, E., Mayr, J. A., Sondheimer, N., and Hajnoczky, G. (2015) The mitochondrial phosphate carrier: Role in oxidative metabolism, calcium handling and mitochondrial disease, *Biochem Biophys Res Commun* ***464***, 369-375.

[128] Baker, Z. N., Cobine, P. A., and Leary, S. C. (2017) The mitochondrion: a central architect of copper homeostasis, *Metallomics : integrated biometal science* ***9***, 1501-1512.

[129] Horng, Y. C., Cobine, P. A., Maxfield, A. B., Carr, H. S., and Winge, D. R. (2004) Specific copper transfer from the Cox17 metallochaperone to both Sco1 and Cox11 in the assembly of yeast cytochrome C oxidase, *J Biol Chem* ***279***, 35334-35340.

[130] Banci, L., Bertini, I., Calderone, V., Ciofi-Baffoni, S., Mangani, S., Martinelli, M., Palumaa, P., and Wang, S. (2006) A hint for the function of human Sco1 from different structures, *Proc Natl Acad Sci U S A* ***103***, 8595-8600.

[131] Banci, L., Bertini, I., Ciofi-Baffoni, S., Gerothanassis, I. P., Leontari, I., Martinelli, M., and Wang, S. (2007) A structural characterization of human SCO2, *Structure* ***15***, 1132-1140.

[132] Banci, L., Bertini, I., Ciofi-Baffoni, S., Leontari, I., Martinelli, M., Palumaa, P., Sillard, R., and Wang, S. (2007) Human Sco1 functional studies and pathological implications of the P174L mutant, *Proc Natl Acad Sci U S A* ***104***, 15-20.

[133] Morgada, M. N., Abriata, L. A., Cefaro, C., Gajda, K., Banci, L., and Vila, A. J. (2015) Loop recognition and copper-mediated disulfide reduction underpin metal site assembly of CuA in human cytochrome oxidase, *Proc Natl Acad Sci U S A* ***112***, 11771-11776.

[134] Ghosh, A., Trivedi, P. P., Timbalia, S. A., Griffin, A. T., Rahn, J. J., Chan, S. S., and Gohil, V. M. (2014) Copper supplementation restores cytochrome c oxidase assembly defect in a mitochondrial disease model of COA6 deficiency, *Hum Mol Genet* ***23***, 3596-3606.

[135] Pacheu-Grau, D., Bareth, B., Dudek, J., Juris, L., Vogtle, F. N., Wissel, M., Leary, S. C., Dennerlein, S., Rehling, P., and Deckers, M. (2015) Cooperation between COA6 and SCO2 in COX2 maturation during cytochrome c oxidase assembly links two mitochondrial cardiomyopathies, *Cell metabolism* ***21***, 823-833.

[136] Calvo, S. E., Compton, A. G., Hershman, S. G., Lim, S. C., Lieber, D. S., Tucker, E. J., Laskowski, A., Garone, C., Liu, S., Jaffe, D. B., Christodoulou, J., Fletcher, J. M., Bruno, D. L., Goldblatt, J., Dimauro, S., Thorburn, D. R., and Mootha, V. K. (2012) Molecular diagnosis of infantile mitochondrial disease with targeted next-generation sequencing, *Science translational medicine* ***4***, 118ra110.

[137] Baertling, F., M, A. M. v. d. B., Hertecant, J. L., Al-Shamsi, A., L, P. v. d. H., Distelmaier, F., Mayatepek, E., Smeitink, J. A., Nijtmans, L. G., and Rodenburg, R. J. (2015) Mutations in COA6 cause cytochrome c oxidase deficiency and neonatal hypertrophic cardiomyopathy, *Human mutation* ***36***, 34-38.

[138] Kozjak-Pavlovic, V., Prell, F., Thiede, B., Gotz, M., Wosiek, D., Ott, C., and Rudel, T. (2014) C1orf163/RESA1 is a novel mitochondrial intermembrane space protein connected to respiratory chain assembly, *J Mol Biol* ***426***, 908-920.

[139] Martinez Lyons, A., Ardissone, A., Reyes, A., Robinson, A. J., Moroni, I., Ghezzi, D., Fernandez-Vizarra, E., and Zeviani, M. (2016) COA7 (C1orf163/RESA1) mutations associated with mitochondrial leukoencephalopathy and cytochrome c oxidase deficiency, *J Med Genet* ***53***, 846-849.

[140] Mohanraj, K., Wasilewski, M., Beninca, C., Cysewski, D., Poznanski, J., Sakowska, P., Bugajska, Z., Deckers, M., Dennerlein, S., Fernandez-Vizarra,

E., Rehling, P., Dadlez, M., Zeviani, M., and Chacinska, A. (2019) Inhibition of proteasome rescues a pathogenic variant of respiratory chain assembly factor COA7, *EMBO molecular medicine*, ***11***.

[141] Higuchi, Y., Okunushi, R., Hara, T., Hashiguchi, A., Yuan, J., Yoshimura, A., Murayama, K., Ohtake, A., Ando, M., Hiramatsu, Y., Ishihara, S., Tanabe, H., Okamoto, Y., Matsuura, E., Ueda, T., Toda, T., Yamashita, S., Yamada, K., Koide, T., Yaguchi, H., Mitsui, J., Ishiura, H., Yoshimura, J., Doi, K., Morishita, S., Sato, K., Nakagawa, M., Yamaguchi, M., Tsuji, S., and Takashima, H. (2018) Mutations in COA7 cause spinocerebellar ataxia with axonal neuropathy, *Brain* ***141***, 1622-1636.

[142] Culotta, V. C., and Gitlin, J. D. (2001) Disorders of copper transport., In *The Metabolic and Molecular Basis of Inherited Disease.* (Scriver, C. R., Beaudet, A. L., Sly, W. S., and Valle, D., Eds.), pp 3105-3126, McGraw-Hill, New York.

[143] Danks, D. M. (1995) Disorders of copper transport. , In *The Metabolic and Molecular Basis of Inherited Disease.* (Scriver, C. R., Beaudet, A. L., Sly, W. M., and Valle, D., Eds.), pp 2211-2235, McGraw-Hill, New York.

[144] Kaplan, J. H., and Lutsenko, S. (2009) Copper transport in mammalian cells: special care for a metal with special needs, *J Biol Chem* ***284***, 25461-25465.

[145] Axelsen, K. B., and Palmgren, M. G. (1998) Evolution of substrate specificities in the P-type ATPase superfamily, *J Mol Evol* ***46***, 84-101.

[146] Schaefer, M., Roelofsen, H., Wolters, H., Hofmann, W. J., Muller, M., Kuipers, F., Stremmel, W., and Vonk, R. J. (1999) Localization of the Wilson's disease protein in human liver, *Gastroenterology* ***117***, 1380-1385.

[147] Petris, M. J., Mercer, J. F., Culvenor, J. G., Lockhart, P., Gleeson, P. A., and Camakaris, J. (1996) Ligand-regulated transport of the Menkes copper P-type ATPase efflux pump from the Golgi apparatus to the plasma membrane: a novel mechanism of regulated trafficking, *EMBO J* ***15***, 6084-6095.

[148] Schaefer, M., Hopkins, R. G., Failla, M. L., and Gitlin, J. D. (1999) Hepatocyte-specific localization and copper-dependent trafficking of the Wilson's disease protein in the liver, *Am J Physiol* ***276***, G639-646.

[149] Linz, R., and Lutsenko, S. (2007) Copper-transporting ATPases ATP7A and ATP7B: cousins, not twins, *J Bioenerg Biomembr* ***39***, 403-407.

[150] DiDonato, M., Hsu, H. F., Narindrasorasak, S., Que, L., Jr., and Sarkar, B. (2000) Copper-induced conformational changes in the N-terminal domain of the Wilson disease copper-transporting ATPase, *Biochemistry* ***39***, 1890-1896.

[151] Fatemi, N., Korzhnev, D. M., Velyvis, A., Sarkar, B., and Forman-Kay, J. D. (2010) NMR characterization of copper-binding domains 4-6 of ATP7B, *Biochemistry* ***49***, 8468-8477.

[152] DiDonato, M., Zhang, J., Que, L., Jr., and Sarkar, B. (2002) Zinc binding to the NH2-terminal domain of the Wilson disease copper-transporting ATPase:

implications for in vivo metal ion-mediated regulation of ATPase activity, *J Biol Chem* ***277***, 13409-13414.

[153] Larin, D., Mekios, C., Das, K., Ross, B., Yang, A. S., and Gilliam, T. C. (1999) Characterization of the interaction between the Wilson and Menkes disease proteins and the cytoplasmic copper chaperone, HAH1p, *J Biol Chem* ***274***, 28497-28504.

[154] Lutsenko, S., Petrukhin, K., Cooper, M. J., Gilliam, C. T., and Kaplan, J. H. (1997) N-terminal domains of human copper-transporting adenosine triphosphatases (the Wilson's and Menkes disease proteins) bind copper selectively in vivo and in vitro with stoichiometry of one copper per metal-binding repeat, *J Biol Chem* **272**, 18939-18944.

[155] Niemiec, M. S., Dingeldein, A. P., and Wittung-Stafshede, P. (2014) T versus D in the MTCXXC motif of copper transport proteins plays a role in directional metal transport, *J Biol Inorg Chem* ***19***, 1037-1047.

[156] Banci, L., Bertini, I., Cantini, F., Massagni, C., Migliardi, M., and Rosato, A. (2009) An NMR study of the interaction of the N-terminal cytoplasmic tail of the Wilson disease protein with copper(I)-HAH1, *J Biol Chem* ***284***, 9354-9360.

[157] Miranda-Vizuete, A., Rodriguez-Ariza, A., Toribio, F., Holmgren, A., Lopez-Barea, J., and Pueyo, C. (1996) The levels of ribonucleotide reductase, thioredoxin, glutaredoxin 1, and GSH are balanced in Escherichia coli K12, *J Biol Chem* ***271***, 19099-19103.

[158] Berndt, C., Lillig, C. H., and Holmgren, A. (2008) Thioredoxins and glutaredoxins as facilitators of protein folding, *Biochim Biophys Acta* ***1783***, 641-650.

[159] Sun, C., Berardi, M. J., and Bushweller, J. H. (1998) The NMR solution structure of human glutaredoxin in the fully reduced form, *J Mol Biol* ***280***, 687-701.

[160] De Benedetto, M. L., Capo, C. R., Ferri, A., Valle, C., Polimanti, R., Carri, M. T., and Rossi, L. (2014) Glutaredoxin 1 is a major player in copper metabolism in neuroblastoma cells, *Biochim Biophys Acta* ***1840***, 255-261.

[161] Bouldin, S. D., Darch, M. A., Hart, P. J., and Outten, C. E. (2012) Redox properties of the disulfide bond of human Cu,Zn superoxide dismutase and the effects of human glutaredoxin 1, *Biochem J* ***446***, 59-67.

[162] Banci, L., Bertini, I., Cantini, F., Felli, I. C., Gonnelli, L., Hadjiliadis, N., Pierattelli, R., Rosato, A., and Voulgaris, P. (2006) The Atx1-Ccc2 complex is a metal-mediated protein-protein interaction, *Nat Chem Biol* **2**, 367-368.

[163] Banci, L., Bertini, I., Calderone, V., Della-Malva, N., Felli, I. C., Neri, S., Pavelkova, A., and Rosato, A. (2009) Copper(I)-mediated protein-protein interactions result from suboptimal interaction surfaces, *Biochem J* ***422***, 37-42.

[164] Yang, Y., Jao, S., Nanduri, S., Starke, D. W., Mieyal, J. J., and Qin, J. (1998) Reactivity of the human thioltransferase (glutaredoxin) C7S, C25S, C78S,

C82S mutant and NMR solution structure of its glutathionyl mixed disulfide intermediate reflect catalytic specificity, *Biochemistry* ***37***, 17145-17156.

[165] Bunce, J., Achila, D., Hetrick, E., Lesley, L., and Huffman, D. L. (2006) Copper transfer studies between the N-terminal copper binding domains one and four of human Wilson protein, *Biochim Biophys Acta* ***1760***, 907-912.

[166] Anastassopoulou, I., Banci, L., Bertini, I., Cantini, F., Katsari, E., and Rosato, A. (2004) Solution structure of the apo and copper(I)-loaded human metallochaperone HAH1, *Biochemistry* ***43***, 13046-13053.

[167] Hatori, Y., and Lutsenko, S. (2013) An expanding range of functions for the copper chaperone/antioxidant protein Atox1, *Antioxidants & redox signaling* ***19***, 945-957.

[168] Marley, J., Lu, M., and Bracken, C. (2001) A method for efficient isotopic labeling of recombinant proteins, *Journal of biomolecular NMR* ***20***, 71-75.

[169] Lothian, A., and Roberts, B. R. (2016) Standards for Quantitative Metalloproteomic Analysis Using Size Exclusion ICP-MS, *J Vis Exp* ***110***, 53737.

[170] Ferguson-Miller, S., and Babcock, G. T. (1996) Heme/Copper Terminal Oxidases, *Chem Rev* ***96***, 2889-2908.

[171] Rak, M., Benit, P., Chretien, D., Bouchereau, J., Schiff, M., El-Khoury, R., Tzagoloff, A., and Rustin, P. (2016) Mitochondrial cytochrome c oxidase deficiency, *Clinical science (London, England : 1979)* ***130***, 393-407.

[172] Stiburek, L., Vesela, K., Hansikova, H., Hulkova, H., and Zeman, J. (2009) Loss of function of Sco1 and its interaction with cytochrome c oxidase, *American journal of physiology. Cell physiology* ***296***, C1218-1226.

[173] Leary, S. C. (2010) Redox regulation of SCO protein function: controlling copper at a mitochondrial crossroad, *Antioxidants & redox signaling* ***13***, 1403-1416.

[174] Soma, S., Latimer, A. J., Chun, H., Vicary, A. C., Timbalia, S. A., Boulet, A., Rahn, J. J., Chan, S. S. L., Leary, S. C., Kim, B. E., Gitlin, J. D., and Gohil, V. M. (2018) Elesclomol restores mitochondrial function in genetic models of copper deficiency, *Proc Natl Acad Sci U S A* ***115***, 8161-8166.

[175] Cavallaro, G. (2010) Genome-wide analysis of eukaryotic twin CX9C proteins, *Molecular bioSystems* ***6***, 2459-2470.

[176] Banci, L., Bertini, I., Cefaro, C., Ciofi-Baffoni, S., Gallo, A., Martinelli, M., Sideris, D. P., Katrakili, N., and Tokatlidis, K. (2009) MIA40 is an oxidoreductase that catalyzes oxidative protein folding in mitochondria, *Nat Struct Mol Biol* ***16***, 198-206.

[177] Barthe, P., Yang, Y. S., Chiche, L., Hoh, F., Strub, M. P., Guignard, L., Soulier, J., Stern, M. H., van Tilbeurgh, H., Lhoste, J. M., and Roumestand, C. (1997) Solution structure of human p8MTCP1, a cysteine-rich protein encoded by

the MTCP1 oncogene, reveals a new alpha-helical assembly motif, *J Mol Biol* ***274***, 801-815.

[178] Banci, L., Bertini, I., Ciofi-Baffoni, S., Jaiswal, D., Neri, S., Peruzzini, R., and Winkelmann, J. (2012) Structural characterization of CHCHD5 and CHCHD7: two atypical human twin CX9C proteins, *J Struct Biol* ***180***, 190-200.

[179] Krissinel, E., and Henrick, K. (2004) Secondary-structure matching (SSM), a new tool for fast protein structure alignment in three dimensions, *Acta Crystallogr D Biol Crystallogr* ***60***, 2256-2268.

[180] Aoyama, H., Muramoto, K., Shinzawa-Itoh, K., Hirata, K., Yamashita, E., Tsukihara, T., Ogura, T., and Yoshikawa, S. (2009) A peroxide bridge between Fe and Cu ions in the O2 reduction site of fully oxidized cytochrome c oxidase could suppress the proton pump, *Proc Natl Acad Sci U S A* ***106***, 2165-2169.

[181] Sideris, D. P., and Tokatlidis, K. (2010) Oxidative protein folding in the mitochondrial intermembrane space, *Antioxidants & redox signaling* ***13***, 1189-1204.

[182] Jones, S., and Thornton, J. M. (1995) Protein-protein interactions: a review of protein dimer structures, *Progress in biophysics and molecular biology* ***63***, 31-65.

[183] Banci, L., Bertini, I., Ciofi-Baffoni, S., and Tokatlidis, K. (2009) The coiled coil-helix-coiled coil-helix proteins may be redox proteins, *FEBS Lett* ***583***, 1699-1702.

[184] Ostergaard, H., Tachibana, C., and Winther, J. R. (2004) Monitoring disulfide bond formation in the eukaryotic cytosol, *The Journal of cell biology* ***166***, 337-345.

[185] Voronova, A., Meyer-Klaucke, W., Meyer, T., Rompel, A., Krebs, B., Kazantseva, J., Sillard, R., and Palumaa, P. (2007) Oxidative switches in functioning of mammalian copper chaperone Cox17, *Biochem J* ***408***, 139-148.

[186] Wong, J. W., and Hogg, P. J. (2010) Analysis of disulfide bonds in protein structures, *Journal of thrombosis and haemostasis : JTH* ***8***.

[187] Schmidt, B., Ho, L., and Hogg, P. J. (2006) Allosteric disulfide bonds, *Biochemistry 45*, 7429-7433.

[188] Marques, J. R., da Fonseca, R. R., Drury, B., and Melo, A. (2010) Conformational characterization of disulfide bonds: a tool for protein classification, *Journal of theoretical biology* ***267***, 388-395.

[189] Boal, A. K., and Rosenzweig, A. C. (2009) Structural biology of copper trafficking, *Chem Rev* ***109***, 4760-4779.

[190] Xue, Y., Davis, A. V., Balakrishnan, G., Stasser, J. P., Staehlin, B. M., Focia, P., Spiro, T. G., Penner-Hahn, J. E., and O'Halloran, T. V. (2008) Cu(I) recognition via cation-pi and methionine interactions in CusF, *Nat Chem Biol* ***4***, 107-109.

[191] Vogtle, F. N., Burkhart, J. M., Rao, S., Gerbeth, C., Hinrichs, J., Martinou, J. C., Chacinska, A., Sickmann, A., Zahedi, R. P., and Meisinger, C. (2012) Intermembrane space proteome of yeast mitochondria, *Mol Cell Proteomics* ***11***, 1840-1852.

[192] Ghosh, A., Pratt, A. T., Soma, S., Theriault, S. G., Griffin, A. T., Trivedi, P. P., and Gohil, V. M. (2016) Mitochondrial disease genes COA6, COX6B and SCO2 have overlapping roles in COX2 biogenesis, *Hum Mol Genet* ***25***, 660-671.

[193] Jett, K. A., and Leary, S. C. (2017) Building the CuA site of cytochrome c oxidase: a complicated, redox-dependent process driven by a surprisingly large complement of accessory proteins, *J Biol Chem* ***293***, 4644-4652.

[194] Timon-Gomez, A., Nyvltova, E., Abriata, L. A., Vila, A. J., Hosler, J., and Barrientos, A. (2017) Mitochondrial cytochrome c oxidase biogenesis: Recent developments, *Seminars in cell & developmental biology* ***76***, 163-178.

[195] Sreerama, N., and Woody, R. W. (2000) Estimation of protein secondary structure from circular dichroism spectra: comparison of CONTIN, SELCON, and CDSSTR methods with an expanded reference set, *Anal Biochem* ***287***, 252-260.

[196] Harten, S. K., Oey, H., Bourke, L. M., Bharti, V., Isbel, L., Daxinger, L., Faou, P., Robertson, N., Matthews, J. M., and Whitelaw, E. (2015) The recently identified modifier of murine metastable epialleles, Rearranged L-Myc Fusion, is involved in maintaining epigenetic marks at CpG island shores and enhancers, *BMC biology* ***13***, 21.

[197] Wilkins, M. R., Lindskog, I., Gasteiger, E., Bairoch, A., Sanchez, J. C., Hochstrasser, D. F., and Appel, R. D. (1997) Detailed peptide characterization using PEPTIDEMASS--a World-Wide-Web-accessible tool, *Electrophoresis* ***18***, 403-408.

[198] Johnston, A. J., Hoogenraad, J., Dougan, D. A., Truscott, K. N., Yano, M., Mori, M., Hoogenraad, N. J., and Ryan, M. T. (2002) Insertion and assembly of human tom7 into the preprotein translocase complex of the outer mitochondrial membrane, *J Biol Chem* ***277***, 42197-42204.

[199] McKenzie, M., Lazarou, M., Thorburn, D. R., and Ryan, M. T. (2007) Analysis of mitochondrial subunit assembly into respiratory chain complexes using Blue Native polyacrylamide gel electrophoresis, *Anal Biochem* ***364***, 128-137.

[200] Schneider, C. A., Rasband, W. S., and Eliceiri, K. W. (2012) NIH Image to ImageJ: 25 years of image analysis, *Nature methods* ***9***, 671-675.

[201] Otwinowski, Z., and Minor, W. (1997) [20] Processing of X-ray diffraction data collected in oscillation mode, *Methods Enzymol* ***276***, 307-326.

[202] Winn, M. D., Ballard, C. C., Cowtan, K. D., Dodson, E. J., Emsley, P., Evans, P. R., Keegan, R. M., Krissinel, E. B., Leslie, A. G., McCoy, A., McNicholas, S. J., Murshudov, G. N., Pannu, N. S., Potterton, E. A., Powell, H. R., Read, R. J., Vagin, A., and Wilson, K. S. (2011) Overview of the CCP4 suite and current developments, *Acta Crystallogr D Biol Crystallogr* ***67***, 235-242.

[203] Emsley, P., Lohkamp, B., Scott, W. G., and Cowtan, K. (2010) Features and development of Coot, *Acta Crystallogr D Biol Crystallogr* ***66***, 486-501.

[204] Murshudov, G. N., Skubak, P., Lebedev, A. A., Pannu, N. S., Steiner, R. A., Nicholls, R. A., Winn, M. D., Long, F., and Vagin, A. A. (2011) REFMAC5 for the refinement of macromolecular crystal structures, *Acta Crystallogr D Biol Crystallogr* ***67***, 355-367.

[205] Chen, V. B., Arendall, W. B., 3rd, Headd, J. J., Keedy, D. A., Immormino, R. M., Kapral, G. J., Murray, L. W., Richardson, J. S., and Richardson, D. C. (2010) MolProbity: all-atom structure validation for macromolecular crystallography, *Acta Crystallogr D Biol Crystallogr* ***66***, 12-21.

[206] McCoy, A. J., Grosse-Kunstleve, R. W., Adams, P. D., Winn, M. D., Storoni, L. C., and Read, R. J. (2007) Phaser crystallographic software, *J Appl Crystallogr* ***40***, 658-674.

[207] Krissinel, E., and Henrick, K. (2007) Inference of macromolecular assemblies from crystalline state, *J Mol Biol* ***372***, 774-797.

[208] Chen, V. B., Arendall, W. B., 3rd, Headd, J. J., Keedy, D. A., Immormino, R. M., Kapral, G. J., Murray, L. W., Richardson, J. S., and Richardson, D. C. (2010) MolProbity: all-atom structure validation for macromolecular crystallography, *Acta Crystallogr D Biol Crystallogr* ***66***, 12-21.

[209] Blatch, G. L., and Lassle, M. (1999) The tetratricopeptide repeat: a structural motif mediating protein-protein interactions, *BioEssays : news and reviews in molecular, cellular and developmental biology* ***21***, 932-939.

[210] D'Andrea, L. D., and Regan, L. (2003) TPR proteins: the versatile helix, *Trends Biochem Sci* ***28***, 655-662.

[211] Kajava, A. V. (2001) Review: proteins with repeated sequence--structural prediction and modeling, *J Struct Biol* ***134***, 132-144.

[212] Mittl, P. R., and Schneider-Brachert, W. (2007) Sel1-like repeat proteins in signal transduction, *Cellular signalling* ***19***, 20-31.

[213] Andrade, M. A., Perez-Iratxeta, C., and Ponting, C. P. (2001) Protein repeats: structures, functions, and evolution, *J Struct Biol* ***134***, 117-131.

[214] Cerveny, L., Straskova, A., Dankova, V., Hartlova, A., Ceckova, M., Staud, F., and Stulik, J. (2013) Tetratricopeptide repeat motifs in the world of bacterial pathogens: role in virulence mechanisms, *Infect Immun* ***81***, 629-635.

[215] Deltcheva, E., Chylinski, K., Sharma, C. M., Gonzales, K., Chao, Y., Pirzada, Z. A., Eckert, M. R., Vogel, J., and Charpentier, E. (2011) CRISPR RNA maturation by trans-encoded small RNA and host factor RNase III, *Nature* ***471***, 602-607.

[216] Ong, S. E., Blagoev, B., Kratchmarova, I., Kristensen, D. B., Steen, H., Pandey, A., and Mann, M. (2002) Stable isotope labeling by amino acids in cell

culture, SILAC, as a simple and accurate approach to expression proteomics, *Molecular & cellular proteomics : MCP* ***1***, 376-386.

[217] Seabrook, S. A., and Newman, J. (2013) High-throughput thermal scanning for protein stability: making a good technique more robust, *ACS combinatorial science* ***15***, 387-392.

[218] Luthy, L., Grutter, M. G., and Mittl, P. R. (2004) The crystal structure of Helicobacter cysteine-rich protein C at 2.0 A resolution: similar peptide-binding sites in TPR and SEL1-like repeat proteins, *J Mol Biol* ***340***, 829-841.

[219] Luthy, L., Grutter, M. G., and Mittl, P. R. (2002) The crystal structure of Helicobacter pylori cysteine-rich protein B reveals a novel fold for a penicillin-binding protein, *J Biol Chem* ***277***, 10187-10193.

[220] Lawrence, M. C., and Colman, P. M. (1993) Shape complementarity at protein/protein interfaces, *J Mol Biol* ***234***, 946-950.

[221] Scheufler, C., Brinker, A., Bourenkov, G., Pegoraro, S., Moroder, L., Bartunik, H., Hartl, F. U., and Moarefi, I. (2000) Structure of TPR domain-peptide complexes: critical elements in the assembly of the Hsp70-Hsp90 multichaperone machine, *Cell* ***101***, 199-210.

[222] Brinker, A., Scheufler, C., Von Der Mulbe, F., Fleckenstein, B., Herrmann, C., Jung, G., Moarefi, I., and Hartl, F. U. (2002) Ligand discrimination by TPR domains. Relevance and selectivity of EEVD-recognition in Hsp70 x Hop x Hsp90 complexes, *J Biol Chem* ***277***, 19265-19275.

[223] Gatto, G. J., Jr., Geisbrecht, B. V., Gould, S. J., and Berg, J. M. (2000) Peroxisomal targeting signal-1 recognition by the TPR domains of human PEX5, *Nat Struct Biol* ***7***, 1091-1095.

[224] Lee, D. S., Flachsova, E., Bodnarova, M., Demeler, B., Martasek, P., and Raman, C. S. (2005) Structural basis of hereditary coproporphyria, *Proc Natl Acad Sci U S A* ***102***, 14232-14237.

[225] Gupta, N., and Ragsdale, S. W. (2011) Thiol-disulfide redox dependence of heme binding and heme ligand switching in nuclear hormone receptor rev-erb{beta}, *J Biol Chem* ***286***, 4392-4403.

[226] Soto, I. C., Fontanesi, F., Myers, R. S., Hamel, P., and Barrientos, A. (2012) A heme-sensing mechanism in the translational regulation of mitochondrial cytochrome c oxidase biogenesis, *Cell metabolism* ***16***, 801-813.

[227] Deredge, D. J., Huang, W., Hui, C., Matsumura, H., Yue, Z., Moenne-Loccoz, P., Shen, J., Wintrode, P. L., and Wilks, A. (2017) Ligand-induced allostery in the interaction of the Pseudomonas aeruginosa heme binding protein with heme oxygenase, *Proc Natl Acad Sci U S A* ***114***, 3421-3426.

[228] Hofbauer, S., Hagmuller, A., Schaffner, I., Mlynek, G., Krutzler, M., Stadlmayr, G., Pirker, K. F., Obinger, C., Daims, H., Djinovic-Carugo, K., and Furtmuller, P. G. (2015) Structure and heme-binding properties of HemQ (chlorite dismutase-like protein) from Listeria monocytogenes, *Arch Biochem Biophys* ***574***, 36-48.

[229] Gao, J. L., Kwan, A. H., Yammine, A., Zhou, X., Trewhella, J., Hugrass, B. M., Collins, D. A. T., Horne, J., Ye, P., Harty, D., Nguyen, K. A., Gell, D. A., and Hunter, N. (2018) Structural properties of a haemophore facilitate targeted elimination of the pathogen Porphyromonas gingivalis, *Nature communications* ***9***, 4097.

[230] Lad, L., Schuller, D. J., Shimizu, H., Friedman, J., Li, H., Ortiz de Montellano, P. R., and Poulos, T. L. (2003) Comparison of the heme-free and -bound crystal structures of human heme oxygenase-1, *J Biol Chem* ***278***, 7834-7843.

[231] Bianchetti, C. M., Yi, L., Ragsdale, S. W., and Phillips, G. N., Jr. (2007) Comparison of apo- and heme-bound crystal structures of a truncated human heme oxygenase-2, *J Biol Chem* ***282***, 37624-37631.

[232] Wardell, M., Wang, Z., Ho, J. X., Robert, J., Ruker, F., Ruble, J., and Carter, D. C. (2002) The atomic structure of human methemalbumin at 1.9 A, *Biochem Biophys Res Commun* ***291***, 813-819.

[233] Oosterheert, W., van Bezouwen, L. S., Rodenburg, R. N. P., Granneman, J., Forster, F., Mattevi, A., and Gros, P. (2018) Cryo-EM structures of human STEAP4 reveal mechanism of iron(III) reduction, *Nature communications* ***9***, 4337.

[234] Cliff, M. J., Harris, R., Barford, D., Ladbury, J. E., and Williams, M. A. (2006) Conformational diversity in the TPR domain-mediated interaction of protein phosphatase 5 with Hsp90, *Structure* ***14***, 415-426.

[235] Schuck, P. (2000) Size-distribution analysis of macromolecules by sedimentation velocity ultracentrifugation and lamm equation modeling, *Biophys J* ***78***, 1606-1619.

[236] Kabsch, W. (2010) XDS, *Acta Crystallogr D Biol Crystallogr* ***66***, 125-132.

[237] Evans, P. R., and Murshudov, G. N. (2013) How good are my data and what is the resolution?, *Acta Crystallogr D Biol Crystallogr* ***69***, 1204-1214.